A Precision Measurement of the Spin Structure Functions *g(p/1)* and *g(d/1)**

Terrence S. Toole

Stanford Linear Accelerator Center
Stanford University
Stanford, CA 94309

SLAC-Report-735
December 2000

Prepared for the Department of Energy
under contract number DE-AC02-76SF00515

Printed in the United States of America. Available from the National Technical Information Service, U.S. Department of Commerce, 5285 Port Royal Road, Springfield, VA 22161.

*Ph.D. thesis, American University, Washington, DC 20016

A PRECISION MEASUREMENT OF THE SPIN STRUCTURE FUNCTIONS g_1^p AND g_1^d

by

Terrence S. Toole

submitted to the

Faculty of the College of Arts and Sciences

of American University

in Partial Fulfillment of

the Requirements for the Degree

of Doctor of Philosophy

in

Physics

Chair:

Stephen E. Rock

Raymond G. Arnold

Peter E. Bosted

Larry R. Medsker

Dean of the College

Date

2000

American University

Washington, D.C. 20016

A PRECISION MEASUREMENT OF THE

SPIN STRUCTURE FUNCTIONS $\mathbf{g}_1^p$ AND $\mathbf{g}_1^d$

BY

Terrence S. Toole

ABSTRACT

In Experiment E155 at the Stanford Linear Accelerator Center, the spin dependent structure function $g_1(x, Q^2)$ was measured for both the proton and deuteron. This was accomplished by scattering 48.3 GeV highly polarized electrons (0.813 ± 0.020) off polarized $^{15}NH_3$ (proton) and ^{6}LiD (deuteron) targets. Data were collected in March and April of 1997 using three fixed angle, momentum analyzing spectrometers centered at 2.75°, 5.5°, and 10.5°. This enabled a kinematic coverage of $0.01 < x < 0.9$ and $1\,\mathrm{GeV}^2 < Q^2 < 40\,\mathrm{GeV}^2$. At an average Q^2 of $5\,\mathrm{GeV}^2$, the integrals in the measured region were $\int_{0.014}^{0.9} g_1(x)dx = 0.119 \pm 0.002(\mathrm{stat.}) \pm 0.009(\mathrm{syst.})$ for the proton and $0.043 \pm 0.003(\mathrm{stat.}) \pm 0.003(\mathrm{syst.})$ for the deuteron. Using a perturbative QCD analysis which included a global data set, the results were found to be consistent with the Bjorken Sum Rule.

Asymmetry measurements also were made using photoproduced hadrons. Data were collected concurrently with the g_1 data. For the proton, the asymmetries were small and non-zero. The deuteron measurements were consistent with zero.

ACKNOWLEDGEMENTS

Many thanks to my advisor Steve Rock and the rest of the AU/UMass group at SLAC: Ray Arnold, Peter Bosted, and Zen Szalata. All have been incredibly generous with their time and expertise. I have found the group's enthusiasm for work and for life to be contagious. Also, I have had the good fortune to work closely with Peter, who has provided me with an example towards which to strive. Thanks to Larry Medsker for taking time out of his busy schedule to participate on my committee.

I also would like to thank my collaborators on the E154/E155 experiments and the SLAC staff. The success of both experiments would not have been possible without the countless hours of effort put in by the many people involved. My fellow E155 dissertation students, Paul King, Greg Mitchell, Paul McKee, Al Tobias, and Frank Wesselmann, were a pleasure to work with and learn from. I look forward to crossing paths with all of them many times in the future.

Special thanks to Lee Sorrell. He has been a great help during my entire involvement in E155. The quality of my education and life has been bumped up a few notches due to Lee.

I would like to express my gratitude to some people back at the American

University home office in Washington, DC who have made my experience with the program a positive one. Bruce Flanders, Howard Reiss, and Romeo Segnan were great to study under and I am glad that they made themselves as accessible as they did. Yana Shabaev, Amy Roberts, Kathleen Workman, and Marlene Temes were always enjoyable to talk with and have helped me out more times than I can count. My life around the physics department was made better by the presence of my fellow students such as Paul Depietro, Sam Gompers, and Niki Hatzilambrau.

Life at and around SLAC was quite good thanks to many of the people mentioned above as well as Nawal Benmouna, Steve Churchwell, Robin Erbacher, Dave Reyna, Mike Woods and the SLAC Spinors, and the SLAC Soccer Club. Extra thanks to Greg Mitchell, with whom I have had the pleasure of many wonderful and diverse conversations.

The support of my family over the years is much appreciated. My folks and my brother and sisters were always interested in hearing how things were going. Their phone calls, emails, and visits were often highpoints in the time surrounding them.

Most of all, thanks to my wife Julie for taking a chance and coming out to California with me. Her patience, love, support, encouragement, and patience[1] while I was working on this dissertation and everything else during the last few years was more than I could have ever hoped to receive.

[1] Julie was really patient.

CONTENTS

LIST OF TABLES

LIST OF FIGURES

CHAPTER 1

INTRODUCTION

One of the defining characteristics of a nucleon is its spin. Explaining how the spin is distributed among the nucleon's components has been the driving force behind a collection of experiments which have been performed over the past few decades. The spin is often thought of in terms of three pieces,

$$\frac{1}{2} = \frac{1}{2}\Delta\Sigma + \Delta G + L_z, \tag{1}$$

where $\Delta\Sigma$ and ΔG are the net spin contributions from the quarks and gluons respectively, and L_z is the contribution from the orbital angular momentum of the components. While some information is available regarding the quark contribution, very little is known about that of the gluons, and virtually nothing is known of the orbital angular momentum term. The efforts of the E155 collaboration, which will be the focus of this dissertation, were aimed at providing a clearer picture of the spin structure of the nucleon, including a more precise determination of the $\Delta\Sigma$ term as well as improving the constraints on ΔG. However, these quantities are not directly observable. Instead, they are extracted from the measurements of the spin structure functions g_1 and g_2. From these measurements, $\Delta\Sigma$ can be determined.

CHAPTER 2

THEORETICAL BACKGROUND

2.1 Deep Inelastic Scattering

In E155, g_1 and g_2 were measured by the Deep Inelastic Scattering (DIS) of polarized electrons off polarized nucleons. The one photon exchange diagram for this process is shown in Figure 1. In the top half of the diagram an incident electron with four momentum $k = (E_0, p)$ and spin s interacts with the target nucleon and scatters with $k' = (E', p')$ at an angle θ in the lab frame relative to the direction of the incident electron[1]. Only the energy and direction of the scattered electron are required to determine $G_{1,2}$ (which are related to $g_{1,2}$). This upper vertex can be described by the lepton tensor [1]

$$L_{\mu\nu} = 2[\underbrace{k_\mu k'_\nu + k'_\mu k_\nu - g_{\mu\nu}(k \cdot k' - m^2)}_{L^{(S)}_{\mu\nu}} + \underbrace{im\epsilon_{\mu\nu\rho\sigma}q^\rho s^\sigma}_{L^{(A)}_{\mu\nu}}] \tag{1}$$

where m is the electron mass, $g_{\mu\nu}$ is the metric tensor, and $\epsilon_{\mu\nu\rho\sigma}$ is the antisymmetric Levi-Cevità tensor ($\epsilon_{0123} = 1$). In the lower half of Figure 1 the nucleon is struck by a virtual photon of four momentum squared $q^2 = (k - k')^2 = -4EE' \sin^2\left(\frac{\theta}{2}\right)$. For a large enough q^2, the virtual photon hits a parton inside the nucleon, the nucleon is blown apart, and the fragments (X) hadronize.

[1] The spin of the scattered electron is not measured. A sum is performed over the final spin states.

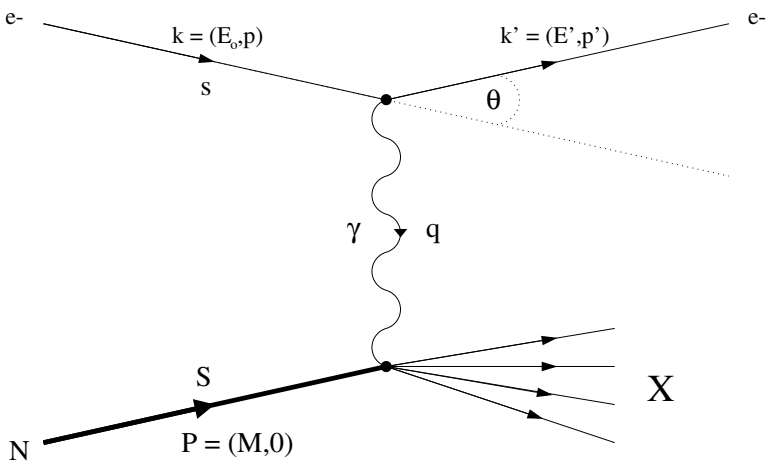

Figure 1: One photon exchange diagram for deep inelastic scattering of an electron of a nucleon.

As with the $e^- - \gamma^*$ vertex, a hadronic tensor ($W^{\mu\nu}$) can be associated with the γ^*-nucleon vertex. This tensor can be separated into symmetric and asymmetric parts ($W^{\mu\nu}_{(S)} + W^{\mu\nu}_{(A)}$) [1],

$$W^{\mu\nu}_{(S)} = \left(-g^{\mu\nu} + \frac{q^\mu q^\nu}{q^2}\right) W_1(\nu, q^2) + \left[\left(P^\mu - \frac{P\cdot q}{q^2} q^\mu\right)\left(P^\nu - \frac{P\cdot q}{q^2} q^\nu\right)\right] \frac{W_2(\nu,q^2)}{M^2} \quad (2)$$

and

$$W^{\mu\nu}_{(A)} = i\epsilon^{\mu\nu\lambda\sigma} q_\lambda \left\{ S_\sigma M G_1(\nu, q^2) + [(P\cdot q) S_\sigma - (S\cdot q) P_\sigma] \frac{G_2(\nu,q^2)}{M} \right\}, \quad (3)$$

where the nucleon has four momentum P, mass M, and spin S. The symmetric piece is expressed in terms of two spin independent structure functions W_1 and W_2. In a similar manner, the asymmetric piece only relies on G_1 and G_2, spin dependent structure functions. All four structure functions are dependent on the energy lost by the electron during the interaction ($\nu = E - E' = \frac{P\cdot q}{M}$) and the momentum transfer (q^2).

The electron-nucleon scattering can be described by the differential cross section [2]

$$\frac{d^2\sigma}{d\Omega dE'} = \frac{\alpha^2}{2Mq^4}\frac{E'}{E}L_{\mu\nu}W^{\mu\nu}. \tag{4}$$

Here Ω is the solid angle and α is the fine structure constant. Expanding Equation 4 with $L^{(S,A)}_{\mu\nu}$ and $W^{\mu\nu}_{(S,A)}$ gives

$$\frac{d^2\sigma}{d\Omega dE'} = \frac{\alpha^2}{2MQ^4}\frac{E'}{E}\left\{L^{(S)}_{\mu\nu}W^{\mu\nu}_{(S)} + L^{(A)}_{\mu\nu}W^{\mu\nu}_{(A)}\right\} \tag{5}$$

where the cross terms cancel. In Equation 5 a change of variables has been made of $Q^2 = -q^2$ where $Q^2 > 0$ GeV^2.

By summing over the spin of the incident electron, one can isolate the spin independent (symmetric) term,

$$\frac{d^2\sigma^{\downarrow\Uparrow}}{d\Omega dE'} + \frac{d^2\sigma^{\uparrow\Uparrow}}{d\Omega dE'} = \frac{8\alpha^2(E')^2}{Q^4}\left\{2\sin^2\left(\frac{\theta}{2}\right)W_1(\nu,Q^2) + \cos^2\left(\frac{\theta}{2}\right)W_2(\nu,Q^2)\right\}, \tag{6}$$

where the arrows $\downarrow\Uparrow$ ($\uparrow\Uparrow$) indicate when the spins of the electron and nucleon were anti-parallel (parallel).

If both of the initial particles are polarized, as in E155, the spin dependent (asymmetric) term in Equation 5 can be isolated by taking the difference of two cross sections with opposite incident electron spins[2]. This is because the asymmetric piece of Equation 1 changes sign when the electron spin is reversed.

$$\frac{d^2\sigma^{\downarrow\Uparrow}}{d\Omega dE'} - \frac{d^2\sigma^{\uparrow\Uparrow}}{d\Omega dE'} = \frac{4\alpha^2E'}{EQ^2}\left\{(E + E'\cos\theta)MG_1(\nu,Q_2) - Q^2G_2(\nu,Q_2)\right\} \tag{7}$$

[2] Also, keeping the electron spin constant and taking the difference of cross sections with opposite nucleon spins would obtain the same result. This is what is done by SMC [4] with muons taking the place of electrons.

In the Bjorken limit [3] of

$$Q^2 \to \infty, \quad \nu \to \infty, \quad \frac{\nu}{Q^2} \text{ fixed} \tag{8}$$

the four structure functions approximately scale *i.e.,* they are independent of Q^2,

$$\left.\begin{aligned} \lim_{Bj} MW_1(\nu, Q^2) &= F_1(x), \\ \lim_{Bj} \nu W_2(\nu, Q^2) &= F_2(x), \\ \lim_{Bj} \tfrac{\nu}{M} G_1(\nu, Q^2) &= g_1(x), \\ \text{and} \qquad \lim_{Bj} \tfrac{\nu^2}{M^2} G_2(\nu, Q^2) &= g_2(x), \end{aligned}\right\} \tag{9}$$

where the variable $x = \frac{Q^2}{2M\nu}$ is the fraction of the nucleon's momentum carried by the struck quark. This is known as Bjorken scaling and approximately holds for $Q^2 \gtrsim 1\,\mathrm{GeV}^2$. The qualifier *approximately* is used because there is a logarithmic dependence on Q^2. For this reason, $F_{1,2}$ and $g_{1,2}$ will be written as functions of both x and Q^2. This scaling arises because the interactions between the partons take much longer than the DIS virtual photon exchange. So the parton-parton interactions can be ignored in the hard scattering calculation. For the case at hand, where the photon can be assumed to be hitting a free parton [5], this is known as asymptotic freedom.

Instead of directly measuring the cross sections in Equations 6 and 7 and then taking the difference, asymmetries (see Equation 10 and 11) are calculated in which the ratios of the differences and sums of the cross sections are considered. With asymmetries, factors due to the acceptance of the spectrometers cancel out, thus reducing the sensitivity to systematic uncertainties and ultimately making the

measurement less difficult.

$$A_{\parallel}(x,Q^2) = \frac{\sigma^{\downarrow\Uparrow} - \sigma^{\uparrow\Uparrow}}{\sigma^{\downarrow\Uparrow} + \sigma^{\uparrow\Uparrow}} \tag{10}$$

$$A_{\perp}(x,Q^2) = \frac{\sigma^{\downarrow\Leftarrow} - \sigma^{\uparrow\Leftarrow}}{\sigma^{\downarrow\Leftarrow} + \sigma^{\uparrow\Leftarrow}} \tag{11}$$

For visual clarity, the shorthand notation of $\sigma^{\downarrow\Uparrow}$ for $\frac{d^2\sigma^{\downarrow\Uparrow}}{d\Omega dE'}$ has been used. Equation 11 is for a nucleon polarized perpendicular to the incident electron beam but in the scattering plane. $A_{\parallel}(x,Q^2)$ and $A_{\perp}(x,Q^2)$ are closer to the quantities that get measured in the lab. In terms of $A_{\parallel}$ and $A_{\perp}$, $g_1(x,Q^2)$ and $g_2(x,Q^2)$ can be expressed as [6]

$$g_1(x,Q^2) = \frac{F_1(x,Q^2)}{D'}\left[A_{\parallel}(x,Q^2) + \tan\left(\frac{\theta}{2}\right)A_{\perp}(x,Q^2)\right] \tag{12}$$

and

$$g_2(x,Q^2) = \frac{F_1(x,Q^2)}{D'}\frac{y}{2\sin(\theta)} \times \left[\frac{[E + E'\cos(\theta)]}{E'}A_{\perp}(x,Q^2) - \sin(\theta)A_{\parallel}(x,Q^2)\right], \tag{13}$$

where $y = \nu/E$ and D' is a depolarization factor given by

$$D' = \frac{(1-\epsilon)(2-y)}{y[1+\epsilon R(x,Q^2)]}. \tag{14}$$

The quantity ϵ is the relative longitudinal polarization of the virtual photon and $R(x,Q^2)$ is the ratio of longitudinal to transverse virtual photon absorption cross sections. These terms will be discussed in the next section.

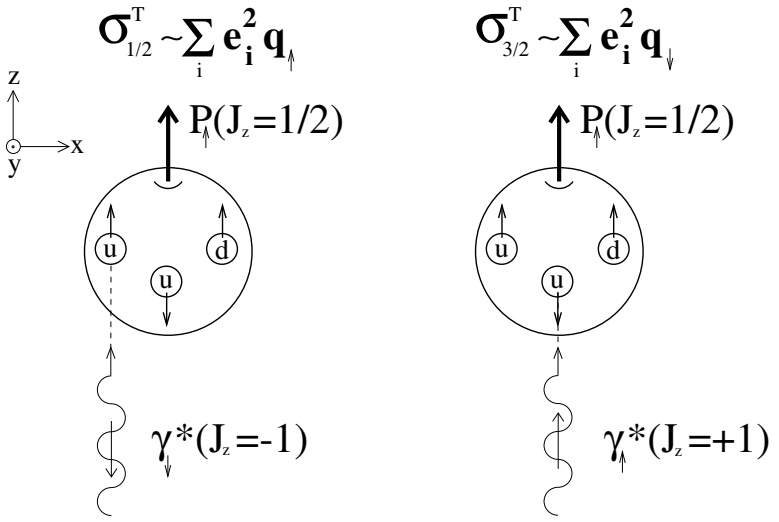

Figure 2: Virtual photon absorption by a simple, three quark proton.

2.2 Virtual Photon - Nucleon Asymmetries

Another set of asymmetries which are related to polarized DIS are the virtual photon-nucleon asymmetries [2, 7, 8, 9]. To look at the interaction in terms of the virtual photon is useful because it is the actual probe being used to study the substructure of the nucleon. These asymmetries use the absorption cross sections ($\sigma^T_{1/2}$ and $\sigma^T_{3/2}$) for a transversely polarized[3] virtual photon γ^* (spin ± 1) by a nucleon whose spin is oriented along the photon's direction of travel. A cartoon of the $\gamma^* p$ interaction is shown in Figure 2, where a simple three quark model of the proton is used. The photon is traveling along the z axis. J_z is the z component of the total angular momentum which in this simple model is all spin (i.e., no orbital angular

[3]By convention, a transversely polarized photon has its spin (± 1) oriented along the direction of travel. As used here, *transverse* describes the direction of the electric and magnetic components of the photon. Additionally, a virtual photon can be longitudinally polarized, in which case the spin is oriented perpendicular to the axis of travel resulting in a helicity of 0. In contrast, in fixed target electron scattering, a longitudinally polarized electron or proton refers to particle's spin being oriented along the direction of the incident electron.

momentum). In the drawing on the left, a virtual photon with negative helicity is incident on proton of ($J_z = +\frac{1}{2}$). Since the quark which interacts with the γ^* will get its spin flipped [2], only the $u(s_z = +\frac{1}{2})$ and $d(s_z = +\frac{1}{2})$ quarks can interact. The $\sigma_{1/2}$ cross section describes this interaction, where the subscript comes from the total $J_z = J_z^{\gamma^*} + J_z^p$ of the system. On the right side of Figure 2, the $\sigma_{3/2}$ case is depicted. Here a virtual photon with positive helicity can only interact with a $q(s_z = -\frac{1}{2})$, which for this example is a u quark.

The virtual photon - nucleon cross sections can be expressed in terms of the four structure functions $g_{1,2}$ and $F_{1,2}$ [7],

$$\sigma_{1/2}^T = \frac{4\pi^2\alpha}{MK}\left(F_1 + g_1 - \frac{2Mx}{\nu}g_2\right), \quad (15)$$

$$\sigma_{3/2}^T = \frac{4\pi^2\alpha}{MK}\left(F_1 - g_1 + \frac{2Mx}{\nu}g_2\right), \quad (16)$$

$$\sigma_{1/2}^L = \frac{4\pi^2\alpha}{K}\left[\frac{F_2}{\nu}\left(1 + \frac{\nu^2}{Q^2}\right) - \frac{1}{M}F_1\right], \quad (17)$$

and

$$\sigma_{3/2}^{TL} = \frac{4\pi^2\alpha}{K}\frac{\sqrt{Q^2}}{M\nu}\left(g_1 + g_2\right), \quad (18)$$

where $K = \nu - Q^2/(2M)$ is the incoming photon flux. By averaging Equations 15 and 16, one gets the total transverse cross section $\sigma_T = 1/2(\sigma_{1/2}^T + \sigma_{3/2}^T)$. The cross section $\sigma_{1/2}^L$ (or σ_L) is for a longitudinally polarized γ^* (helicity = 0) incident on a proton of helicity = $\pm\frac{1}{2}$. However, the simple cartoons of Figure 2 do not lend themselves well to an interpretation of σ_L. The cross section $\sigma_{1/2}^{TL}$ (or σ_{TL}) is an interference term between the transverse and longitudinal amplitudes.

Using the cross sections listed above, the virtual photon - nucleon asymme-

tries can be expressed as

$$A_1 = \frac{\sigma_{1/2} - \sigma_{3/2}}{\sigma_{1/2} + \sigma_{3/2}} = \frac{A_\parallel}{D(1+\eta\zeta)} - \frac{\eta A_\perp}{d(1+\eta\zeta)} \quad (19)$$

and

$$A_2 = \frac{\sigma_{TL}}{\sigma_L} = \frac{\zeta A_\parallel}{D(1+\eta\zeta)} + \frac{A_\perp}{d(1+\eta\zeta)} \quad (20)$$

or conversely,

$$A_\parallel(x,Q^2) = D(A_1 + \eta A_2) \quad (21)$$

and

$$A_\perp(x,Q^2) = d(A_2 - \zeta A_1). \quad (22)$$

The kinematic factors used in Equation 21 and 22 are

$$\epsilon = \frac{1}{1 + 2[1 + \frac{Q^2}{4M^2x^2}]\tan^2(\frac{\theta}{2})}, \quad (23)$$

$$\zeta = \frac{\eta(1+\epsilon)}{2\epsilon}, \quad (24)$$

$$\eta = \frac{\epsilon\sqrt{Q^2}}{E - E'\epsilon}, \quad (25)$$

$$D = \frac{1 - \frac{E'}{E}\epsilon}{1 + \epsilon R(x,Q^2)}, \quad (26)$$

and

$$d = D\sqrt{\frac{2\epsilon}{1+\epsilon}}. \quad (27)$$

$R(x,Q^2) = \sigma_L/\sigma_T$ is the ratio of longitudinal to transverse virtual photon absorption cross sections. For E155 kinematics, R was was typically around 0.2 [11].

As mentioned earlier, ϵ is called the relative longitudinal polarization of the virtual photon. In the literature [2], ϵ is often introduced in the expression for the spin averaged cross section $d^2\sigma/d\Omega dE' = \Gamma(\sigma_T + \epsilon\sigma_L)$ and indicates the contribution of the longitudinal cross section to the total. Γ is the virtual photon flux. So as $\epsilon \to 0$, the σ_L term (*i.e.* 0 helicity term) drops out leaving the spin averaged cross

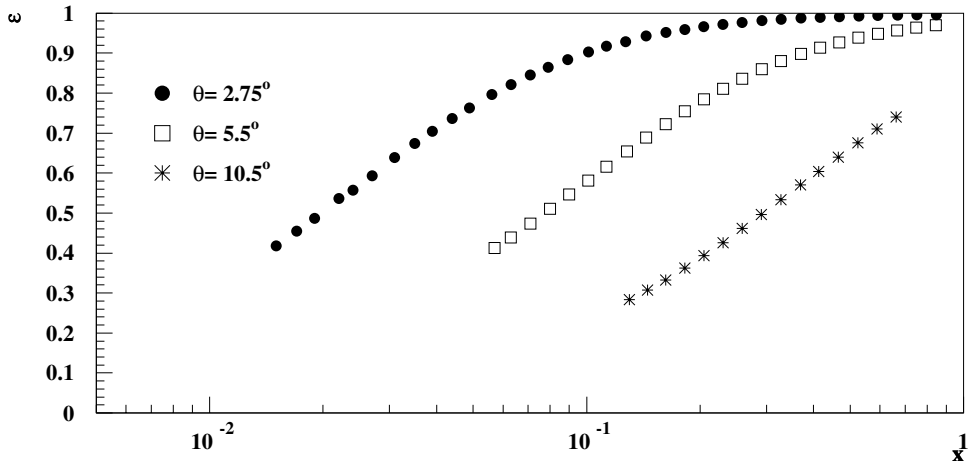

Figure 3: The relative longitudinal polarization of the virtual photon versus x at E155 kinematics.

section to be dominated by the σ_T term. Typical ϵ values at E155 kinematics are shown in Figure 3.

D is called the depolarization factor of the virtual photon. The spin of the incident electron ($\pm 1/2$) is along the the electron's direction of travel. Similarly, the spin of the virtual photon will be parallel (± 1) or perpendicular (0) to the photon's direction of travel. Since the direction of travel for the photon does not necessarily coincide with that of the incident electron, the average helicity of the photon will be less than that of the electron. D reflects the amount of helicity carried off by the virtual photon. From Equation 26 one can show that as $\epsilon \to 0(1)$, D tends toward 1(0). For a virtual photon emitted collinear to the axis of the incident electron, $D = 1$ corresponding to a photon with only longitudinal spin, *i.e.,* a real photon.

η is a kinematic factor that was small for E155 ($\lesssim 0.4$), often less than 0.1. This suppresses the A_2 term in Equation 21 making $A_{\parallel}$ more sensitive to A_1. A

similar relationship existed between A_2 and $A_\perp$ in Equation 22. This arose from $\zeta \approx \eta$ for the range of ϵ values relevant to E155. The net result was a suppression of the A_1 term in Equation 22. This enhanced relationship between A_2 and $A_\perp$ was important in E155x, the follow-up experiment to E155 which focused on $g_2(x, Q^2)$.

Lastly, there are limits on the magnitudes of A_1 and A_2 [12, 13],

$$|A_1| < 1 \quad \text{and} \quad |A_2| \leq \sqrt{\frac{R(1+A_1)}{2}}. \tag{28}$$

These are known as the "positivity constraints".

2.3 Quark Parton Model

One of the events which motivated E155 was the so called "Spin Crisis" of the late 1980's [14]. The spin crisis happened under the light of the naive Quark Parton model (nQPM). In this model, the partons had no transverse motion and therefore no orbital angular momentum ($L_z = 0$ in Equation 1). Also, the gluons did not make a significant contribution to the net spin of the nucleon ($\Delta G = 0$). Thus for the nQPM, the quarks were expected to carry all of the spin ($\Delta\Sigma = 1$). However, the CERN experiment EMC [15, 16] found a net quark spin of $\simeq 0.12 \pm 0.17$, which was much less than 1 (and consistent with 0). Even though the "spin crisis" only existed in the nQPM interpretation [1], it provided the impetus for increased theoretical and experimental activity in the area of spin physics.

In the Quark Parton Model (QPM), the nucleon is made up of gluons and current quarks. The quarks can be separated further into two groups, valence quarks and a sea of virtual quark-antiquark pairs. The gluons and quarks move and interact

leaving the composition of the sea in a constant state of change. However, the time scale for change is greater than the interaction time of the virtual photon (*i.e.*, the impulse approximation) and so, via DIS, a snapshot of the internal structure of the nucleon can be taken. The snapshots are in terms of parton distribution functions (PDFs) which give the probability that the virtual photon struck a parton of momentum fraction x. The spin averaged distribution functions are given as

$$q(x,Q^2) = q_+(x,Q^2) + q_-(x,Q^2) \tag{29}$$

and

$$\overline{q}(x,Q^2) = \overline{q}_+(x,Q^2) + \overline{q}_-(x,Q^2), \tag{30}$$

where q or $\overline{q}$ is the flavor of the quark or anti-quark. The + (-) indicates that the quark spin is parallel (anti-parallel) to that of the parent nucleon. The separation into positive and negative helicities is done in expectation of the polarized distribution functions which are introduced below. Using Equations 29 and 30, the spin independent structure functions F_1 and F_2 can be expressed at leading order as

$$F_1^p(x,Q^2) = \frac{1}{2}\sum_q e_q^2 \left[q(x,Q^2) + \overline{q}(x,Q^2)\right] \tag{31}$$

and

$$F_2^p(x,Q^2) = x\sum_q e_q^2 \left[q(x,Q^2) + \overline{q}(x,Q^2)\right], \tag{32}$$

where e_q is the electric charge. The sum is only over the light quark flavors (u, d, and s) for the beam energies used at SLAC. Combining Equations 31 and 32 gives the Callan-Gross relation [17] $2xF_1(x,Q^2) = F_2(x,Q^2)$.

The polarized distribution functions are obtained by taking the difference,

$$\Delta q(x,Q^2) = q_+(x,Q^2) - q_-(x,Q^2) \tag{33}$$

and $$\Delta\overline{q}(x,Q^2) \;=\; \overline{q}_+(x,Q^2) - \overline{q}_-(x,Q^2). \tag{34}$$

Similar to the spin independent case, the spin structure function g_1 can be expressed at leading order as

$$g_1^p(x,Q^2) = \frac{1}{2}\sum_q e_q^2 \left[\Delta q(x,Q^2) + \Delta\overline{q}(x,Q^2)\right] \tag{35}$$

Ignoring the explicit dependence on Q^2, this is also the expression for $g_1(x)$ in the nQPM. The gluons do not contribute directly at this level. One reason for this is because the gluons have no electric charge. However, the gluons do come into play indirectly in the Q^2 evolution of g_1.

The first moment of g_1 is obtained by integrating Equation 35 over x.

$$\Gamma_1^p(Q^2) \;=\; \int_0^1 g_1^p(x,Q^2)dx \tag{36}$$

$$\;=\; \frac{1}{2}\left[\frac{4}{9}\Delta u(Q^2) + \frac{1}{9}\Delta d(Q^2) + \frac{1}{9}\Delta s(Q^2)\right] \tag{37}$$

where the contributions from light quarks have been listed explicitly and $\Delta q(Q^2) = \int_0^1 [\Delta q(x,Q^2) + \Delta\overline{q}(x,Q^2)]dx$. Assuming isospin symmetry, the above equations can be modified to describe the neutron by exchanging the coefficients of the u and d quarks' contributions. The first moment of g_1^n is then

$$\Gamma_1^n(Q^2) = \frac{1}{2}\left[\frac{1}{9}\Delta u(Q^2) + \frac{4}{9}\Delta d(Q^2) + \frac{1}{9}\Delta s(Q^2)\right]. \tag{38}$$

In experiments, the neutron information is often obtained by considering measurements taken on proton and deuteron targets. E155 used solid ^{6}LiD for this purpose. The deuteron structure function $g_1^d(x,Q^2)$ can be treated as an average of

those for the proton and neutron,

$$g_1^d(x,Q^2) = \frac{g_1^p(x,Q^2) + g_1^n(x,Q^2)}{2}(1 - 1.5\omega_D), \tag{39}$$

where $\omega_D = 0.05 \pm 0.01$ is the probability for the deuteron to be in the D-state [44]. This correction corresponds to the deuteron being in the ground state, with the proton and neutron spins aligned, about 93% of the time. By measuring both the proton and deuteron, the neutron's spin structure function g_1^n can be extracted via Equation 39.

Using SU(3) flavor decomposition the quark distributions can be related to singlet (a_0) and non-singlet (a_3, a_8) proton matrix elements [20]

$$\begin{aligned} a_0 &= \Delta u(Q^2) + \Delta d(Q^2) + \Delta s(Q^2) &&= \Delta\Sigma(Q^2), \\ a_3 &= \Delta u(Q^2) - \Delta d(Q^2) &&= F + D, \\ \text{and} \quad a_8 &= \Delta u(Q^2) + \Delta d(Q^2) - 2\Delta s(Q^2) &&= 3F - D, \end{aligned}$$

where the non-singlet elements are also related to the neutron and hyperon β decay coupling constants F and D. The values for these two constants used in the E155 analysis were $F = 0.463 \pm 0.008$ and $D = 0.804 \pm 0.008$ [21, 22].

After rewriting the first moments of $g_1^{p,n}$ in terms of the non-singlet and singlet matrix elements, and taking into account pQCD corrections to $\mathcal{O}\left(\frac{\alpha_s(Q^2)}{\pi}\right)^3$ [23, 25], Equations 37 and 38 become

$$\Gamma_1^{p,n}(Q^2) = \left(\pm\frac{1}{12}a_3 + \frac{1}{36}a_8\right) \times \left[1 - \frac{\alpha_s(Q^2)}{\pi} - 3.5833\left(\frac{\alpha_s(Q^2)}{\pi}\right)^2 - 20.2153\left(\frac{\alpha_s(Q^2)}{\pi}\right)^3\right] + \frac{1}{9}\Delta\Sigma(Q^2)\left[1 - 0.33333\frac{\alpha_s(Q^2)}{\pi} - 0.54959\left(\frac{\alpha_s(Q^2)}{\pi}\right)^2 - 4.44725\left(\frac{\alpha_s(Q^2)}{\pi}\right)^3\right]. \quad (40)$$

For Γ_1^p (Γ_1^n) the + (-) coefficient on the a_3 term is used. From these expressions for the proton and neutron and from Equation 39, the first moment of the deuteron can be written as

$$\Gamma_1^d(Q^2) = (1 - 1.5\omega_D)\left\{\frac{1}{36}a_8\left[1 - \frac{\alpha_s(Q^2)}{\pi} - 3.5833\left(\frac{\alpha_s(Q^2)}{\pi}\right)^2 - 20.2153\left(\frac{\alpha_s(Q^2)}{\pi}\right)^3\right] + \frac{1}{9}\Delta\Sigma(Q^2)\left[1 - 0.33333\frac{\alpha_s(Q^2)}{\pi} - 0.54959\left(\frac{\alpha_s(Q^2)}{\pi}\right)^2 - 4.44725\left(\frac{\alpha_s(Q^2)}{\pi}\right)^3\right]\right\}. \quad (41)$$

Note that because of the opposite signs on a_3 in Equation 40 for the proton and neutron, this term drops out when Γ_1^p and Γ_1^n are combined. The lack of an a_3 term has the effect of making Γ_1^d more sensitive to the net helicity of the quarks $\Delta\Sigma(Q^2)$ than either Γ_1^p or Γ_1^n.

More information can be gained by performing an NLO QCD fit to g_1. For such an analysis, polarized quark and gluon distributions are parametrized at an initial low value of Q^2 called Q_i^2. For E155 this was done in terms of unpolarized PDFs,

which reduced the number of free parameters. That the polarized and unpolarized PDFs are related is a reasonable assumption to make since they are describing the same quarks. Using the DGLAP equations [27], the polarized PDFs were evolved to the measured Q^2 of the data. The structure function g_1 was then calculated using

$$g_1(x,Q^2) = \frac{1}{2}\sum_q^{N_f} e_q^2 \left[C_q \otimes (\Delta q + \Delta\overline{q}) + \frac{1}{N_f} C_G \otimes \Delta G\right], \tag{42}$$

where the convolution is

$$(C_q \otimes \Delta q)(x,Q^2) = \int_x^1 \frac{dz}{z} C\left(\frac{x}{z},\alpha_s\right)\Delta q(z,Q^2) \tag{43}$$

for Δq. Similar expressions exists for $\Delta\overline{q}$ and ΔG. The coefficient functions are of the form [28]

$$C(x,\alpha_s) = \sum_{k=0}^{\infty}(\frac{\alpha_s}{2\pi})^k C^{(k)}(x). \tag{44}$$

At leading order $C_q^{(0)}(x) = \delta(1-x)$ and $C_G^{(0)}(x) = 0$, the gluon contribution drops out, and as expected Equation 42 reverts back Equation 35. The calculated and measured functions g_1 are compared by performing a χ^2 test. Based on the results of the fit, the parameters of the initial polarized parton distributions are adjusted to improve the agreement between the calculated and measured g_1. The process is iterated until the fit parameters converge.

One of the benefits of performing an NLO fit is that it provides a means of testing the polarized PDFs. The valence quarks tend to dominate in the mid to high x region where the quality and quantity of the data are quite good. For this reason the fits for the polarized valence quark distributions are well determined.

The ability to separate the flavors also exists, but it is limited to the valence quarks. In principle the polarized sea and gluon distributions can be obtained from an NLO pQCD analysis. However, with the present kinematic coverage of the data, both the sea quarks and gluons are poorly constrained.

The fitted g_1 also provides estimates of the shape and magnitude of the structure function in the unmeasured region. Quantities such as $\Gamma_1^{p,n,d}(Q^2)$, which are needed to evaluate sum rules, integrate $g_1(x,Q^2)$ over $0 \leq x \leq 1$. Since g_1 has only been measured for a limited range in x, the contributions from the unmeasured regions need to be estimated. How this is handled is especially important for the low x region, which is not well understood. There are indications that the low x contributions to $\Gamma_1(Q^2)$ may be significant.

In order to compare or combine data from different experiments, the data are evolved to a common Q^2. Traditionally this evolution was performed by assuming that g_1/F_1 was independent of Q^2. This assumption, which is consistent with the data within uncertainties, has no theoretical justification [26]. In the past few years, an alternative approach has been to use the results of the NLO QCD fits to evolve the data,

$$g_1^{exp}(x,Q_0^2) = g_1^{exp}(x,Q_{exp}^2) - \left[g_1^{fit}(x,Q_{exp}^2) - g_1^{fit}(x,Q_0^2)\right], \tag{45}$$

where exp indicates the measured quantities, fit indicates the functions obtained from the NLO QCD analysis, and the desired value of Q^2 is given by Q_0^2. The use of one method of Q^2 evolution over the other has little effect on the calculation

of $\Gamma_1(Q^2)$. Differences wash out due to the integration over x. However, there is more of an effect on the shape of the structure function, which in turn affects the extrapolation to the unmeasured, low x region. Although this method has been employed in the analysis of several groups, it was not the approach taken to achieve the final E155 results. This will be discussed further in Chapter 5.

2.4 Sum Rules

A collection of sum rules exists which arose from different theoretical models and assumptions about how the various components contribute to the spin of the nucleon. One example is Equation 1. Often referred to as the angular momentum sum rule, it separates the spin into quark, gluon, and orbital angular momentum subparts. Others such as the Bjorken Sum Rule (BSR) [30] or the Ellis-Jaffe Sum Rule (EJSR) [31] tend to focus more on the relationships between the spins of different quark flavors. In the past few years the BSR and EJSR have been tested to a reasonable degree of accuracy, through which the BSR has been verified and the EJSR has been shown to be violated. The E155 results were expected to confirm these results. Details of the Bjorken and Ellis-Jaffe sum rules are discussed in the following sections.

2.4.1 Bjorken Sum Rule

The Bjorken Sum Rule has been often referred to as a rigorous prediction of QCD, and that the success or failure of the two is intrinsically linked. This is

primarily due to the fundamental nature of the few assumptions that were used in its derivation. Originally derived using current algebra and assuming isospin symmetry, the sum rule actually pre-dates QCD. It has since been rederived in QCD by way of the Operator Product Expansion [32].

The sum rule relates the first moments of g_1^p and g_1^n to the axial (g_A) and vector (g_V) couplings obtained from neutron β-decay. In the Bjorken scaling limit the BSR can be expressed as

$$\int_0^1 \left[g_1^p(x,Q^2) - g_1^n(x,Q^2)\right] dx = \frac{1}{6}\frac{g_A}{g_V}. \tag{46}$$

A point worth noting is that while the l.h.s. of Equation 46 comes from high energy interactions, the r.h.s. is associated with low energy phenomena. Since tests of the BSR are performed at finite Q^2, which is low compared to the Bjorken limit of $Q^2 \to \infty$, higher order QCD corrections are needed to compare the predicted values with experiment. With these corrections to $\mathcal{O}(\alpha_s)^3$, Equation 46 becomes [23]

$$\Gamma_1^p(Q^2) - \Gamma_1^n(Q^2) = \frac{1}{6}\frac{g_A}{g_V}\left[1 - \frac{\alpha_s(Q^2)}{\pi} - 3.5833\left(\frac{\alpha_s(Q^2)}{\pi}\right)^2 - 20.2153\left(\frac{\alpha_s(Q^2)}{\pi}\right)^3\right]. \tag{47}$$

The correction is the same as the non-singlet correction in Equation 40. Plugging that equation into the l.h.s. of Equation 47, one can see that the singlet term $\Delta\Sigma(Q^2)$ and the non-singlet a_8 cancel. The a_3 term survives, which is independent of a $\Delta s(Q^2)$ contribution (see page 14).

Even though the BSR was originally derived in the mid 1960s, it was not

seriously tested until the early 1990s[4]. The reason for this was the lack of a polarized neutron target. SLAC E142 [38] performed the first test using a ^{3}He target and SMC was the first to use a deuteron target [34]. Since then both ^{3}He and various deuteron targets have been used as a means of determining the neutron term in the BSR. So far the sum rule has been confirmed with an accuracy of about 8% [35].

Since there are no theoretical reasons to expect that the BSR will be violated [36], some groups have assumed its validity in order to extract α_s from the polarized DIS data [35, 36]. The results from these analyses were promising, but more precise data were needed in order to make a determination of α_s that is competitive with other approaches to measuring the quantity. E155 will help in this effort by providing the most precise data on $g_1^p(x, Q^2)$ and $g_1^d(x, Q^2)$ to date.

2.4.2 Ellis-Jaffe Sum Rule

As with the Bjorken Sum Rule, the Ellis-Jaffe Sum Rule is directly concerned with the first moments of $g_1^{p,n}(x, Q^2)$. Whereas the BSR involves the difference of the two moments, the EJSR provides a prediction of each one separately. The EJSR is often given as Equation 40 expressed in terms of the F and D coupling constants given on page 14. In its original form, the sum rule gave the moments as functions of the ratio $\frac{F}{D}$.

The EJSR was derived several years after the BSR. At that time polarized

[4]SLAC E130 [33] tested the Bjorken Sum Rule in the early 1980s only using proton data. An assumption of $A_1^n = 0$ was used which removes the neutron contribution to Equation 47. As a side note, Bjorken himself thought that the sum rule would never be tested.

proton targets were thought to be feasible. However polarized neutron targets, which were needed to test the BSR, presented formidable challenges which were not expected to be overcome in the near future. In order to make a prediction based on g_1^p alone, some assumptions were made. The primary ones used for the EJSR were that strange quarks did not contribute to the spin of the nucleon and that an SU(3) flavor symmetry existed. The first one was implemented as $\Delta s = 0$ in Equations 37 and 38. This also resulted in the equality of the non-singlet matrix elements: $a_3 = a_8$. The assumption arose out of the belief that the total spin was dominated by valence quarks, and since s quarks were only present in the sea, their influence would be negligible. With flavor symmetry, the light quark masses were set equal and contributions of the different flavors of sea quarks were taken to be the same (*i.e.*, $\Delta u_{sea} = \Delta\overline{u} = \Delta d_{sea} = \Delta\overline{d}$). This was then used to relate a_3 and a_8 to strange baryon β-decay measurements. This has been considered to be less accurate than isospin invariance [39].

Due to the model dependence, the EJSR is not considered to be a rigorous prediction of QCD like the BSR. The sum rule differs from measured values by about 2 1/2 standard deviations. Taking into account higher order QCD corrections, the EJSR predicts for the proton and neutron [40]

$$\Gamma_1^p(Q^2 = 5\,\mathrm{GeV}^2) = \quad 0.160 \pm 0.004$$

and

$$\Gamma_1^n(Q^2 = 5\,\mathrm{GeV}^2) = -0.018 \pm 0.004.$$

This can be compared to the 1998 NLO analysis by SMC which contained most of the then-current world data set [29]

$$\Gamma_1^p(Q^2 = 5\,\mathrm{GeV}^2) = \quad 0.121 \pm 0.003\ (\mathrm{stat}) \pm 0.005\ (\mathrm{syst}) \pm 0.017\ (\mathrm{th})$$

and $$\Gamma_1^n(Q^2 = 5\,\mathrm{GeV}^2) = \quad \text{-}0.075 \pm 0.007\ (\mathrm{stat}) \pm 0.005\ (\mathrm{syst}) \pm 0.019\ (\mathrm{th}).$$

Note that the uncertainties are dominated by theoretical contributions. These come from making extrapolations into the unmeasured low x region. More will be mentioned on this point in Chapter 5. In contrast to the $\Delta s = 0$ assumption of the EJSR, current estimates based on published data give [42] $\Delta s = -0.13 \pm 0.03$ at $Q^2 = 1\,\mathrm{GeV}^2$. This is over four standard deviations from zero. The u and d quark contributions associated with this estimate are $\Delta u = 0.79 \pm 0.03$ and $\Delta d = -0.47 \pm 0.03$.

2.5 Hadron Asymmetries

2.5.1 Motivation

Presently, one of the main challenges in spin physics is the determination of ΔG. Measuring $g_1(x, Q^2)$ can provide some insight into this quantity, but as mentioned earlier, gluons do not contribute directly to $g_1(x, Q^2)$ at leading order. They enter indirectly through the DGLAP equations at higher orders (see for example Equation 42). An alternate route to ΔG can be taken by examining the subprocess $\vec{\gamma}\vec{g} \to q\overline{q}$, where the two initial states are polarized. Because the photon only interacts with a gluon of opposite helicity, the asymmetry from this process (assuming massless quarks) is 100%. Future experiments such as Compass[5] [46], which hope to measure ΔG are designed to exploit this interaction, known as photon-gluon fusion.

[5] Compass will use a muon beam to create a virtual photon probe.

E155 has some sensitivity to these processes. The outgoing partons hadronize and many of the resulting particles get detected as part of the "background" to the E155 DIS electron sample. By constructing hadron asymmetries one may be able to distinguish between different models of the polarized gluon contribution to the nucleon.

As in the electron case, the asymmetry can be defined as

$$A_{LL}^{meas} = \frac{\sigma^{\downarrow\Uparrow}_{eN\to h^{\pm}X} - \sigma^{\uparrow\Uparrow}_{eN\to h^{\pm}X}}{\sigma^{\downarrow\Uparrow}_{eN\to h^{\pm}X} + \sigma^{\uparrow\Uparrow}_{eN\to h^{\pm}X}}. \tag{48}$$

The arrows indicate when the relative spins of the beam and target are anti-parallel ($\downarrow\Uparrow$) or parallel ($\uparrow\Uparrow$), except now the detected outgoing particle is a hadron of charge $\pm|e|$. In addition to the charge, the particle's momentum was also measured and in some cases a determination could be made as to whether or not the particle was a pion. Equation 48 is the asymmetry measured in E155. Adjustments made for a less than completely polarized beam and target as well as for additional unpolarized material will be discussed in Chapter 4. Predicted asymmetries can be obtained by expressing Equation 48 in terms of photoproduction cross sections. Using the Weizsäcker-Williams equivalent photon approximation gives

$$A_{LL} = \frac{\int_{E_{min}}^{E} dk\, \Phi(k)\, \{\sigma_{L+} - \sigma_{R+}\}}{\int_{E_{min}}^{E} dk\, \Phi(k)\, \{\sigma_{L+} + \sigma_{R+}\}}. \tag{49}$$

The first (second) index refers to the helicity of the photon (nucleon). Integration is over photon energies (k). Because of the small scattering angles measured in E155, E_{min} is approximately the momentum of the outgoing hadron. The total photon flux is given by $\Phi(k)$ and will be discussed in the following section.

Both the numerator and denominator can be further separated into contributions based on their production mechanisms,

$$A_{LL} = \frac{\Delta\sigma^{direct}_{\gamma q\to gq} + \Delta\sigma^{direct}_{\gamma g\to q\overline{q}} + \Delta\sigma^{resolved}_{qg\to qg} + \Delta\sigma^{resolved}_{q_\alpha q_\beta\to q_\gamma q_\delta} + \Delta\sigma^{resolved}_{q_\alpha \overline{q}_\beta\to q_\gamma \overline{q}_\delta} + \Delta\sigma_{Vp\to\pi^\pm X}}{\sigma^{direct}_{\gamma q\to gq} + \sigma^{direct}_{\gamma g\to q\overline{q}} + \sigma^{resolved}_{qg\to qg} + \sigma^{resolved}_{q_\alpha q_\beta\to q_\gamma q_\delta} + \sigma^{resolved}_{q_\alpha \overline{q}_\beta\to q_\gamma \overline{q}_\delta} + \sigma_{Vp\to\pi^\pm X}}. \quad (50)$$

Quantities with (without) a Δ indicate a polarized (unpolarized) cross section. The *direct* or *resolved* superscript pertains to the situation when the photon interacted with the nucleon's components directly or when it fluctuated into something else (such as a $q\overline{q}$ or g) prior to the interaction. The last term in both the numerator and denominator account for contributions to the asymmetry from Vector Meson Dominance (VMD). For these terms the photon fluctuated into a virtual meson which then interacted with the target nucleon. These cross sections are described below in Section 2.5.3.

In the following sections several topics are discussed relevant to the inclusive hadron asymmetries measured in E155. In addition to the processes responsible for producing the hadrons, some details are given about the production of polarized photons, and the benefits and limitations associated with making this particular measurement within the scope of E155.

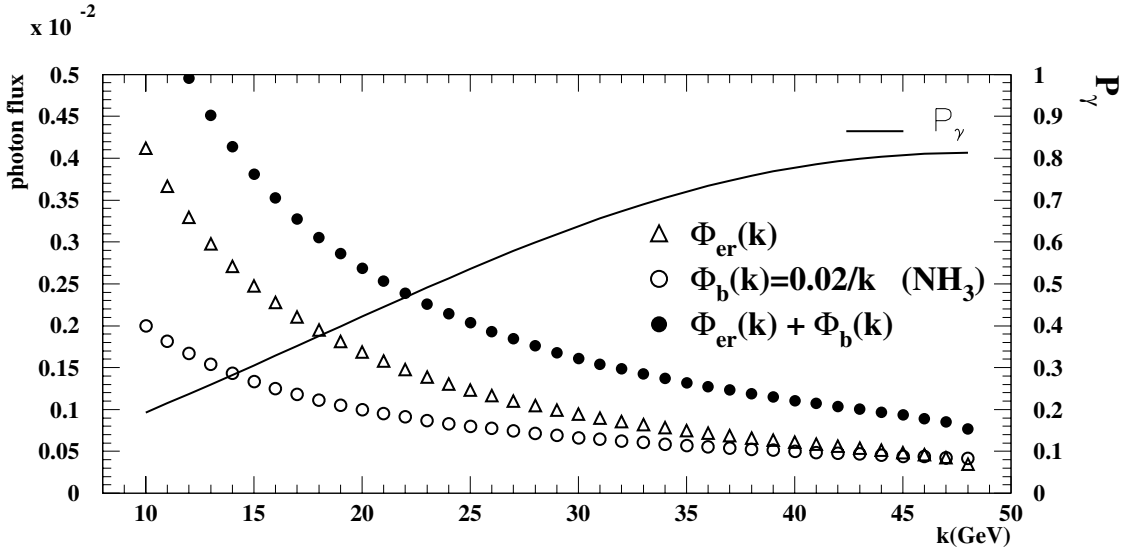

Figure 4: Open points indicate the magnitude of the two different contributions to the photon flux (equivalent radiator and bremsstrahlung) versus photon energy. The sum of the two is plotted as solid circles and the scale for the flux is shown on the left-hand vertical axis. The solid line is the photon polarization as a function of photon energy. The scale for the polarization is shown on the right-hand vertical axis. Above energies of about 40 GeV the photon polarization is essentially that of the incident electron (81.3%).

2.5.2 Polarized Photon Beam

Polarized photons are created by the electron beam as it passes through the target material. There are two main mechanisms at work, each of which contributes roughly the same amount to the photon flux. Because of the $1/Q^4$ factor in the total cross section (see Equation 4), the majority of these photons will be real ($Q^2 = 0$ GeV^2) or quasi-real (low Q^2).

One source for photons is due to electrons emitting bremsstrahlung radiation. This is caused by the electrons interacting with target material upstream of the scattering center. The flux associated with this process is approximately

$$\Phi_b(k) = \frac{t}{2}\frac{dk}{k}, \tag{51}$$

where k is the photon energy and t is the number of radiation lengths of the target material. The factor two comes from taking an average over the target. For E155 targets, $t(^{15}\mathrm{NH_3}) = 0.04$ and $t(^{6}\mathrm{LiD}) = 0.02$.

The second contribution to the photon flux comes from electrons which scatter at close to zero degrees and is described by the equivalent-photon-approximation [47, 48]. For this case, the electron scatters from the nucleon at small forward angles for which the photon's $Q^2 \to 0$. The photon flux is given by [47]

$$\Phi_{er}(k) = \frac{\alpha}{\pi k}\left[\frac{E^2+(E-k)^2}{E^2}\left(\ln\frac{E}{m_e}-\frac{1}{2}\right)+\frac{k^2}{2E^2}\left(\ln\frac{2(E-k)}{k}+1\right)\right. \\ \left.+\frac{(2E-k)^2}{2E^2}\ln\frac{2(E-k)}{2E-k}\right], \tag{52}$$

where the subscript er stands for equivalent radiator. Photon fluxes for each source are plotted as a function of the photon energy in Figure 4. Note that the equivalent-photon-approximation exhibits a similar $1/k$ dependence as the bremsstrahlung spectrum. Both contribute approximately the same amount at the high end of the spectrum while at lower photon energies the equivalent-photon-approximation is about double that from bremsstrahlung.

Also shown in Figure 4 is the dependence of the photon polarization on the energy. This is given by the expression [49]

$$\frac{P_\gamma}{P_e} = \frac{y(4-y)}{4-4y+3y^2}. \tag{53}$$

As discussed in Section 2.1, $y = \nu/E = k/E$. The circular polarization of the photon and longitudinal polarization of the incident electron are given by P_γ and P_e

respectively. For E155, $P_e = 81.3\%$. This is the maximum value attainable for the photon polarization. From Figure 4 one can see that P_γ is close to maximum for energies greater than 40 GeV. At lower photon energies where the flux is increasing, the polarization of the photon quickly drops. These features of the polarization tend to minimize the lower energy photons' contribution to the asymmetry while emphasizing that of the photons at the high end of the spectrum.

Even though the photon flux cancels out in the asymmetry, it is worth examining because it affects the spin averaged cross sections. These can be used as a check to ensure that the models used to explain the polarized data are in reasonable agreement with the measured, unpolarized rates.

2.5.3 Main Sources of Photoproduced Hadrons

Of the particles contained in the E155 hadron data set, the majority were pions. Kaons and protons (or anti-protons) made up a small but not insignificant portion. Because of this imbalance, models made to explain the inclusive hadron asymmetries [45, 47] tend to concentrate on the pion component. The main subprocesses through which pions are generated at E155 kinematics [45, 47, 50] are summarized below.

Direct Photoproduction

For this class of subprocesses, the photon interacts directly with the components of the nucleon. An example diagram for this type, which uses the subprocess

$\gamma q \to gq$, is shown at the top of Figure 5. The difference of cross sections is given by

$$E_h \frac{d\Delta\sigma}{d^3p} = \frac{s - M^2}{-\pi t} \sum_{a,c,d} \int_{z_{min}}^{1} \frac{dz}{z} x^2 \Delta F_{\frac{a}{N}}(x, Q^2) \frac{d\Delta\hat{\sigma}}{d\hat{t}}(\gamma a \to cd) D_{\frac{h}{c}}(z, Q^2). \quad (54)$$

The fraction of the outgoing parton's momentum carried by the detected hadron is denoted by z. The factor E_h, which is the energy of the outgoing hadron, cancels out in the asymmetry. For the overall process, the Mandelstam variables are

$$s = (P + q)^2, \quad t = (q - p)^2, \text{ and } \quad u = (P - p)^2, \quad (55)$$

where P, q, and p are the four-momenta of the target nucleon, photon, and outgoing hadron. As before, x is the nucleon's fractional momentum carried by the struck parton. It can be expressed in terms of the Mandelstam variables as

$$x = \frac{-t}{z(s - M^2) + (u - M^2)}. \quad (56)$$

The polarized PDF for parton a in the nucleon is given by $\Delta F_{a/N}(x, Q^2)$ and $D_{h/c}(z, Q^2)$ is the fragmentation function for the parton c to produce a hadron $h(p)$. An assumption has been made that the polarized and unpolarized fragmentation functions are the same. For the spin independent version of Equation 54, the polarized components (*i.e.*, $\Delta F_{a/N}$ and $\Delta\hat{\sigma}$) are replaced by their unpolarized counterparts.

For the subprocess $\gamma q \to gq$, the polarized and unpolarized cross sections are

$$\frac{d\Delta\hat{\sigma}}{d\hat{t}}(\gamma q \to gq) = \frac{8\pi e_q^2 \alpha \alpha_s}{3\hat{s}^2} \left(\frac{\hat{u}^2 - \hat{s}^2}{\hat{s}\hat{u}} \right) \quad (57)$$

and

$$\frac{d\hat{\sigma}}{d\hat{t}}(\gamma q \to gq) = \frac{8\pi e_q^2 \alpha \alpha_s}{3\hat{s}^2} \left(\frac{\hat{u}^2 + \hat{s}^2}{-\hat{s}\hat{u}} \right). \quad (58)$$

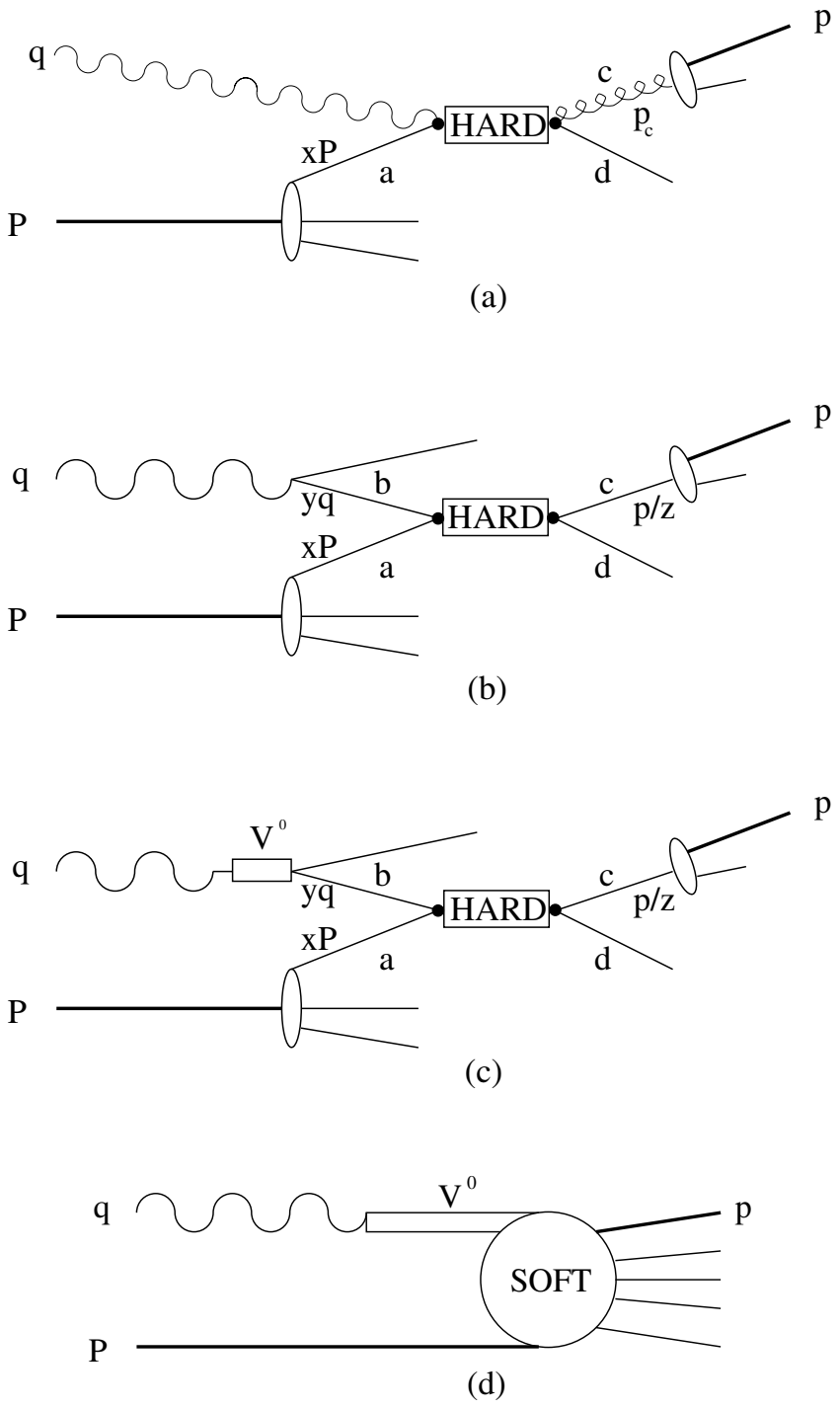

Figure 5: Example diagrams for some of the subprocesses responsible for photoproduced hadrons in E155. (a) Direct photoproduction ($\gamma q \rightarrow gq$). (b) Partonic component of resolved photon with quark-quark scattering. (c) Hadronic component of resolved photon with quark-quark scattering. (d) Hadronic component of resolved photon with a soft hadron produced by VMD. Figures adapted from Reference [51].

The Mandelstam variables for the subprocesses are

$$\hat{s} = (p_a + q)^2, \quad \hat{t} = (q - p_c)^2, \text{ and } \quad \hat{u} = (p_a - p_c)^2, \tag{59}$$

where $p_a = xP$ and p_c is the momentum of the parton leading to the detected hadron. As mentioned earlier, this process is sensitive to the polarized components of the nucleon. Using $A_{LL}(\gamma q \to gq) = \Delta\hat{\sigma}/\hat{\sigma}$, gives a positive asymmetry for this subprocess.

For photon-gluon fusion the subprocess cross sections are

$$\frac{d\Delta\hat{\sigma}}{d\hat{t}}(\gamma g \to q\bar{q}) = -\frac{\pi e_q^2 \alpha \alpha_s}{\hat{s}^2}\left(\frac{\hat{t}^2 + \hat{u}^2}{\hat{t}\hat{u}}\right) \tag{60}$$

and

$$\frac{d\hat{\sigma}}{d\hat{t}}(\gamma g \to q\bar{q}) = \frac{\pi e_q^2 \alpha \alpha_s}{\hat{s}^2}\left(\frac{\hat{t}^2 + \hat{u}^2}{\hat{t}\hat{u}}\right). \tag{61}$$

Taking $\Delta\hat{\sigma}/\hat{\sigma}$, one can see that the asymmetry from this isolated process is 100%, which is in the opposite direction of the A_{LL} obtained from $(\gamma q \to gq)$.

The last subprocess in this category, $\gamma p \to \pi q'$, is higher twist. Here the hadron is produced at *short distance* instead of by fragmentation as in the previous two subprocesses. The outgoing quark from the subprocess can radiate a gluon which converts to a $q\bar{q}$ pair. Half of the pair combines with the outgoing quark to create the pion. Whereas the pions created by fragmentation will be part of a jet, the pions from the short distance process will be kinematically isolated.

Its contribution to the overall cross section is

$$E_h \frac{d\Delta\sigma}{d^3p} = \frac{(s - M^2)x^2}{-\pi t} \sum_q \Delta F_{\frac{q}{N}}(x, Q^2) \frac{d\Delta\hat{\sigma}}{dt}(\gamma q \to \pi q'). \tag{62}$$

with the subprocess

$$\frac{d\hat{\sigma}}{dt}(\gamma q \to \pi q') = \frac{128 g_F^2 \pi^2 \alpha \alpha_s^2}{27(-t)\hat{s}^2} I_\pi^2 \left(\frac{e_q}{\hat{s}} + \frac{e_{q'}}{\hat{u}}\right)^2 \left[\hat{s}^2 + \hat{u}^2 + \lambda\lambda_q(\hat{s}^2 - \hat{u}^2)\right]. \qquad (63)$$

The Mandelstam variables are

$$\hat{s} = (p_a + q)^2, \quad \hat{t} = t, \text{ and } \quad \hat{u} = (p_a - p)^2. \qquad (64)$$

In Equation 63, λ is the photon helicity and λ_q is twice the helicity of the struck quark. For this measurement, the flavor factor $g_f(\pi^+) = 1$ and I_π is the distribution amplitude of the meson. For the asymptotic distribution amplitude, $I_\pi = \sqrt{3} f_\pi/2$ with $f_\pi \approx 93$ MeV [47].

The unpolarized predicted $\pi^\pm$ rates for to all three direct processes are shown for the 5.5° spectrometer in Figure 6. Rates from $\gamma g \to q\bar{q}$ and $\gamma q \to gq$ are added together for the "fragmentation" curve. At higher momenta, the short distance and fragmentation contributions begin to overtake pions produced by soft processes (VMD curve), which will be discussed below.

Resolved Photon Subprocesses

Instead of striking the target nucleon directly the photon can interact through its partonic component, where it fluctuates into a $q\bar{q}$ pair or a gluon, or through it hadronic component, where a vector meson is created prior to the interaction. An example diagram for the partonic component is shown in Figure 5(b). Here the photon turns into a $q\bar{q}$ pair followed by the newly created q scattering off a target quark. For the hadronic component, the interaction that takes place involves

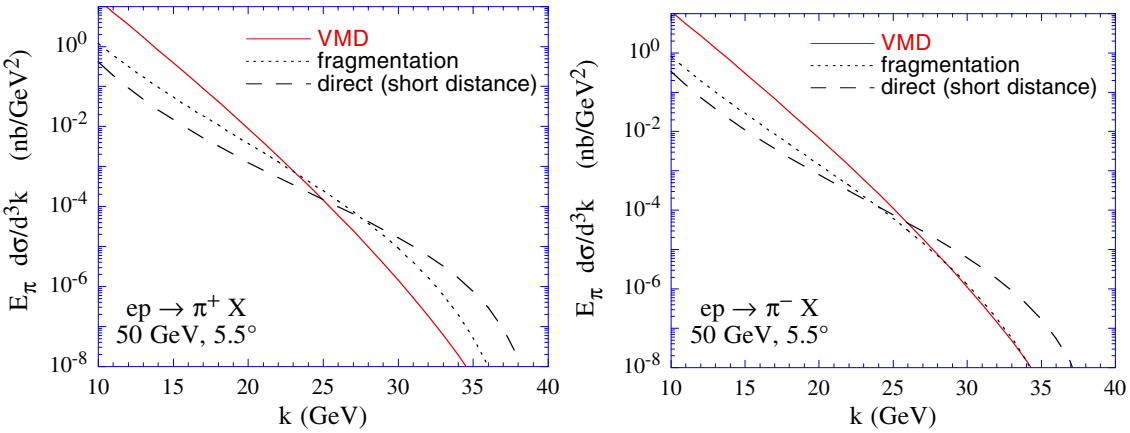

Figure 6: Predicted unpolarized differential cross sections for the three main $\pi^{\pm}$ generating processes. On the left (right) is when the detected particle is a π^{+} (π^{-}). Both correspond to the E155 5.5° spectrometer with a proton target. Figures are from [45].

a parton from the meson hitting a parton from the target nucleon. An example is shown in Figure 5(c). In the following discussion the hadronic and partonic components will be combined together.

For a high p_T hadron produced by a resolved photon, the polarized cross section is given by

$$E_h \frac{d\Delta\sigma}{d^3p} = \sum_{a,b,c,d} \int_{y^q_{min}}^{1} dy \int_{z_{min}}^{1} dz \frac{x^2(s-M^2)}{-\pi z t} \Delta F_{\frac{b}{\gamma}}(y^q, Q^2) \Delta F_{\frac{a}{N}}(x, Q^2) \frac{d\Delta\hat{\sigma}}{d\hat{t}}(ab \to cd) D_{\frac{h}{c}}(z, Q^2). \tag{65}$$

The unpolarized version is obtained by replacing the polarized quantities ($\Delta\sigma$, $\Delta F_{b/\gamma}$, $\Delta F_{a/N}$, and $\Delta\hat{\sigma}$) with their spin averaged counterparts. As in Figures 5(b) and 5(c), the incident quarks are indexed with "a" coming from the nucleon and "b" originating from the photon. The outgoing quark line "c" leads to the detected hadron. The splitting function of the photon into a parton b is denoted by $\Delta F_{b/\gamma}$.

Analogous to Bjorken x, the fractional momentum of the photon carried by the new created quark is given by y^q [6]. As before, z is the fractional momentum of the quark c carried by the detected hadron. In terms of the Mandelstam variables for the overall process, the lower limits of integration are

$$y^q_{min} = \frac{-(u - M^2)}{(s - M^2) + t} \qquad \text{and} \qquad z_{min} = \frac{-(u - M^2) - yt}{y(s - M^2)}. \tag{66}$$

There are three relevant subprocesses for the resolved photon contribution: (1) a quark or anti-quark from the photon hits a gluon in the nucleon[7] ($qg \to qg$), (2) quark-quark or antiquark-antiquark scattering ($q_\alpha q_\beta \to q_\alpha q_\beta$), and (3) quark-antiquark scattering ($q_\alpha \bar{q}_\beta \to q_\delta \bar{q}_\gamma$). The corresponding cross sections are [52]

$$\frac{d(\Delta)\sigma}{d\hat{t}}(qg \to qg) = \frac{\pi\alpha_s^2}{\hat{s}^2}(\hat{s}^2 \pm \hat{u}^2)\left(\frac{1}{\hat{t}^2} - \frac{4}{9\hat{s}\hat{u}}\right), \tag{67}$$

$$\frac{d(\Delta)\sigma}{d\hat{t}}(q_\alpha q_\beta \to q_\alpha q_\beta) = \frac{\pi\alpha_s^2}{\hat{s}^2}\frac{4}{9}\left\{\frac{\hat{s}^2 \pm \hat{u}^2}{\hat{t}^2} + \delta_{\alpha\beta}\left[\frac{\hat{s}^2 \pm \hat{t}^2}{\hat{u}^2} - \frac{2\hat{s}^2}{3\hat{t}\hat{u}}\right]\right\}, \quad \text{and} \tag{68}$$

$$\frac{d(\Delta)\sigma}{d\hat{t}}(q_\alpha \bar{q}_\beta \to q_\delta \bar{q}_\gamma) = \frac{\pi\alpha_s^2}{\hat{s}^2}\frac{4}{9}\left\{\delta_{\alpha\delta}\delta_{\beta\gamma}\frac{\hat{s}^2 \pm \hat{u}^2}{\hat{t}^2} \pm \delta_{\alpha\beta}\delta_{\gamma\delta}\left[\frac{\hat{t}^2 + \hat{u}^2}{\hat{s}^2} - \delta_{\alpha\delta}\frac{2\hat{u}^2}{3\hat{s}\hat{t}}\right]\right\}. \tag{69}$$

Unpolarized (polarized) cross sections use the upper (lower) signs. The Mandelstam variables for these resolved photon subprocesses are given by

$$\hat{s} = (p_a + p_b)^2, \quad \hat{t} = (p_a - p_c)^2, \text{ and } \quad \hat{u} = (p_b - p_c)^2. \tag{70}$$

At E155 kinematics, the unpolarized contribution from the resolved photon is predicted to be small compared to contributions from other processes.

[6] The quantity y^q is given as y in Reference [47]. Here y is used as the fractional energy lost by the incident electron ($y = \nu/E = k/E$).

[7] Reference [50] defines $\Delta F_{g/\gamma} = 0$ at leading order and so the converse of this process (*i.e.,* a gluon from the photon hitting a target quark) is not needed.

Soft Processes

The contributions considered so far have been for the case of hard scattering (*i.e.,* high transverse momenta) where pQCD can be used in calculating the predicted rates. However, the transverse momentum range accessible by E155 (0.5 GeV $\lesssim p_T \lesssim$ 3.8 GeV) overlaps with the gray transitional region between hard and soft processes. A substantial portion of the pions produced in the medium to lower momentum range are thought to come from soft processes, which need to be addressed with nonperturbative calculations. The primary mechanism for the soft contribution was assumed to be Vector Meson Dominance (VMD), where the photon can fluctuate into a ρ, ω, or ϕ prior to hitting the target nucleon. Because the hadron is formed before the interaction, the process can be associated with the hadronic component of the resolved photon process. Figure 5(d) gives an example diagram for this process.

The contribution to the unpolarized cross section from VMD was estimated in [45] by

$$E_\pi \frac{d\sigma^{resolved}}{d^3p}(Vp \to \pi^+ X) = \frac{\alpha}{\alpha_\rho^{eff}}(1.16) E_\pi \frac{d\sigma}{d^3p}(pp \to \pi^- X)\Big|_{90^\circ c.m.} g(\xi), \qquad (71)$$

where $\alpha_\rho^{eff} = 2.44$ is an effective $\gamma - \rho$ coupling constant and the factor 1.16 is the result of several approximations which were used to equate the $(Vp \to \pi^+ X)$ and $(pp \to \pi^- X)|_{90^\circ c.m.}$ cross sections. A functional form of an empirical fit to data from Reference [53] was used for the pp cross section. The quantity $g(\xi)$ is a function of

the scaled rapidity,

$$g(\xi) = \left(1 - \frac{(\xi - \xi_0)^2}{(\xi_{max} - \xi_0)^2}\right)^2, \tag{72}$$

where $\xi = (Y - Y_{target})/(Y_{projectile} - Y_{target})$ and Y is the longitudinal rapidity[8] defined as $\sinh(Y) = (p_L/p_T^2 + m^2)^{\frac{1}{2}}$. In Equation 72, ξ_0 is the value halfway between the maximum and minimum values of ξ for a given p_T.

The soft contribution to the unpolarized cross section is shown in Figure 6. One can see that for the expected $\pi^{\pm}$ rates in the 5.5° spectrometer, VMD contributions dominate up to momenta of about 25 GeV. Because of the lower p_T values associated with the 2.75° spectrometer, one can expect this contribution to be considerable up to higher momenta for that spectrometer.

For soft contributions to the polarized cross sections, although studies indicate that the VMD contributions to A_{LL} may be small [55], no direct information is known. The authors of [45] assume that the polarized cross section is zero. In terms of the predicted A_{LL} (Equation 50), at lower momenta the denominator is significantly increased while the numerator is not. This has a net effect of reducing the predicted asymmetry in the region where VMD is the dominant mechanism.

2.5.4 Benefits and Limitations of this Measurement

Some mention should be made of what can be gained by investigating inclusive hadron asymmetries and to what extent they can be explored within the context of E155.

[8] The quantity Y is given as y in References [45, 54].

The quantity A_{LL} has the potential to be sensitive to different models of polarized PDFs. In a region where the fragmentation processes dominate, this sensitivity can be used to provide constraints on ΔG. An earlier version of the theoretical model discussed here suggested that the E155 data overlapped with such a region. However, disagreement between the data and calculation led to a modification of the model in which contributions due to soft processes were included.

In making measurements of $g_1^{p,n,d}$, corrections need to be made to account for pions which were misidentified as electrons[9]. A better understanding of the pion asymmetry will help to reduce the uncertainty on the spin structure function measurement.

As described in previous sections, many processes contribute to the E155 hadron data sample. This may make interpretation of the data difficult. However, understanding how much and how the different contributions enter into the overall process may prove useful in future attempts at similar measurements.

Hadron asymmetries were not the primary physics goal of E155. Even though the overall data set contained a considerable number of hadrons, the setup, which includes the detectors and analysis code, was optimized to detect electrons and to reject pions. This aspect becomes more important at the highest momenta where the π^-/e^- ratio becomes quite low.

[9] This will be discussed more in Section 4.8.6.

CHAPTER 3

EXPERIMENTAL SETUP

3.1 Electron Beam

3.1.1 Source

E155 used a polarized electron beam provided by the SLAC Accelerator Operations Group. Figure 7 shows the setup of the source used during the E155 run. The source of the beam utilized a strained lattice GaAs/GaAsP photo-cathode illuminating by a flashlamp-pumped Ti:sapphire laser [56]. This produced electron bunches (or spills) at a frequency of 119 Hz. A "witness pulse" was created at a rate of 1 Hz by exciting the same photo-cathode with a YAG-pumped Ti:sapphire laser. This pulse had different characteristics and was used by Main Control Center (MCC) for beam diagnostics. The beam polarization was chosen pseudo-randomly on a spill to spill basis. This was done by reversing the circular polarization of the laser light with a Pockels cell.

The number of electrons per spill was chosen depending on the target material and target mode[1] in End Station A (ESA). For a proton (deuteron) target in parallel mode, each spill contained about $3\times10^9 e^-$/spill ($3.3\times10^9 e^-$/spill). For perpendicular

[1]Target mode refers to the orientation of the target's spin with respect to the direction of the incident beam.

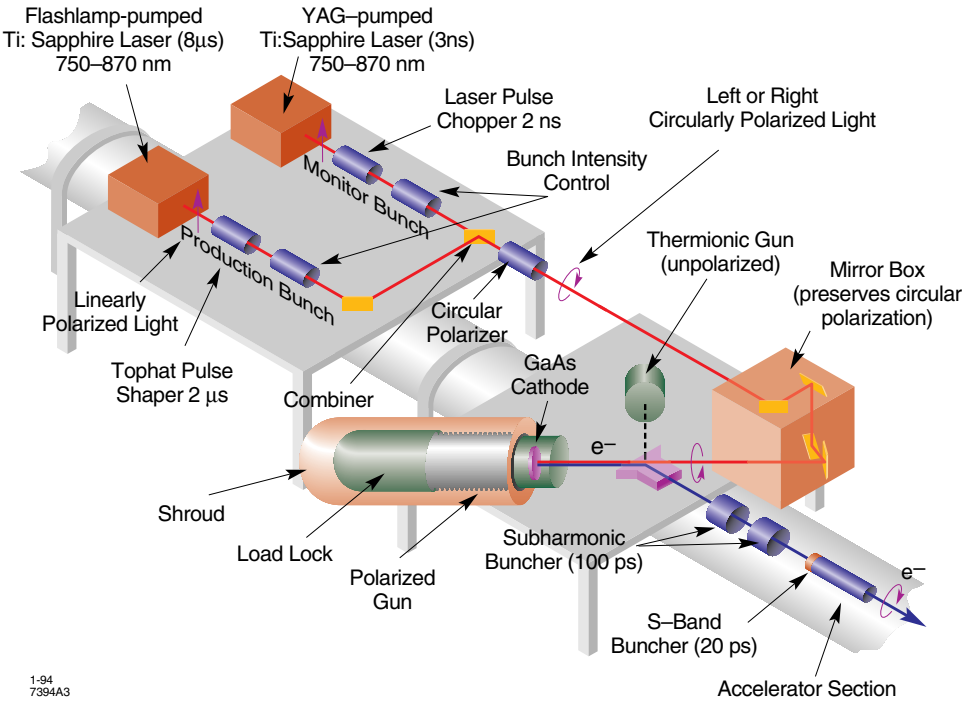

Figure 7: Layout for the SLAC polarized source used during E155.

running, these rates were lowered to about 1.3×10^9 e^-/spill (1.5×10^9 e^-/spill) for proton (deuteron). Incident beam currents differed due to the overall hit rates experienced by the detectors for the various target configurations.

3.1.2 Accelerator

From the source the electron bunches were injected into the 3.2 km long SLAC linac. The linac is divided up into 30 sectors, with eight klystron tubes providing microwave power to each sector. Each klystron operated at 2856 MHz and was capable of a peak power output of 65 MW. The linac accelerated the electrons up to 48.7 GeV using a technique called SLAC Energy Doubling (SLED)[58, 59]. With SLED, most of output pulse from a klystron gets stored in a resonant cavity.

Towards the end of the pulse, the phase of the pulse is flipped by 180° causing the stored portion to be released and added to the remaining output from the klystron. This pulse is then sent to the accelerator. SLED increases the beam energy at the expense of the spill length. For E155, spill lengths were typically 250 ns long and were extended to 420 ns towards the end of the run[2]. To guide the electrons down the linac, a system of magnets and beam position monitors (BPM's) was used.

3.1.3 A-line

At the end of the accelerator is the Beam Switchyard (BSY). Here a pair of pulsed magnets directed the witness pulse into the beam dump D-10. Also in the BSY two DC magnets steered the beam into the A-line, a section of beam transport connecting the linac to ESA. By design, the A-line defined the final energy used in ESA. Prior to E154 it was upgraded to handle a higher energy beam [60]. The A-line creates a total bend of 24.5° from the linac. The first 0.5° of bending comes from the two DC magnets mentioned above and 12 dipoles each contribute 2°. The dipoles were connected in series to an identical magnet located outside of the A-line in MCC. A flip coil, which continuously measured the field in the reference magnet, was used to monitor the beam energy at the target. The information from these measurements was written to tape several times an hour. The A-line also contained several quadrupole magnets to help control the spot size at the target.

About halfway through the A-line is an adjustable collimator called SL-10.

[2]For comparison, spill lengths used in E143 were around 2 μs.

SL-10 limits the fractional energy spread $\Delta E/E$ of the beam. For E155 this collimator was set to 0.8% FWHM.

At the end of the linac an electron's spin is oriented along (or against) the direction of the beam. As the electron moves through the A-line, the spin will precess by an amount that depends upon the beam energy [61]. The relationship between these quantities is given by

$$\Delta\theta_{precession} = \frac{E}{m}\left(\frac{g-2}{2}\right)\Delta\theta_{bend}, \tag{1}$$

where $(g-2)/2 = 1.159652193 \times 10^{-3}$ is the electron magnetic moment anomaly and E and m are the energy and the mass of the electron. $\Delta\theta$ is in radians. For the spin to be aligned with the direction of the beam in ESA, it must precess by an integer number of π radians. Since the bend to the A-line cannot be changed, this condition is satisfied for only certain values of the incident energy. However, while the electrons traversed the A-line bend, they were losing energy in the form of synchrotron radiation [62]. The loss in energy ΔE is given by

$$\Delta E = \frac{2\Delta\theta_{bend}}{3}\frac{e^2}{4\pi\epsilon_0}\frac{1}{\rho}\left(\frac{E}{m}\right)^4, \tag{2}$$

where $\rho = 85.927$ m is the bending radius, e is the charge of the electron, and ϵ_0 is the permittivity of free space. Combining Equation 1 and Equation 2 and integrating over the possible bend angles gives allowed beam energies for E155. The energies actually used are presented in Table 1. The beam lost about 400 MeV (160 MeV) due to synchrotron radiation at the energy used for parallel (perpendicular) running.

Table 1: Beam energies used in E155.

target mode	linac energy (GeV)	ESA energy (GeV)	$\Delta\theta_{precession}$
perpendicular	38.93	38.77	12π
parallel	48.75	48.35	15π

To reduce the effects of beam heating and radiation damage on the target, two Helmholtz coils were used to vary the position of the beam at the target on a spill to spill basis. The coils were located just upstream of the ESA alcove about 60 m before the target. At the target the beam was rastered over circular area 20 mm in diameter, slightly smaller than the diameter of the target cup. The step size was 0.3 mm in x and y and after four passes over the target the pattern would begin to repeat. Figure 8 shows the spots of the target that have been hit by the beam after almost one complete pass.

3.1.4 Beam monitoring

In addition to the MCC reference magnet to measure the beam's energy, there were a number of other devices used to monitor different properties of the beam. In describing the ESA beam monitors, a right handed coordinate system will be used to reference the electron beam in ESA. For this convention, the beam line lies along the z axis with the origin located at the center of the target and with electrons traveling in the $+z$ direction. x and y correspond to the horizontal and vertical directions respectively.

To determine the number of electrons per spill, there were two toroids located

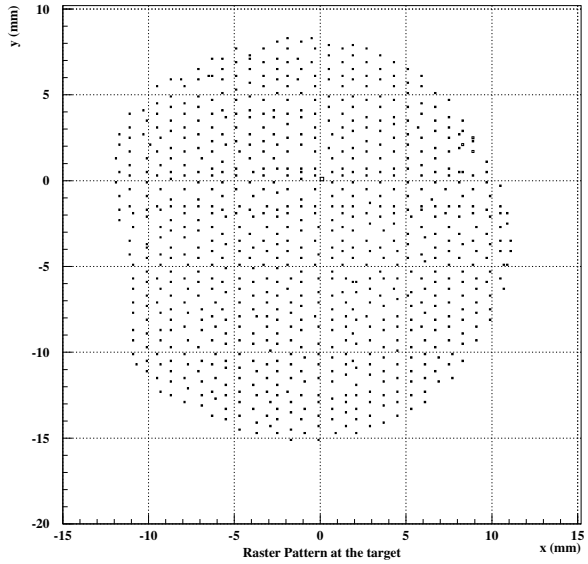

Figure 8: Cross section of the E155 raster pattern at the target. The pattern shown is created by almost one complete pass in which the beam was swept from right to left. To illustrate the granularity of the pattern, the beam's spot size in the plot is smaller to scale than the actual spot size at the target. The vertical position of the spot was scanned from top to bottom at one x location and then from bottom to top at the next. After four passes the raster pattern would start over.

upstream of the target [63], historically named toroid2 and toroid3. Each was made of an iron ring wrapped with a coil of wire. The coil was connected to an RC circuit and a pre-amplifier. The number of electrons per spill was proportional to the amplitude of the signal. During E155, the toroids were calibrated remotely from the counting house several times a day.

Several pieces of equipment were used to ascertain the position and quality of the beam at various locations. Two devices which provided more of the qualitative beam information were the "good spill" and "bad spill" monitors. Both were of similar construction but were complementary in terms of their implementation. Each consisted of a paddle of plastic scintillator read out by a PMT. The plastic was

wrapped in black tape to make it light tight. The output from the PMT was sent to both an ADC and an oscilloscope. Values from the ADC were written to tape and a video camera was used to pipe the trace of the oscilloscope to monitors in Counting House A and in MCC. The video was monitored continuously and gave shift workers a feel for the quality of the beam and the length of the spill as well as a quick visual check as to whether or not the beam was on. The bad spill monitor was located in the ESA alcove and was sensitive to the beam halo and to beam scraping at the SL-10 collimator and other A-line components. A large signal from the bad spill monitor was an indication that the beam was not entering ESA cleanly and that beam tuning might be required. There were actually two good spill monitors which were referred to as "good spill" and "good spill 2". Both were located in the target area. One was slightly downstream of the target and 2 m below the beam line. The other was just off to the south side of the target[3] and was at the same height as the beam line. A steady output signal came from the good spill monitors when the beam was hitting the target. When the beam would pass through the support structure which surrounded the target, a larger and uneven signal was created.

A device called a foil array was used to measure the position and the profile of the beam at the target. The foil array consisted of two arrays located about 9 m downstream of the target. Each array contained 48 brass foils separated by 1 mm. The foils were 10 cm long by 1 mil thick. One array had its foils oriented vertically

[3]The beam traveled from west to east in ESA. Since the beam was focused at the target, the spot size was slightly smaller there.

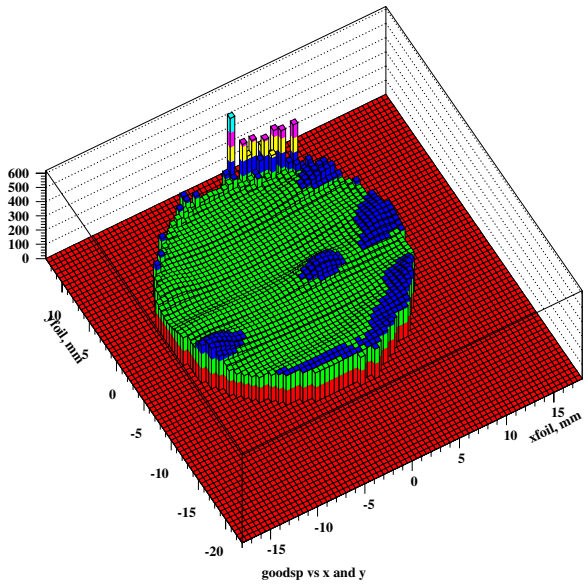

Figure 9: Output from online program "spillmap". x and y information are obtained from the foil arrays. The height of the histogram is from the good spill's ADC and was accumulated since the beginning of the run. The peaks at the top of the plot indicate that the beam was clipping the top of the target cup and needed to be lowered.

to measure the x position of the beam and the other used horizontal foils for a y measurement. The spot size of the beam at the foil array was around 1.2 mm $\times$ 0.5 mm ($x \times y$).

An online piece of software which was used for beam tuning was called "spillmap". Spillmap combined the output from the foil arrays together with the signal from the good spill monitor. This provided real time information about the beam at the target for all points in the raster pattern. An example of the spillmap output is shown in Figure 9. In the sample given there are several peaks (higher rates at the good spill monitor) located in the upper region of the target. These peaks indicate that the beam was hitting some of the target's support structure when it was rastered over the top part of the target. For this particular situation

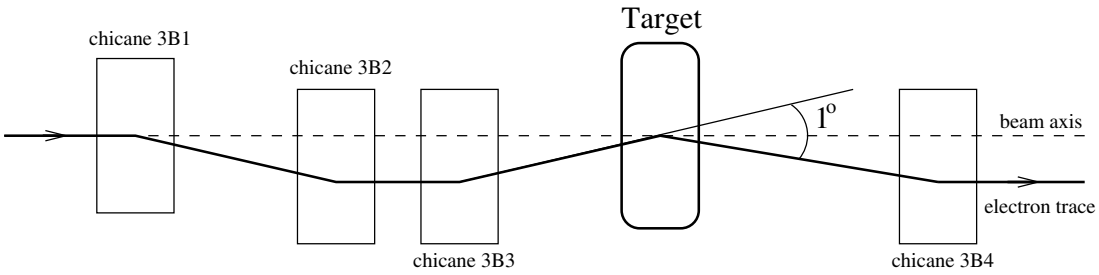

Figure 10: Diagram of the Chicane magnets used during perpendicular mode running. Drawing is not to scale.

the center of the raster pattern would have been moved downward. The peaks could be removed later during the analysis phase with data cuts.

3.1.5 Chicane Magnets

When the target was set up so that the spin was perpendicular to the incident electrons, the field from the target magnet exerted a force on the beam. As a means of compensating the effects of this force, four dipoles magnets known as the "chicane magnets" were used. Three of them were upstream of the target and one was downstream. A diagram of the chicane system is shown in Figure 10. The downstream chicane ensured that the beam from the target area made it into the beam pipe so that it could be directed to the beam dump which is due east of ESA.

3.1.6 Møller Polarimeter

For measuring the beam polarization, E155 used a Møller polarimeter. The device is based on Møller scattering [64] which describes the elastic scattering of two electrons. If both electrons are longitudinally polarized, the cross section will be larger when the spins are anti-aligned than when they are aligned. The relationship

between these two combinations of spin orientations and the beam polarization is given by

$$A_N = \frac{N_{\uparrow\uparrow} - N_{\uparrow\downarrow}}{N_{\uparrow\uparrow} + N_{\uparrow\downarrow}} = A_{zz}(\theta_{CM}) P_B^{\parallel} P_T^{\parallel}, \tag{3}$$

where $N_{\uparrow\uparrow(\uparrow\downarrow)}$ are the number of scattered electrons when the incident and target electrons' spins were parallel (anti-parallel) and A_N is the background subtracted measured asymmetry. P_B and P_T are the polarizations of the beam and target foil. $A_{zz}(\theta_{CM})$ is the theoretical asymmetry at the center of mass scattering angle

$$A_{zz}(\theta_{CM}) = -\frac{(7 + \cos^2\theta_{CM})\sin^2\theta_{CM}}{(3 + \cos^2\theta_{CM})^2}. \tag{4}$$

The beam used for polarization measurements was the same as that used during normal data taking except that it was not rastered and was not focussed at the z location of the E155 target. Also, while Møller data were being collected, the E155 target was moved out of the beam line[4] and regular data taking was put on hold. Møller runs were taken approximately twice a week. Both a single arm and a double arm Møller polarimeter were used. Although the two polarimeters could collect data simultaneously, often only single arm measurements were taken. This was because the single arm polarimeter could run at a higher rate thus enabling it to make a faster measurement.

The Møller system was upstream of the E155 target and consisted of target foils followed by a single dipole magnet to bend the trajectories of the scattered

[4]Part of the reason for moving the E155 target out of the beam line was to protect it from the unrastered beam. However, not having the target in position also reduced the background rates in the Møller detectors, which were located upstream but near the E155 target.

electrons away from the beam line. Downstream of the magnet were the detector packages which counted the number of scattered electrons.

For a target of polarized electrons, ferromagnetic foils were used in which the atomic electrons occupying unfilled shells were polarized. Foil thicknesses of 20, 30, 40, and 154 μm were used and were made of 49% Co, 49% Fe, and 2% Va. The Møller target was located in the ESA alcove and was moved into the beam line for Møller data runs via remote control from Counting House A. To polarize the foils a Helmholtz coil provided a $\pm$100 G magnetic field and smaller pickup coils were used to measure the foil polarization. Foil polarization measurements were taken before and after E155, for which the post-run values either agreed with or were within $< 0.6\%$ of the pre-run measurement [65]. Typical polarizations were around 0.082.

A tungsten mask was used to define the acceptance of the Møller spectrometer. The mask was located upstream of B0 and about 10 m downstream of the foils. B0 was the Møller dipole magnet and was typically set for a field strength of $\approx$ 38.4 kG-m. In the center of B0 was an iron septum. A hole in the middle of the septum allowed the unscattered beam electrons to pass through the magnet relatively unaffected by the field.

As mentioned above, two independent detector packages were used to count the scattered electrons and they were known as the single arm and double arm Møller polarimeters. Slightly upstream of the detectors was a sheet of lead a few radiation lengths thick. This shielded the detectors from some of the lower energy background particles and also acted as a pre-radiator. The lead covered the area in

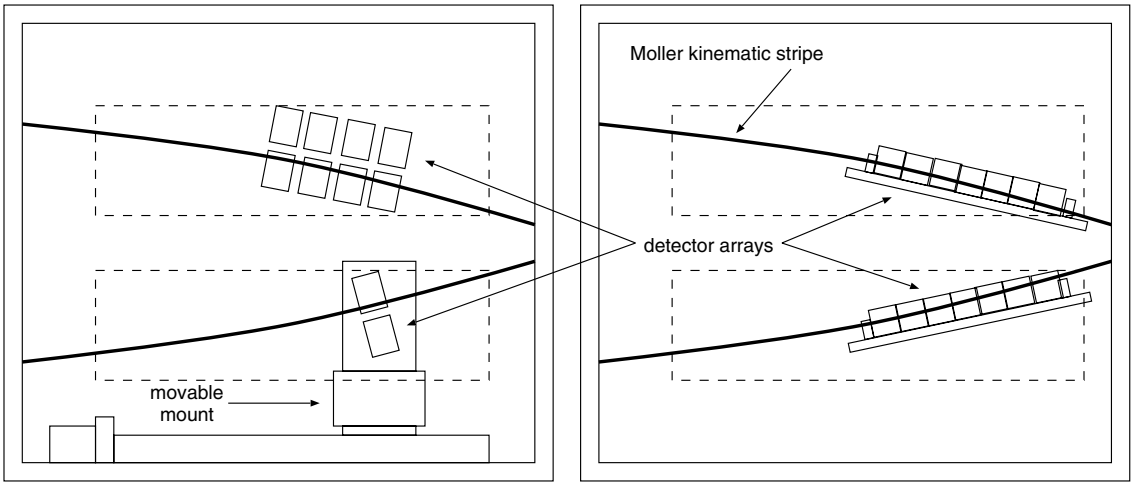

Figure 11: Drawing of a downstream view of the single arm (left) and double arm (right) Møller detectors. Although here they are shown separately, in actuality the double arm was in the shadow of the single arm detectors. For reference, the beam pipe was to the right and incident electrons were traveling into the page.

front the detectors.

The single arm polarimeter was designed to measure only one of the scattered electrons from each Møller interaction, but to provide an integrated signal over each beam pulse. The detector package was essentially that used for E154 [66] with a few modifications. A sketch of the layout is shown on the left hand side of Figure 11. It consisted of five silicon detectors (two pads per detector). The four coarse pitch detectors made up the "top" set which was above the beam line. Each of the four contained 12 channels and was set in a fixed position to detect scattered electrons at $93^\circ \lesssim \theta_{CM} \lesssim 104^\circ$. The fifth ("bottom") detector was the fine pitch detector and contained 48 channels. It was located below the beam line and could be moved in x and y directions remotely from the counting house. The bottom detector was centered at $\theta_{CM} \approx 94^\circ$. Since one of the electrons will scatter at $90^\circ - \Delta\theta_{CM}$ and

the other at $90^\circ + \Delta\theta_{CM}$, both top and bottom detectors were placed in the $> 90^\circ$ region to avoid double counting.

The beam polarization as measured by the single arm detector was $0.813 \pm 0.002(\text{stat}) \pm 0.020(\text{syst})$. A breakdown of the systematic error is given in Table 2. The analyzing power[5] was calculated using a Monte Carlo model, which included the field strength of B0, Levchuk corrections [68], losses due to multiple scattering and bremsstrahlung radiation, detector resolution, and detector gaps. The Levchuk effect takes into account the fact that the target electron was not a free electron at rest but was bound and in motion about the nucleus. The background shape referred to in Table 2 comes from the a fit to the background in the unpolarized contribution ($N_{\uparrow\uparrow} + N_{\uparrow\downarrow}$ term) to Equation 3. The integration range refers to the number of ADC channels included in the determination of the Møller peak for a particular θ_{CM}.

The double arm measured both outgoing scattered Møller electrons by requiring a coincidence between corresponding points (i.e. $90^\circ \pm \Delta\theta_{CM}$) in its two arms. This detector package was similar to the one used in E143 [67]. Each arm contained 7 lead glass blocks which operated under the same principles as the shower counters (see Section 3.3.5). The layout of the double arm detectors is shown on the right hand side of Figure 11. Part of the double arm blocks was in the shadow of the single arm detectors, but since the silicon detectors were negligibly thin, this did

[5] The analyzing power is the theoretical asymmetry $\times$ the target polarization ($A_{zz} \times P_T$) from Equation 3.

Table 2: Contributions to the single arm Møller systematic error.

Foil polarizations:	common	1.2%
	foil to foil	1.2%
Analyzing power (Monte Carlo stat + syst, $\int B \cdot dl$)		1.0%
Sensitivity to background shape		1.2%
Sensitivity to integration range		0.4%
Analysis Technique		0.9%
total		2.5%

not have an effect on the signal seen in the lead glass. By requiring both scattered electrons, the double arm was less sensitive to the background signal.

The beam polarization measured by the double arm was $0.805 \pm 0.002(\text{stat}) \pm 0.032(\text{syst})$[6]. A limited study of systematic affects was done for the double arm polarimeter.

There was no evidence of the polarization changing as a function of time over the course of the experiment [71]. This was in part due to the quantum efficiency (QE) of the photocathode which had a very slow rate of decrease during the data taking period. It should also be noted that no recesiation of the photocathode was done during E155. A constant value of 0.81 ± 0.02 [71] was used for the beam polarization in the analysis. This is a weighted average of the double arm and single arm measurements.

[6] The central value and systematic error are from [69]. No statistical error was given for the double arm result in this meeting's notes. The statistical error reported here was taken from [70].

3.2 Polarized Target

At the center of the experimental setup were the solid cryogenic targets. The target system was set up and maintained by a group led by the University of Virginia. To study the proton, E155 used frozen ammonia ($^{15}NH_3$) and for a deuteron target the material was lithium deuteride (^{6}LiD). For polarization purposes, the material was kept in a 5 T magnetic field at $\approx$ 1 K. The technique of Dynamic Nuclear Polarization (DNP) was employed as a means of polarizing the nucleons. Polarization measurements were taken continuously using a Nuclear Magnetic Resonance (NMR) system. Typical polarization values of 80% (22%) were obtained for the proton (deuteron).

3.2.1 Dynamic Nuclear Polarization

For DNP, paramagnetic centers were introduced into the target material prior to its use as an E155 target. This was accomplished by irradiating the material in a low energy electron beam [72]. Electrons interacted with the nucleons through a dipole-dipole coupling. In the presence of a magnetic field, the energy levels of the electron-nucleon system split by an amount proportional to the field strength and the magnetic moments of the particles. An example of these levels for the proton target is shown in Figure 12. The separation ΔE between levels A$\leftrightarrow$B or C$\leftrightarrow$D is determined by the flip of a proton spin and A$\leftrightarrow$C or B$\leftrightarrow$D by an electron spin flip. ΔE is given by

$$\Delta E = h\nu_i = g_i \mu_i B, \tag{5}$$

where g_i and μ_i are the g-factor and magnetic moment of the particle in question and B is the strength of the magnetic field. For an electron, $\mu_e = \mu_B = 5.8 \times 10^{-11}$MeV T^{-1} and $g_e = -2.0$. Likewise for a proton, $\mu_p = 2.79\mu_N = 8.8 \times 10^{-14}$MeV T^{-1} and $g_p = 5.6$. At thermal equilibrium the particles are essentially unpolarized with the majority of the nuclear spin orientations being divided equally between the lower two states. This is called the natural polarization and for a particle with spin 1/2 (proton) or spin 1 (deuteron) is

$$P_t\left(\frac{1}{2}\right) = \tanh\left(\frac{g_i\mu_i \mathrm{B}}{2k_BT}\right), \tag{6}$$

$$P_t(1) = \frac{4\tanh\left(\frac{g_i\mu_iB}{2k_BT}\right)}{3+\tanh^2\left(\frac{g_i\mu_iB}{2k_BT}\right)}, \tag{7}$$

where g_i, μ_i, and B are the same as above, k_B is Boltzmann constant, and T is the temperature of the material.

Due to selection rules, transitions from A↔D (see Figure 12) or B↔C are suppressed by about three orders of magnitude when compared to the transitions involving only an electron spin flip [73], *i.e.*, A↔C or B↔D. Using microwaves of a chosen frequency, typically around 140 GHz, the system can be pumped to induce the forbidden transitions.

For an example, consider a target that is to be polarized in the negative enhancement mode[7], populating level C in Figure 12. To achieve polarization the material is illuminated with microwaves of frequency $\nu = \nu_e + \nu_p$, where $\nu_{e,p}$ come

[7]The negative enhancement mode has the nucleons' spins aligned against the direction of the magnetic field. For positively enhanced polarization, the spins are aligned with the field.

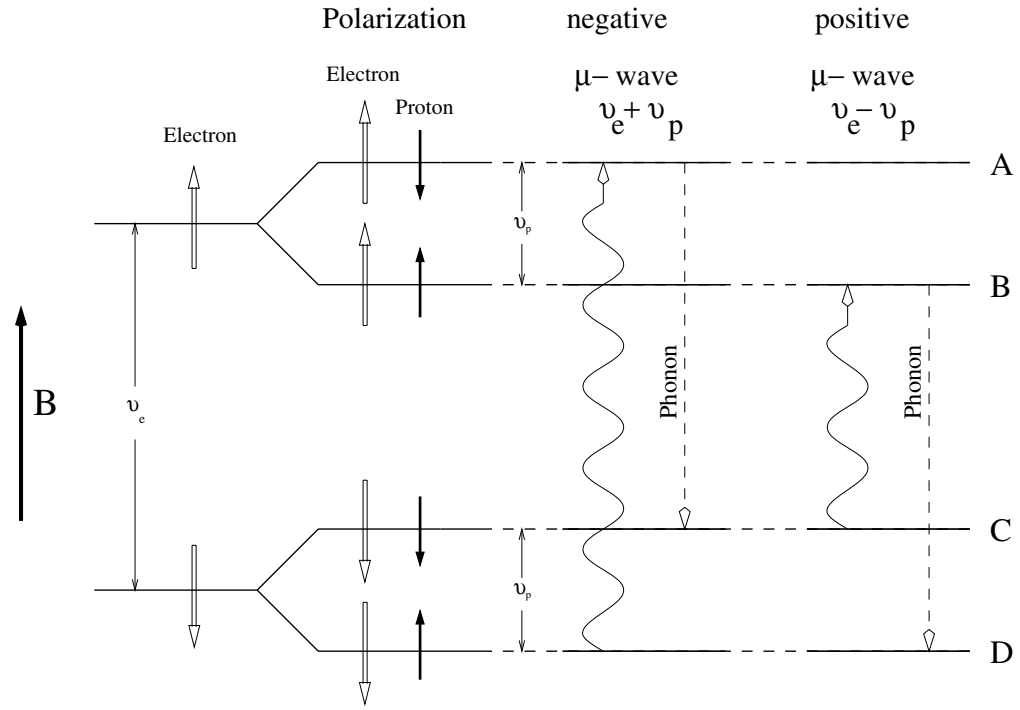

Figure 12: Energy levels used in polarizing the proton. Figure was adapted from Reference [78].

from Equation 5. This will populate level A at the expense of level D. From level A the system is allowed to decay to either levels B or C. However, the transition from A→C is more likely because of the short relaxation time (msec) of the electron spin compared to that of the nucleon (minutes). The difference in the relaxation times stems from a much stronger coupling of the electron to the lattice than of the nucleon to the lattice.

Since the number of paramagnetic sites introduced into the target material for DNP is relatively small, the majority of target nucleons are not near a polarizing center. These nucleons become polarized through a process of spin diffusion. For example, once a proton is polarized using the method described above, it can

exchange its spin with a nearby proton which can in turn exchange its spin with a nearby proton and so on. Also, since the first proton in this chain of events has become unpolarized, it is once again available to be polarized via microwave induced excitations. In this way the polarization spreads out from the centers to the rest of the target nucleons.

Whenever the target material was bombarded by electrons, which was the case during normal E155 data taking, new polarizing centers were being added to the material. The effect this had on the target polarization is shown in Figure 13. At first the new centers helped to increase the maximum polarization. However, after a certain point the polarization began to decrease. If too many centers were introduced into the material, they began to depolarize the target by the same spin exchange mechanism described above. This situation (radiation damage) occurred after the material had spent an extended period of time in the beam. Some of the centers were removed by annealing the target, which involves warming the material for a short period of time. This usually took around 20 minutes for $^{15}NH_3$. One partially successful anneal was performed on the ^{6}LiD material which took about 30 minutes to complete [74]. The anneal temperatures were ~ 80 K for $^{15}NH_3$ and ~ 185 K for ^{6}LiD .

Aside from the overall catenary-like shape of Figure 13, there is also some structure which stands out. The vertical trends, called "spin-ups", were periods without beam during which the polarization was built up. The build up was necessary because the target material lost some of its polarization due to the material

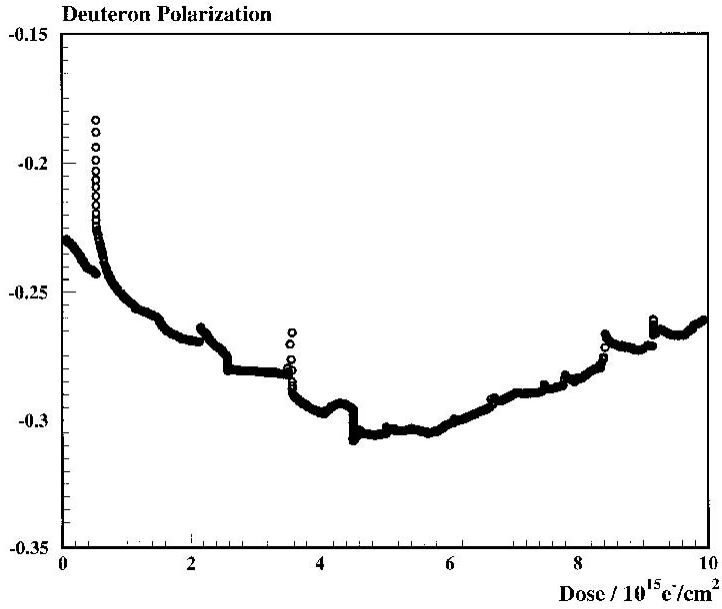

Figure 13: Deuteron polarization versus dose accumulated during normal E155 running conditions. The polarization initially increased (became more negative) and then decreased as more paramagnetic centers were deposited in the material. Approximately $1 \times 10^{14} e^{-}/cm^{2}$ were accumulated during one data run. This plot covers about 130 runs.

being moved out of the homogeneous region of the magnetic field. This was done to do calibrations with unpolarized target material or to do beam steering which required the raster magnets to be turned off.

3.2.2 Target Materials and Setup

As mentioned above, the target materials used were $^{15}NH_3$ for the proton and ^{6}LiD for the deuteron. There were a number of factors that went into these choices of materials. $^{15}NH_3$ had been used previously [75, 76] because it was known to have a high maximum polarization ($> 90\%$) which could be reached in a relatively short amount of time (30-60 minutes). The material was resistant to radiation damage which made it possible to keep a high polarization for an extended period of time.

During E155, $^{15}NH_3$ samples were used in a high intensity beam for 8 to 16 hours before the polarization was low enough ($\sim$ 70%) to require annealing. After an anneal the material typically reached polarizations close to its pre-anneal maximum value.

^{6}LiD was chosen as a deuteron target material for E155 instead of ND_3, which was the material used in E143. One of the advantages of ^{6}LiD is that it is five times as radiation resistant as ND_3. This meant less frequent anneals which resulted in less down time. Another benefit was that ^{6}LiD had an effective dilution factor[8] of about 0.36 compared to about 0.23 for ND_3. The larger dilution factor came about because ^{6}Li could be considered essentially as an α particle plus a polarizable deuteron [77].

The E155 target setup was similar to the one used in E143 [75] and many components were common to both systems. A schematic of the setup is shown in Figure 14. The target assembly housing which is outlined in Figure 14 was $\approx$ 1 m across.

The target material was contained in copper coated aluminum cups 2.5 cm in diameter by 3 cm long. The cups had two removable endcaps made from 0.0254 mm thick aluminum. In order to move the target material in and out of the beam line, the cups were fixed in an insert, a device that was $\approx$ 1.5 m long by $\approx$ 3cm $\times$ 3cm in cross section. Each insert held three cups, two of which were filled with either type of target material. A third cup was called the "dummy" target and contained a

[8] See Section 4.8.3 for details.

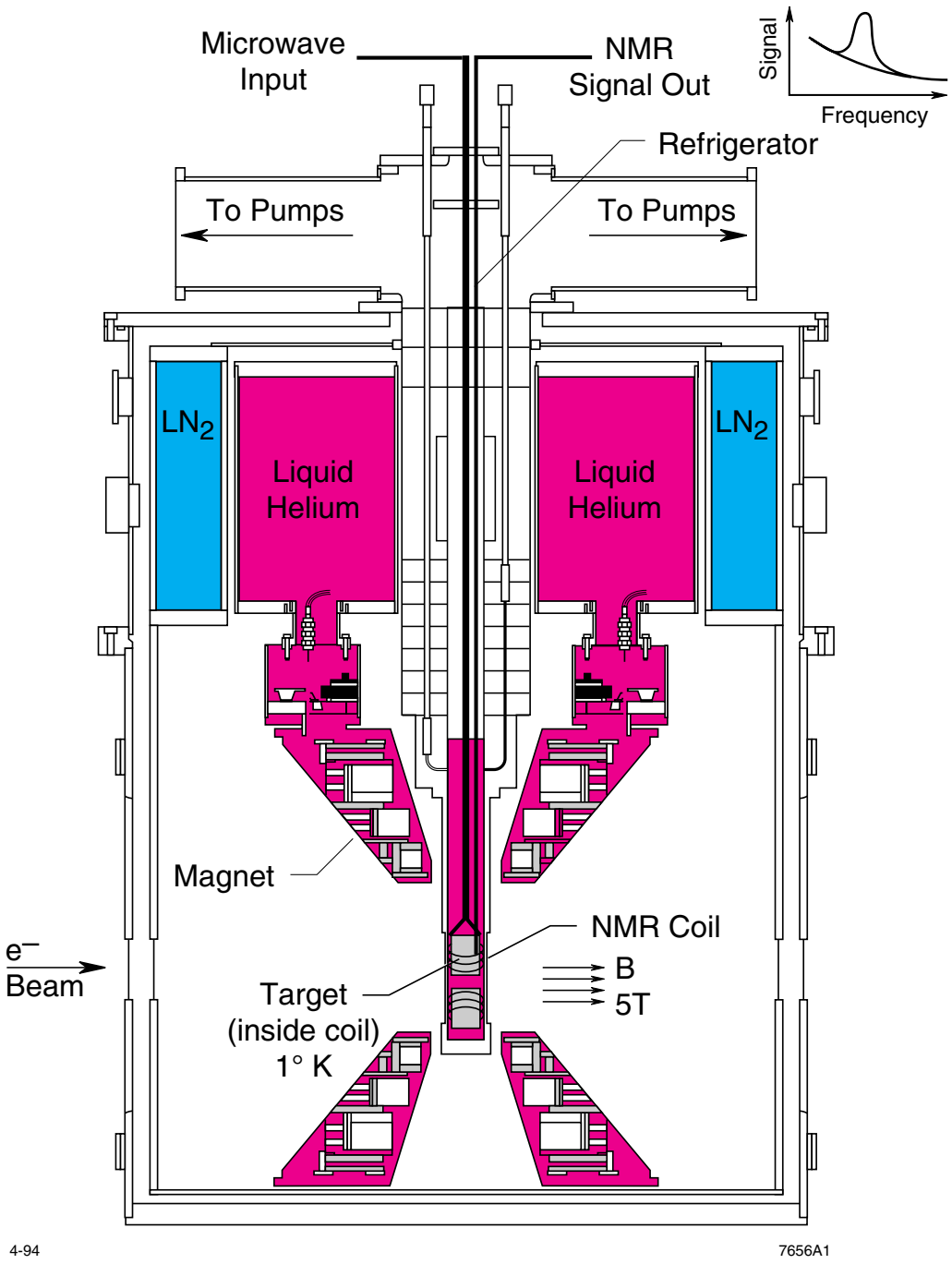

Figure 14: Cross-section of the E155 target.

piece of either beryllium or carbon (pyrolitic graphite) and was used for calibration purposes. The carbon was approximately the same mass and number of radiation lengths as the $^{15}NH_3$. Likewise was the case for the beryllium for ^{6}LiD. In addition to the three cups, there were slots for a solid target (another piece of carbon or beryllium, possibly of a different thickness) and a hole which was large enough to allow the unrastered beam to pass through. The insert could be moved vertically by a stepper motor which was controlled remotely from the counting house. This allowed any of the target positions (i.e. calibration, actual, or hole) to be moved into the beam line. The insert also housed lines which delivered microwaves to and NMR signals from the ^{6}LiD or $^{15}NH_3$. Cables for the NMR signals connected coils which were embedded in the target material to the rest of the NMR system which was located outside of the main assembly. The NMR system is further discussed in Section 3.2.3.

The target material was immersed in a ^{4}He bath which kept the material at ≈ 1 K. To ensure uniform cooling, which was important in attaining homogeneous polarization, the ^{6}LiD and $^{15}NH_3$ were in a granular form. The material resembled fishtank gravel where each bead of material was ≈ 3 mm in diameter.

A superconducting split coil magnet was used to create the 5 T field. The field had a homogeneity of 10^{-4} over a region of 30 mm in diameter. For the majority of E155, the target field was parallel to the direction of the incident beam. Toward the end of the run, data were taken in which the target polarization was perpendicular to the beam. To orient the magnetic field perpendicular to the beam, the entire

target assembly was rotated 90°. For both the parallel and perpendicular modes, the direction of the target field was reversed periodically to reduce any potential systematic effects.

3.2.3 Polarization Measurements

An NMR system was used to measure the polarization of various nuclear species. Central to this system was an LRC circuit, in which the inductor was comprised of target material and an NMR coil. The coil was embedded in the target material and was oriented so that it created a magnetic field perpendicular to the field of the target magnet. Different coil configurations were used to measure protons and deuterons. For the deuteron polarization, the coil had a four loop turn and ran from top to bottom of the target cup. The proton NMR coil was either a straight wire or had a single loop and was centered in a horizontal plane of the middle of the cup. The resistor and capacitor of the LRC circuit were contained in an electronics package called a Liverpool Q-meter [81], which was located outside of the target assembly. Using a variable capacitor, the LRC circuit was tuned so that the resonance frequency of the circuit matched the Larmor frequency of the nucleon [82].

Using an RF signal generator, the frequency in the coil was swept back and forth over the Larmor frequency. When the sweep was close to the Larmor frequency, the target material emitted or absorbed energy. This caused the inductance to change which altered the impedance of the circuit. At constant current, this change

in impedance was measured as a change in the voltage. This was accomplished with a Phase Sensitive Device which compared the voltage output from the RF generator to the voltage across the LRC circuit.

Some difficulties were encountered measuring the proton polarization. A stray capacitance is believed to have existed in parallel with the NMR coil which violated the constant current requirement. This led to non-linearities that affected the large proton signal. The suspected source of the problem was the metal target cups used in E155. Proton polarizations had to be corrected offline using information from radiation damage curves of the $^{15}NH_3$. More details on the difficulties and correction procedure can be found in References [83] and [84].

A sample of the enhanced deuteron signal [72] over the range of frequencies 32.709 MHz $\pm$ 25 kHz is shown in Figure 15. The peak corresponds to the Larmor frequency. Note that away from the Larmor frequency, the signal drops to zero. The area under the curve is proportional to the deuteron polarization.

The relation between the area (A) and the target polarization (P) is given by

$$P_{enh} = \frac{A_{enh} P_{TE}}{A_{TE}}, \tag{8}$$

where enh is for enhanced polarization and refers to measurements taken with polarizing microwaves turned on. The TE subscript indicates measurements taken at Thermal Equilibrium. TE's were calibration measurements taken with both the beam and the microwaves turned off. When thermal equilibrium was reached, the

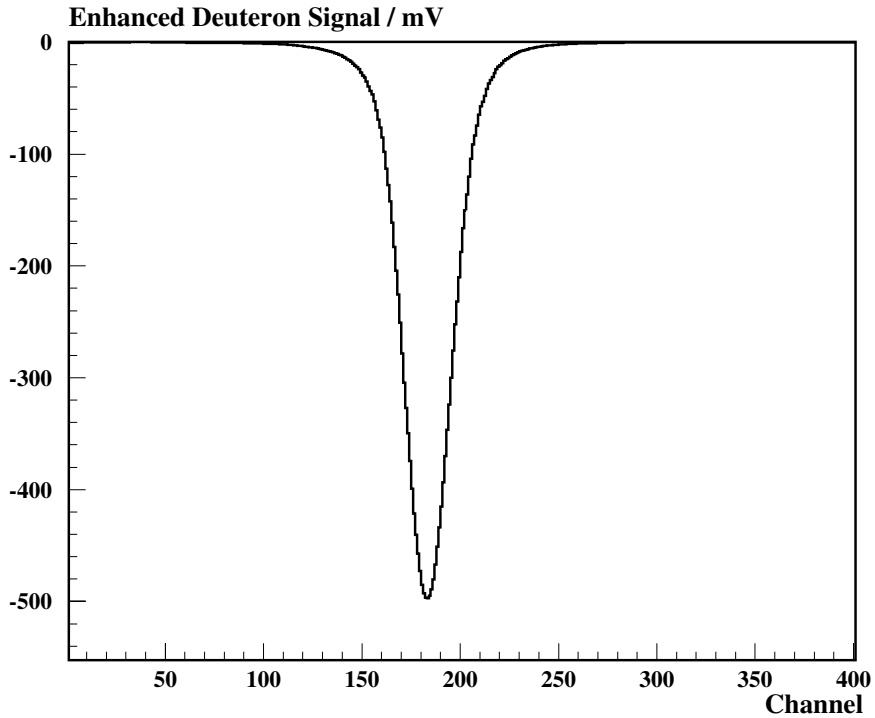

Figure 15: NMR signal for the enhanced deuteron polarization. The horizontal axis corresponds to a frequency range of 32.709 MHz $\pm$ 25 kHz.

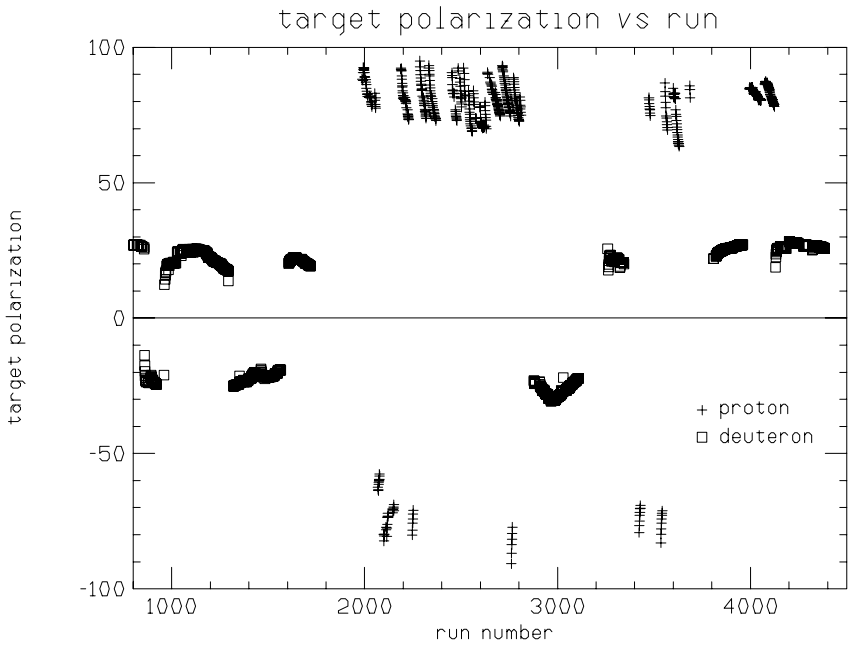

Figure 16: Polarization Values for the proton and deuteron targets versus run number.

spin temperature was equal to the lattice temperature. In this case, by measuring the lattice temperature, the polarization can be calculated via Equations 6 or 7. Most TE measurements were performed after an anneal or when the target insert was filled with new material. Anneals and target fills affected how the material sat in the target cup (target material would settle during an anneal), thus affecting the inductance of the NMR circuit. This drove the need for new calibration constants.

Polarization measurements were recorded a few times a minute. The values were averaged so that in the final analysis, one polarization was used for an entire data run (typically covering around 25 minutes). Target polarizations versus run number for the proton and deuteron are presented in Figure 16. The sign indicates the enhancement of the target polarization, which was reversed periodically. Proton

polarizations are given by crosses and are greater in magnitude than are those for the deuteron. The proton data appear as many short lines which slope to the right and toward zero. This sloping is due to radiation damage. After the polarization value reached a certain point, the material was annealed and the polarization almost returned to its previous maximum value. The cycle was repeated over and over. With more cycles, the curves became progressively steeper, due to the material damaging more quickly. Eventually, a switch was made to new target material. Deuteron polarizations are shown as squares and were typically around $\pm 25\%$. The increasing-then-decreasing structure displayed in Figure 13 is seen clearly around runs 1000 and 3000.

3.3 Spectrometers

Three momentum analyzing spectrometers were used to detect the scattered particles. The spectrometers were centered at fixed angles of 2.75°, 5.5°, and 10.5°, where the angle is measured with respect to the direction of the incident electrons. While the two smaller angle spectrometers were also used in E154, the spectrometer at 10.5° was new for this experiment. All three had the same general setup. At the upstream end was a set of magnets and collimators to control the flow of particles that reach the detector region. Next a combination of hodoscopes and Cherenkov detectors were arranged to provide position information and particle identification. At the end was a segmented lead glass calorimeter which measured the particle's energy and position. A drawing of the setup is shown in Figure 17. To shield the

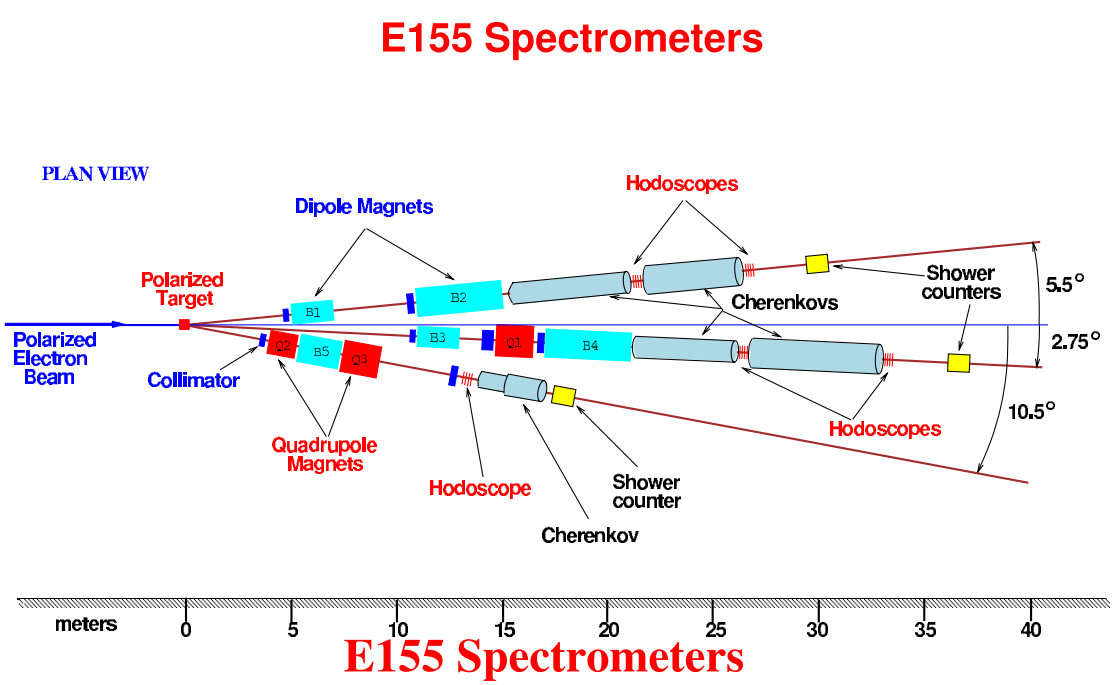

E155 Spectrometers

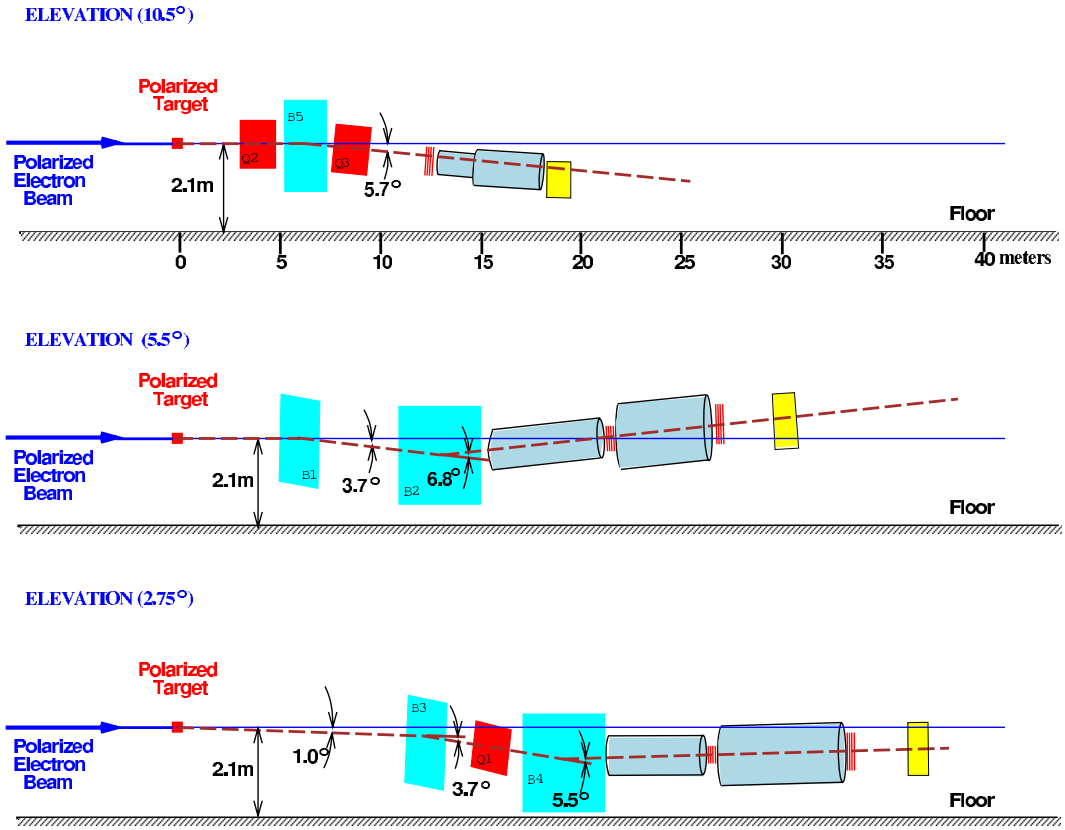

Figure 17: Top plot is an overhead view of the E155 target and spectrometer layout. In the bottom three plots a side view of each spectrometer is presented.

Table 3: Parameters for E155 spectrometers.

	2.75°	5.5°	10.5°
x_{Bj}	0.01 to 0.9	0.05 to 0.9	0.08 to 0.8
Q^2 $(GeV/c)^2$	1 to 7	4 to 19	8 to 40
max solid angle (msr)	0.1	0.5	1.5
momentum range (GeV/c)	10 to 44	10 to 39	6 to 20

detector elements from the ambient radiation in the End Station (mostly neutrons and soft photons), the spectrometers were enclosed in huts made from concrete blocks.

Each spectrometer was assigned a right handed coordinate system in which the x axis is horizontal and y is the vertical axis. The z axis is along the 2.75°, 5.5°, or 10.5° line in the direction of the scattered particle.

Characteristics of the individual spectrometers are shown in Table 3. When combined together, the three spectrometers allowed for a kinematic coverage of $0.01 \leq x \leq 0.9$ and $1\ \text{GeV}^2 \leq Q^2 \leq 40\ \text{GeV}^2$. This is shown graphically in Figure 18. Note that with the inclusion of the 10.5° spectrometer, the accessible Q^2 range doubled.

3.3.1 Magnets

Magnets were used in the upstream end of each spectrometer as a momentum selector for the particles scattered from the target. The 2.75° and 5.5° magnets were configured in a "reverse bend" setup [85]. Using two dipoles, a particle entering the spectrometer first was steered downwards, then upwards. This configuration had

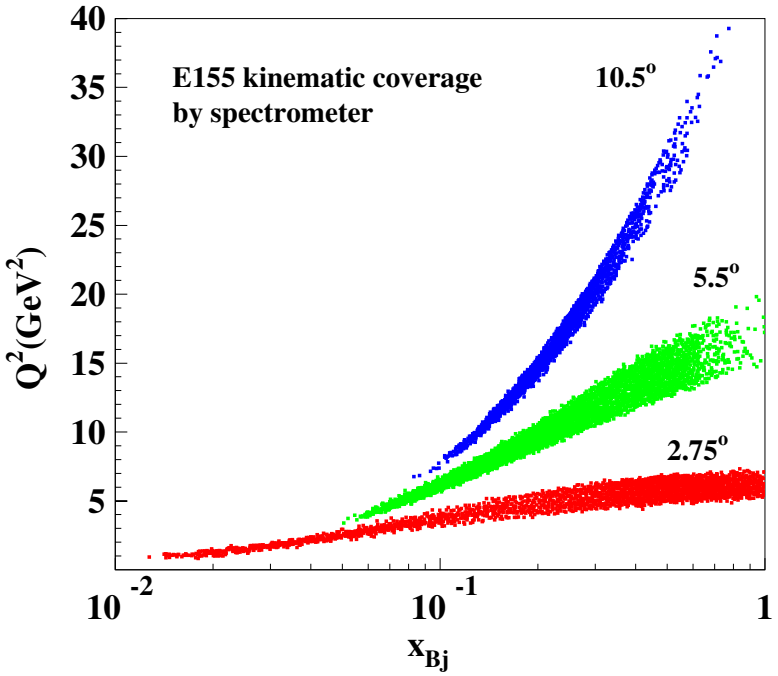

Figure 18: Q^2 versus x_{Bj} for the three E155 spectrometers.

two main advantages over a setup in which the magnets bend in the same direction. First, a larger momentum range was attainable than if both magnets were bending in the same direction. Second, neutral backgrounds such as π^0's and photons needed to bounce twice off the magnets if they were to reach the detector area. This helped to keep the background rates down. However, since the "reverse bend" does not produce the dispersion achieved in a "same bend" setup, the momentum resolution is not as good for the "reverse bend". The effect of the "reverse bend" setup on electron trajectories is illustrated in the 2.75° and 5.5° side view plots of Figure 19.

While the 5.5° used just two dipoles (B1 and B2), the 2.75° had two dipole magnets (B3 and B4) separated by a quadrupole (Q1). Q1 defocussed the particle trajectories in the horizontal plane. This spread out the hits to make optimal use

of the sensitive area available in each detector. The defocussing also gave a better position-momentum correlation, which was used in pion rejection.

The 2.75° and 5.5° magnet apertures were filled with helium contained in thin-windowed boxes. This reduced the radiation length with which an electron could interact before it reached the detectors.

The 10.5° was set up as a single bend with one dipole magnet (B5) located between two quadrupoles (Q2 and Q3). Using two quadrupoles enabled the spectrometer to be sensitive over a large solid angle. Q2 defocussed (focussed) the trajectories in the vertical (horizontal) direction. This increased the range in the scattering angle θ of the trajectories which would be bent by B5. Similar to the 2.75° quadrupole, Q3 focussed in the vertical direction to provide a position-momentum correlation and to reduce the rate of background hits. The optics for the 10.5° are shown in the bottom two plots of Figure 19.

The spectrometer optics were calibrated and rechecked a number of different ways. One method involved mapping the field of each magnet and using the information as input into a Monte Carlo simulation (see Figure 19). Another calibration was done by taking "sieve slit data" during E155. This involved placing a tungsten mask (which contained a grid of holes) in front of a spectrometer opening. The electrons were able to enter the spectrometer only through the holes. Using the data analysis, the expected and actual reconstructed "holes" were compared. For the 10.5° spectrometer some data were collected with two different masks placed in front of the opening of the spectrometer. The first was called "jailbars" and

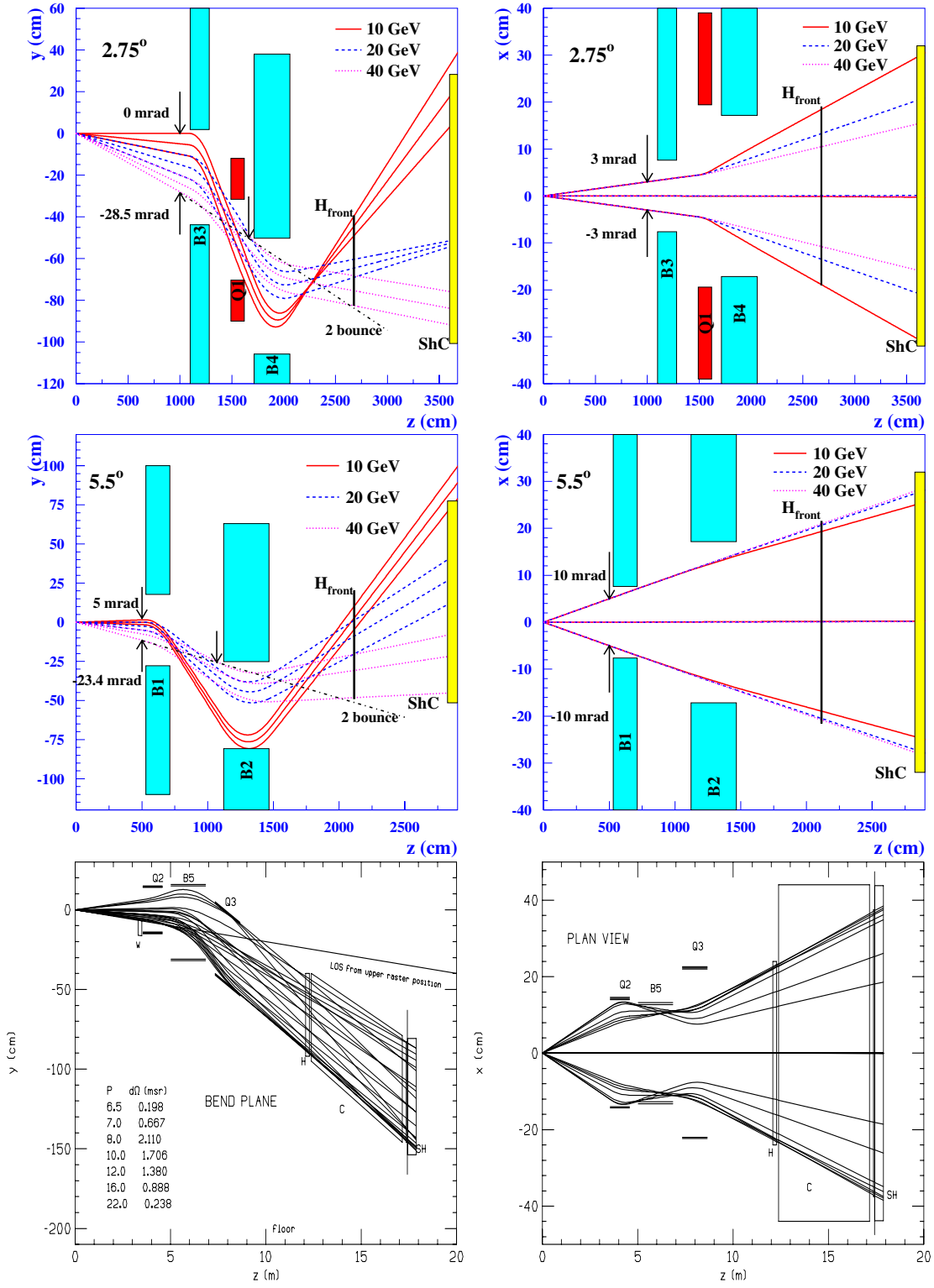

Figure 19: Rows going from top to bottom show the optics for the 2.75°, 5.5°, and 10.5° respectively. In the left column is a side view of each of each spectrometer and on the right is the plan view. The 2.75° and 5.5° plots are from Reference [86] and the 10.5° plots are from Reference [87].

consisted of lead bricks blocking out vertical stripes of area at the mouth of the collimator. In the second configuration, which was called "letter box", lead bricks outlined the outer edges of the mouth. Both masks were based on the same idea as the sieve slits: blocking off a portion of the acceptance as a test of the understanding of the spectrometer optics.

Also during the experiment two energy scans were performed. In the first one, which took place during the checkout period, the incident energy was varied between 40 GeV to 48 GeV. The second one occurred towards the end of the run and used beam energies ranging from 37 GeV to 40.5 GeV. Measured rates as a function of incident energy were compared to predicted values. Both energy scans suggested that the momentum determination in both the 2.75° and 5.5° spectrometers was a few percent low [90]. The energy scan and sieve slit data resulted in corrections to the optics model.

In December of 1997, a test beam experiment (T418) was performed for the benefit of E155/E155x [87]. With two dipole magnets located at the position of the E155 target, single electrons at selected energies were directed into the 10.5° and also into parts of the 2.75°. This allowed for a direct means of calibrating those two spectrometers [88] [89].

3.3.2 Collimators

To regulate the rates experienced by each spectrometer, collimators were interspersed throughout their magnet regions. This enabled each spectrometer to

be run optimally for a given set of beam/target conditions. The collimators also helped to define the ranges of momentum and of θ and ϕ which were accessible by a spectrometer. A typical collimator had two movable jaws, each consisting of an inch of tungsten followed by four inches of lead and was used to define the $\pm x$ or $\pm y$ edges of the acceptance. Other collimators, such as the last 2.75° collimator (2SC4) or the 10.5° "eyebrow" collimator, were made from lead and were in fixed positions. These defined only one edge of the acceptance. The collimators also helped to shield the spectrometers from low momentum pions.

3.3.3 Hodoscopes

Hodoscopes were used to help determine the track which a particle followed through the spectrometer. When combined with an understanding of the optics, the track information provided a measurement of a particle's momentum and the scattering angle at the target.

A spectrometer's hodoscope system consisted of multiple planes, and each plane contained fingers mounted in a frame. For an example see Figure 20. The fingers were made from plastic scintillator with a non-scintillating light guide leading to a PMT. A picture of a finger from the 10.5° hodoscope is shown in Figure 21. When a charged particle passed through a finger, it would deposit a small amount of energy which placed some of the molecules that it passed into an excited state. When the molecules relaxed they emitted the absorbed energy in the form of light. A typical relaxation time for scintillator used in E155 (eg. BICRON BC420) was less

than 2 ns. A portion of the emitted light traveled down the scintillator and through a light guide to a PMT. To improve the efficiency of the bar to internally reflect light, the outer edges of the plastic were polished and the fingers were wrapped in aluminum foil. To prevent light leaks, the fingers were wrapped in black electrical tape. Various models of PMT's were used to detect the signals. For example, Hamamatsu R4014, R4140, or R4124 PMT's were used in the 2.75° and 5.5° hodoscopes, and the 10.5° PMT's were Hamamatsu R329-02. To reduce the effect of magnetic fringe fields, each PMT was fitted inside a tube made from μ-metal shielding. In all three spectrometers the PMT signal was sent through a discriminator and to a multi-hit TDC. The 2.75° and 10.5° systems used LRS[9] 3412 discriminators and LRS 3377 TDC's. For the 5.5° the electronics were LRS 4413 discriminators and LRS 2277 TDC's. The summed output from each of the discriminators was also fed into a scaler which was used to monitor the experiment in real time.

The 2.75° spectrometer utilized 10 planes of hodoscopes. Six were between the two Cherenkov tanks and four more were after the second Cherenkov tank (2C2) and before the shower counter. Each plane measured two dimensions of the position of the particle, the z coordinate plus one transverse dimension. Some details are presented in Table 4. The naming convention has the hodoscopes numbered with the "H1" plane being the furthest upstream and increasing in number as one proceeds towards the downstream end of the spectrometer. A plane whose name ended in "X" had fingers which were set vertically to measure the x position of the particle.

[9] Lecroy Research Systems.

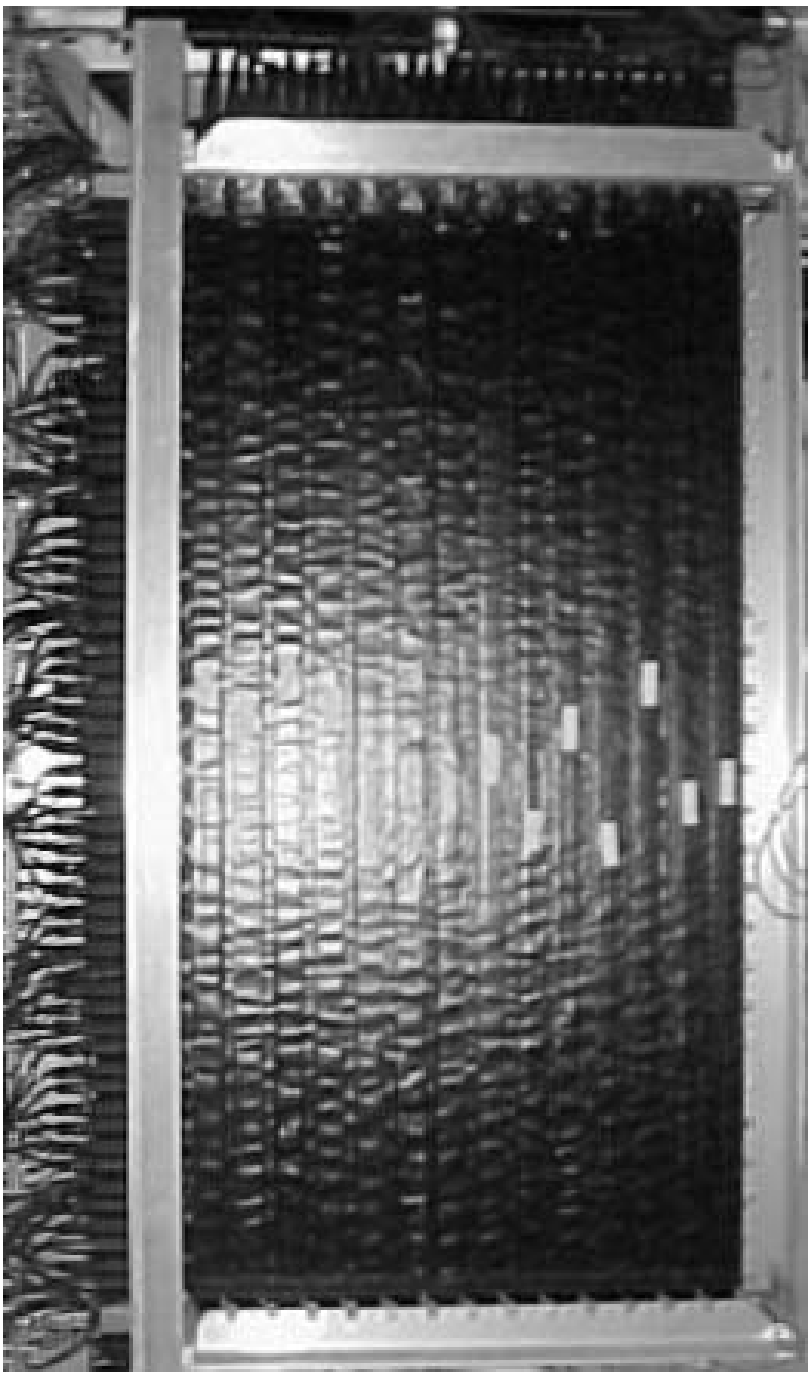

Figure 20: Picture of 5.5° hodoscope plane 5H6X. View is of the upstream side of detector. For scale, the active area of the plane is 51 cm across by 107 cm top to bottom. The PMT's from 5H7Y are visible along the left hand side.

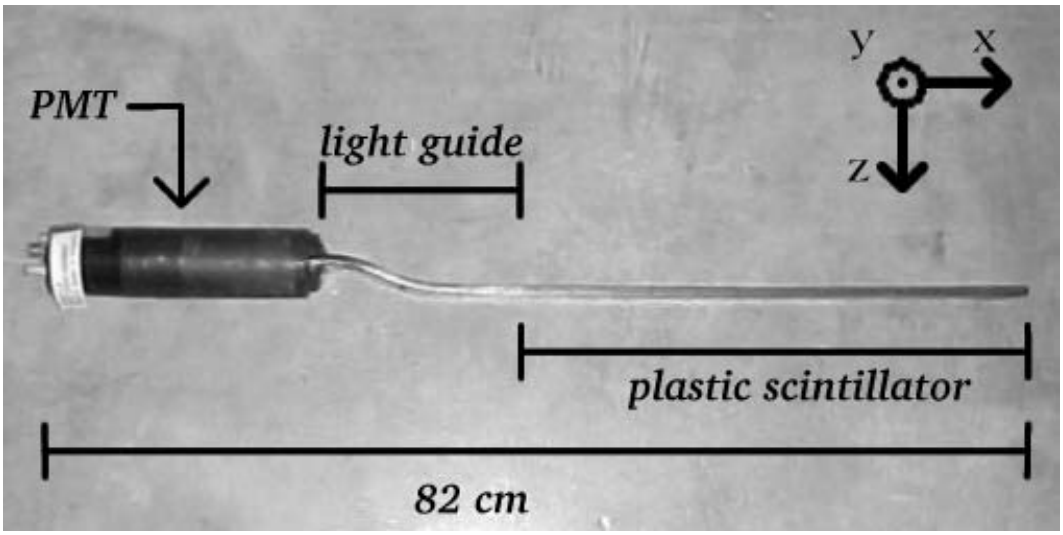

Figure 21: Side view of a 10.5° hodoscope finger.

Likewise, a plane which ended in "Y" had it's fingers stacked horizontally for the y position. The "U" and "V" planes' fingers were set at $\pm 15°$ ($\pm 45°$) to the horizontal in the 2.75° (5.5°) spectrometer. These planes also provided a level of redundancy on the the position measurement.

Some of the planes used in the 2.75° contained split fingers. These fingers were physically separated in the middle by a piece of opaque material to ensure that the signal from one side did not leak into the other. Each half had its own PMT to read out the light pulse. Using split fingers helped to reduce the hit rate per detector element seen in the 2.75° system.

In the 5.5° there were eight planes total. Similar to the 2.75° , a set of four was in between the two Cherenkov tanks and four more were between the second Cherenkov tank and the shower counter.

The 10.5° had only one plane of hodoscopes located just upstream of the

Cherenkov tank. Its 32 fingers were evenly distributed among four sub-planes placed 7.3 cm apart.

3.3.4 Cherenkov detectors

Overview

To aid in particle identification, E155 employed five threshold Cherenkov detectors. Using these detectors in conjunction with the shower counters we were able to separate electrons from the majority of background particles that entered into the spectrometers.

Each Cherenkov detector was a cylindrical vacuum vessel, several meters in length and approximately one and a half meters in diameter (see Figure 22). Details of the individual tanks are presented in Tables 5 and 6. The tanks were filled with a $N_2 + CH_4$ gas mixture at sub-atmospheric pressures. Controlling the gas pressures enabled us to manipulate the index of refraction (and thus the speed of light) in the detectors. A charged particle that passed through a tank created Cherenkov light if it was traveling faster than the speed of light in the gas. This light traveled roughly in the same direction as the particle. Mirrors located at the downstream end of the detector collected the light and focussed it on the face of a single 5" PMT located inside the tank but outside of the spectrometer acceptance for most particles. The Cherenkov system's electronics read out the signal from the PMT and sent it to the data acquisition system.

Table 4: E155 Hodoscope parameters.

spectrometer	plane	number of fingers	dimensions plane (mm) x	dimensions plane (mm) y	dimensions finger (mm) width	dimensions finger (mm) depth	z position (mm)	angle (°)
2.75° (front)	2H1U	44	360	370	12.0	5.0	26,652	15
2.75° (front)	2H2V	44	360	370	12.0	5.0	26,652	-15
2.75° (front)	2H3X	32*	360	410	12.7	12.7	26,914	90
2.75° (front)	2H4Y	36*	360	410	12.7	12.7	26,914	0
2.75° (front)	2H5Y	21	430	420	30.0	6.4	27,171	0
2.75° (front)	2H6X	28	380	590	20.0	6.4	27,171	90
2.75° (rear)	2H7X	45*	510	990	12.7	12.7	33,909	90
2.75° (rear)	2H8Y	42*	510	990	25.4	12.7	33,909	0
2.75° (rear)	2H9Y	54	510	1020	30.0	6.4	34,164	0
2.75° (rear)	2H10X	27	510	1070	30.0	6.8	34,164	90
5.5° (front)	5H1U	25	430	690	45.0	6.4	20,969	45
5.5° (front)	5H2X	23	430	690	30.0	6.4	21,133	90
5.5° (front)	5H3Y	36	430	690	30.0	6.4	21,133	0
5.5° (front)	5H4V	25	430	690	45.0	6.4	21,318	-45
5.5° (rear)	5H5U	21	510	1070	75.0	10.0	26,048	45
5.5° (rear)	5H6X	27	510	1070	30.0	6.4	26,228	90
5.5° (rear)	5H7Y	55	510	1070	30.0	6.4	26,228	0
5.5° (rear)	5H8V	21	510	1070	75.0	10.0	26,506	-45
10.5° (front)	10H1Y	8	480	520	48.0	6.2	12,020	0
10.5° (front)	10H2Y	8	480	520	48.0	6.2	12,090	0
10.5° (front)	10H3Y	8	480	520	48.0	6.2	12,170	0
10.5° (front)	10H4Y	8	480	520	48.0	6.2	12,240	0

Notes:

Angle shown is measured with respect to the horizontal axis of the spectrometer. An asterisk (*) next to the number of fingers indicates that that plane used split fingers and so the number of channels is twice the number of fingers. The x and y given for the plane indicate the active area. The z position is the distance from the target to the center of the plane.

Figure 22: Two views of 2C2, the 2.75° downstream Cherenkov tank. The top drawing shows the south side of the entire tank. The bottom drawing zooms in on the downstream section with a view from the beam line (north) side of the tank. The "C" shaped lead shielding around the PMT is visible in the bottom sketch. Baffles are represented by the hatched disks.

Table 5: E155 Cherenkov parameters.

	2C1	2C2	5C1	5C2	10C
tank length (m)	5.6	6.5	5.8	4.3	4.8
radiator length (m)	5.3	6.1	5.6	4.0	4.5
inner diameter (cm)	105.4	160	105.4	160	91.4/116.8/127
number of mirrors	2	3	2	3	2
mirror size $[x(\text{cm})\times y(\text{cm})]$	51x39	71x44	51x39	71x44	44x71
time resolution (ns)	1.05	1.05	1.05	1.05	1.05
temperature ($^\circ C$)	18.9 ± 0.4 (17.5 ± 0.3)	16.3 ± 0.6 (15.6 ± 0.5)	13.6 ± 0.1 (12.9 ± 0.2)	14.5 ± 0.1 (13.7 ± 0.2)	17.3 ± 0.4 (16.3 ± 0.1)
pressure (psi)	1.325 ± 0.005 (1.342 ± 0.005)	1.316 ± 0.006	1.897 ± 0.005 (1.912 ± 0.005)	1.914 ± 0.005 (1.931 ± 0.005)	2.88 ± 0.04 (1.916 ± 0.005)
PMT id number	LA0101	LA0105 (T1198)	T1196	T1199	LA0104

Notes:

Measured values are given except where otherwise noted. Aside from the first six items, the quantities presented are from the runs 2877 through 2926. The numbers in parentheses refer to the same quantity during the runs 1357 through 1397. No parenthetical value means that the quantity was the same for both sets.

Table 6: E155 Cherenkov parameters, continued from Table 5.

		2C1	2C2	5C1	5C2	10C
e^- efficiency		91.1 ± 0.1	93.8 ± 0.1	95.9 ± 0.2	93.6 ± 0.2	72.0 ± 0.5
		(91.0 ± 0.1)	(94.3 ± 0.1)	(96.0 ± 0.2)	$(93.0 \pm 0.2$	(65.1 ± 0.6)
π^- threshold (GeV)	(meas.)	20.2 ± 0.1	19.5 ± 0.1	15.9 ± 0.1	16.4 ± 0.1	–
	(pred.)	19.3 ± 0.1	19.3 ± 0.1	16.0 ± 0.1	15.9 ± 0.1	13.2 ± 0.2
	(pred.)					(16.0 ± 0.1)
π^- threshold turnon width (GeV)		5.6 ± 0.2	5.3 ± 0.1	3.4 ± 0.2	3.7 ± 0.2	–
		(6.2 ± 0.2)				
light yield (photo-electrons)	(meas.)	3.3 ± 0.1	4.5 ± 0.1	4.7 ± 0.1	4.4 ± 0.1	7.6 ± 1.0
	(meas.)	(3.5 ± 0.1)	(5.7 ± 0.1)			(4.8 ± 0.7)
	(pred.)	3.9 ± 0.1	4.5 ± 0.2	6.0 ± 0.2	4.3 ± 0.2	7.2 ± 0.3
	(pred.)					(4.8 ± 0.2)
operating voltage (V)		2190	2016	2458	2420	2210
		(2160)	(2000)	(2430)	(2390)	

Cherenkov Effect

As mentioned above, a particle passing through one of the tanks will produce Cherenkov radiation if it is traveling faster than the speed of light inside the tank. The radiation will be emitted as a cone of light and the angle of this cone is related to the index of refraction of the gas inside the tank by Equation 9. This is called Cherenkov relation, where θ is the Cherenkov angle,

$$\cos\theta = \frac{1}{\beta n} \tag{9}$$

$\beta = v/c$, and n is the index of refraction of the radiator. At $\theta = 0$ is the threshold velocity, $v_{th} = c/n$, below which a particle will not emit any radiation.

Momentum Threshold

One can express the threshold velocity equation in terms of momentum thresholds, which is worthwhile since E155 used momentum analyzing spectrometers. This gives

$$p_{th} = m_i c/\sqrt{n^2 - 1}, \tag{10}$$

where $p_{i_{th}}$ and m_i are the threshold momentum and mass for a particle of type i. For illustrative purposes, pions will be used since they comprise the majority of the background particles.

One can set the threshold by choosing an appropriate index of refraction. This is done by adjusting the density of the gas (via the pressure) according to the

Lorenz-Lorentz Equation [94]

$$\frac{n(\lambda)^2 - 1}{n(\lambda)^2 + 2} = \rho K(\lambda), \tag{11}$$

where $n(\lambda)$ is still the index of refraction, ρ is the density of the gas, and $K(\lambda)$ is the gas dispersion constant. Using the Lorenz-Lorentz Equation together with Equation 10 and treating $N_2 + CH_4$ as an ideal gas, one can express the threshold as a function of the gas temperature and pressure. This relation is more useful since the temperature and pressure are measured directly. The predicted π^- threshold is given by Equation 12,

$$p_{th} = m_\pi \sqrt{\frac{1}{3}\frac{RT}{MPK}} \tag{12}$$

where as before, p_{th} is the pion's threshold momentum and m_π is the pion mass. T and P are the temperature and pressure of the gas. M is the molecular mass of $90\%N_2 + 10\%CH_4$ determined using partial pressures. R is the ideal gas constant and K is a constant from the Lorenz-Lorentz equation. For $N_2 + CH_4$ at STP and using the values in PDG [22], one obtains $K = 1.74 \times 10^{-4}$ l/g.

Over the course of the data taking period, the temperature and pressure fluctuated by approximately ± 1.5 K and ± 0.01 PSI respectively. This variation was not enough to cause a significant change in the π^- threshold. In Figure 23 two curves show the π^- threshold versus pressure at different temperatures. The two temperatures used encompass most of the values encountered during the run. Varying the pressure by a few hundredths PSI or the temperature by a few degrees changes the threshold by less than 1% Therefore, the π^- thresholds were stable

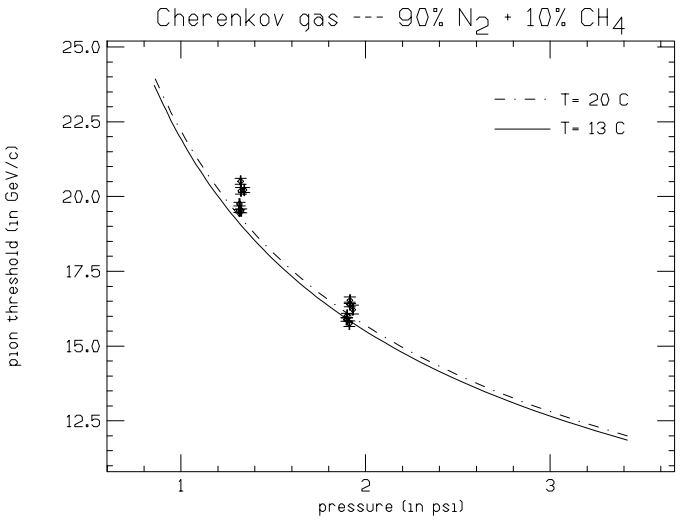

Figure 23: π^- threshold as a function of gas pressure. Points are measured values from the 2.75° and 5.5°. Curves show the expected values. The two curves are at different temperatures illustrating that the threshold was not very sensitive to the temperature fluctuations seen during E155. Over the data taking period, the pressure fluctuation was ±0.01 psi. This variation did not have an impact at the pressures the tanks were operated (1.3, 1.9, and 2.8 psi).

during the experiment.

Note that in terms of properties of the particle of interest, the momentum threshold depends only on the mass. Once the threshold is known for one type of particle, the value for other types can be determined by multiplying the threshold by the ratio of the masses. For example, the momentum threshold for electrons in 2C1 was

$$\begin{aligned} p_{th}(e^-) &= p_{th}(\pi^-) \times \frac{m_e}{m_\pi} \\ &= 19.3 \text{ GeV} \times \frac{0.5\,\text{MeV}}{139.6\,\text{MeV}} \\ &= 0.07 \text{ GeV}. \end{aligned} \tag{13}$$

This value is well below the momentum of any electron expected to enter the detector area of the spectrometer. By design, the Cherenkov detectors should have fired for

all scattered electrons.

One also can measure the π^- threshold directly, by measuring Cherenkov efficiency for π^- candidates versus momentum. As seen in Figure 24, the efficiency will have a turnon region which can be fit with an error function with an offset. The halfway point of the turnon region is defined as the π^- threshold and the duration of the turnon region is called the turnon width[10].

For the 2.75° and 5.5° spectrometers, the π^- efficiency for the C1 tank was given by

$$\pi^- \, eff(C1) = \frac{(E > 2)(p > 10)(track)(E/p < 0.6)(C1_{Vmin} > 15)}{(E > 2)(p > 10)(track)(E/p < 0.6)}. \qquad (14)$$

A comparable equation is used for C2. In Equation 14, E is the cluster energy in GeV. This quantity comes from the shower counter, which will be discussed in Section 3.3.5. The track momentum is p measured in GeV, *track* requires that the hits be on a track, and $C1_{Vmin}$ is a minimum pulse height cut on the 2C1 signal in FADC units.

To extract the π^- momentum threshold from the π^- efficiency plot, the error function fit mentioned above was used. The results from these fits[11] are shown in Table 6 and are plotted on along with a curve of the predicted values in Figure 23. The predicted and measured values agree reasonably well, although at the lower pressure the curve is slightly below the data.

Note that no requirements were made of C2 in Equation 14. If C2 happened

[10] Width comes from the σ of the Gaussian distribution used in the error function.
[11] Fits are only from the 2.75° and 5.5° tanks.

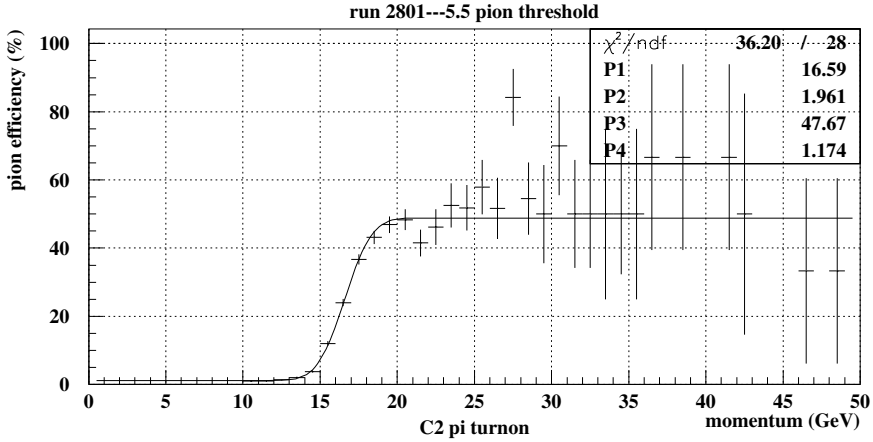

Figure 24: Cherenkov pion efficiency vs. momentum. This plot shows the effective pion threshold of the 5C2 detector. The threshold is defined as the halfway point of the turnon region. For the plotted parameters shown: P1 is the threshold, P2 is the width of the turnon region, P3 is a scale factor, and P4 is the height of the lower plateau.

to be set at a higher momentum threshold than C1 and requirements were made of C2, then a particle with momentum below the C2 threshold would have been cut from the sample. This could bias the C1 measurement towards the C2 threshold. Unfortunately, not using a C2 requirement allowed some contribution from kaons and protons into the denominator of Equation 14. When using only the shower counter and hodoscopes, these particles were indistinguishable from π^-'s, but they did not have enough momentum to fire the Cherenkov detectors.

In the case of the 10.5° spectrometer, the task of determining the π^- threshold from the data was not as straight forward. This was due in part to the difficulty of identifying π^-'s with only the 10.5° shower counter and a few hodoscope fingers. For this reason, no measured value of the π^- threshold is given in Table 5.

Table 7: Details of the PMTs used in the E155 Cherenkov system.

characteristic	
model	Hamamatsu
spectral response	200 nm - 640 nm
peak quantum efficiency	21% at 380 nm
photocathode	bialkali
dynode structure	14 stages, linear focus
anode pulse rise time	2.2 ns
transit time spread	1.2 ns
gain	$\sim 3 \times 10^7$

Notes:
Adapted from Reference [96].

Light Yield

The expected number of photo-electrons for particles well above threshold is given by

$$N_{p.e.}(predicted) = N_0 L \langle \sin^2(\theta) \rangle \tag{15}$$

where

$$N_0 = 2\pi\alpha Z^2 \int R(\lambda)T(\lambda)QE_{PMT}(\lambda)C(\lambda)\frac{d\lambda}{\lambda^2}. \tag{16}$$

Here N_0 is the quality factor and was dependent primarily on the properties of the mirror and the PMT. In E155 Hamamatsu R1584 PMTs were used. Some details of the tubes are presented in Tables 5 and 7. More can be found in Reference [97]. L is the effective length of the detector, and $\sin^2(\theta)$ comes from the Cherenkov relation (Equation 9) and is based on the index of refraction of the radiator. In Equation 16, λ is the wavelength of the Cherenkov light produced, Z is the charge of the particle and α is the fine structure constant. The efficiency of the detector

Table 8: Typical values for quantities used in determining the photon detection efficiency.

$T_g(\lambda > 130\,nm)$	$R_m(\lambda > 170\,nm)$	$QE_{PMT}(\lambda \approx 400\,nm)$	$C(\lambda < 385\,nm)$
100%	83%	25%	82%

Notes:
T_g is the transmission coefficient of the gas. R_m is the reflectivity of the mirror. QE_{PMT} is the quantum efficiency of the PMT cathode and C is the quantum efficiency of the wavelength shifter.

comes from the combination of the remaining terms: the reflectivity of the mirror $R(\lambda)$, the transmission coefficient of the gas $T(\lambda)$, the quantum efficiency of the the PMT cathode $QE_{PMT}(\lambda)$, and the quantum efficiency of the wavelength shifter[12] $C(\lambda)$. Typical values for these quantities are presented in Table 8. Since the E154 mirrors and PMTs are the same ones used here, and the transmission coefficients for the gases used in the two experiments are comparable[13], N_0 from E154 can be used to determine the expected number of photo-electrons. From the information presented in [96] one obtains an average value of $N_0 = 142\,\mathrm{cm}^{-1}$.

It should be noted that the quantities that affect N_0, such as the the reflectivity of the mirror or the quantum efficiency of the wavelength shifter may have decreased since the last direct measurements of their efficiencies were made. However, the reduction in efficiency was not expected to be enough to significantly affect the operation of the detector. For this reason, the individual efficiencies that

[12] The wavelength shifter was layer of p-terphenyl that coated the face of the tube. It absorbed photons in the near UV range and re-emitted them into the visible range ($\sim$ 390 nm) where the R1584s have a higher QE [97].

[13] The transmission coefficient for E154 may have been a little lower due to Oxygen contamination. An effort was made to avoid this problem by leak checking the tanks prior to E155 [102].

go into Equation 16 were not remeasured during the period between E154 and E155. The usefulness of the predicted number of photo-electrons is that it provides a rough estimate of the light yield. Using the quality factor from E154 together with Equation 15 gives the values presented in Table 5. Implied in this method is the simplification that the five detectors differed only in gas temperature, gas pressure, and the effective length of the tank. Mirror reflectivity and quantum efficiency of the PMT and wavelength shifter were assumed to be the same. The results from this approach are discussed below.

The measured number of photo-electrons comes about by examining the Cherenkov pulse height spectrum for electrons. For the 2.75° and the 5.5° spectrometers (using the C1 tank as an example) the electron definition is given in Equation 17. The 10C electron definition is in 18.

$$e^-(\mathrm{C1}) = (E > 9)(p > 9)(track)(0.8 < E/p < 1.2)(C2_{Vmin} > 25) \quad (17)$$

$$e^-(\mathrm{10C}) = (E > 5)(p > 5)(track)(PR\,hit)(E/p > 0.8) \quad (18)$$

The notation used here follows that of Equation 14 on page 82. A sample pulse height spectrum is shown in Figure 25. This particular example uses 10.5° data during run 2801. Since only a few photo-electrons are being counted, the distribution is Poissonian in nature. By measuring the mean (μ) and the width (2σ) of the peak one can ascertain the number of photo-electrons via Equation 19 [14]. The results

[14]For a Poissonian distribution $\mu = \sqrt{\sigma}$. In Equation 19 scale factors cancel out leaving only μ.

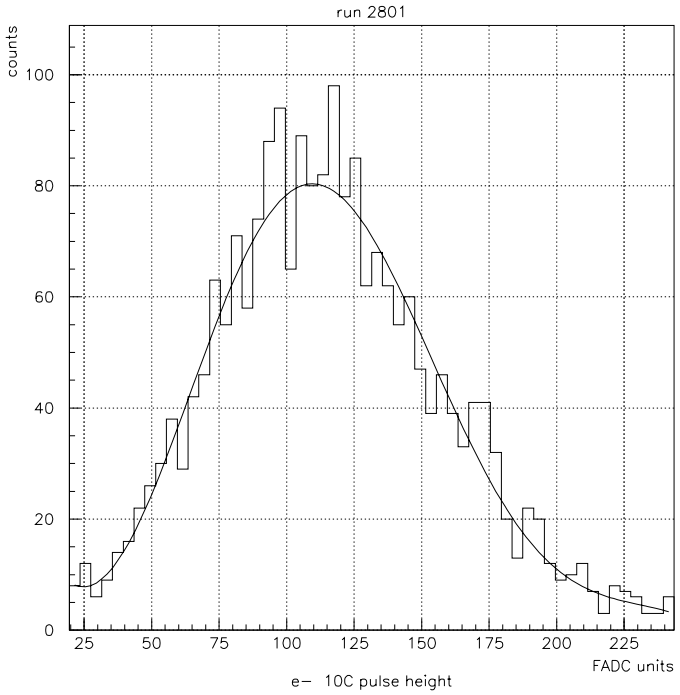

Figure 25: Pulse height spectrum for electrons in 10C during run 2801.

from such measurements are presented in Table 5.

$$N_{p.e.}(measured) = \left(\frac{\mu}{\sigma}\right)^2 \tag{19}$$

In comparing the measured number of photo-electrons to the predicted values, there are a few points worth noting. The values agree well for 10C, 5C2, and the later run set of 2C2. Thus the average N_0 from E154 is a good approximation of the actual quality factor. The earlier and later run sets do not agree well for the measured value of 2C2. Since the main difference between these two sets is that a new PMT was installed during the interim, the disagreement is a measure of the difference of the quantum efficiency of the PMT/wavelength shifter combinations of the old and new PMTs. The predicted values for 2C1 and 5C1 overshoot

the expected values by 13% and 21% respectively. However, the earlier and later measured values for these two detectors found similar answers giving confidence to those numbers. The E154 quality factor does not represent the PMT/wavelength shifter/mirror components well for those two tanks. Lastly, the 10C gas pressure was increased around run 2000. This increase improved the light yield by $\approx 50\%$ and is seen in both the measured and predicted values.

Another effect of the 10C pressure increase is that it lowered the π^- threshold from 16 GeV to 13 GeV. This change was deemed advantageous because it increased the electron signal and aided in electron-pion separation. The number of pions that were able to fire the detector was increased slightly due to the lower threshold, but this effect was small compared with the improved separation between e^-'s and π^-'s. The ratio of π^-'s to e^-'s in the 10.5° spectrometer goes from a small fraction at a momentum of 16 GeV to about 1 at 13 GeV, which is approximately the value of the π^-/e^- ratio seen in the 2.75° spectrometer at the π^- threshold of 19.5 GeV.

A Brief History of the E155 Cherenkov Tanks

Of the five detectors used in E155, four of them (the 2.75° and 5.5° tanks) were originally constructed for the SLAC experiment E142 [100]. These tanks were also used in E143 [101]. For E154 sections were added to 2C1, 2C2, and 5C1 which extended them to their present length (see Table 5 for dimensions). As seen in Equation 15, this is one means of increasing the light yield but it does not affect the π^- threshold (Equation 12). The E154 collaboration also used a different electronics

setup to read out the signal [96]. Flash ADCs replaced ADCs and TDCs with 4 levels of discriminators became a backup system. E155 used the same electronics setup as E154. The electronics are discussed in more detail below. In preparation for E155 we refurbished the existing tanks and constructed a new tank for the 10.5° spectrometer.

Construction of 10C

The 10.5° Cherenkov tank was fabricated at SLAC for E155. Groups from American University, Institut des Sciences Nucléaires, SLAC, Smith College, and the University of Massachusetts contributed to the projected.

The body of 10C consisted of three cylindrical sections arranged (from the upstream to downstream end) in increasing diameter. Dimensions of the tank are given in Table 5. The two smaller sections previously made up "the whale", a vacuum vessel used just downstream of the target in E154. The end windows were hydro-formed from 1.5 mm thick aluminum sheets. This type of window satisfied the requirements of having a safe and reliable vacuum vessel with as few grams of material present within the acceptance of the spectrometer. Prior to the experiment the tank was leak checked and was found to have a rate of rise of 0.6 mTorr/day, which was greater than the recommended allowance of 0.1 mTorr/day [102]. There was a concern that after a few weeks oxygen would start interfering with the Cherenkov signal. For this reason the gas was replaced roughly halfway through the two month run of E155. During the run, no deterioration of the signal

due to oxygen contamination was seen.

In filling the tank the gas was sent first through two filters, a molecular sieve and a charcoal filter. These extra precautions were used to ensure the purity of the gas. The tank could be filled and emptied remotely from the counting house. Sensors in the tank enabled the gas temperature and pressure to be monitored and the values were written to tape every ten to fifteen minutes.

The spherical mirrors used to collect the light were manufactured at CERN [103, 104] and were of the same dimensions as those used in the C2 tanks of the smaller angle spectrometers. They were positioned vertically at the downstream end of the tank. The mirrors were focussed on a PMT centered on the floor of the tank about 60 cm upstream. Drawings of the mirrors and PMT are shown in Figure 26.

To align the mirrors, the expected electron trajectories were determined and a subset of these were tabulated for three z locations. The collection of alignment points also included electron trajectories along the edge of the acceptance as well as photon rays from the largest possible Cherenkov cone produced by the "acceptance edge" electrons. Set 1 was at the upstream window, Set 2 was at $\approx 2/3$ of the distance to the downstream window, and Set 3 was at the mirrors. The points from Sets 1 and 2 were scribed onto pieces of Plexiglas which were then bolted to the tank at the appropriate z location. For set 2, the Plexiglas was fastened to an Aluminum ring which was installed to support the collimation baffles (discussed in the next section). A HeNe laser positioned just outside the upstream window was shone through each pair of corresponding points on the two pieces of Plexiglas and onto

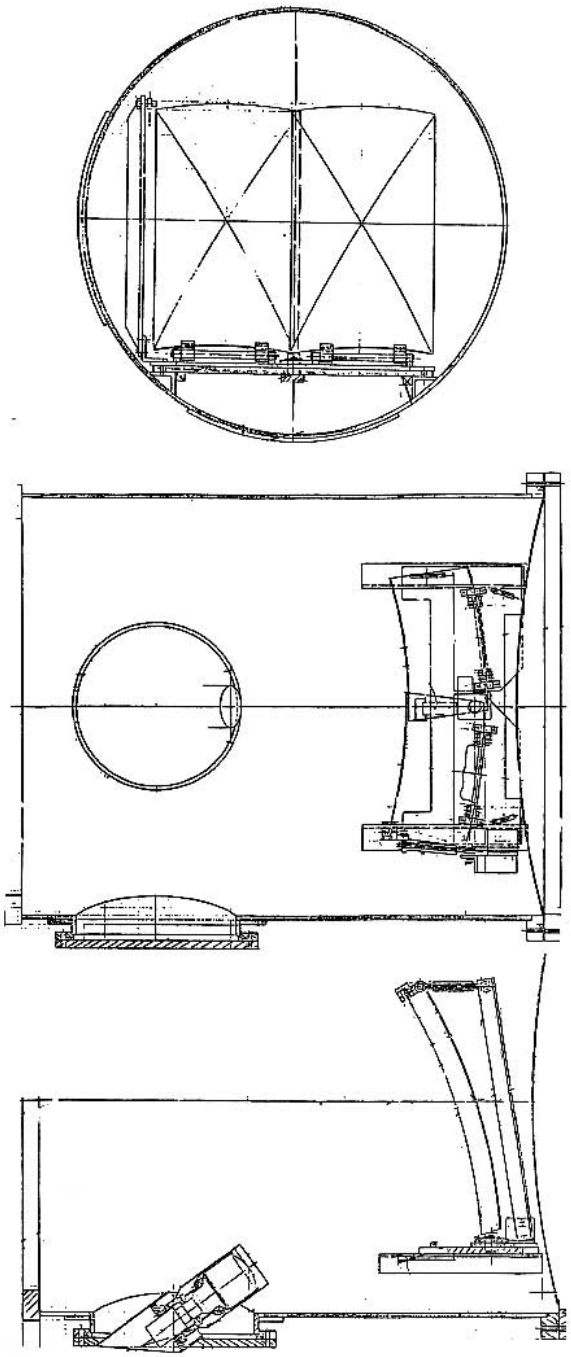

Figure 26: Three drawings of the 10C mirrors. In the top plot are the two mirrors viewed from inside the tank looking downstream. The middle plot shows an overhead view of the PMT, PMT access port, side access port, and mirror platform. In the bottom plot is a side view of the PMT and the mirrors.

the mirror. For stability, the laser was mounted on a surveying transit. From the mirror the laser beam was reflected to a piece of graph paper placed at the location of the PMT face. Figure 27 shows the sample of electron trajectories at the mirror location and the measured locations of the reflected rays at the face of the PMT.

The PMT was a Hamamatsu R1584 with a 5" face [97]. Bases for the PMT were made at SLAC. The tube had a peak quantum efficiency of $\approx 25\%$ at $\lambda \approx 400$ nm and was operated at +2210 V. To improve the detector's sensitivity to the Cherenkov light in the UV region, the face of the PMT was coated with ~ 230 nm of p-terphenyl [97] [105]. The tube was seated within a shell of μ metal shielding to reduce the impact of fringe fields from the spectrometer magnets.

As a means of testing the PMT during the experiment, a blue LED was affixed to the bottom of the mirror mount and aimed at the PMT face. The unobstructed output from the LED was too bright for the sensitive PMT and accompanying electronics. Therefore several small sheets of aluminized mylar foil were place at the front end of the LED housing to attenuate the light output.

The tank was fitted with collimation baffles and lead shielding around the PMT. These features were also added to the E154 tanks and are discussed in the next section.

Modifications of Existing Detectors

In E154 the Cherenkov detectors encountered a significant amount of background signal [106]. An effort was made to reduce the total background using several

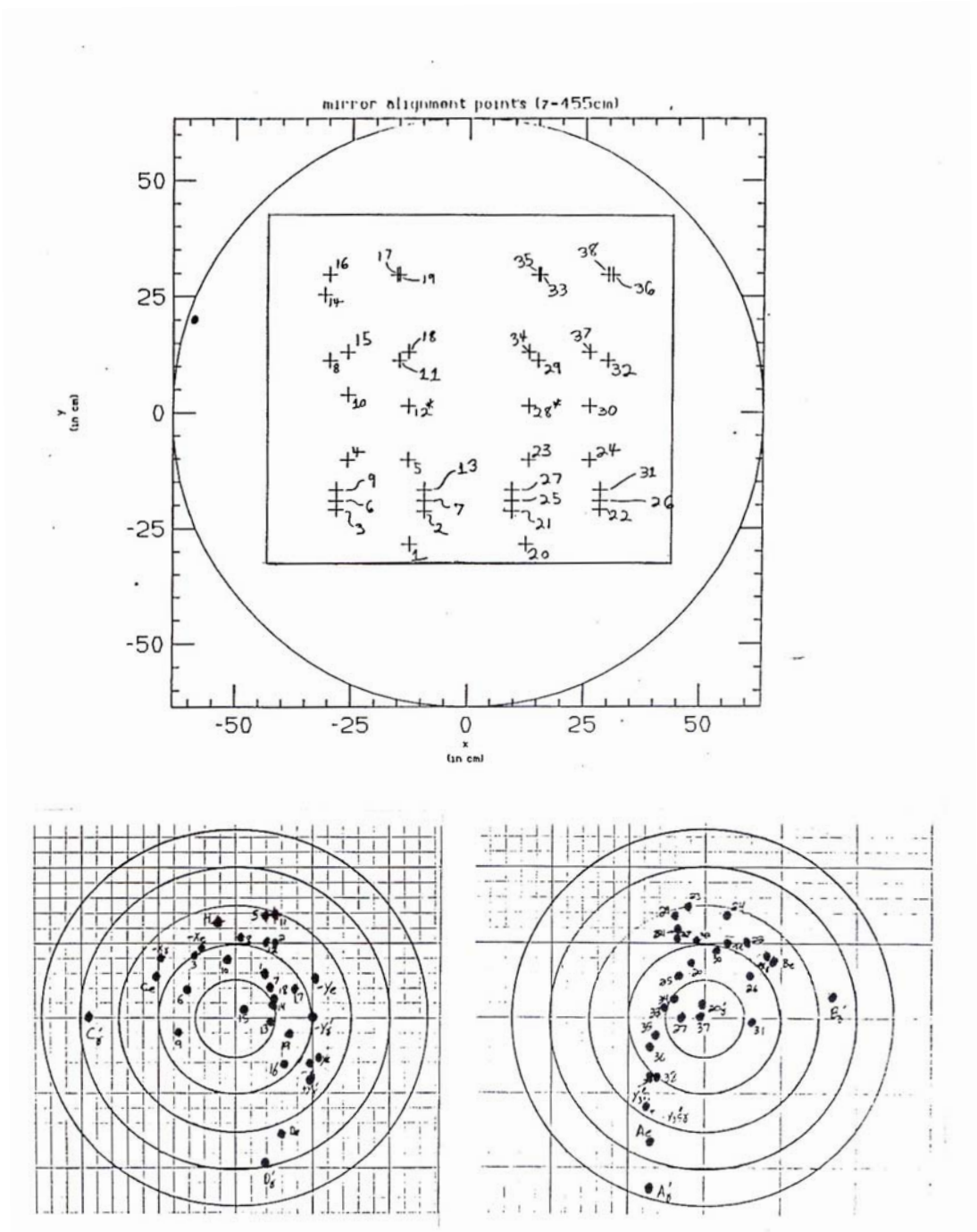

Figure 27: The top plot shows selected 10.5° electron trajectories at the 10C mirror location. The outer edge of the two mirrors is designated by the inner square. On the lower right are the points of the $+x$ mirror at the face of the PMT. Likewise, the $-x$ mirror's alignment points on the PMT face are given in the lower left. The $+(-)x$ refers to the mirror closer to (further away from) the beam line.

techniques, each one addressing particular components of the background.

The backgrounds in question were any particles that should not have fired the Cherenkov detector but did. One source of background signal was generated by the remnants of the beam scraping the beam pipe down stream of the target region. This scraping would create a spray of particles, some of which would pass through the spectrometers transversely. A similar spray would be created by a particle hitting the metal of a magnet or a collimator upstream of the detectors. Sometimes this would result in secondary particles traveling through part or all of the spectrometer. These included knock-on electrons above the electron momentum threshold. In the Cherenkov detector, background hits were also created by particles such as π^-'s that were below the momentum threshold but would create scintillation light while traveling through the gas radiator.

Collimation baffles and curtains: A portion of the background signal came from particles that passed through the inside of the tank but at some point were outside of the spectrometer acceptance. These particles may have created either scintillation or Cherenkov light. To cut down on this contribution, collimation baffles and curtains were installed in all of the tanks. An example of the baffles can be seen in Figure 22. The curtains are not included in this picture for the sake of clarity but were located on the sides of the tank between the mirrors and the downstream baffle. Both the baffles and curtains were made from black anodized aluminum.

Lead shielding around the PMT: Some of the background came from particles

hitting the PMT directly. The main source of this background was from low energy particles coming from the central beam pipe. An effort was made to protect the side of the PMT towards the central beam pipe by seating it within an alcove made from lead (see Figure 22). The shielding was typically $\geq$ 2 inches thick as seen by an approaching particle. To prevent the lead shielding from extending into the acceptance, the support structure for the PMT had to be modified. With the new mount the PMT was able to be moved further back into the tank's access port.

Gas test: Particles passing through the tank but without enough momentum to create Cherenkov light could still fire the detector by creating scintillation light in the Nitrogen gas. Prior to E155 several potential Cherenkov gases were studied with a focus on their ability to quench scintillation light [107]. During the checkout phase of the run two of the gases were tested to ensure that they reduced the scintillation light without adversely affecting the Cherenkov light yield. The gases tested were $90\%\,N_2 + 10\%\,CH_4$ and $95\%\,N_2 + 5\%\,H_2$ and were found to reduce the scintillation light by $(46 \pm 2)\%$ and $(36 \pm 8)\%$ respectively when compared to straight N_2 [108]. The percentages of CH_4 and H_2 were chosen because they constituted the highest mixing allowed within safe/nonflammable limits.

No noticeable deterioration in the Cherenkov light yield was observed in either of the gases. $N_2 + CH_4$ was used for the main E155 data run because it provided the greatest reduction in the scintillation background.

Lead lining the beamside wall of the 2.75° *hut:* As mentioned above, part of the background was due to the beam scraping the beampipe downstream of the

target. To reduce the sensitivity of the 2.75° spectrometer to this source, a wall of lead was installed between the detectors and the beamside wall. The lead was $\approx$ 4 to 6 inches thick and essentially extended from the floor to the ceiling of the hut. In the z direction the lead ran along both Cherenkov tanks as well as the 2.75° hodoscopes.

Electronics

Two systems were used to read out the signal from each PMT, a primary system and a backup system. Figure 28 shows a diagram of the Cherenkov electronics. The primary system received its signal from the PMT's anode and used a Struck DL 515 Flash ADC (FADC) to digitize the output. A sample of the output is given in Figure 29 where time is along the horizontal axis and pulse height in FADC units is along the vertical (256 FADC units $\approx$ -2 Volts).

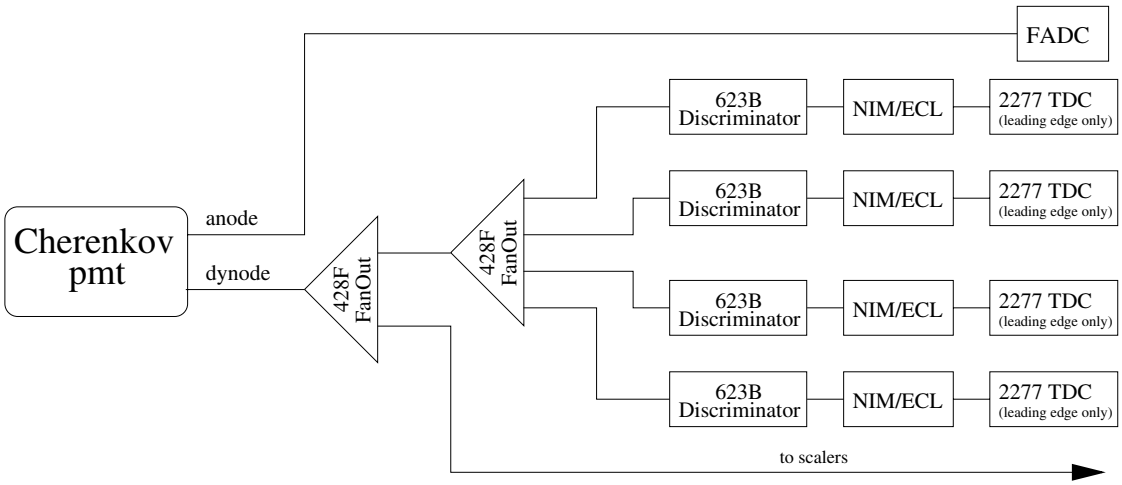

Figure 28: Electronics diagram describing the readout of a 2.75° or 5.5° Cherenkov detector. The FADC units were made by Struck. All other modules shown are from Lecroy Research Systems.

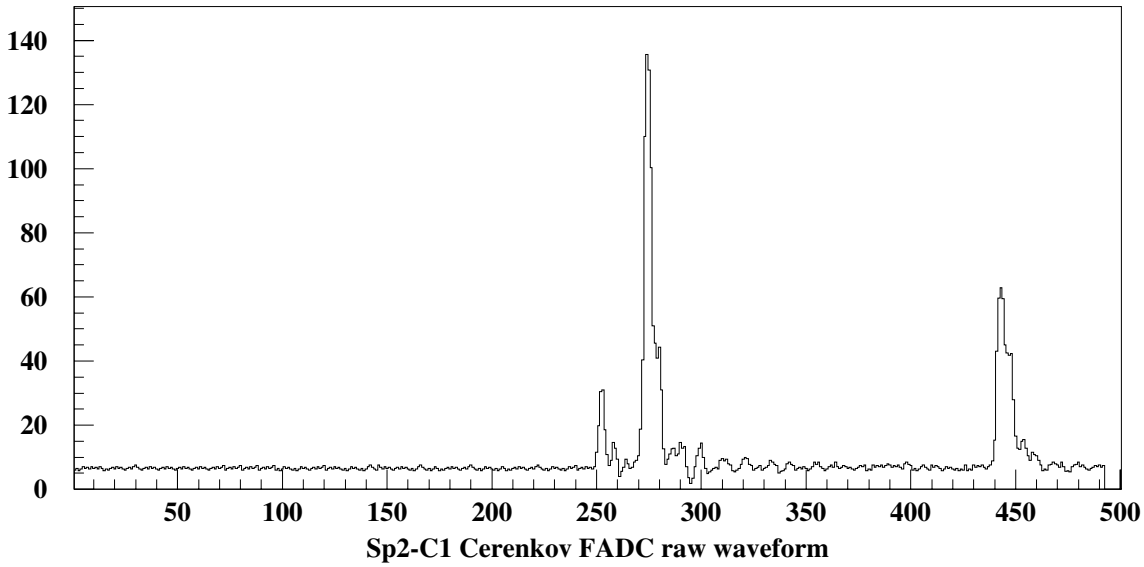

Figure 29: Cherenkov raw waveform readout from the Flash ADC. The horizontal axis is time in 1.05 ns bins and the vertical axis is in Flash ADC units.

The FADC boards have four input channels and were used with a 238 MHz external clock. An external clock was used because the 250 MHz internal clock was not synchronized with the start signal for the other TDCs (*i.e.*, those in the hodoscope and shower counter systems). The external clock utilized as a source the 119 MHz output from *SLC FIDO II* in Counting House A. Unfortunately, the external clock exhibited a periodic drift of $\approx \pm 0.5$ ns. The cycle lasted for about 3 hours. To account for the drift a time offset per run was inserted in the software. Earlier in the experiment before this effect was understood the drift would cross over the start of the readout cycle causing the FADC times to shift in the middle of a run by 4.2 ns. When this happened it was necessary to correct the FADC times with the backup system.

This correction was done by calculating the difference between each hit found

with the primary system and the closest hit in time registered by the backup system. Pulse height information of the hit was taken into consideration. An average difference was determined for each spill. If the average was within some time window (eg: 3 ns $\leq \overline{\Delta t} \leq$ 6 ns), then all times in that spill were shifted by -4.2 ns. When there were no backup hits with which to compare, the decision was made on the previous spill's information.

Inputs into a FADC module were interleaved with delay cables. The output from the PMT was sent to the input of channel 0, the output from channel 0 was sent to the input of channel 1, the output from channel 1 was sent to the input of channel 2 and so on. As a result, every 4.2 ns a snapshot was taken where the waveform was sampled at four evenly spaced intervals. This resulted in a resolution of 1.05 ns. A board read all of a PMT's output for the duration of the beam spill plus a little extra time before and after. The typical read time lasted for about 500 - 600 ns.

The backup system for each tank used the dynode output from the PMT which was fanned out to a set of Lecroy 3412 discriminators. 2.75° and 5.5° tanks used four levels of discrimination. Each level was sent to a Lecroy 2277 TDC which recorded only the leading edge. In the 10.5° two levels of discriminators were fed into a 2277 hit expander and then into a 3377 TDC. The upper level read leading edge only while the lower level recorded both leading and trailing edges.

As mentioned above, the backup system was used for a few runs to synchronize the FADC hit times. This fix could be turned on for a given tank for any

run. When the fix was on, the size of the shift was determined individually for each spill. There was also a subset of about 100 runs in which the 5C2 FADC failed. For these runs the backup system provided both the time and some limited pulse height information for the data analysis.

The dynode signal was also used as input into a scaler. This was used in coincidence with scalers from other detectors to gauge the spectrometer's electron detection rate in real time during the E155 data taking period.

Software

Figure 30 shows a flow chart of the Cherenkov pulse finding algorithm. As seen in the flowchart there are three main sections to the code.

In the the first section, a raw waveform (see Figure 29) is used as input. The waveform is scanned for potential pulses. Next a pedestal subtraction is performed by removing the candidate events and calculating the average height of the remaining waveform.

In the second section, each pulse's characteristics are determined. These include an improved time measurement, the pulse height and integrated charge as well as information such as whether or not the hit saturated the FADC. After each pulse has been analyzed, the expected pulse shape[15] is subtracted from the waveform at the appropriate location. This was done to reduce the effects of pile-up on later

[15]The expected pulse shape is obtained by taking the average shape of many "1 hit" spills. This averaged shape is normalized and then scaled by the integrated charge of the pulse currently being analyzed.

hits and to avoid reconstructing any features[16] of the pulse shape as hits.

The last section makes adjustments such as applying time offsets. If the TDCs are needed to correct the Cherenkov time, that code is executed here by a flag set in a constants file. After passing a few sensibility checks on the pulse's information (see Figure 30) the event is saved to the hit bank.

3.3.5 Shower Counters

For energy measurements each spectrometer contained a segmented lead glass electromagnetic calorimeter located at the downstream end of the detector system.

An incident electron will create an electromagnetic shower in the lead glass through a series of bremsstrahlung radiation emissions and pair productions. This cycle will continue until the created particles are below the critical energy [17]. As the remaining particles continue to travel through the lead glass, those moving faster than the speed of light in the glass (i.e. $\gtrsim 0.7$ MeV) will create Cherenkov light which is detected by the PMTs located at the downstream end of the detector. The total number of particles above Cherenkov threshold and the distance each travels in the lead glass will determine the light yield for the shower. As a result, the amount of light recorded will be proportional to the energy of the incident particle.

The majority of hadrons (mostly pions) deposited only a small fraction of their energy in the detector. Using the ratio of the shower energy to the momentum

[16] For example, if the signal had a ringing, the secondary peaks should not be detected as new hits.

[17] Below the critical energy, the particle is more likely to lose its energy through ionization than through bremsstrahlung.

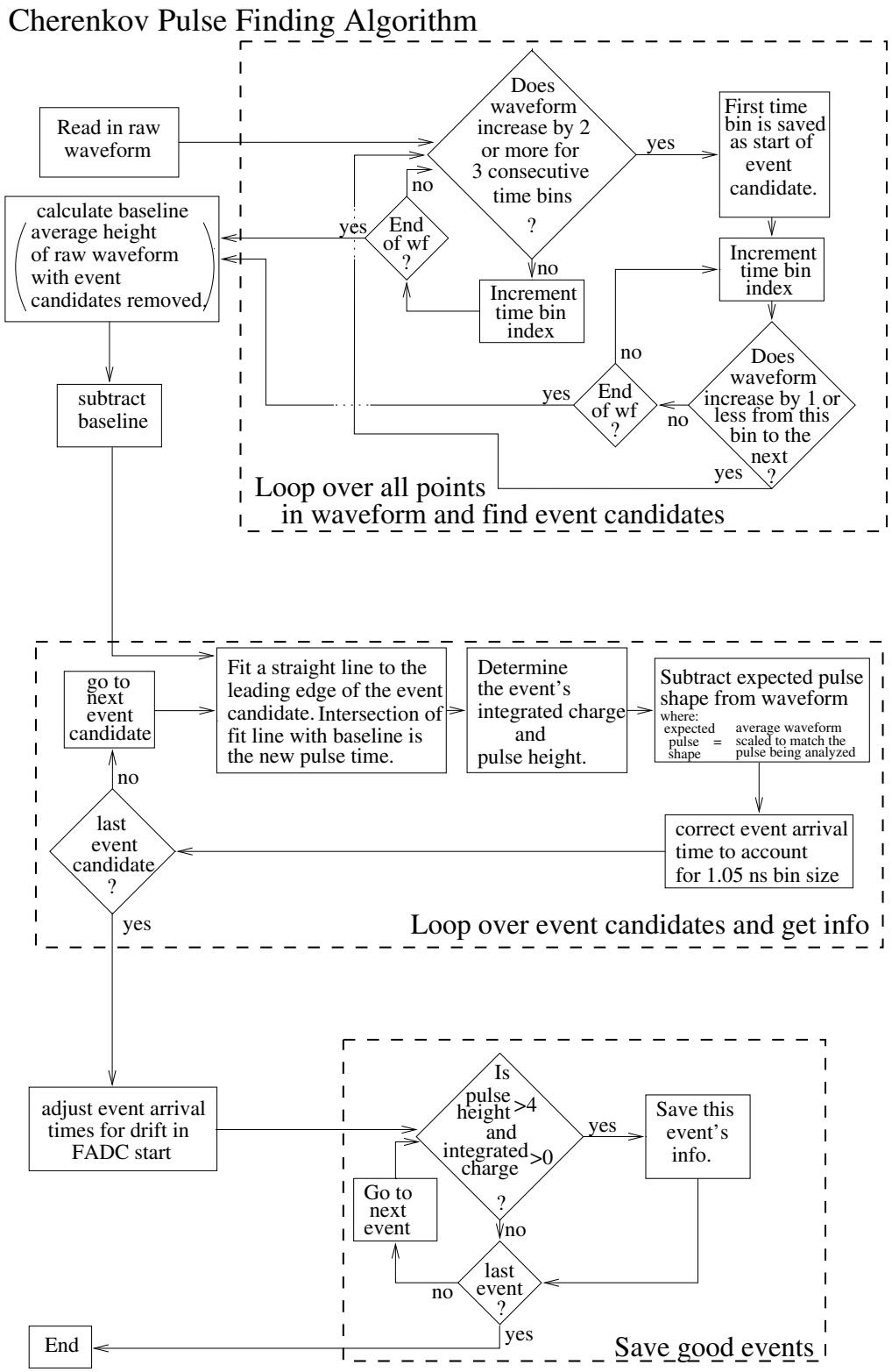

Figure 30: Flow chart of the pulse finding algorithm used for the Cherenkov analysis.

of the particle (obtained from tracking information) provided a strong means of separating electrons from pions. This is further discussed in Section 4.7.

A portion of the background particles is made up of muons. Muons are more likely to create only Cherenkov light in the lead glass than they are to begin a shower. As is the case for pions, the ratio of energy to momentum is an effective means to separate the muons from electrons.

The 2.75° and 5.5° shower counters consisted of an array of lead glass blocks 10 blocks (wide) by 20 blocks (high). A sketch of the 2.75° shower counter configuration is shown on the right hand side of Figure 31. The blocks were used earlier in the ASP experiment [109] on the SLAC PEP ring as well as in E142, E143, and E154. Each block was 6.2 cm × 6.2 cm × 75 cm, had an index of refraction n=1.58 and a radiation length X_0 = 3.17 cm. The detector was $\approx 24X_0$ long, which is sufficient to contain the longitudinal shower. Each block was individually wrapped in aluminum foil and then in black tape to make it light tight. For further protection against light leaks, the entire stack of blocks was encased in an aluminum shell. A picture of the 2.75° shower counter is shown on the left hand side of Figure 31.

Each block was read out with an Amperex XP2212PC PMT. The PMTs were glued to the blocks with optical epoxy. The PMT signal was sent through a passive splitter, with one output from the splitter going to an ADC and the other through a discriminator to a TDC. Because of the lower rates in the 5.5°, only one level of discrimination was used for that spectrometer. 64 of the 2.75° blocks which experienced the highest instantaneous rates had a system of TDC's with three levels

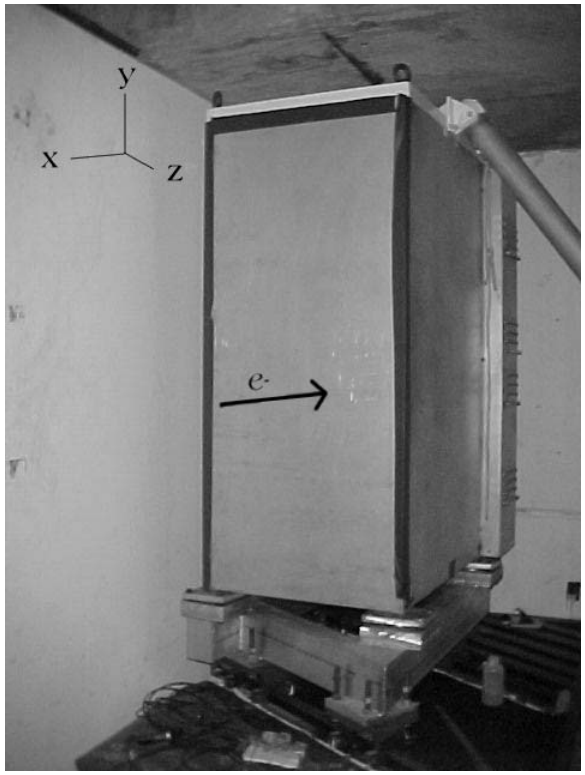

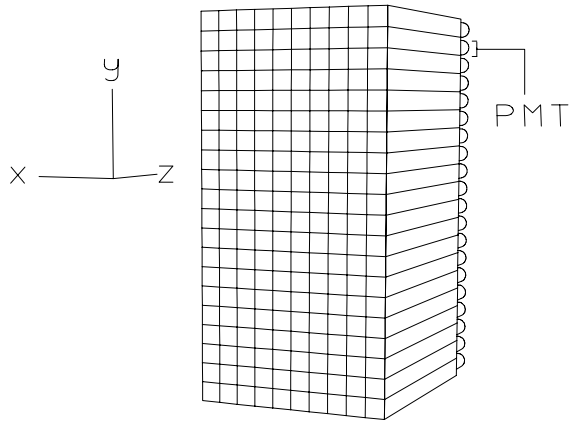

Figure 31: On the left is a photo of the 2.75° shower counter. On the right is a drawing showing the inner arrangement of the same detector.

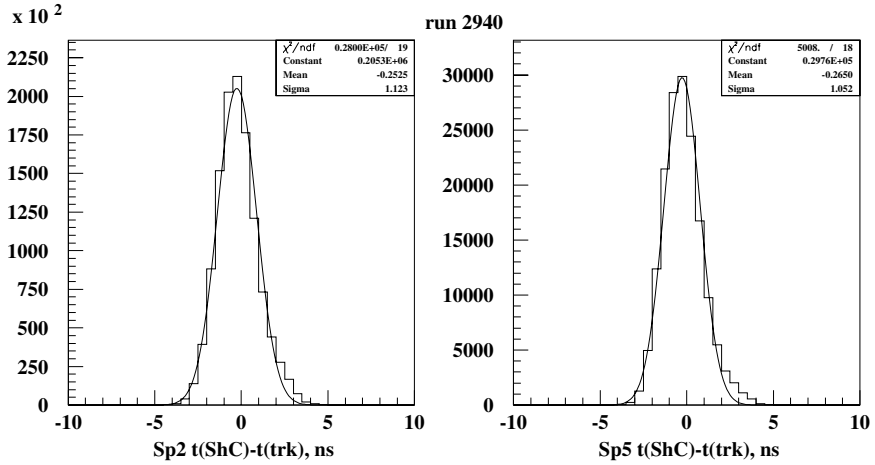

Figure 32: Time resolution for the 2.75° and 5.5° shower counters. The fit is a Gaussian.

of discrimination. The remaining 136 blocks in the 2.75° used two levels of TDC's. Details of the electronics setup are shown in Figure 33 for the 2.75° and Figure 34 for the 5.5° and 10.5° .

The time resolution for the shower counters was around 1 ns. This was determined by Gaussian fit to a timing residual histogram of shower counter hit times - tracking hit times (see Section 4.2 for tracking information). Sample histograms with fits are shown in Figure 32 for the 2.75° and 5.5° spectrometers.

The energy resolution for the 2.75° shower counter was measured to be about $\frac{15\%}{\sqrt{E'}}$ [88]. This was done as part of T418 [112], a test beam used for calibration purposes that took place following the E155 main run. For T418 approximately 1 electron per spill was sent into the 2.75° and 10.5° spectrometers.

A Hamamatsu L2360 Xenon lamp was used as a test signal to ensure that the PMT and accompanying electronics were working during the run. The signal from the lamp was sent to each block by way of a fiber optic cable and was controlled

Table 9: Details of the lead glass blocks used in the 10.5° shower counter.

	A	B	C	D
dim (cm^3) $x \times y \times z$	$14.6 \times 14.6 \times 35$	$10.5 \times 10.5 \times 25$	$14.6 \times 14.6 \times 40$	$75 \times 6.2 \times 6.2$
used earlier in:	SLAC-ESA 8 GeV spectrometer	SLAC-ESA NE04 spectrometer	SLAC-ESA 8 GeV spectrometer	SLAC-PEP ASP detector
number of blocks	4	3	23	10
lead glass type	SF-5	SF-6	SF-5	SF-2
length in X_0	14.2	14.8	16.2	1.96
PMT type	Phillips XP2041/00	Hamamatsu 1911-05	Phillips XP2041/00	RCA 8575
position	TA 4 inner blocks of bottom row	TA bottom row corners and top row $-x$ corner	TA blocks not covered by columns A or B	PR

remotely from Counting House A. The Xenon lamp was used mostly during the checkout period.

The 10.5° shower counter was separated into 2 distinct parts, the pre-radiator PR and total absorber TA. The TA was similar to the calorimeters used in the other two spectrometers and consisted of 30 lead glass blocks stacked into 6 columns by 5 rows. Three different types of blocks were used in the TA. Parameters of the blocks are presented in Table 9. The electronics used to read out the signal were similar to those used in the 2.75° and 5.5° shower counters. Details are shown in Figure 34.

Since the 10.5° only had one Cherenkov detector, an active pre-radiator was

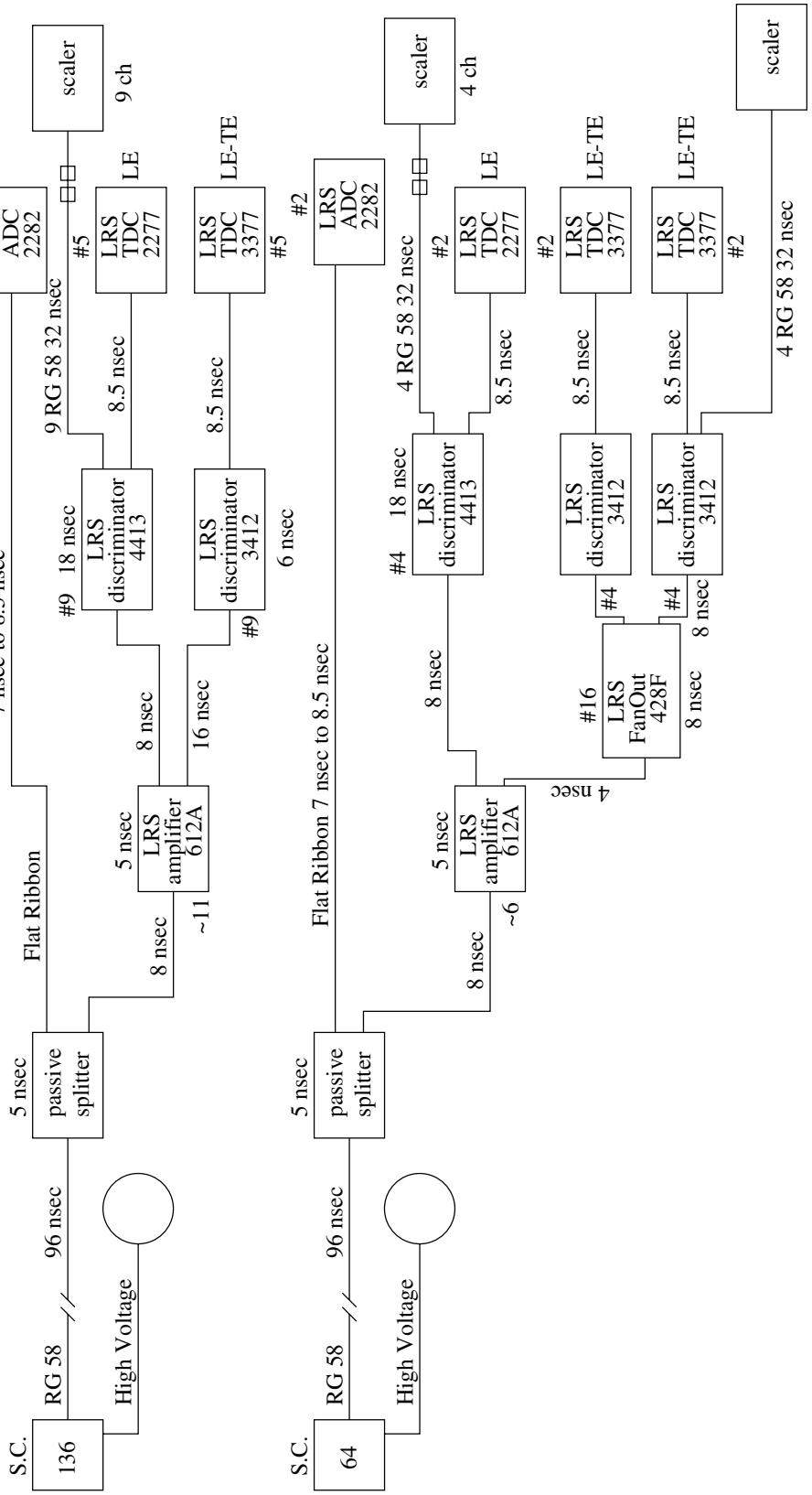

Figure 33: Electronics diagrams for 2.75° shower counter detector. Each of the 64 blocks which experienced the highest instantaneous rate had an additional discriminator and TDC.

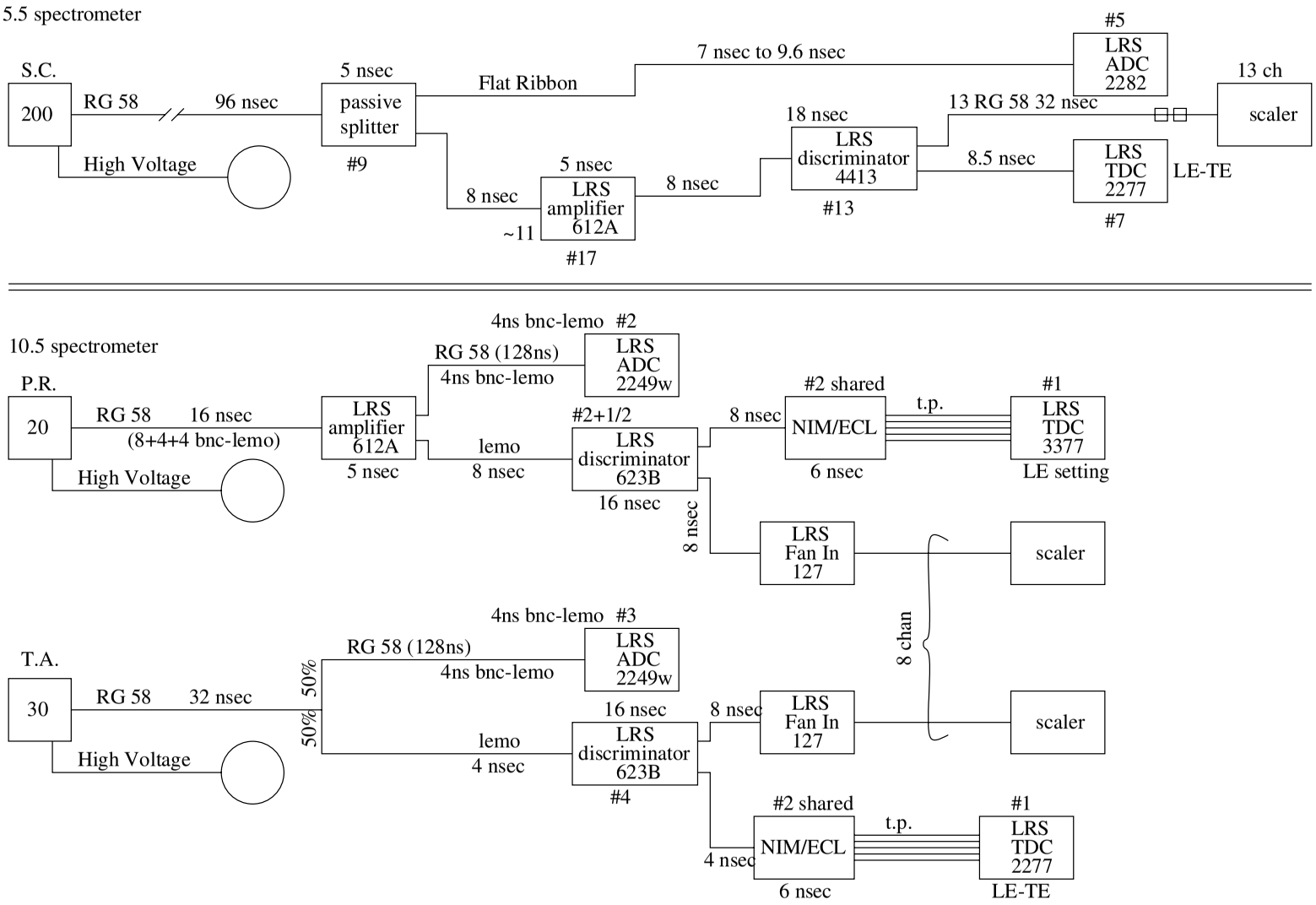

Figure 34: Electronics diagrams for the 5.5° and 10.5° shower counters.

included to help separate electrons from pions. Unlike pions which will most likely only create Cherenkov light while passing through the lead glass, the electrons will begin to shower in the PR. This leads to a larger light yield for electrons than for pions.

The PR was located just upstream of the TA and used the same type and size of blocks which were used for the 2.75° and 5.5° shower counters. Ten blocks were stacked vertically and were perpendicular to the spectrometer axis. Each PR block was read out by two PMTs located on the $\pm x$ ends. Readout electronics for the PR PMTs are also shown in Figure 34.

An LED was used for calibration purposes and as a test of the 10.5° shower counter electronics during the run. The LED signal was distributed to the blocks via fiber optic cables and was controlled remotely from Counting House A.

3.3.6 Data Acquisition System

The electronics used to read out data from the individual detector systems were described in the previous sections of this chapter. Much of the electronics were kept in the 2.75° hut in ESA. This allowed the signal cables to be kept short. To move the data from the electronics to the data tapes, E155 used a VME based Data Acquisition system (DAQ) with CAMAC interfaces. The CAMAC interfaces enabled the existing pool of electronics to be used. Details of this system are described in References [113, 114]. The system was designed to be able to read out a little more than 1 MB per second and typically functioned at a rate of about 800

kB per second.

E155 used a triggerless DAQ in which a snapshot was taken of all of the relevant beam and spectrometer information for each spill. Accumulated data were divided up into sections called runs. A typical run was $\approx$ 1100 MB in size, contained $\approx 175,000$ spills, and took about 25 minutes to accumulate. Many of the details involved with packaging the data into runs was handled automatically by a program called DAQcntrl.

From the VME system mentioned above, the data were read to a disk and when a run was completed the information would be copied to a tape. Approximately 2000 tapes were used to house the E155 data set. While most contain raw data, some of the tapes contain either Møller or calibration data. The calibration data includes pedestal data from the electronics, LED data from the systems that had LED test setups installed, and toroid calibrations. Calibration runs were usually performed every few hours. Each set lasted a few minutes during which the electron beam was suppressed.

While the data were being read to the disk, a sample of spills were available for online analysis. This was mostly used to insure that the various detector components were functioning in an acceptable manner.

CHAPTER 4

DATA ANALYSIS

4.1 Data Collection

E155 collected data for two and a half months from mid-February through the end of April 1997. The first two weeks of the run were used as a checkout period, during which the beam was operated at 30 Hz. A variety of equipment calibrations and detector studies were performed during the low rate running conditions. These studies included timing in the electronics modules and an energy scan to calibrate the A-line [71]. For parallel running, the beam energy was varied from 48 to 40 GeV. Among the detector studies were a Cherenkov gas test (see Section 3.3.4) and high voltage scans for the hodoscopes. Also during checkout data were taken with the spectrometer apertures partially obstructed by tungsten sieve slits to look at momentum reconstruction or completely blocked with lead bricks for background studies.

At the beginning of March, the rate of spills delivered to ESA was increased to 120 Hz. Only data collected during high rate running were used to determine $A_{\parallel}$ and $A_{\perp}$. In addition to polarized DIS data, other types of runs performed during this period included calibration data (see Section 3.3.6), Møller runs for

beam polarization measurements, and positron runs[1].

The data were stored on a set of 1 GB tapes with typically one data run per tape. These were known as the raw data tapes and contained TDC, ADC, and FADC information from the beam and spectrometer electronics. To analyze one run consumed the better part of a day, with the bulk of the processing time spent finding shower clusters and tracks. To save computer (and calendar) time, the tapes were preprocessed once and then the tracks, shower clusters, Cherenkov hits, etc. could be used later as needed. This method will be explained in Section 4.3.

4.2 Clustering and Tracking

Quantities such as the time, position, and energy of each shower cluster were calculated from the TDC and ADC outputs of the shower counter. The cluster position was determined by a weighted average of the x and y positions of the 9 shower blocks (3×3 square) which contained the shower[2]. Weighting factors came from the energy deposited in each block [115]. In the case of overlapping showers, a technique called energy sharing was used to separate the clusters. The amount of energy given to each shower was determined by examining the duration of the pulse times.

A track was the path taken by a particle when it traveled through one of the spectrometers. Two exclusive categories of tracks known as classes were used for

[1]Positron runs were performed periodically to estimate the contributions from pair symmetric processes. For these runs, the spectrometer magnets were operated with their polarities reversed. This is discussed in more detail in Section 4.8.5.

[2]Essentially all of the energy from electron shower was contained within the shower counter. Typically only a fraction of a hadron's energy was detected.

the E155 analysis:

class 1: shower cluster + 1 or more Cherenkov hits + hodoscope hits[3]

class 2: shower cluster + (no Cherenkov hit) + hodoscope hits

A shower cluster was the starting point of a track candidate. It was then paired with any Cherenkov hits (one per tank) which occurred in time[4] with the cluster. Next, hodoscope hits were sought out which were in time with the track. The spatial information of the hodoscope hits, when put together with an understanding of the spectrometer optics, were required to correspond to a physically realizable track. For example, the track should point back to the target and should be contained within the geometry of the detector package. Once a track was found, different pieces of information associated with it were recorded for later use. In addition to the different detector hits, other recorded information included:

$p \rightarrow$ Track momentum, used as E' in calculating x and Q^2 of an event.

$\theta \rightarrow$ Scattering angle in the horizontal (non-bend) plane. This angle was measured with respect to the central trajectory of the spectrometer.

$\phi \rightarrow$ Scattering angle in the vertical (bend) plane. This angle too was measured with respect to the central trajectory of the spectrometer.

Although particles which produced an insignificant or no shower cluster did make their way through the detectors, these tracks were not reconstructed to increase the processing speed of raw data tapes.

[3] Typically a minimum number of three hodoscope hits per package were required. Four hits were required of the 2.75° front hodoscopes with its six planes and higher hit rates.

[4] Two hits are considered to be *in time* if their time difference is small (less than ±3 ns) after both the particle's time of flight and the time required to read out each signal are taken into account.

4.3 Data Summary Tapes

To cut down on the computer time overhead involved with analyzing the raw data, the tapes were preprocessed to determine tracks, shower clusters, and Cherenkov hits. The output along with selected information from the beam and shower counter systems were written to Data Summary Tapes (DSTs). Minimal data cuts were made in creating the DSTs. The advantages of the DSTs were twofold. Not only did they take much less time to process but they were also considerably smaller in terms of the file size on tape.

Two sets of DSTs were produced. The first set was labeled "DST1" and covered the run range from 803 to 4384. This set was created in the summer of 1997. However, there were hardware and software conversion problems associated with the 10.5° spectrometer. For example, variations in gains of the hodoscope and shower counter PMTs, due to fringe fields from the nearby 2.75° and 5.5° spectrometer magnets, needed to be corrected. Also the shower counter TA PMTs experienced a pulse ringing which made finding clusters difficult [111]. Reasons such as these made the DST1 version of the 10.5° data inadequate for analysis purposes. By January of 1998 significant progress had been made on 10.5° issues so a second set of DSTs were produced, which were called DST2. Because no major improvements were made on the 2.75° and 5.5° reconstruction since DST1, the DST2 tapes only contained data from the beam and the 10.5° spectrometer. Due to hardware problems which limited the usefulness of earlier runs, DST2 production began at run 1026.

4.4 Student Analysis

Two semi-independent analyses of the data were undertaken. Both used the same set of DST tapes as their starting point. One was carried out by Peter Bosted and is described in references [116, 117, 118, 119, 120]. The other was performed by the E155 thesis students. From here on the two will be referred to as the Bosted analysis and the student analysis, with the latter being the focus of the following pages. The two analyses were compared at various different levels and times. This provided a means of cross checking which sometimes uncovered subtle discrepancies between the two efforts.

4.5 Run Selection

Prior to a spill by spill analysis, a list of good data runs was assembled and pruned to remove runs which had irreparable problems. For the student analysis, run lists were constructed for each spectrometer on the basis of target material and the mode of the spectrometer magnets (*i.e.*, positron or electron). Table 10 shows the total number of runs in each category. Reasons for which a run was cut are listed below. Depending on the type of problem, a run could have been removed from either all lists or only from the list of one spectrometer. For example, if a 10.5° magnet was down for a particular run, then this run would be removed from the 10.5° list but would still be used for the 2.75° and 5.5° analyses. Other runs, such as those with problems which stem from the beam, target, or DAQ areas, would be removed from all lists. The majority of runs for a given spectrometer mode are

Table 10: Number of good data runs per spectrometer for proton and deuteron targets.

	parallel				perpendicular			
	proton		deuteron		proton		deuteron	
	e^-	e^+	e^-	e^+	e^-	e^+	e^-	e^+
2.75°	575	59	471	110	79	5	196	8
5.5°	620	38	470	142	82	5	209	8
10.5°	605	51	551	59	83	5	204	8

Notes:

Parallel and perpendicular refer to the direction of the target magnet's field with respect to the incident beam. e^- and e^+ are used to indicate the mode of the spectrometer magnets.

used in all three spectrometers.

Reasons that a run was removed from the good run list:

- A spectrometer magnet was off. Usually due to a magnet power supply tripping off.
- Runs taken during checkout were not used.
- No runs were used for the 2.75° analysis during the period in which the Cherenkov detector 2C2 was down. This down time lasted from run 2043 to run 2140.
- No runs prior to run 1026 were used for the 10.5° analysis.
- Runs with less than 0.05 incident peta-electrons were cut. During high rate running, this cut-off corresponds to $\sim$ 2 minutes of calendar time. Typical reasons for terminating a run so soon were that the beam quality might have degraded suddenly or the beam delivery might have been interrupted (for example, due to a problem with a linac component).

- The sign of the beam polarization was recorded by four different means[5]. A few runs were cut because there was not a unanimous agreement between these four helicity bits for a significant number of spills.
- Mixed up spills: This item concerns the manner in which the data are read out and stored on tape. Each spill's information was divided into sections called *subspills*. A mixed up spill occurred when the spill number of the subspill did not match the spill number of the parent spill. Few runs were removed for this reason. Usually, these runs were aborted as a result of automated checks designed to look for potential DAQ problems.
- Certain beam conditions would cause an increase in the number of noise hits in the detector packages. In a few cases, this increase impeded the readout of a spill's data. The level of disruption was displayed in a quantity called the *% busy*. On a few occasions the % busy was high enough to warrant that the run be removed from the data set.
- Runs were cut if the target polarization was below 10%.
- ^{6}LiD data taken with target insert 5, lower cell were not used. These data were inconsistent with the rest of the deuteron data. Details are presented in reference [122].

Table 11: Beam cuts used for E155.

0 ADC counts $<$	good spill	$<$ 2000 ADC counts
0 ADC counts $<$	bad spill	$<$ 2000 ADC counts
$0.5 \times 10^9 e^-$/spill $<$	toroid 2	$< 5.0 \times 10^9 e^-$/spill
$0.5 \times 10^9 e^-$/spill $<$	toroid 3	$< 5.0 \times 10^9 e^-$/spill
-20.0 mm $<$	foil array x	$<$ 15.0 mm
-20.0 mm $<$	foil array y	$<$ 15.0 mm
0.2 mm $<$	foil array dx	$<$ 5.0 mm
0.1 mm $<$	foil array dy	$<$ 5.0 mm
four out of four polarization bits agreed		

4.6 Beam Cuts

Runs were analyzed one spill at a time and within each spill the data were examined in pieces based on sections of the experimental setup. First the beam data were processed, followed by those of the 2.75°, 5.5°, and lastly the 10.5° spectrometer data. Before the analysis code began to look for events in the spectrometer data, several checks known as the *beam cuts* were made to ensure the quality of the beam for that spill. Some of the cuts also were a safeguard against any unforeseen glitches in the computer code or detector electronics that might have gone unnoticed. A summary of the beam cuts used for E155 are presented in Table 11 and a short description of each is given in the following paragraphs.

The good and bad spill cuts were made on the ADC readouts of those detectors. Typical values were 230 and 20 for the good and bad spill respectively. Sample

[5] The four sources for the beam helicity were known as PMON, High Voltage line, MACH line, and Veto line.

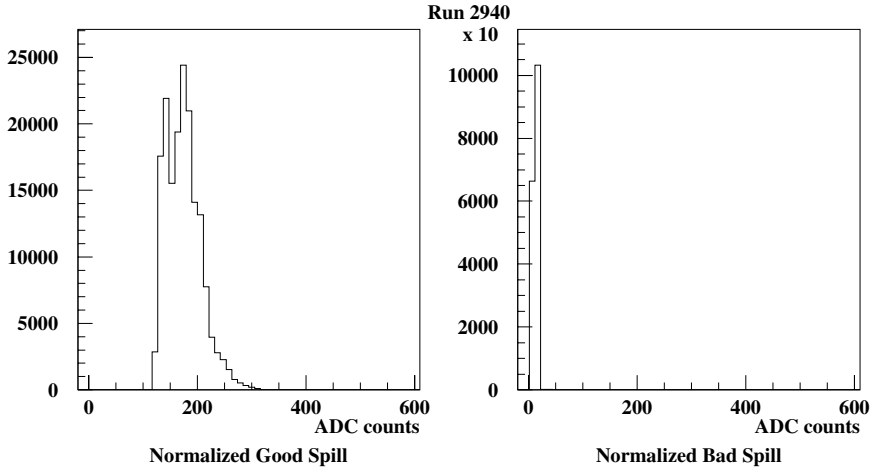

Figure 35: Spectra for the good spill and bad spill detectors.

histograms from one run's worth of data are shown in Figure 35.

Toroid cuts were software limits placed on the incident beam current. The minimum value of $5 \times 10^8\, e^-$/spill removed the witness pulse from the data set. A large portion of the E155 data were collected between beam currents of $3 \times 10^9\, e^-$/spill and $4 \times 10^9\, e^-$/spill. Over the course of a data run, the beam current was relatively stable. The current was raised or lowered by request of the shift workers. Usually this was done in response to the detectors' hit rates at the time. For example, good beam conditions were sometimes accompanied by lower background rates (*i.e.* lower overall hit rates). This allowed the beam current to be increased which in turn increased the DIS data rate. Figure 36 shows the beam current histogram from run 2940.

Cuts on the beam position were made in terms of the beam's properties at the foil array. Since these detectors were downstream of the target, and because the optics of ESA had the beam focussed at the target, the dimensions of the beam at

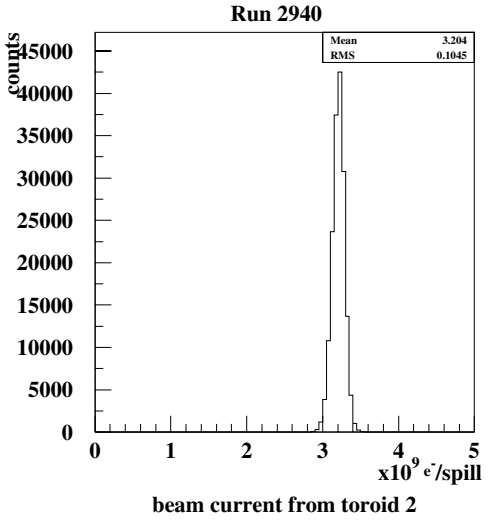

Figure 36: Beam current spectrum for the deuteron run 2940.

the foil array were slightly larger than they were at the target. Also, the effective center of the foil array did not coincide with the center of the target. The target center was located at approximately (-2.5 mm,-2.3 mm) in (x, y) on the foil array during parallel running and at (-2.5 mm,-7.0 mm) for the perpendicular mode.

Even though the envelope of the raster pattern was circular (for an example, see Figure 8 or Figure 9), limits imposed on the beam position were rectangular in nature. Studies were performed which looked at $A_{||}$ and g_1 as a function of raster radius [90, 123]. Neither quantity was affected by the position of the beam on the target. For example, in [90], the proton data were split into three subsets,

$$\begin{aligned} & r & < 6.0\text{mm} \\ 6.0\text{mm} < & r & < 8.5\text{mm} \\ 8.5\text{mm} < & r & \end{aligned}$$

where r is the raster radius. The integral of g_1^p was calculated for each set and all three were in good agreement.

Another raster cut that was examined was that of a crescent shaped cut on the south side of the target to be used for the 10.5° analysis. Some of the scattered electron events detected by the high θ side of the 10.5° spectrometer had the potential to pass through more material in the target assembly than did the events detected in other parts of the spectrometer. A negative aspect of the cut was that it removed 15% of the 10.5° data set. Comparing the integrals $g_1^{p,d}$ of the cut events with the uncut events showed that the two sets agreed. For this reason, the crescent shaped raster cut was dropped [120].

In Table 11, foil array dx and dy pertain to the width of the beam at the foil array. Sample distributions for these two quantities are presented in Figure 37. Note that the lower cut on dy is less than that of dx. Every so often the automated fitting routine calculated a value for dy which was below the lower limit. When the cut spills were examined in detail, no problems were found. One possibility is that the beam was only hitting one foil on the y array which made the fit difficult to do. For these reasons, the minimum allowed vertical spot size was lowered to include these ill-fitted but otherwise good spills.

As mentioned earlier, the beam helicity was determined by a pseudo-random number generator and recorded by four different means. All four values were required to be in agreement for the spectrometer data of the spill to be processed.

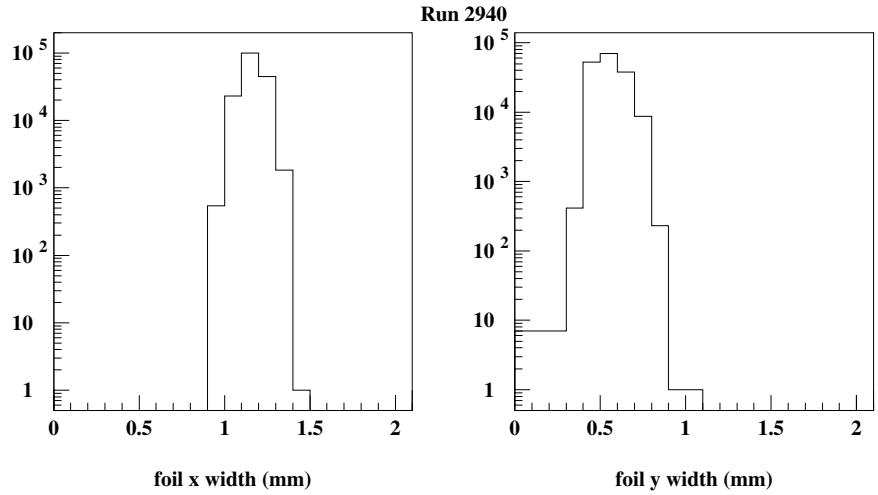

Figure 37: Histograms showing the beam profile in x and y.

4.7 Event Selection

4.7.1 Electron Definition

Once a spill passed the beam cuts, each spectrometer's data were checked for electrons. The 2.75° and 5.5° arms had similar detectors package and so the same electron definition was used for each. The electron definition used was:

- class 1 track
- $0.8 < E'/p < 1.2$
- 2 Cherenkov hits in coincidence
- $\sqrt{(\text{C1 pulse height}) \times (\text{C2 pulse height})} > 40$ FADC units
- Shower cluster cannot be centered[6] on an edge block
- $0.01 < x_{bj} < 0.9$

[6] The shower created by electron was typically contained within a 3×3 grid of shower blocks where the bulk of the energy was in the center block.

Details of the individual cuts are explained below. Both higher and lower cut levels as well as additional cuts were explored and used in detector studies. Since they did not lead towards any obvious advantage (for example, they did not improve the signal to background ratio), they were not included in the "good" electron definition.

For the 10.5° spectrometer, a purely track based definition was not an effective means of extracting the electrons from the raw data. This was due in part to a lack of redundancy in the 10.5° detector package and also to issues related to the newness of the setup[7]. Instead, a hybrid definition was used in identifying electrons [120] in which a track based definition was supplemented by a non-tracking component. The student implementation of the hybrid definition was split into a three-tiered structure which was organized around the shower cluster:

part 1 (track based)

- cluster was used in a class 1 track
- $E'/p > 0.75$
- C1 pulse height> c1vmin(low)
- C1 pulse time within ±3 ns of shower cluster time
- $\begin{cases} E' > 7 \text{ GeV} & \text{(no ADC saturation)} \\ E' > 5 \text{ GeV AND } p > 7 \text{ GeV/c} & \text{(with ADC saturation)} \end{cases}$

part 2 (track based) cluster failed part 1

- cluster was used in a class 1 track

[7]For example, problems with the magnetic shielding on the 10.5° hodoscope PMT's hurt the hit and tracking efficiency in the earlier runs. Once this problem was understood and corrected, the efficiencies were much improved.

- $E'/E'_{min} > 0.9$ (replaces $E'/p > 0.75$ in part 1)
- C1 pulse height> c1vmin(*high*)

  (replaces C1 pulse height> c1vmin(*low*) in part 1)
- C1 pulse time within ± 3 ns of shower cluster time
- $\begin{cases} E' > 7 \text{ GeV} & \text{(no ADC saturation)} \\ E' > 5 \text{ GeV} \quad \text{AND} \quad p > 7 \text{ GeV/c} & \text{(with ADC saturation)} \end{cases}$

part 3 (non-tracking) cluster failed both parts 1 and 2

- No ADC saturation
- $E' > 7$ GeV
- $E'/E'_{min} > 0.9$
- C1 pulse height> c1vmin(*high*)
- C1 pulse time within ± 3 ns of shower cluster time

A large portion of the good electrons were defined by part 1. Most of the events which satisfied the non-tracking part 3 came from earlier deuteron runs or were collected during perpendicular mode running.

For both types of electron definition, the E'/p cut pertains to the Energy/momentum ratio of the scattered particle. While most hadrons only deposited a fraction of their energy in the shower counter, usually all of an electron's energy was deposited there. This led to an E'/p of 1 for electrons and less than 1 for hadrons and muons. A sample E'/p spectrum from the 2.75° spectrometer is shown in Figure 38. Cuts from the smaller angle spectrometers' electron definition (see page 121) were used in making the histogram. The portion of the spectrum

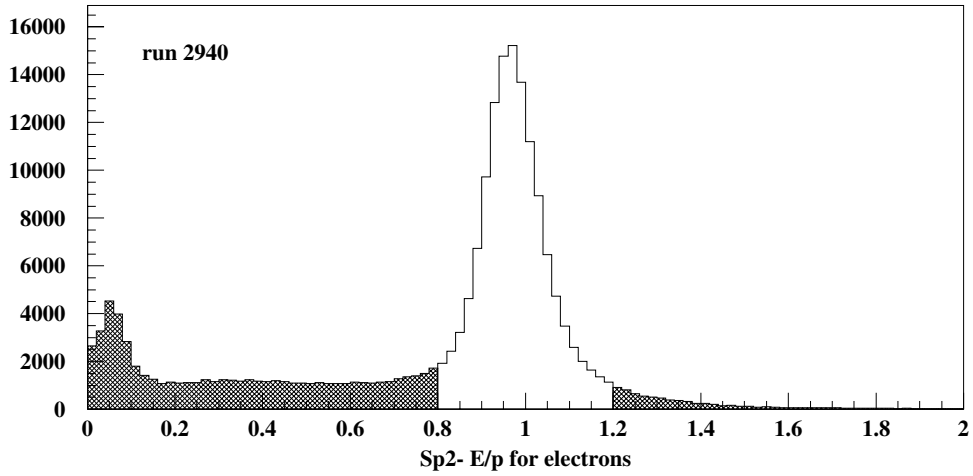

Figure 38: Energy/momentum ratio for 2.75° spectrometer electron definition described in the text. The shaded area indicates the data removed by the E'/p cut.

removed by the E'/p cut has been shaded. Hadrons which began to shower in the calorimeter created a small bump in the $0.2 < E'/p < 0.5$ region, which is barely visible in this plot. The number of counts from this source drops as E'/p increases and is small (but non-zero) in the "good" electron region. This contribution was called the *pion contamination* to the electron data set and its removal is the subject of a later section. At $E'/p < 0.1$ is a peak which is predominantly caused by non-showering particles that passed through the detector.

Events were not used if the associated shower cluster was centered on an edge block. Showers in these blocks were prone to losing part of the shower energy to the space surrounding the detector. This caused E' and E'/p to be artificially low and also made calibrating these blocks difficult.

In some sections of the 10.5° electron definition an E'/E'_{min} cut was used in place of E'/p. The two cuts served the same purpose. E'_{min} was determined by the

Table 12: Minimum required energy deposition for an electron in each row of the 10.5° shower counter TA.

row	1	2	3	4	5
E'_{min} (GeV)	5.8	7.8	9.2	10.4	12.2

Notes:

Row 1 was the bottom row.

vertical position of the cluster. Due to the single bend of the 10.5° spectrometer, each row of the shower counter was associated with a minimum momentum that a particle needed if it was to reach that part of the detector. E'_{min} values were calculated in a simulation of the spectrometer optics by P. Bosted and are presented per shower counter row in Table 12.

For the 2.75° and 5.5° Cherenkov detectors, a cut was used which made use of the product of the pulse heights from the two tank coincidence [124]. The logic behind the cut was to retain particles which created a large signal in one tank but possibly a small signal in the other. Pions above threshold would typically create a small signal in both tanks. Although an electron could produce a small signal, the average pulse height for an electron was a bit larger than that of the pion (see next section). Even less likely was for an electron to generate a small signal in both detectors. Figure 39 shows a 2-D box plot of 2C2 pulse height versus 2C1 pulse height. The data sample is for an electron definition which requires a class 1 track, $0.8 < E'/p < 1.2$, and a neural network[8] cut of $NN > -0.97$. In the center of the

[8] The neural network used only input from the shower counter to determine whether the cluster was created by a pion ($NN = -1$) or an electron ($NN = +1$). Neural network information was used in detector studies but was not a part of the event selection cuts used for the final analysis.

Figure 39: Pulse height spectra from the 2.75° Cherenkov tanks. Box plot is of 2C2 versus 2C1 for an electron definition. The line drawn corresponds to $\sqrt{(\text{C1 pulse height}) \times (\text{C2 pulse height})} = 40$ FADC units. Data are from run 2940. The concentration in the center is due to electrons while that in the lower left is from pions.

plot is a concentration due to electrons. Pions are the cause of the grouping in the lower left hand corner. A line has been drawn at the cutoff, which corresponds to a value of $\sqrt{(\text{C1 pulse height}) \times (\text{C2 pulse height})} = 40$ FADC units. Cuts at 20, 30, and 50 FADC units were also studied. A cut of 40 FADC units was decided upon because it led to both a high Cherenkov efficiency and a low rate of pion contamination at the pion threshold. In the region of the pion threshold, these two effects combined to give a smaller error on the asymmetry than would have been achieved by a lower cutoff value [124].

A similar type of product cut was examined for the 10.5° analysis where the pre-radiator (PR) of the shower counter was to take the place of the second Cherenkov tank. Unfortunately the PR was insensitive in discriminating between pions and electrons and so the cut was not used. Instead a *high/low* pulse height cut was implemented only for the Cherenkov signal. The value depended on the strength of the supporting evidence from the other systems that the event under consideration was an electron. Studies showed that the *high* pulse height requirement produced a data sample with a higher purity but lower efficiency than did the *low* cut. c1vmin(*low,high*) were (30,40) for runs prior to 2103 and (45,60) after run 2103. At 2103 the gas pressure in 10C was increased to aid in electron - pion separation.

4.7.2 Pion/Hadron Definition

Because of the triggerless data acquisition system, the data for many pions and muons, as well as some kaons and anti-protons (or protons), were written

to tape. Definitions to extract pions and hadrons also were implemented for the 2.75° and 5.5° spectrometers. Using the convention of the previous section, a collective hadron set (π's, K's, and p's) was defined as:

- class 1 or class 2 track
- $E'/p < 0.6$
- $E' > 1.5$ GeV
- Shower cluster cannot be centered on an edge block.
- $p > 9$ GeV/c

Only the lower portion of the E'/p spectrum was included to remove electrons. A sample of the hadron E'/p is shown in Figure 40. The hatched area, which was eliminated by the E'/p cut, contains the vast majority of electron events. As before, clusters centered on edge blocks were eliminated because they could lead to an artificially low E' and E'/p. The lower bound on E' was used to cut non-showering particles from the shower counter data, most of which were muons. In Figure 38, the peak below $E'/p < 0.1$ was due mainly to non-showering particles. The measured hadron rate as a function of momentum is shown for both targets in Figure 41.

The pion data set was a subset of the hadrons'. In addition to the cuts listed above, a two Cherenkov hit coincidence was also required. This limited the effectiveness of the definition to events with momenta over the Cherenkov pion threshold[9]. Since the results were reported in momentum bins, appropriate cuts were

[9] The pion threshold was set around 19 (16) GeV/c in the 2.75° (5.5°) Cherenkov tanks [125].

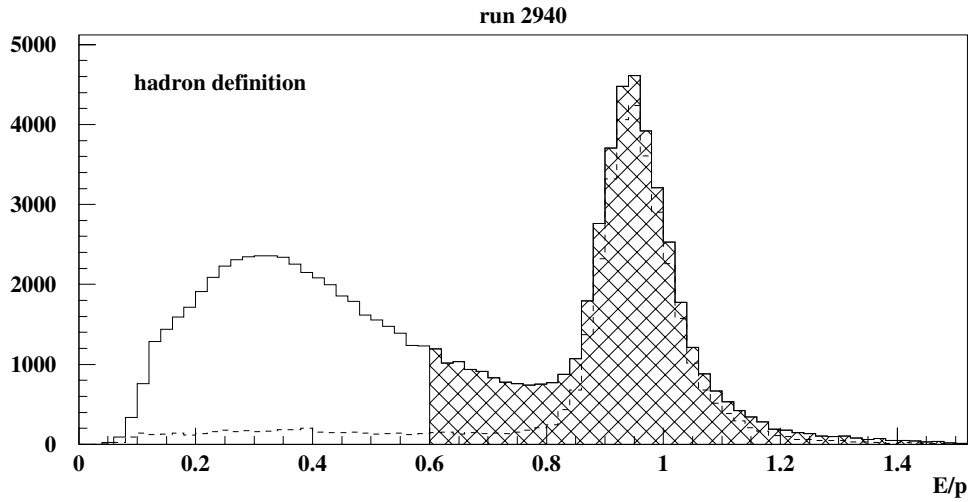

Figure 40: E'/p spectrum for 5.5° hadrons. Cuts used are: (a) class 1 or 2 track, (b) $E' > 1.5$ GeV, (c) No clusters centered on an edge block (d) $p > 9$ GeV/c. Hatched area indicates the data removed by the E'/p cut. The dashed line is an E'/p spectrum for a pion definition which required cuts (a-d) plus coincidence hits the two Cherenkov tanks.

made during a later stage of the analysis to remove any particle whose momentum was below threshold. In this region if the Cherenkov detector fired for a hadron, the signal was most likely due to something else, such as the particle creating scintillation light. Below threshold, a $\pi^{\pm}$ was indistinguishable from another hadron, thus making a positive identification of the pion difficult. The momentum cuts were not made on the data shown in Figure 41, where the $\pi^{\pm}$ curves exhibit bumps at the momentum threshold.

The effect that the additional requirement of a two Cherenkov hit coincidence had on the hadron E'/p spectrum can be seen in the difference between the solid and dashed lines in Figure 40. Including this cut caused a large portion of the hadron sample to be removed ($E'/p \lesssim 0.8$) while the electron data ($E'/p \approx 1$) was essentially left in tact. This result was somewhat to be expected. Comparing the

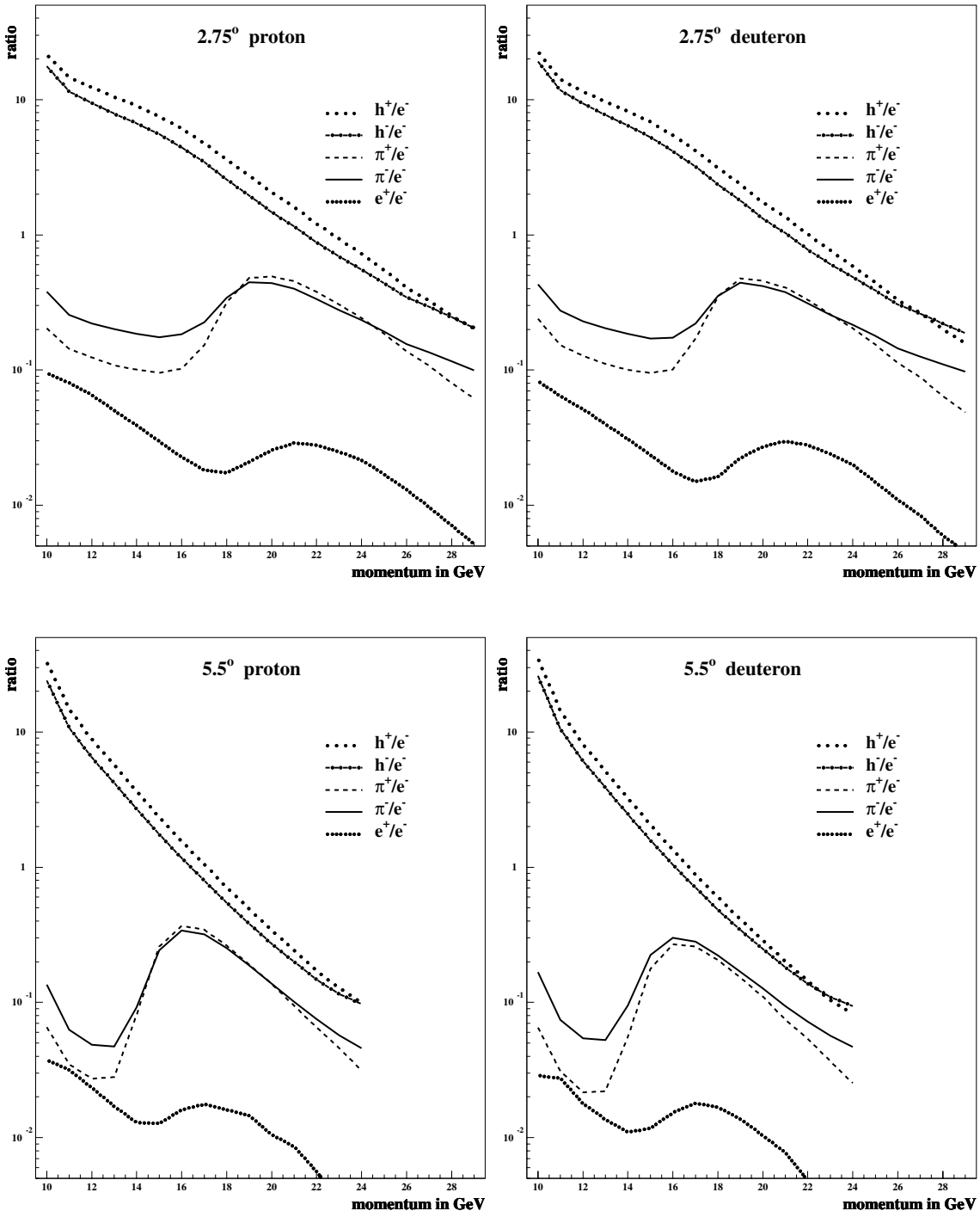

Figure 41: Detected hadron and positron rates for the 2.75° and 5.5° spectrometers. Cuts for the different particle definitions are described in the text (Electrons on page 121, hadrons and pions on page 128). The bump in the $\pi^{\pm}$ and e^{+} curves are due to the pion threshold in the Cherenkov tanks. Events below threshold were cut from the pion data sample but were included in the hadron sample which did not contain any Cherenkov requirements. The 2.75° plots were made with runs with large spectrometer acceptance only.

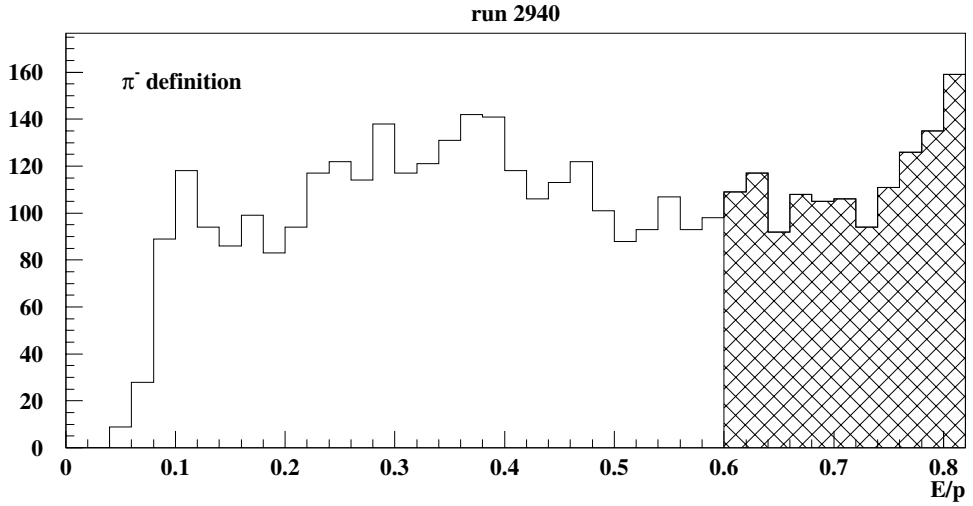

Figure 42: E'/p spectrum for pions detected in the 5.5° spectrometer. Area removed by the E'/p cut is marked by the hatched area. In addition to the cuts described in the text, an additional requirement of $p > 16$ GeV was made for this plot. Normally, that cut was made at a later stage of the analysis.

hadron and pion data in Figure 41, one can see that many hadrons were below the pion threshold[10]. Also by design of the Cherenkov detectors, all electrons should have created a sizable signal in both tanks. So the two tank coincidence picked out electron-like events, which included pions above threshold. A close-up of the E'/p spectrum for π^-'s is shown by itself in Figure 42. The region removed by the cut again is hatched with the electron peak now off the right hand side of the plot.

Other than each Cherenkov tank having a hit within a certain time window, no further pulse height requirement was made[11]. Compared to the light yield for electrons, the expected yield for pions (above threshold) was[12]

$$\frac{N_{p.e.}(\pi^-)}{N_{p.e.}(e^-)} = 1 - \left(\frac{p_{th}}{p}\right)^2, \tag{1}$$

[10]Kaon and proton thresholds were well above that of the pion.
[11]Due to the Cherenkov pulse finding algorithm there was an implicit cut of ~ 6 FADC units.
[12]This ratio can be calculated from the relations given in Section 3.3.4

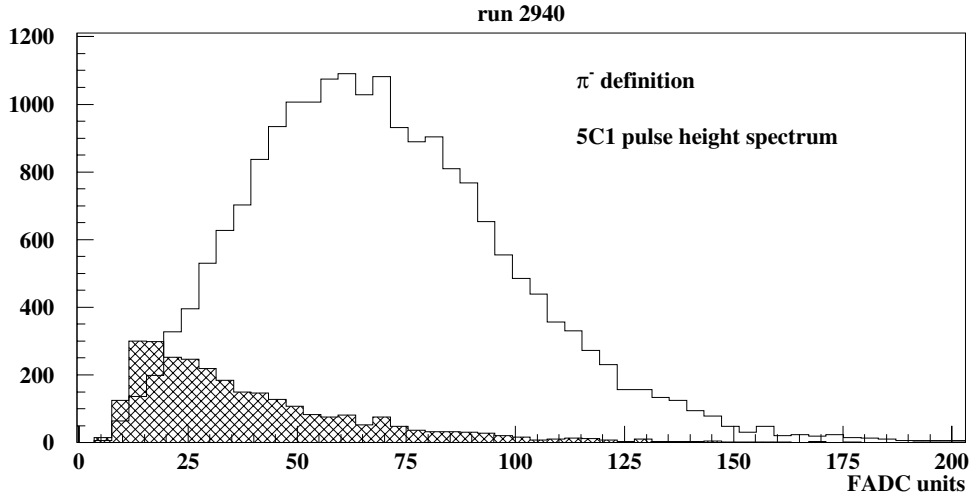

Figure 43: Cherenkov pulse height distribution for pions (hatched area) and electrons (outlined area). The light yield for pions is typically less than that obtained by electrons.

where p_{th} is the pion momentum threshold and p is the momentum of the particle. This ratio gives values of around 0.1 to 0.4 for 5.5° pions in the momentum range just above threshold, which were the majority of pions likely to fire the Cherenkov tanks. A sample Cherenkov pulse height spectrum is shown in Figure 43. Pions are presented in the hatched area and for comparison an electron spectrum also has been shown[13].

A number of other cuts were studied prior to arriving at the final pion and hadron definitions. These test definitions produced cleaner definitions but too severely reduced the sample size and so were not used in the final definitions. Since they were part of understanding the pion/hadron sample, these cuts are briefly mentioned here.

[13] In addition to the electron and pion cuts in the text, the data in Figure 43 were also required to have $p > 16$ GeV/c.

One test cut placed tighter restrictions on the time difference allowed between the shower cluster and the hit in each Cherenkov tank (to reduce random coincidences). Another cut only used a shower cluster if there were no other clusters within ± 5 ns (to improve the tracking efficiency). In an effort to pick out hadrons which began to shower, clusters were required to cover two or more shower blocks. Also, the fraction of the energy contained in the central block of the shower had to be between 0.75 and 0.2. For one particular run and using the 2.75° spectrometer, this fraction was in the region of 0.82 ± 0.05 for electrons and 0.45 ± 0.15 for pions. Lastly, in an attempt to weed out any low quality tracks, a phase space cut on the $x - dx$ tracking parameters was implemented.

All of these cuts were tried in the high rate environment of the 2.75° spectrometer, but only the "no other clusters within ± 5 ns" cut was included in some of the 5.5° test definitions.

4.8 Asymmetries

When a preliminary "good" particle definition was established, 20 or so variations of it were also assembled and the DST's were processed for the whole tape set at once. The multiple definitions were used as a time saving device to study the effects different cuts made on the results. Even though a DST could be analyzed in less than a 1/2 hour, there existed ~ 1400 runs to process and associated with each one was a setup time which could last from under a minute to around 1/4 hour. This resulted in a considerable overhead for reprocessing the tapes.

The output from each DST was saved in a "counts" file[14]. Within each file, the data were organized based on their definition number, x, Q^2, and the helicity of their parent beam spill. For pion and hadron definitions the momentum of the scattered particle was recorded in place of x_{bj}. Since different beam cuts were sometimes imposed from one definition to the next, the total incident charge per helicity was saved independently for each definition.

From the counts files raw asymmetries were determined using Equation 2,

$$A_{\parallel}^{raw}(x) = \frac{\left(\frac{N(x)}{Q}\right)^{\downarrow\Uparrow} - \left(\frac{N(x)}{Q}\right)^{\uparrow\Uparrow}}{\left(\frac{N(x)}{Q}\right)^{\downarrow\Uparrow} + \left(\frac{N(x)}{Q}\right)^{\uparrow\Uparrow}}, \tag{2}$$

where N was the number of events detected when the direction of the beam polarization was parallel ($\uparrow\Uparrow$) or anti-parallel ($\downarrow\Uparrow$) to that of the target. Here $Q^{\downarrow,\uparrow\Uparrow}$ is the total charge incident on the target for each beam helicity. A comparable expression was used for data collected during perpendicular running.

As with any experiment, E155 was performed in an environment over which there was finite control. Because the experiment had to run in a limited amount of time, the beam current (and thus the data taking rate) were kept as high as possible and as a result not every event was detected[15]. Also, every detected event was not necessarily from the process we wished to study. Therefore, corrections were made to the data to account for the additional effects experienced by the electron prior to, during, or following its interaction at the target. Due to the nature of the individual

[14] These were a second level of summary files which used the extension ".count". For example, the file r2801.count held the events found in run 2801.

[15] The efficiency for detecting electrons in the 2.75° and 5.5° spectrometers was estimated to be $\gtrsim 80\%$.

corrections, different ones were applied at different stages of the analysis process. Here is a list of the corrections made:

electroweak correction	(A_{ew})	target polarization	(P_t)
beam polarization	(P_b)	dilution factor	(f)
nuclear corrections	(C_1, C_2)	rate dependence	(ΔA_{rate})
pion contamination	($A_{\pi^\pm}$)	radiative corrections	(A_{RC}, f_{RC})
positron correction	($A_{e^+}^{meas}$)		

These corrections were needed so that $A_{\|}$ could be determined from the raw asymmetry. The manner in which they were applied is indicated in Equations 3 and 4.

$$A_{\|}^{run}(x,Q^2) = \frac{[A_{raw}(x,Q^2) - \Delta A_{rate}(x) - P_b A_{ew}(x,Q^2)]}{f(x) P_t P_b C_1} + C_2 A_{\|}^{nuc}(x) \tag{3}$$

$$\begin{aligned} A_{\|}(x,Q^2) = & \frac{1}{f_{RC}(x,Q^2)} \left\{ \frac{1}{\alpha_{e^-}(x)} \left[A_{\|}^{run}(x,Q^2) \right.\right. \\ & \left.\left. - \frac{\alpha_{e^+}(x)}{1-\alpha_{\pi^+}(x)} \left[A_{e^+}^{meas}(x) - \alpha_{\pi^+}(x) A_{\pi^+}(x) \right] - \alpha_{\pi^-}(x) A_{\pi^-}(x) \right] \right\} \\ & + A_{RC}(x,Q^2) \end{aligned} \tag{4}$$

Equation 3 contains the corrections that were applied on a run by run basis, *i.e.*, as the data from the individual runs were added together. After the combining of run data, a second level of corrections were made. The ones applied at this point are collected together in Equation 4.

Two of the quantities in Equation 3, P_t and P_b, were discussed in earlier sections and will only be briefly mentioned here. The remaining corrections from both

equations are described on the following pages. The beam and target polarizations adjusted the asymmetry to account for the beam and target being less than completely polarized. Since the polarization values were between 0 and 1, their effect was to increase the absolute value of the raw asymmetry.

4.8.1 Electroweak Correction

One of the first corrections to the raw asymmetry was to remove a small but noticeable contribution due to the interference term from γ and Z° exchange in electron-nucleon scattering. Known as the electroweak asymmetry, the quantity is defined as [126]

$$A_{ew} = \frac{\sigma_R - \sigma_L}{\sigma_R + \sigma_L}, \tag{5}$$

where $\sigma_{R(L)}$ is the cross section for right (left) handed electrons. The asymmetries measured in E155 are not concerned with only the beam helicity but rather a combination of the beam and target helicities. Note that the numerator in Equation 2 is antiparallel minus parallel. Whether left or right handed electrons were used in the antiparallel term depended on the direction of the target polarization. If equal amounts of data were collected with the target polarized $\Uparrow$ and $\Downarrow$ (parallel and antiparallel) to the incident electrons' motion, the A_{ew} contribution would cancel out.

For the E155 analysis, the electroweak asymmetry was accounted for per run. The form of the correction was [127, 128]

$$A_{ew}(x) = -10^{-4} Q^2(x) \left(0.77 \left[1 + 0.44 R_s(x)\right] + 0.11 Y\right), \tag{6}$$

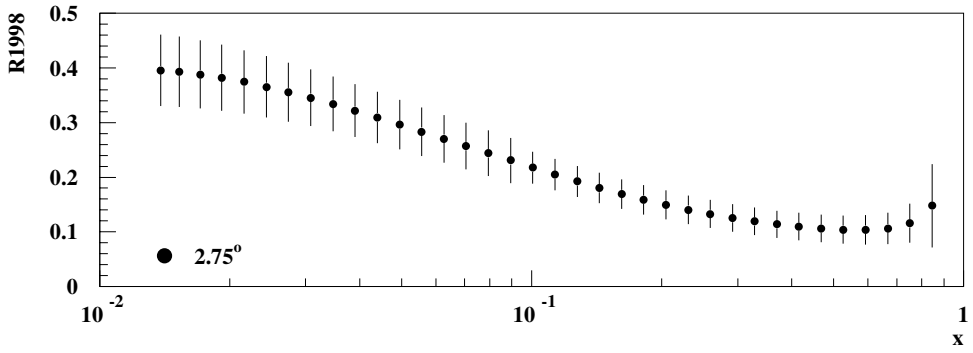

Figure 44: $R(x, Q^2)$ as a function of x at the 2.75° spectrometer's kinematics. The fit R1998 [11] was used for R.

where the measured average Q^2 at each x bin was used and

$$Y = \frac{1-(1-y)^2}{1-(1-y)^2-\frac{y^2 R}{1+R}}. \tag{7}$$

As in Section 2.1, y was the fraction of energy lost by the electron and $R = \sigma_L/\sigma_T$, the ratio of longitudinal to transverse cross sections for virtual photon absorption, was taken from the R1998 fit [11]. To give a feel for this parameter, fit results using R1998 at the 2.75° spectrometer's kinematics are presented in Figure 44. The uncertainties from the fit were used in calculating the systematic error of g_1. Lastly, an approximation was used for $R_s(x)$, which was a ratio of light quark distributions [127]

$$R_s(x) = \frac{2s(x)}{u(x)+d(x)} \approx \begin{cases} 0.5 & \text{for } x < 0.2 \\ 0.0 & \text{for } x > 0.2. \end{cases} \tag{8}$$

The dependence of the electroweak asymmetry on the beam polarization was taken into account when the correction was made. This is seen in the A_{ew} term within the brackets in Equation 3.

4.8.2 Rate Dependence

All of the E155 detector packages had an inherent dead time. This corresponded to some finite amount of time between input signals needed to distinguish between one hit and the next. If the total rates (*i.e.*, electrons plus background particles) in the spectrometers are too high, this will begin to impact the efficiencies of the detectors. Since the E155 measurements primarily are concerned with asymmetries, an issue of greater importance is whether or not these efficiencies have any dependence on the beam and target polarizations.

To determine and correct for rate dependent effects, a method was used which was developed by P. Zyla for the E154 analysis [96]. Each detector package was assumed to have a rate dependent contribution to the measured asymmetry. This was modeled as

$$\Delta A_{rate}(x) = \alpha_{hodo}(x)A^{hodo} + \alpha_{cher}(x)A^{cher} + \alpha_{shw}(x)A^{shw}, \tag{9}$$

where $\Delta A_{rate}(x)$ was the total correction which was included in Equation 3 and A_i was the asymmetry of normalized rates in the i^{th} detector system. These were calculated on a run by run basis. Average values for the asymmetries over all "good" runs are presented in Table 13. The α_i's were the relative change in the efficiency for the i^{th} system and were defined as

$$\alpha_i \equiv \frac{N^e(N) - N^e(2N)}{N^e(N)} \tag{10}$$

where $N^e(N)$ was the reconstruction efficiency for electrons in that system and $N^e(2N)$ was the reconstruction efficiency when the data rate was doubled. To

Table 13: Average values for the asymmetries of the rates during E155.

	$^{15}NH_3$		^6LiD	
	2.75°	5.5°	2.75°	5.5°
	$(\times 10^{-4})$	$(\times 10^{-4})$	$(\times 10^{-4})$	$(\times 10^{-4})$
$\langle A^{hodo} \rangle$	4.17 ± 0.04	7.27 ± 0.08	0.28 ± 0.05	0.88 ± 0.10
$\langle A^{cher} \rangle$	19.11 ± 0.34	44.33 ± 0.69	3.28 ± 0.41	9.39 ± 0.83
$\langle A^{shw} \rangle$	12.67 ± 0.35	40.01 ± 0.10	0.57 ± 0.43	11.98 ± 0.13

Notes:

Uncertainties given are the standard deviations from the approximately 500 runs averaged together for each target.

simulate a doubled data rate, a program called "pulse fiction" was used. This program merged together the data from two consecutive spills for the FADC's, TDC's, and ADC's. Adjustments were made for the TDC dead time and leading-trailing edge behaviors. To give a feel for the size and shape of the coefficients, example α_i's from run 2795 are plotted in Figure 45. The values are on the order of a few percent and are relatively flat in the mid to high x region.

The net effect of the rate dependence correction was about 1% for the 2.75° and 5.5° spectrometers [71]. This analysis was not performed on the 10.5° spectrometer. However, the overall rates were much lower in that spectrometer.

An interesting result from this procedure is shown in Figure 46 [129]. Plotted as a function of x is the effect that doubling the rate would have had on the reconstructed momentum and energy. Here $\Delta E = \frac{E(N)-E(2N)}{E(N)}$ and a similar expression was used for Δp. The change in energy was due to the simulated pile up in the shower counter. The momentum is rather insensitive to an increase in rates. This is good because the track momentum is the quantity used for E' in the calculation

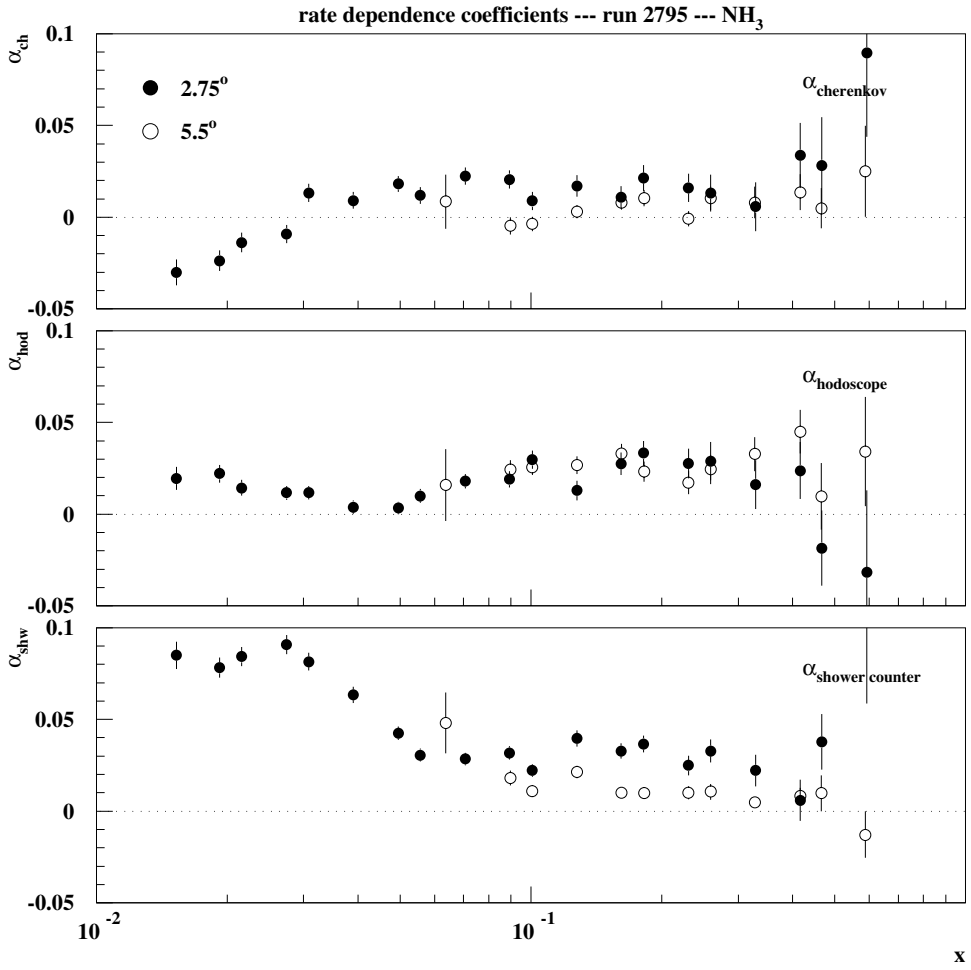

Figure 45: Coefficients for the rate dependent corrections are plotted as a function of x.

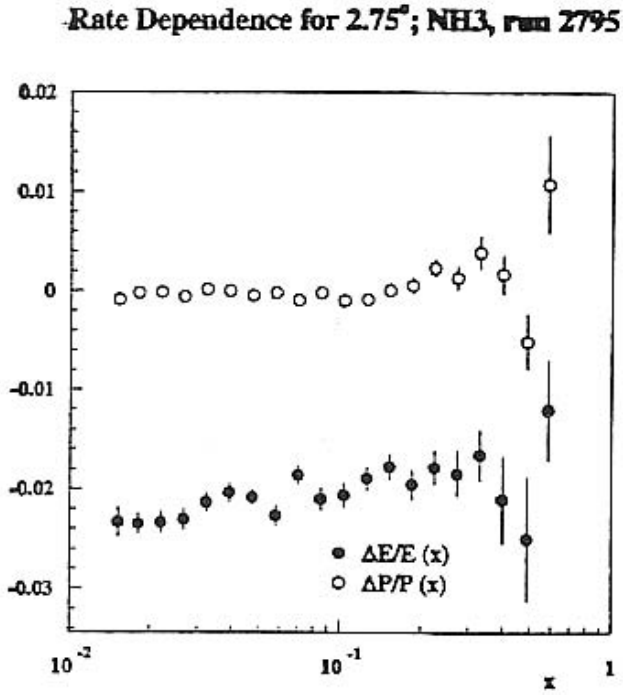

Figure 46: Rate dependence of the reconstructed energy and track momentum. Plot is from Reference [129].

of the kinematic variables.

4.8.3 Dilution Factor

Ideally, one would like all of the electrons used in making the raw asymmetries (Equation 2) to have scattered from polarized protons or deuterons. However many of the events scattered from the nuclei of materials which were part of the overall target setup. Even though efforts were made to limit the amount of additional material, the quantity in the spectrometers' acceptance was not negligible. A breakdown of the amount seen by electrons before entering the 2.75° spectrometer during parallel running is shown in Table 14. These nuclei were unpolarized and the number of events were equal in the $N^{\downarrow\Uparrow}$ and $N^{\uparrow\Uparrow}$ terms. This led to a cancellation

Table 14: Additional material (in g/cm^2) seen by electrons before entering the 2.75° spectrometer [118].

Item	Material	Length (in g/cm^2)
beam window	aluminum	0.019
air	air	0.012
outer vacuum can window	aluminum	0.020
liquid N_2 shield	aluminum	0.010
4K shield	aluminum	0.007
tailpiece	aluminum	0.034
target endcap	aluminum	0.007
NMR coil (for ^{6}LiD)	aluminum	0.014
liquid helium in tgt cup	helium (liq)	0.206
target endcap	aluminum	0.007
tailpiece	aluminum	0.034
4K shield	aluminum	0.007
liquid N_2 shield	aluminum	0.010
outer vacuum can window	aluminum	0.024
air	air	0.006
helium bag window	aluminum	0.006
helium	helium (gas)	0.005

Notes:

The order, from top to bottom, is that encountered by an incident electron. For illustrative purposes, the deuteron sample's aluminum NMR coil has been assumed. (Other NMR coil configurations were also used during the experiment.) The amount of liquid helium in the target cup depends on the packing fraction. For this example, $p_f = 0.526$). Values are the same or smaller for the 5.5° and 10.5° spectrometers.

of these events in the numerator of Equation 2 but not in the denominator.

To adjust for these additional counts in the denominator, the asymmetries were divided by f, the dilution factor, which was defined for the proton target by

$$f = \frac{\text{number of events scattered off } p \text{ (in } H_3 \text{ of } {}^{15}\text{NH}_3\text{)}}{\text{total number of events detected}}. \tag{11}$$

An analogous expression was used for the deuteron target's dilution factor. One can see from Equation 11 that in an ideal situation, there would be only polarized protons and no additional material present so that $f = 1$.

The dilution factors were calculated as a function of x and applied on a run to run basis. Average values for both targets and for each spectrometer are shown in Figure 47.

For ${}^{15}\text{NH}_3$, the dilution factor was calculated by [130]

$$f = \frac{N_p\sigma_p}{N_p\sigma_p + (1-\eta_N)N_N\sigma_{15} + \eta_N N_N\sigma_{14} + \Sigma_i w_i N_i \sigma_i}, \tag{12}$$

where N_N and N_p are the number densities of nitrogen and protons, σ are cross sections and the subscripts 14 and 15 are used to distinguish ${}^{14}\text{N}$ and ${}^{15}\text{N}$. The sum over $w_i N_i \sigma_i$ takes into account unpolarizable materials (*i.e.* the items in Table 14) weighted by the acceptance. The factor $\eta_N = \frac{{}^{14}\text{N}}{{}^{14}\text{N}+{}^{15}\text{N}}$ is the fraction of nitrogen that was ${}^{14}\text{N}$. For the material used in E155, $\eta_N = 2\%$ [71].

Likewise, the dilution factor for ${}^{6}\text{LiD}$ was calculated as

$$f = \frac{N_D\sigma_D}{(1-\eta_p)N_D\sigma_D + \eta_p N_D\sigma_p + (1-\eta_L)N_L\sigma_6 + \eta_L N_L\sigma_7 + \Sigma_i w_i N_i \sigma_i}, \tag{13}$$

with D and L subscripts for deuteron and lithium. The subscripts 6 and 7 are for ${}^{6}\text{Li}$

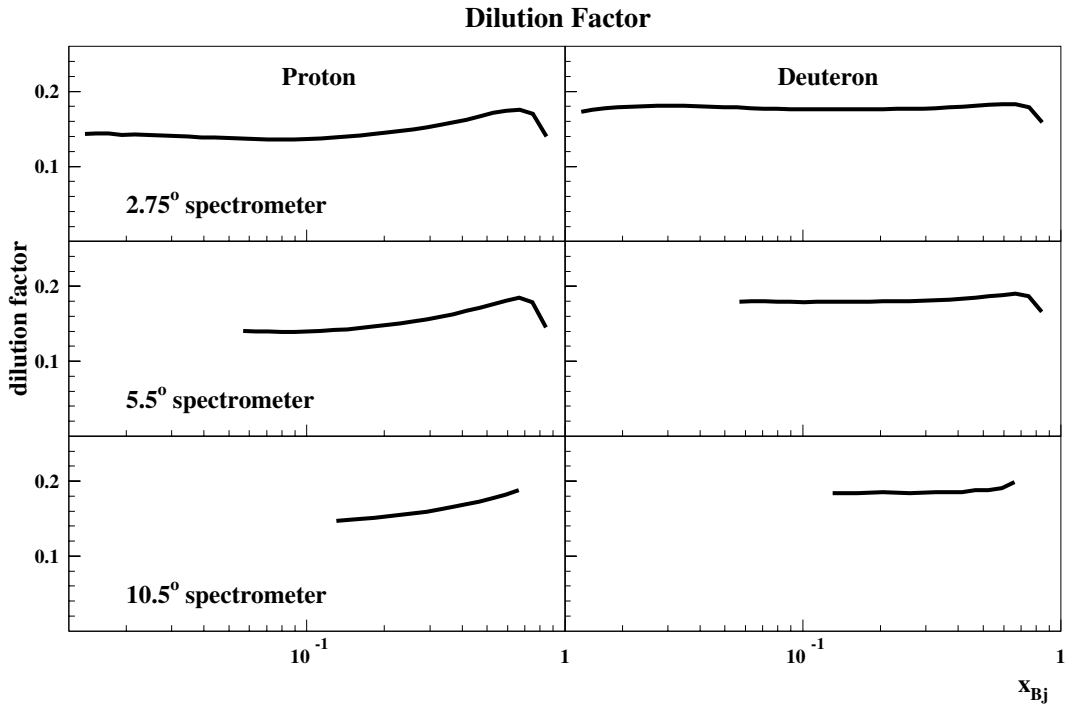

Figure 47: Dilution factors for the proton and deuteron targets for all three spectrometers. The values shown are averages over parallel running data.

and ^{7}Li. Similar to above, the η factors indicate the percentage of contamination for ^{7}Li in lithium ($\eta_L = \frac{^7\mathrm{Li}}{^7\mathrm{Li} + ^6\mathrm{Li}}$) and the amount of hydrogen that replaced deuterium ($\eta_p = \frac{\mathrm{H}}{\mathrm{H+D}}$). For E155, $\eta_L = 4.4\%$ and $\eta_p = 2.4\%$ [131]. The number densities (N) were calculated using

$$N = \frac{n\rho z}{M}, \tag{14}$$

with Avagadro's number n, the density ρ, the material thickness z, and the atomic mass M. In order to determine N for the target material, the amount of material within the target cup needed to be measured. Since the form of the target material was granular, the volume of the target cup was not completely filled with $^{15}NH_3$ or ^{6}LiD . There were gaps between the pieces which allowed the liquid helium to flow

and evenly cool the target. The fraction of the cup filled with material was called the packing fraction (p_f), so that the effective material thickness from Equation 14 could be expressed as $z_{tgt} = p_f \times z_{cup}$. Conversely, the thickness of liquid helium in the target cell was $z_{LHe} = (1 - p_f) \times z_{cup}$.

The packing fraction was measured for each cup in each target insert. This was done by comparing the measured rates for a polarized target to those for a solid target. As mentioned earlier, Be and pyrolitic graphite (^{12}C) were used as solid targets to compare with ^{6}LiD and $^{15}NH_3$ respectively. Each material was chosen to match roughly the atomic number of its corresponding target material. The thickness of the solid target was cut to match the number of grams of the target material. Hence the number of radiation lengths for the solid and actual target were approximately the same. Using solid targets instead of an empty cup minimized the differences in radiative corrections and rate dependent effects [132]. The ratio of rates for $^{15}NH_3$ and pyrolitic graphite are expressed in Equation 15 [130], which can then be solved for p_F. The same convention as above is used here and $\kappa = n\rho/M$ from Equation 14.

$$\frac{Rate_{NH_3}}{Rate_C} = \tag{15}$$

$$\frac{\kappa_p z_{cup}\sigma_p + (1-\eta_N)\kappa_N p_f z_{cup}\sigma_{15} + \eta_N \kappa_N p_f z_{cup}\sigma_{14} + \kappa_{LHe}(1-p_f)z_{cup}\sigma_{LHe} + \Sigma_i N_i \sigma_i}{\kappa_C z_C \sigma_C + \kappa_{LHe}(z_{cup} - z_C)\sigma_{LHe} + \Sigma_i N_i \sigma_i}$$

The packing fraction was calculated for each target cup in each insert. Values used in E155 are given in Table 15.

Table 15: Packing fractions used by the student analysis.

insert	cell	target material	packing fraction	weight target mat'l (gm/cm^2)	weight liquid He (gm/cm^2)
1	upper	^6LiD	0.526 ± 0.013	1.310 ± 0.071	0.206 ± 0.007
	lower	^6LiD	0.575 ± 0.013	1.432 ± 0.076	0.185 ± 0.006
2	upper	$^{15}NH_3$	not used	not used	not used
	lower	$^{15}NH_3$	0.584 ± 0.031	1.607 ± 0.087	0.181 ± 0.010
3	upper	$^{15}NH_3$	0.570 ± 0.019	1.568 ± 0.054	0.187 ± 0.007
	lower	$^{15}NH_3$	0.555 ± 0.015	1.527 ± 0.044	0.194 ± 0.007
4	upper	$^{15}NH_3$	0.540 ± 0.033	1.486 ± 0.092	0.200 ± 0.013
	lower	$^{15}NH_3$	0.586 ± 0.021	1.612 ± 0.060	0.180 ± 0.007
5	upper	^6LiD	0.534 ± 0.017	1.330 ± 0.077	0.203 ± 0.008
	lower	^6LiD	0.554 ± 0.014	1.379 ± 0.075	0.194 ± 0.006
6	upper	$^{15}NH_3$	0.594 ± 0.017	1.634 ± 0.049	0.177 ± 0.006
	lower	$^{15}NH_3$	0.610 ± 0.021	1.678 ± 0.060	0.170 ± 0.007
10	upper	^6LiD	0.522 ± 0.026	1.300 ± 0.090	0.208 ± 0.011
	lower	$^{15}NH_3$	0.583 ± 0.040	1.604 ± 0.111	0.181 ± 0.013

Notes:

These packing fractions are consistent with the values calculated by the Bosted analysis [122]. In the left most columns are the amount of target material and liquid helium in each target cup.

Table 16: Densities for target materials and liquid helium at 1 K.

Material	Density ρ (gm/cm^3)
$^{15}NH_3$	0.917 ± 0.009
^{6}LiD	0.83 ± 0.04
LHe	0.145 ± 0.003

Using the packing fraction, one can determine the amount of target material or liquid helium contained within a target cup. These values are included in Table 15. The weight of the each was obtained by multiplying the density of the substance by the expression for the effective material thickness (z_{tgt} or z_{LHe}) given above. The error of the material weight was calculated assuming that the uncertainties of the density and packing fraction are uncorrelated. For the values presented here, the densities[16] used are given in Table 16.

4.8.4 Nuclear Corrections

Some of the detected electrons scattered from material in the target other than the desired target nucleon, *i.e.,* protons in the hydrogen of $^{15}NH_3$ or deuterons in ^{6}Li or D of ^{6}LiD . If these other nuclei were unpolarized, then the extra events diluted the asymmetry. Adjustments for this situation were made with the dilution factor discussed in the previous section. When the nuclei were polarized, the asymmetry was artificially increased or decreased depending upon the polarization direction. How corrections for the polarized case were handled are the subjects of

[16]The densities for $^{15}NH_3$ and liquid helium are from Reference [132]. The uncertainties were given in Reference [133] as 1% and 2% for $^{15}NH_3$ and liquid helium respectively. For ^{6}LiD , both the density and uncertainty were taken from Reference [136].

the next two sections.

Nitrogen Correction

For the ammonia target, these corrections primarily adjusted the measured asymmetry for events that scattered from the unpaired proton in ^{15}N. Due to the negative magnetic moment of ^{15}N, this proton was oppositely polarized to those in hydrogen. The ^{15}N polarization was estimated using the expression [135]

$$P_{15} = 0.136P_p - 0.183P_p^2 + 0.335P_p^3. \tag{16}$$

This fit came from polarization measurements of ^{15}N and residual protons which were taken following the E143 experiment.

The correction took the form

$$C_1 = 1 + C_p \tag{17}$$

where

$$C_p = (1 - \eta_N)\frac{N_N}{N_p}\frac{P_{15}}{P_p}\beta_{15}g_{15}^{EMC}. \tag{18}$$

A brief description and typical values of the different terms are presented in Table 17. More details and a derivation of Equation 17 can be found in References [130] and [134]. The effect of C_1 was small; it adjusted the asymmetry by about 2%. The manner in which C_1 was applied to the measured asymmetry was shown in Equation 3 on page 135. As with the other correction factors in Equation 3, C_1 was applied on a run by run basis. The C_2 correction took into account events

Table 17: Components of the nuclear corrections for the proton target.

parameter	typical value	syst. err. relative (%)	description
η_N	0.02 ± 0.000	0	$\frac{^{14}N}{^{14}N+^{15}N}$, fraction of all nitrogen atoms that were ^{14}N
β_{15}	-0.333 ± 0.023	7	from Clebsch-Gordon coefficients in the nitrogen wave function
N_N/N_p	0.333 ± 0.000	0	ratio of number densities of protons and nitrogen; 1 N atom per 3 protons
P_{15}	0.160 ± 0.008	5	^{15}N polarization
P_p	0.800 ± 0.056	7	corrected proton polarization
g_{15}^{EMC}	1.000 ± 0.015	1.5	^{15}N EMC effect
C_p	0.024 ± 0.005	20	second term in C_1 correction
C_1	1.024 ± 0.005	0.5	C_1 correction

Notes:

For completeness, the value for C_1 is also included. Errors were taken from References [71], [134], and [135].

that scattered from ^{14}N present in the $^{15}NH_3$ sample. This term was assumed to be negligible for E155.

^{6}LiD Corrections

The nuclear corrections for the ^{6}LiD material served two main purposes. Similar to the $^{15}NH_3$ correction, it was used to adjust the asymmetry for events that scattered from additional material in the ^{6}LiD sample. As discussed in Section 4.8.3, this "additional" material was ^{7}Li contamination of ^{6}Li ($\eta_L = 4.4\%$) and ^{1}H contamination of D ($\eta_p = 2.4\%$). The second purpose was to account for the effective deuteron in the ^{6}Li atom [77]. Unpaired nucleons in ^{6}Li were aligned with the nuclear spin 86.6% of the time. This was calculated with 8 models that predicted

the magnetic moment of ^{6}Li to better than 2% [77]. Similar values were obtained with a model independent approach (85%) [77] and by a Green's Function Monte Carlo prediction [138]. Treating ^{6}Li as a polarized deuteron plus an unpolarized α particle increased the available number of polarizable deuterons in ^{6}LiD. This made it a more attractive target material.

The corrections for ^{6}LiD were determined using

$$C_1 = (1 - \eta_p) + (1 - \eta_L)\frac{P_6}{P_d}\beta_6 g_6^{EMC}\frac{1}{\gamma_d} \tag{19}$$

and

$$C_2 = -\frac{1}{C_1}\left[\eta_p \frac{P_p}{P_d} + \eta_L \frac{P_7}{P_d}\beta_7 g_7^{EMC}\right]\frac{\sigma_p}{\sigma_d} \tag{20}$$

where an explanation of the terms along with sample values are presented in Table 18. Again, the manner of application for the two corrections was given in Equation 3 on page 135. The deuteron in ^{6}Li entered through the C_1 term. Values ranged from $1.77 \leq C_1 \leq 1.89$ with an average of 1.86. Combining this with the the average dilution factor of 0.19 gave an effective dilution factor of around 0.35. This can be compared to $f \approx 0.22$ for ND_3, which also was considered as a deuteron target for E155.

The C_2 term adjusted the deuteron asymmetry for events that scattered from residual protons in the target material. In Equation 3, a fit to the world data for $A_\parallel^p$ was used for the $A_\parallel^{nuc}$ factor. Values for C_2 ranged from $-0.030 \leq C_2 \leq -0.023$.

[17] The 12.6% relative uncertainty applied to C_2 comes from Reference [136] where it is presented as the error on the quantity C_7. The coefficient C_7 is defined as $C_7 = -C_1 \times C_2$. This difference is small since δC_2 is a small part of the total systematic error.

Table 18: Components of the nuclear corrections for the deuteron.

parameter	typical value	syst. err. relative (%)	description
η_p	0.025 ± 0.001	5	$\frac{H}{H+D}$, fraction of all H that was ^1H
η_L	0.046 ± 0.002	5	$\frac{^7Li}{^7Li+^6Li}$, fraction of Li that was ^7Li
P_d	0.200 ± 0.008	4	deuteron polarization
P_p	0.040 ± 0.005	13	proton pol. (an estimated limit)
P_6	0.200 ± 0.008	4	^6Li polarization, used EST estimate
P_7	0.667 ± 0.067	10	^7Li polarization, used EST estimate
β_6	0.866 ± 0.012	1.3	model calculation of effective neutron pol. as fraction of ^6Li pol. in $^6Li = \alpha + p + n$
g_6^{EMC}	1.000 ± 0.025	2.5	^6Li EMC effect
β_7	0.667 ± 0.067	≤ 10	Clebsch-Gordon coefficient for extreme shell model; effective pol. of proton in ^7Li as a fraction of the ^6Li pol.
g_7^{EMC}	1.000 ± 0.025	2.5	^7Li EMC effect
$F_2^p/(2F_2^d)$	0.600 ± 0.012	2	used to get $\frac{\sigma_p}{\sigma_d}$; see Figure 48
γ_d	0.925 ± 0.012	1.3	$1 - 1.5\omega_D$ deuteron D-state correction. $\omega_D = 0.05 \pm 0.01$
C_1	1.86 ± 0.05	2.7	nuclear correction on deuteron target
C_2	-0.026 ± 0.003	12.6	nuclear correction on deuteron target[17]

Notes:

For completeness, the nuclear corrections C_1 and C_2 also are included. Errors were taken from References [136] and [137].

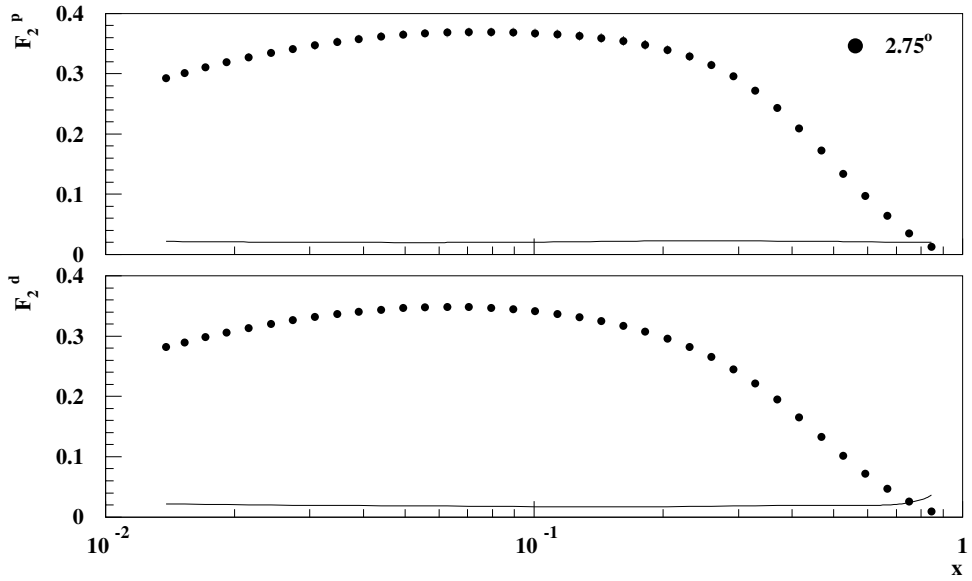

Figure 48: $F_2(x, Q^2)$ is plotted as a function of x at the 2.75° spectrometer's kinematics for the proton and deuteron. The function was obtained from an NMC fit [154]. The relative uncertainty from the fit is shown as a solid line on the bottom of each plot.

4.8.5 Pair Symmetric Background

Not all of the particles used in constructing the raw electron asymmetries were from the DIS process needed to determine g_1. A small portion of the events were either charged hadrons which satisfied the data cuts or electrons created by pair symmetric processes. The latter contribution was also known as the positron correction for reasons which will be explained shortly. Because the hadron part was mostly pions, it was dubbed the pion contamination. It will be discussed in the next section.

Background particles were attributed to pair symmetric processes [139] if the detected electron stemmed from the production of an e^+e^- pair. These mostly came from π^0's, which could decay into background electrons by way of several

Table 19: Branching ratios for π^0 decay [140].

π^0 Decay Modes	Branching Ratio (%)
$\gamma\gamma$	98.978 ± 0.032
$e^+e^-\gamma$	1.198 ± 0.032
remaining modes	$\ll 0.1$

mechanisms. A typical series of decays might be

$$\gamma p \rightarrow \pi^0 X \hookrightarrow \gamma\ e^+\ e^- \qquad \text{or} \qquad e^- N \rightarrow \pi^0 X \hookrightarrow \gamma\ \gamma \hookrightarrow e^+\ e^-.$$

In the first instance a real or low Q^2 photon was created by an incident electron (see Section 2.5.2 for more details). The photon interacts with the target creating a π^0. For this example the π^0 undergoes a Dalitz decay ($\pi^0 \rightarrow \gamma\ e^+\ e^-$). In the second example given above, the π^0 decays into two photons. As shown in Table 19, this is more likely to happen than a Dalitz decay. One of the photons then produces an electron-positron pair. Because the $\gamma \rightarrow e^+\ e^-$ process needs to take place in the field of a nucleus, any material between the target and the detectors would tend to enhance this component of the pair symmetric background. This dependence was used in studying the effect that a thicker section of the target support structure, which overlapped with part of the 10.5° spectrometer's acceptance, had on the rates of that spectrometer [116].

To correct for this background, both the size and helicity dependence of the positron correction needed to be determined. The first step in accomplishing this was to collect positron data. Periodically the polarity of the spectrometer magnets

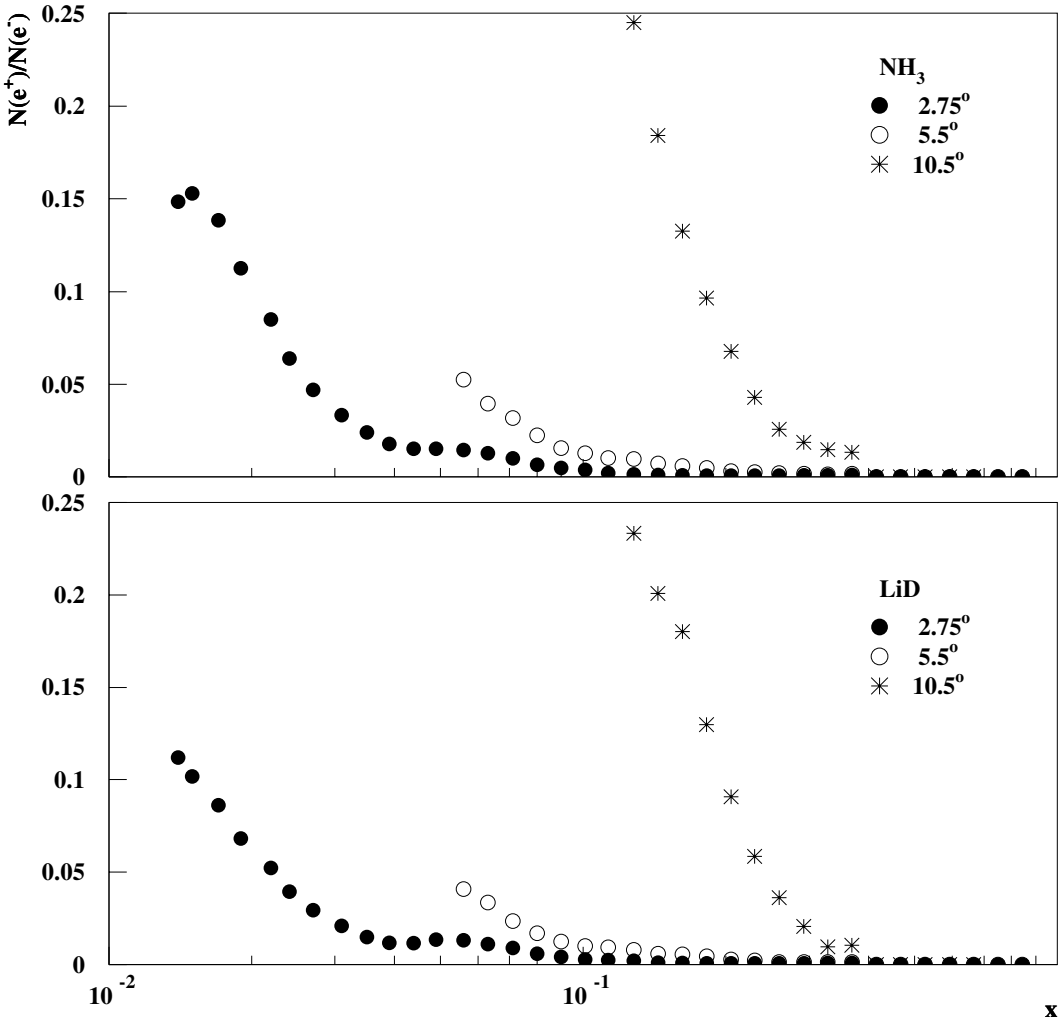

Figure 49: Electron-positron ratios for the $^{15}NH_3$ target (top) and ^{6}LiD target (bottom).

were reversed for a series of runs. In this configuration the DIS electrons would not reach the detectors but the positrons from the processes described above would, thus enabling a measurement of the pair symmetric background. The standard "good" electron definition was applied to these data. The relative magnitude of the background was studied by examining e^+/e^- ratios, which are shown in Figure 49. Contamination was maximum in the lower x bins accessible to a particular

spectrometer, but quickly dropped with increasing x. As seen in Figure 49, typical maximum values were in the range of 5% to 20%.

Positron asymmetries were constructed using Equation 2. Adjustments were made for beam polarization, target polarization, dilution factor, $C1$ and $C2$ nuclear corrections, and the electroweak correction. This was done in the same manner as they were applied in Equation 3.

The measured $A_{\|}$ for positrons[18], which will be referred to as A_{e^+}, are shown in Figures 50 and 51. Because of the large uncertainties, an average asymmetry was determined for each spectrometer and target type. In applying the correction, A_{e^+} was assumed to be equal to the average over all x. The average values are presented in Table 20. To calculate the average, no points were used which had a statistical error greater than 1.0. Almost all are consistent with zero within one standard deviation. The manner in which the positron correction was applied will be deferred until after the pion background is discussed.

4.8.6 Pion Background

The E155 hadron background was predominantly made up of pions but also contained a non-negligible number of kaons and a smaller number of protons and anti-protons. The main processes responsible for creating the hadron background were described in Section 2.5.3.

[18] The asymmetries are plotted as a function of x because the correction gets applied per x-bin. However, since properties of the positrons were used to compute x, the physical meaning of the variable is not the same as that used for DIS electrons. If one were interested in positron asymmetries for their own sake, then perhaps a better variable would be the particle momentum.

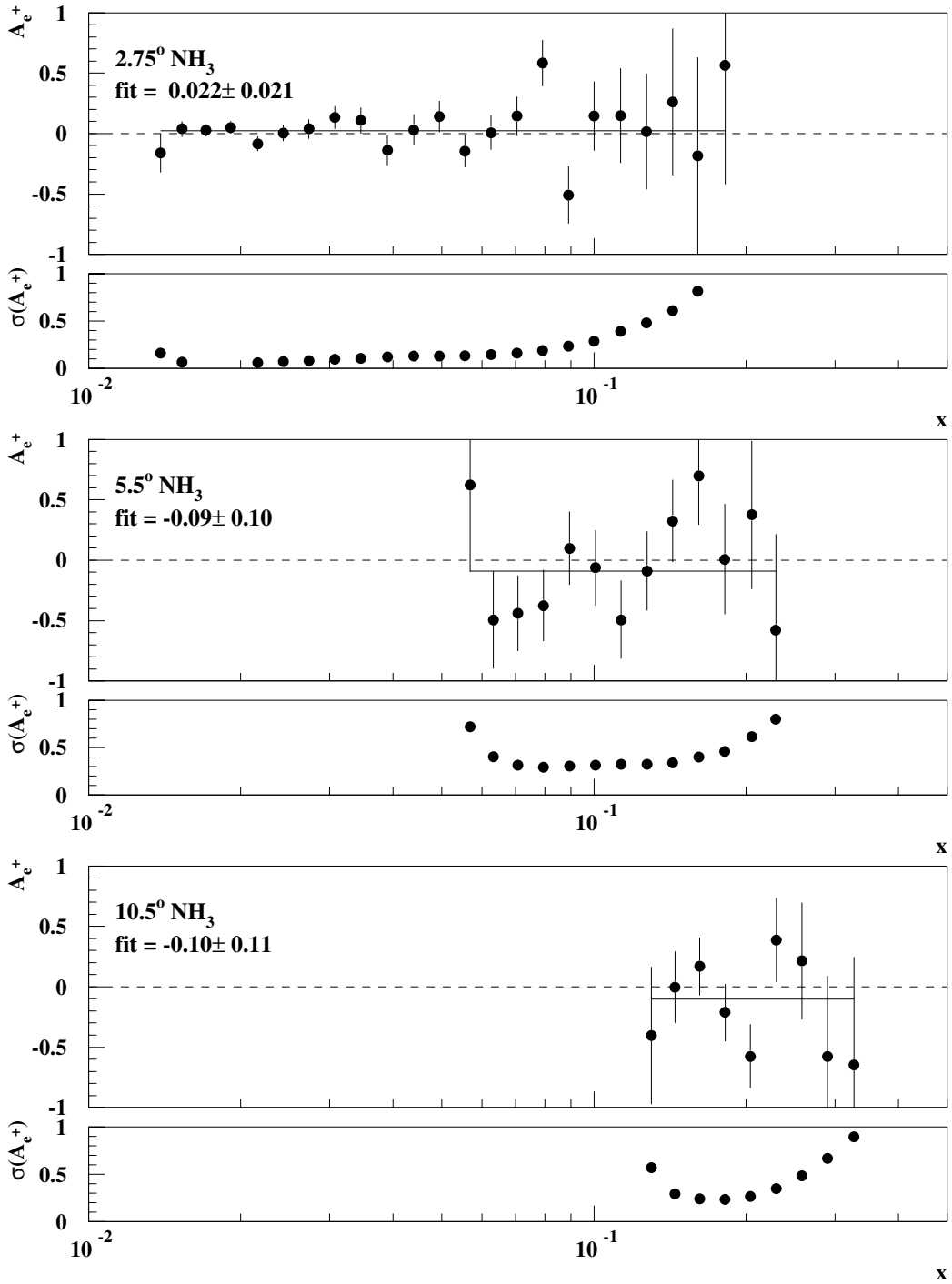

Figure 50: Positron asymmetries by spectrometer for the $^{15}NH_3$ target with statistical errors only. The statistical errors also have been plotted beneath each asymmetry, showing how the rates decrease at the high and low x values of a given spectrometer.

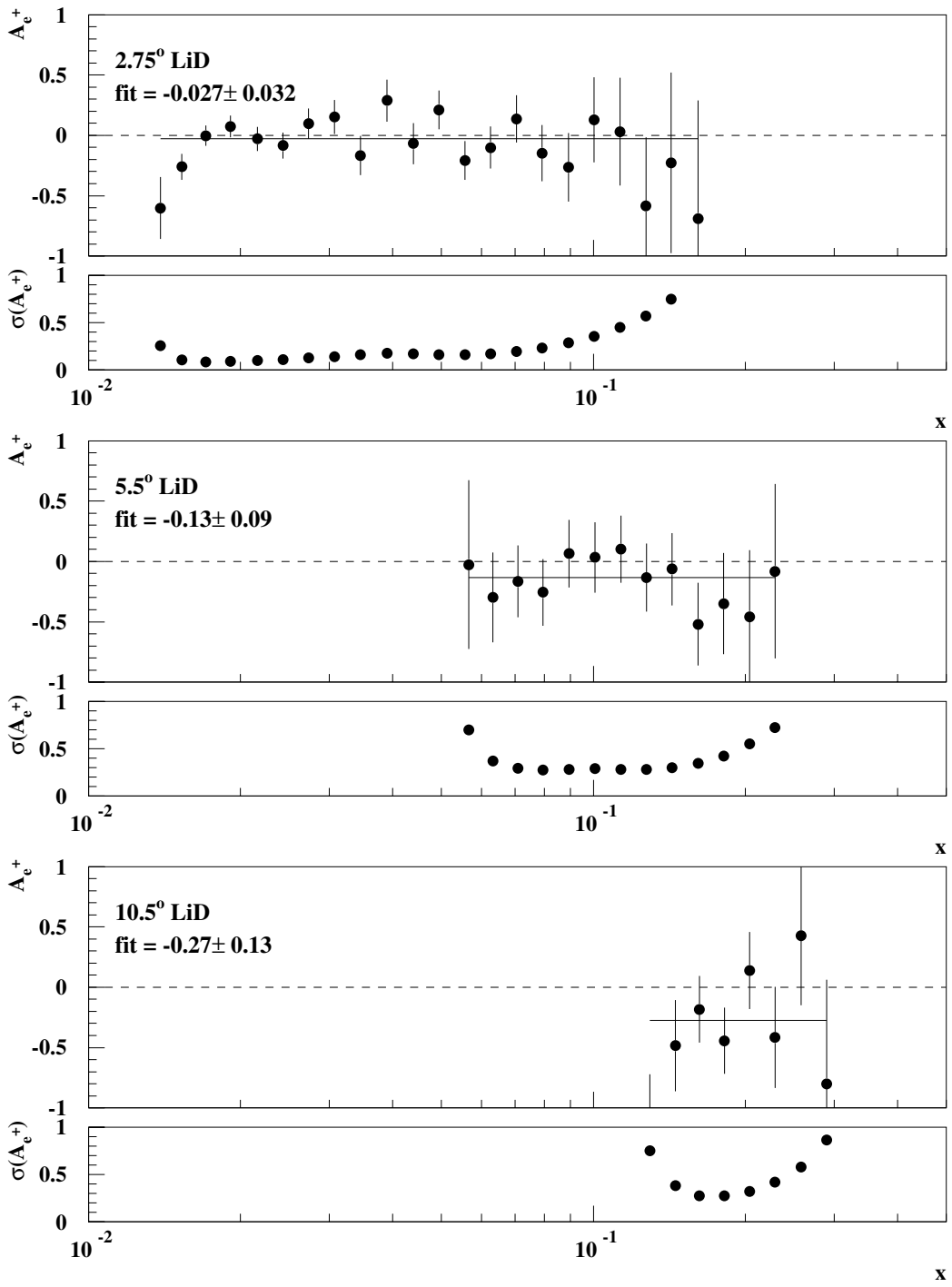

Figure 51: Same as Figure 50, but for data collected on a ^{6}LiD target.

Table 20: Average asymmetries for negative hadrons (A_{π^-}), positive hadrons (A_{π^+}), and positrons (A_{e^+}).

		$^{15}NH_3$	^6LiD
A_{π^-}	2.75°	0.0068 ± 0.0008	-0.0012 ± 0.0013
	5.5°	0.0082 ± 0.0025	0.0080 ± 0.0042
	10.5°	—	—
A_{π^+}	2.75°	0.0135 ± 0.0020	0.0021 ± 0.0023
	5.5°	0.0297 ± 0.0086	0.0087 ± 0.0065
	10.5°	—	—
A_{e^+}	2.75°	0.022 ± 0.021	-0.027 ± 0.032
	5.5°	-0.09 ± 0.10	-0.13 ± 0.09
	10.5°	-0.10 ± 0.11	-0.27 ± 0.13

Notes:

Only statistical errors are presented.

A correction was needed to adjust the data for hadrons that were misidentified as electrons. In order for a particle to be misidentified, two main criteria had to be satisfied which distinguished electron and hadron events in the data. First, the particle must have created a sizable signal in the spectrometer's Cherenkov tanks. This condition was met for pions with momenta greater than the Cherenkov detector's pion threshold. However, by design the number of pions above threshold are a small fraction of the total number of pions detected in a given spectrometer. The second requirement was that the particle needed to deposit most of its energy in the shower counter. Although this does not happen often, large hadron showers did occur or they could be mimicked by overlapping hits or random coincidences. As will be shown below, the frequency for satisfying both criteria was quite low. The hadron contamination was typically a few percent or less.

Similar to the case for positrons, to correct for pions one must know the helicity dependence and the extent of the contamination. For the 2.75° and 5.5° spectrometers, the magnitude of the contamination was determined for each x bin by examining E'/p spectra. This method was employed in E154 [71, 141]. A subset of runs were used for this technique. For each x bin, two E'/p spectra were constructed, one using the good electron definition (minus the E'/p cut) and the other using a pion definition (also without the E'/p cut). Both distributions were fit in the region $0.2 \leq E'/p \leq 1.8$, and the magnitude of the fitted curves were scaled to match in the range $0.2 \leq E'/p \leq 0.4$. The area beneath each curve was calculated in the "good electron" region of $0.8 \leq E'/p \leq 1.2$. The ratio of these areas gave the hadron contamination for that x bin. To give a feel for the method and the level of the contamination, E'/p spectra for electrons and pions are presented in Figure 52 where the pion distribution (hatched) has been normalized to that of the electron for $0.2 \leq E'/p \leq 0.4$. One can see that in the region $0.8 \leq E'/p \leq 1.2$, the pion distribution is small in comparison to the electron's.

In Figure 53, the hadron contaminations as a function of x are shown for the 2.75° and 5.5° spectrometers for data collected during electron (top two plots) and positron (bottom two plots) modes of running. The plotted quantity is called α_i and is the relative rate of the i^{th} component of the background. These α_i's are used in the correction for hadron contaminations and will be discussed in more detail in the next section. As was shown in Figure 41, the pion rates quickly decrease with increasing momentum, which means that they will decrease with increasing x.

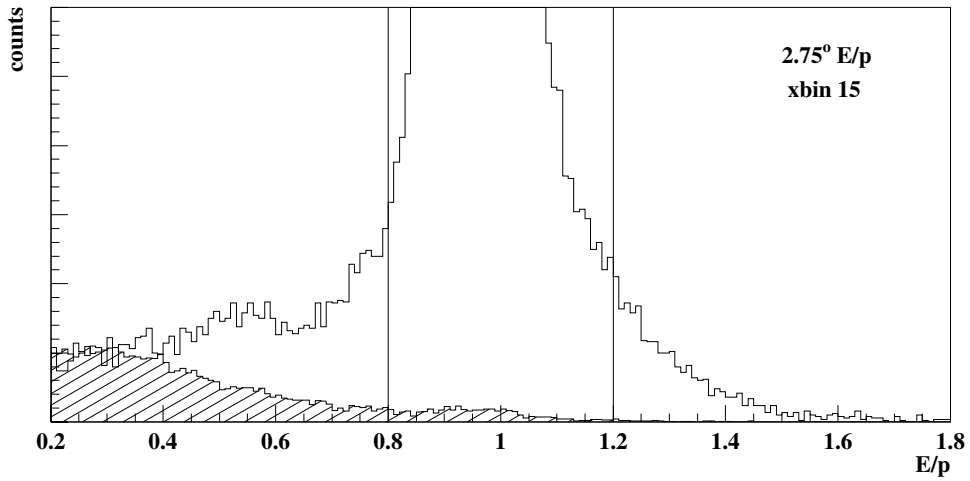

Figure 52: E'/p spectra for pions (hatched) and electrons (clear) in x bin 15 ($x = 0.056$) of the 2.75° spectrometer. The pion spectrum was normalized to that of the electron in the region [0.2,0.4]. Note that in the region used to define a good electron, [0.8,1.2], the magnitude of the pion distribution is much less than the electron's.

Because of the greater number of pions available at low x one may expect a larger contamination in that region, which is indeed the case. For positron running the pion contamination increases with x in the low to mid x range. This may be due to the small positron rates (see Figure 49) and the comparatively larger availability of π^+'s.

For the helicity dependence of the contamination, average asymmetries were calculated using measured $A_{LL}(p)$ from the inclusive hadron data set (see Section 4.11 for details). In applying the correction, averages were then assumed to hold over the range of measured x values. The values obtained for 2.75° and 5.5° positive and negative hadrons are given in Table 20. No 10.5° values are presented. The limited number of detectors in the 10.5° spectrometer, while adequate for hadron rejection, were not sufficient to extract a hadron sample from that spectrometer's

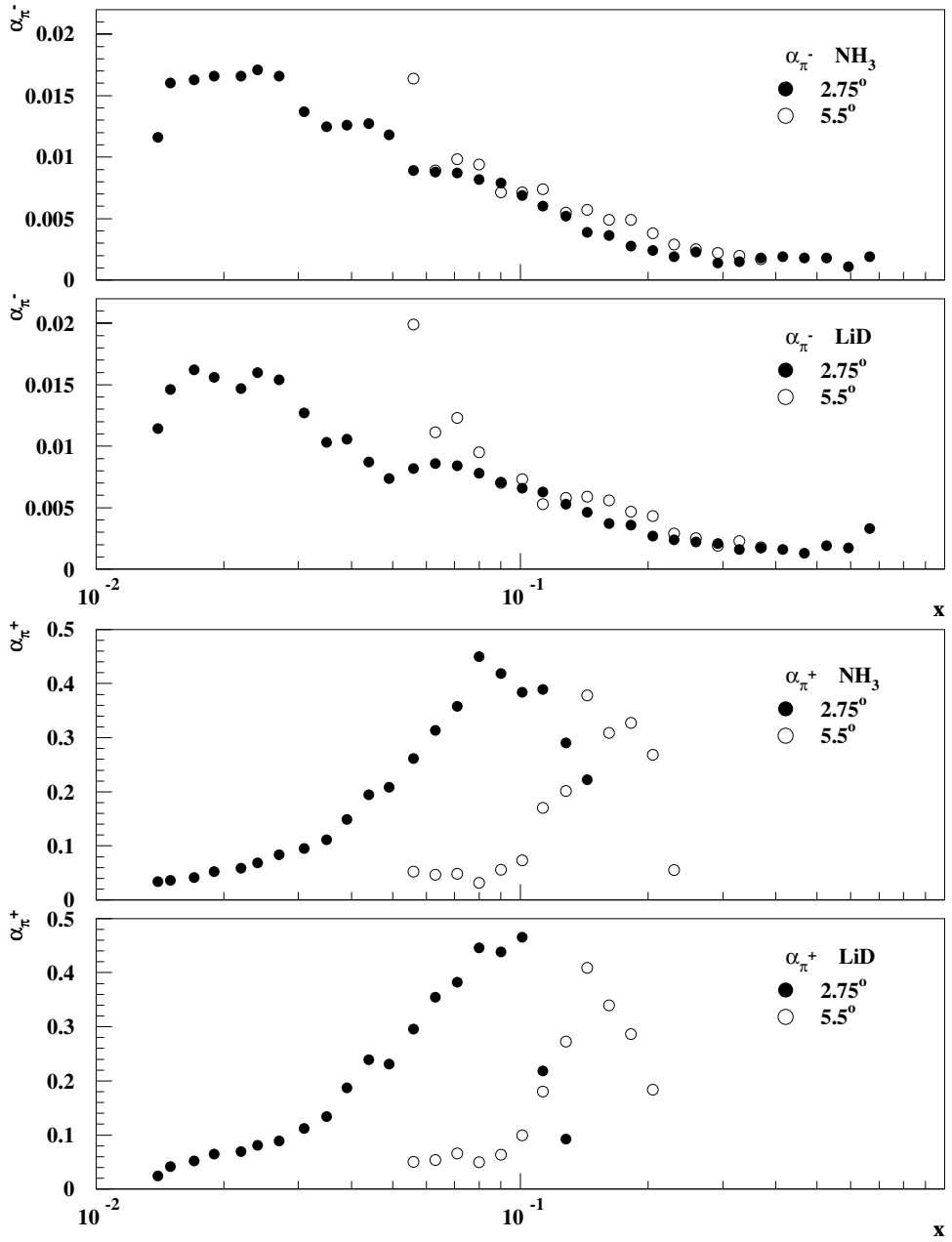

Figure 53: Hadron contamination as a function of x for data collected when the spectrometers were set for negative particles (top two plots) and positive particles (lower two plots). At higher x, the α_{π^+} were set to zero because the data rate was too low.

data.

4.8.7 Pion and Positron Corrections

Adjustments to the measured asymmetry to account for pair symmetric backgrounds and pions were applied at the same point in the analysis. The method used was based on the E154 procedure described in [142]. For both the electron and positron runs, the measured asymmetries were expressed as the sum of their various parts. In the case of electron mode running this gave

$$A_{e^-}^{meas}(x) = \alpha_{e^-}(x)A_{e^-}(x) + \alpha_{e_\gamma^-}(x)A_{e_\gamma^-}(x) + \alpha_{\pi^-}(x)A_{\pi^-}(x), \tag{21}$$

where $A_{e^-}(x)$ is the desired asymmetry from DIS electrons, and the subscripts e_γ^- and π^- indicate contributions to the measured asymmetry from pair symmetric processes and negative hadrons respectively. Here the quantity $A_{e^-}^{meas}$ is the same as $A_{\|}^{run}$ in Equation 3. Values used in the analysis were assumed to be constant in x and are presented in Table 20.

As mentioned earlier, the α_i coefficients are weighting factors which indicate the fraction of all events that were due to the i^{th} contribution. These coefficients were defined as

$$\alpha_i(x) = \frac{N_i(x)}{N_{e^-}(x) + N_{e_\gamma^-}(x) + N_{\pi^-}(x)}, \tag{22}$$

where N is the number of events normalized to the incident beam charge. With this definition, one gets $\alpha_{e^-}(x) + \alpha_{e_\gamma^-}(x) + \alpha_{\pi^-}(x) = 1$. When practical, the coefficients were extracted from the data. The ratio e^+/e^- (which is also $\alpha_{e_\gamma^-}/\alpha_{e^-}$) is plotted

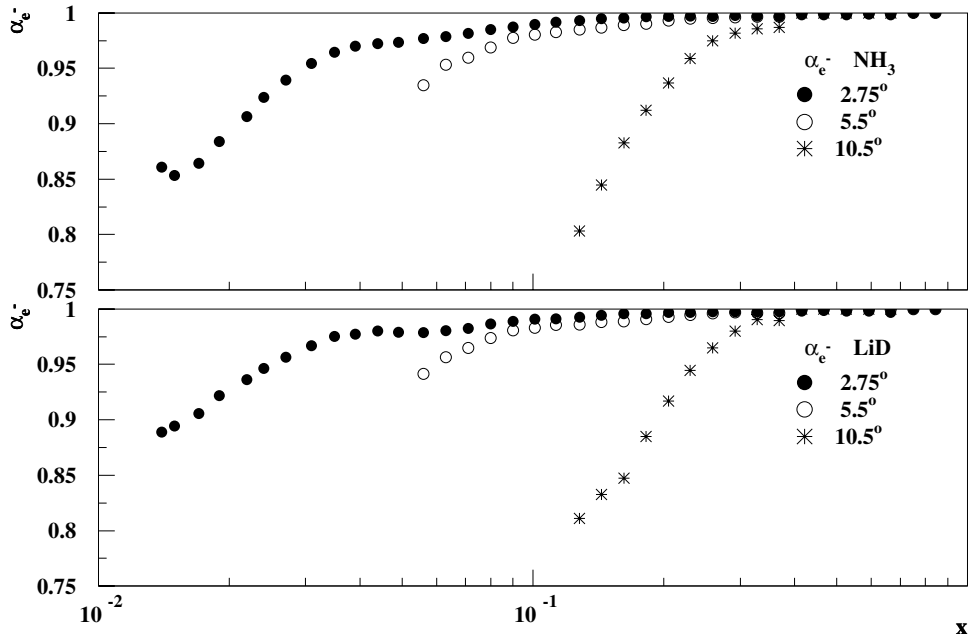

Figure 54: The fraction of events in the measured asymmetry which were attributed to DIS electrons.

in Figure 49. Since α_{e^-} is often close to 1, which means the number of events in the measured asymmetry were predominantly from DIS electrons (see Figure 54), the e^+/e^- ratio closely follows the quantity $\alpha_{e^-_\gamma}(x)$.

The pair symmetric term in Equation 21 was determined by examining positron data. This was discussed in Sections 4.8.5. Analogous to Equation 21, a decomposition of the measured positron asymmetry gives

$$A^{meas}_{e^+}(x) = \alpha_{e^+}(x)A_{e^+}(x) + \alpha_{\pi^+}(x)A_{\pi^+}(x), \tag{23}$$

where the subscripts follow the same convention as before. For the E155 analysis, $\alpha_{e^+}(x) = 1 - \alpha_{\pi^+}(x)$ and $A_{e^+}(x) = A_{e^-_\gamma}(x)$. The latter equality connects Equations 21 and 23 which leads to a background subtracted DIS electron asymmetry

$$A_{e^-}(x) = \tag{24}$$

$$\frac{1}{\alpha_{e^-}}\left[A_{e^-}^{meas}(x) - \frac{\alpha_{e^-_\gamma}(x)}{1-\alpha_{\pi^+}(x)}\left[A_{e^+}^{meas}(x) - \alpha_{\pi^+}(x)A_{\pi^+}(x)\right] - \alpha_{\pi^-}(x)A_{\pi^-}(x)\right].$$

This expression can be found embedded in Equation 4.

4.8.8 Radiative Corrections

The focus of E155 was to measure the spin dependence of electron-nucleon scattering via the one virtual photon exchange[19]. Ideally, one would like to restrict what happens in the End Station to this single process, known as the Born process. Realistically a collection of higher order processes also could have occurred and in fact did affect the measurement. Often these processes manifested themselves as energy losses to the electron and caused either an overestimation of incident electron's energy (E) or an underestimation of the energy of the scattered electron (E'). As a result, the x value determined for such an event was lower than it should have been. This leads to some of the events being shifted into lower x-bins and skewing the shape of the measured asymmetry. Such effects on the data were accounted for with radiative corrections.

Typically these corrections are separated into two groups, internal and external. Internal corrections deal with processes that occur within the field of the scattering nucleus. These included vertex corrections at the electron vertex and vacuum polarization as well as contributions from elastic or inelastic tails due to internal bremsstrahlung either prior to or following the scattering. The most significant contributions to the internal corrections came from the elastic tails [143].

[19] See Figure 1 on page 3 and the accompanying discussion.

With the ^{6}LiD target there also were contributions from quasi-elastic tails when the electron scattered off a single nucleon inside the deuteron. Internal corrections were made up to $\mathcal{O}(\alpha^3)$.

The internal corrections were applied to the measured asymmetries through the expression

$$A_{int} = \frac{\sigma^p_{int}}{\sigma^u_{int}} = \frac{\sigma^p_{Born}(1+\delta_{\rm V}) + \sigma^p_{el} + \sigma^p_{inel}}{\sigma^u_{Born}(1+\delta_{\rm V}) + \sigma^u_{el} + \sigma^u_{inel}} \tag{25}$$

where the p and u superscripts were used to indicate polarized and unpolarized cross sections. The $\delta_{\rm V}$ is for vertex corrections. Contributions from internal bremsstrahlung are given by the σ_{el} and σ_{inel} terms.

External corrections accounted for effects due to interactions the electron could have before or after the scattering process. The electron traveled through a significant amount of material enroute to and from the scattering nucleus. Interactions with this material could have caused energy loss and also could have depolarized the electron. At the E155 energies, the primary mechanism for external radiative effects was bremsstrahlung.

The radiated asymmetry (A^{rad}) is the internal radiated asymmetry (A_{int}) adjusted for the probability that the electron emitted "external" bremsstrahlung radiation [144]. This is the corrected asymmetry presented in Equation 4 without the radiative correction terms.

The correction was separated into two terms, an additive one (A_{RC}) and a multiplicative one (f_{RC}). The additive correction was associated more with the

polarized radiative corrections and changed the effective asymmetry in a given x-bin. The multiplicative term was used for the unpolarized radiative corrections and changed the effective number of events in a particular bin. The f_{RC} term also was used to ensure a proper treatment of the statistical errors for the E155 data.

To determine the corrections, a fit was made to the world data set of $A_1(x, Q^2)$. Whenever possible data without radiative corrections were used. The asymmetry A_1 was chosen over g_1 for a variety of reasons. Fits to A_1 were found to be more robust [144] and A_1 was more closely related to the quantity measured in E155. In addition, positivity constraints on A_1 ensured physical results.

The functional form of the fit was [143]

$$A_1(x, Q^2) = x^{\alpha}(a + bx + cx^2)\left(1 + \frac{d}{Q^2}\right) \tag{26}$$

and asymmetries for all three target nucleons were fit simultaneously. This was done through Equation 39, $2g_1^d = (1 - 1.5\omega_D)(g_1^p + g_1^n)$, which connected the proton and neutron to each other as well as to the deuteron.

The results of the fits were used as the initial input into the program RC-SLACPOL. This is a piece of code which was developed at SLAC by L. Stuart. It was based on the ideas presented by Kukhto and Shumeiko in Reference [145]. The code was used as part of an iterative procedure where the output was fed back into the code until convergence was procured. Ultimately, the final output was the Born asymmetry and convergence of the results was obtained when the A_{RC} term did not change significantly from one iteration to the next. This condition usually was met

within less than 10 iterations. The additive correction A_{RC} was defined as

$$A_{RC}(x,Q^2) = A^{Born}(x,Q^2) - \frac{A^{radiated}(x,Q^2)}{f_{RC}(x,Q^2)}. \quad (27)$$

Both A_{RC} and f_{RC} are plotted in Figure 55 for the proton and Figure 56 for the deuteron. In all cases the A_{RC} term is positive at high x and negative at low x. The net effect of this term is to raise the high x end of the measured asymmetry and lower the low x region. This is a nice illustration of the ideas discussed above. In particular, that the radiative corrections are adjusting for events at higher x (where the asymmetry is larger) that have been shifted down in x (where the asymmetry is smaller) due to energy lost by the electron.

As seen in Figures 55 and 56, the multiplicative term (f_{RC}) is greater than one at high x and steadily decreases to values less than one in the lower x region. This trend can be explained by considering Equation 10, in which $A_{||}$ is expressed as the ratio of spin dependent to spin independent cross sections. Recall that f_{RC} is associated with the unpolarized radiative corrections and adjusts the effective number of events in a given bin. Since radiative effects shift events into lower x bins, multiplying the denominator (*i.e.*, the unpolarized part) in the high x region by a number greater than one compensates for this loss. Similarly, multiplying the denominator in the low x region by f_{RC} less than one corrects for the gain in events experienced by those bins.

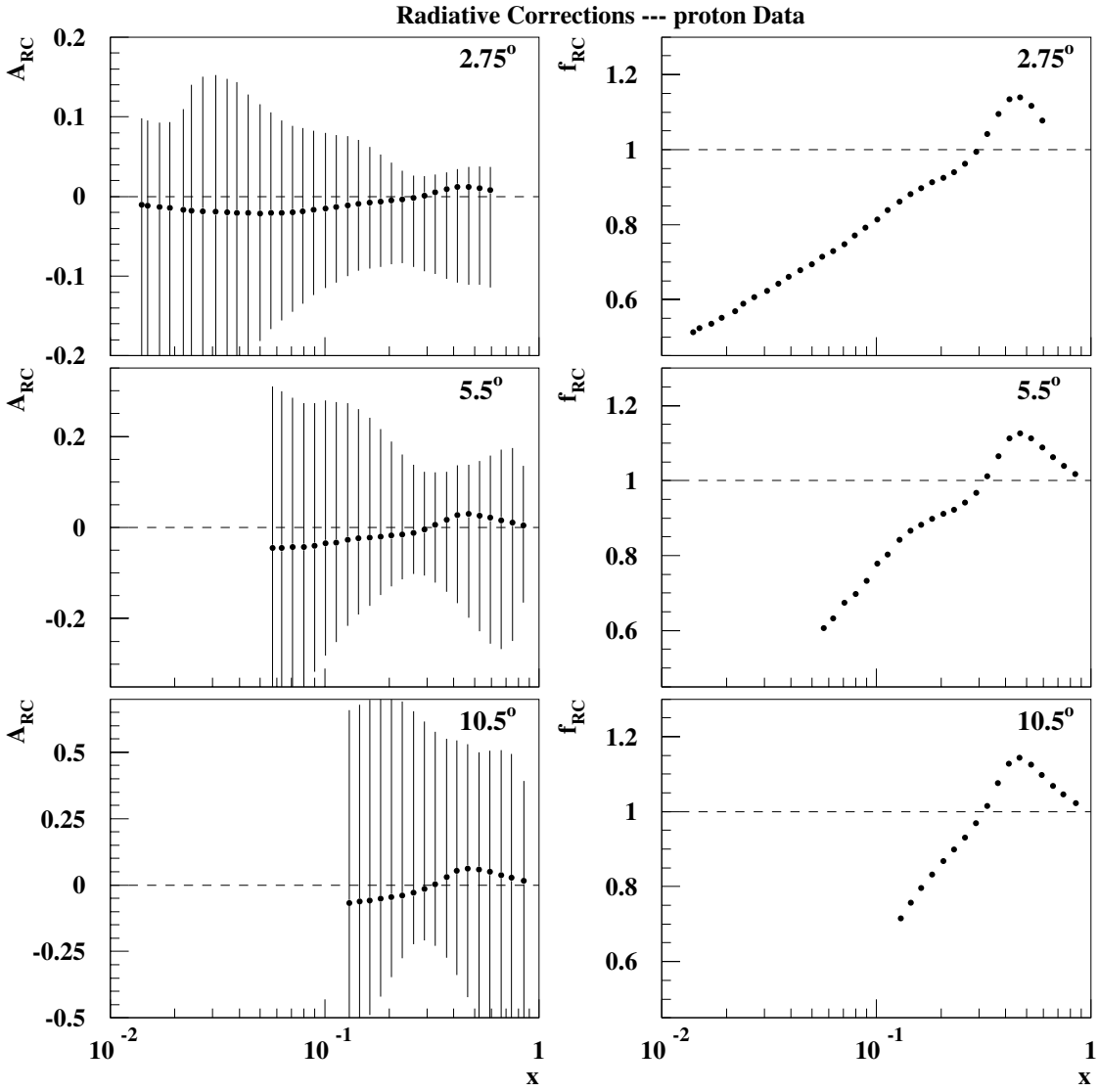

Figure 55: Additive (left column) and multiplicative (right column) parts of the radiative corrections are shown for the proton data for all three spectrometers as a function of x. Systematic errors are plotted with the A_{RC} term. Statistical errors are negligible on the vertical scales used here. Data are taken from the appendices of Reference [143].

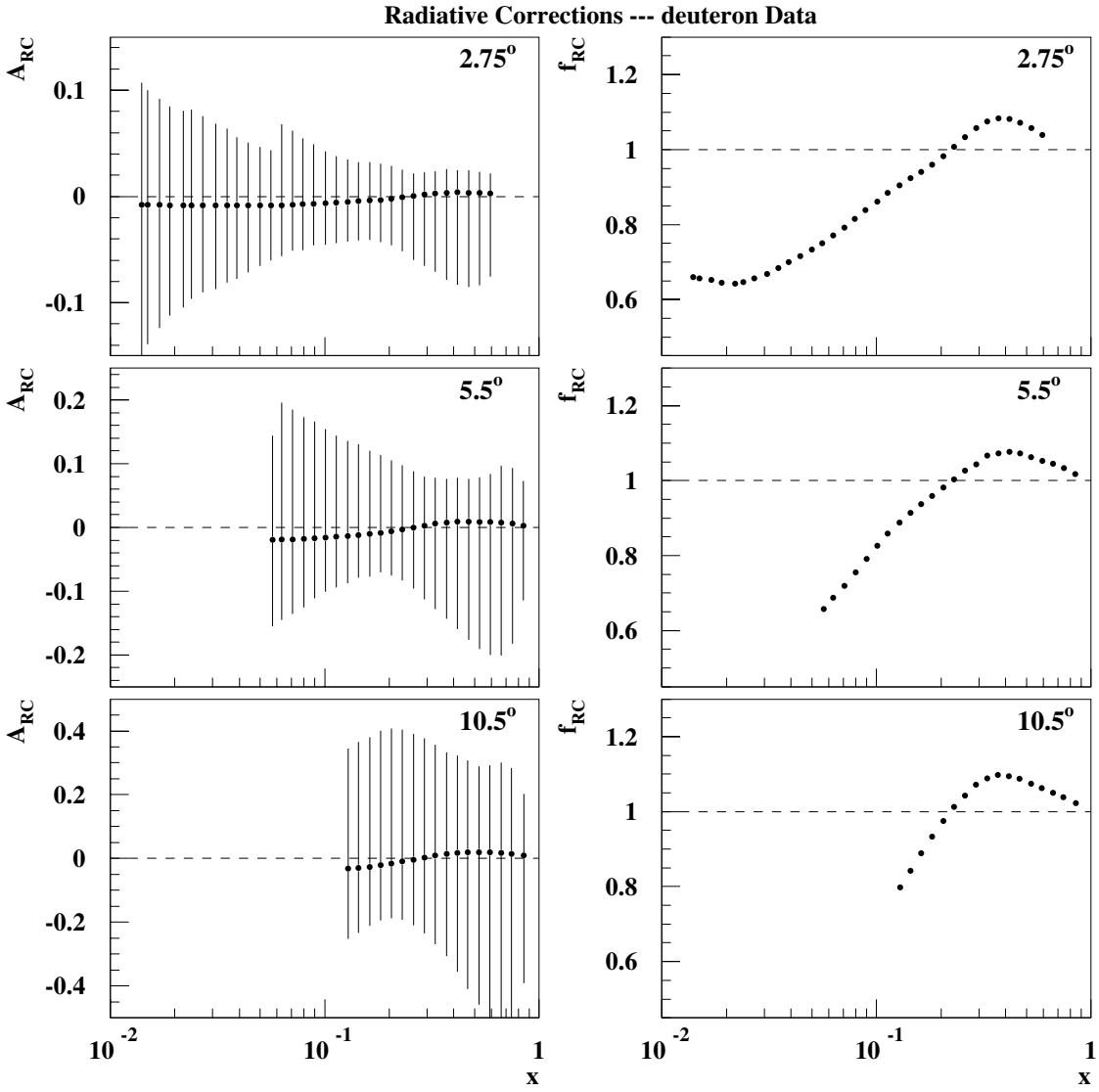

Figure 56: Additive (left column) and multiplicative (right column) parts of the radiative corrections are shown for the deuteron data for all three spectrometers as a function of x. Systematic errors are plotted with the A_{RC} term. Statistical errors are negligible on the vertical scales used here. Data are taken from the appendices of Reference [143].

4.9 Checks for False Asymmetries

A series of tests were performed on $A_{\parallel}(x)$ to ensure that the measurements were not biased by some facet of the experimental setup. Data collected on each target type and for each spectrometer were divided into two independent sets. The dividing line usually was chosen such that the sets were approximately equal in size. From each set, an $A_{\parallel}(x)$ was determined with adjustments made for beam and target polarizations, dilution factor, and nuclear and electroweak corrections. Examples of two such asymmetries are shown in the top plots of Figure 57. This example uses 2.75° $^{15}NH_3$ data that has been separated into events detected when the incident electrons were hitting the left or right hand side of the target. A distribution which represents how well these two sets agree can be created by taking the difference of the sets weighted by their combined errors,

$$D(x_i) = \frac{A_{\parallel}^{A}(x_i) - A_{\parallel}^{B}(x_i)}{\sqrt{\sigma_{A_i}^2 + \sigma_{B_i}^2}}, \tag{28}$$

where the A and B tags are used to indicate quantities from the two independent sets. For sets in good agreement, one can expect the distribution to take the shape of a Gaussian centered at 0 with a sigma of 1. Large deviations from either of these parameters may indicate an unexpected influence in the asymmetry. The plot in the lower right hand corner of Figure 57 shows the distribution of differences and corresponding fit from this example with the results from the fit presented in Figure 58. The left and right halves of the raster pattern agree well for the 2.75° $^{15}NH_3$ data.

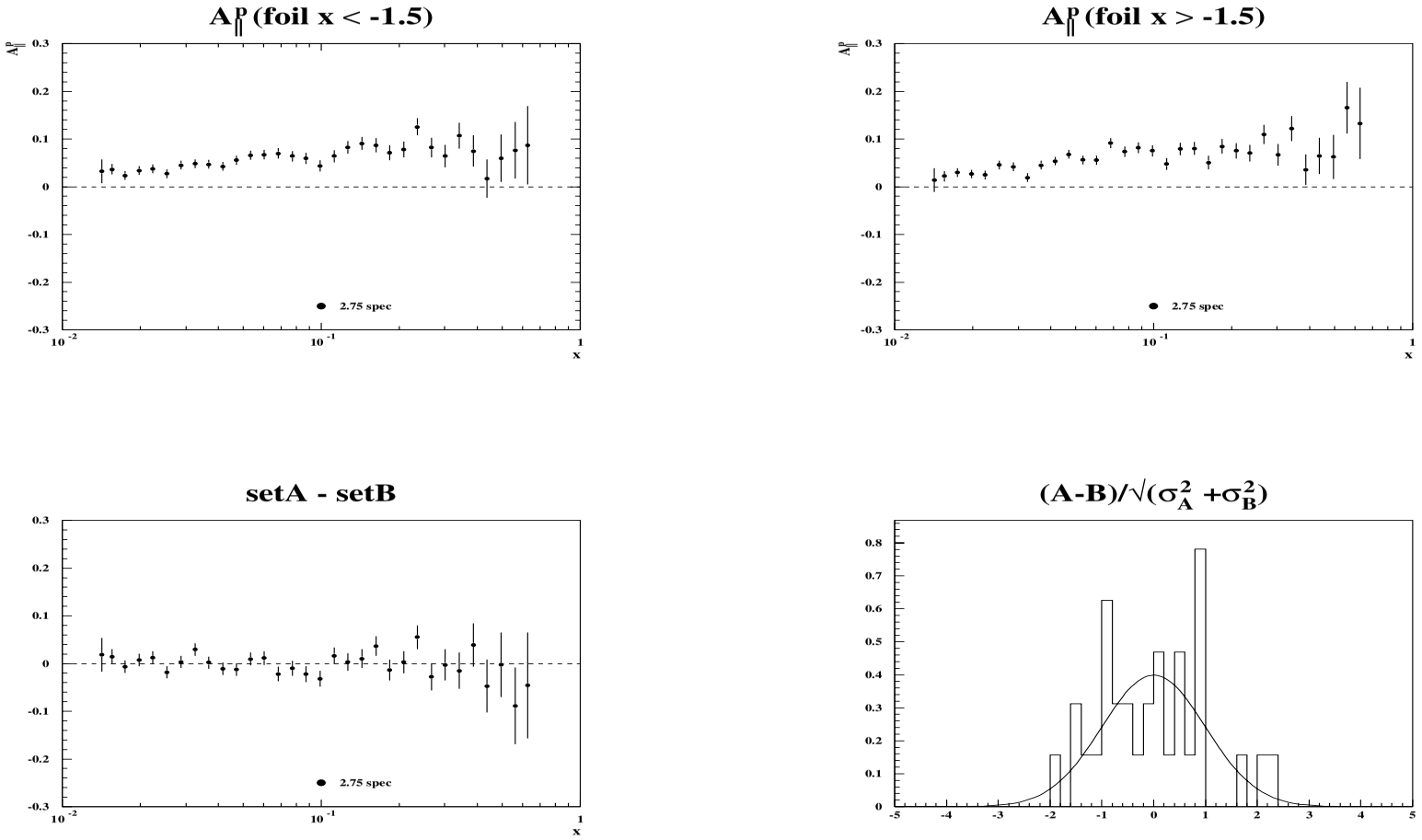

Figure 57: Intermediate steps of one method used to test the effect of different aspects of the experiment on the asymmetry. In this example, two independent subsets of the data were used to compare the left and right halves of the raster position. In the top two plots are asymmetries measured with the 2.75° spectrometer for each set. Lower plots show the difference between the sets and the resulting distribution of differences with a Gaussian fit.

The third column in the top of Figure 58 shows the results of a χ^2 test, which is a variation on Equation 28 and is given by

$$\frac{\chi^2}{N} = \frac{1}{N}\sum_{i=1}^{N}\left(\frac{A_{\|}^{A}(x_i) - A_{\|}^{B}(x_i)}{\sqrt{\sigma_{A_i}^2 + \sigma_{B_i}^2}}\right)^2, \tag{29}$$

where N is the number of x bins in a given spectrometer. A high value of $\frac{\chi^2}{N}$ points to disagreement between the two sets. Previous experiments [149] used the χ^2 test with a range of $\frac{\chi^2}{N} < 2$ to indicate that no significant effect on the data was observed from the quantity being tested. In the right half of Figure 58, asymmetries averaged over the measured x range are presented. Dotted lines separate pairs of independent data sets. Comparisons of average asymmetries offer a different but complimentary check to the Gaussian fit described above. While the error on the mean of the Gaussian is determined by how many x-bins are accessible to a given spectrometer, the average asymmetry's error depends on the number of events contained in the set. Graphically, this provides an extra piece of information which is useful when comparing a small subset to the rest of the data. The advantage of determining the mean and sigma is that the comparison is performed on a point to point basis. One can imagine comparing two lines, one sloped, one horizontal, which have the same average height. The distinction could show up in the determination of the sigma parameter, but not in the average asymmetry.

Results of tests performed on data collected using both target types with all three spectrometers are shown in Figures 58 to 63. The criteria used to divide the data are described below:

foil x → Left and right halves of the raster pattern, determined by the distribution of the beam on the foil arrays.

foil y → Top and bottom halves of the raster pattern.

raster → Cuts on the raster radii, used to separate inner and outer areas of the target. May show sensitivity to beam heating or to extra material in the target such as the NMR coil with the inner radius or the target cup with the outer one.

time slot → One of six zero crossings of the 360 Hz 3 phase PG&E power used to generate timing fiducials. The accelerator only uses two timing slots when operating at 120 Hz [150]. The beam polarization (and hence the asymmetry) should be independent of the time slot.

vpk → Pulse height from the Cherenkov detector. Cherenkov spectra for the electron definition were divided in half. Pulse height should not matter but hadrons, with their small Cherenkov signal and small $A_{\|}$, were more likely to contaminate the lower half of the spectrum.

coll. acc. → Settings for the 2.75° collimator.

Aew → Correction to account for the electroweak asymmetry. Three versions are given for the 2.75° and 5.5° $^{15}NH_3$ data. These three show the effect of applying or not applying the correction, or what happens if the correction is applied in the wrong direction.

east,west → Direction of the target magnet's field. The incident beam of electrons traveled from west to east in End Station A.

E/p → Energy/momentum ratio of the detected electrons. Spectra were split in half. Similar to the test on Cherenkov spectra in that hadron contamination was more likely to occur in the lower half of the spectra.

c1time → Event time for a particle passing through the first (or only) Cherenkov tank in a spectrometer's detector package. Used to divide the data into the early half and later half of the beam spill. If the first half of the beam spill locally depolarized the target (for example, via heating) this would change what the electrons in the tail of the spill scattered off. One would expect such an effect to show up in this test.

DST1 a,b,c → DST1 "a" was the main set of DST tapes for the 2.75° and 5.5° analysis. DST1 "b" and "c" were a small subset of runs returned to the "good" run set after some known problems were fixed. The majority of DST1 "b" and "c" runs were for data collected with a ^{6}LiD target.

edge clust → If an event's shower cluster was centered on an edge block of the shower counter, it was referred to as an edge cluster. Because the signal was recorded near the physical end of the detector, varying amounts of energy were lost. Also, since the edge blocks had fewer neighboring blocks, they were more difficult to calibrate.

% busy → A DAQ parameter. A high percent busy indicated that not all of the 5.5° and 10.5° spectrometer data was being read out. Runs with high percent busy readings were not used in the final analysis.

Most of the results show a good agreement between the pairs of data studied. A

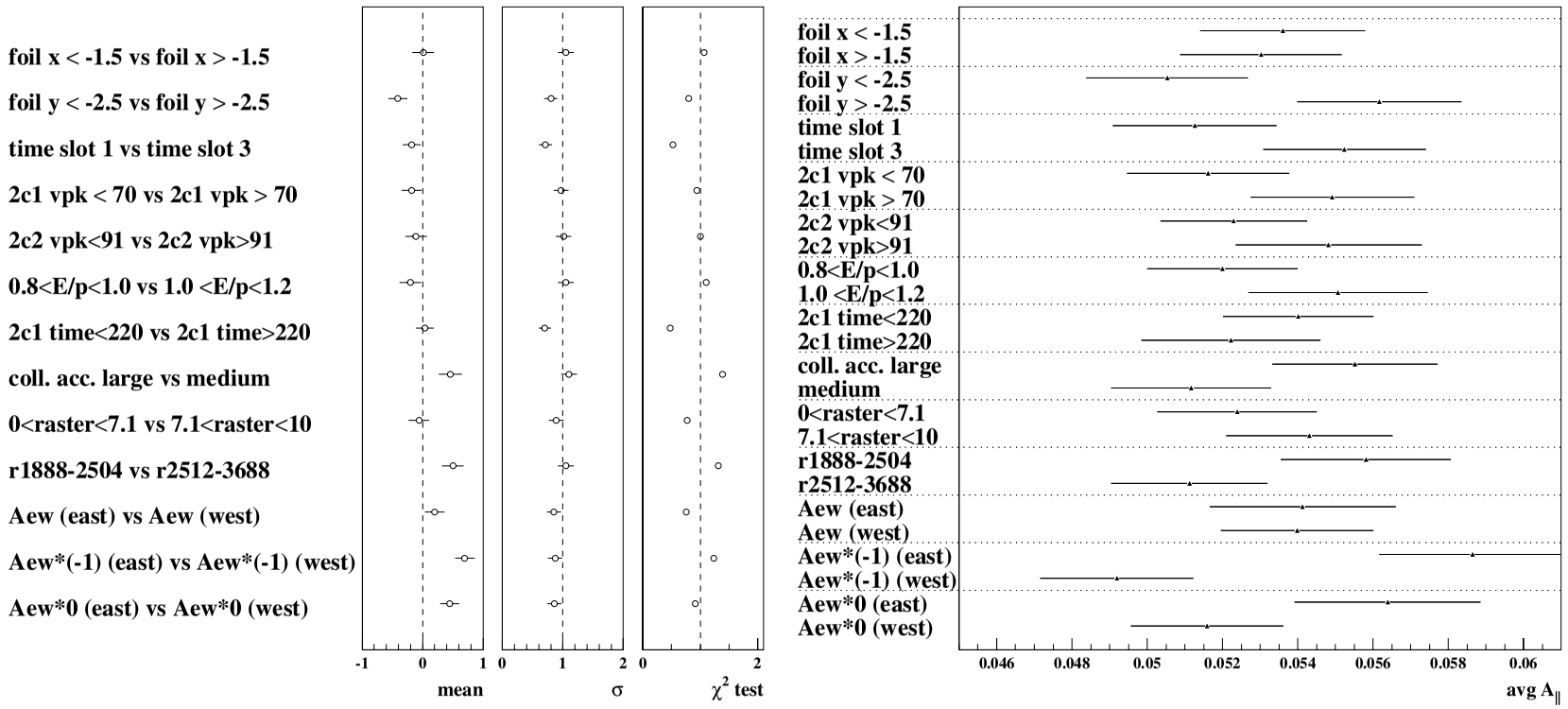

Figure 58: On the left are fit results and χ^2 values from different tests performed on 2.75° $^{15}NH_3$ data. The plot on the right shows the average asymmetries for the independent sets of data used in each test.

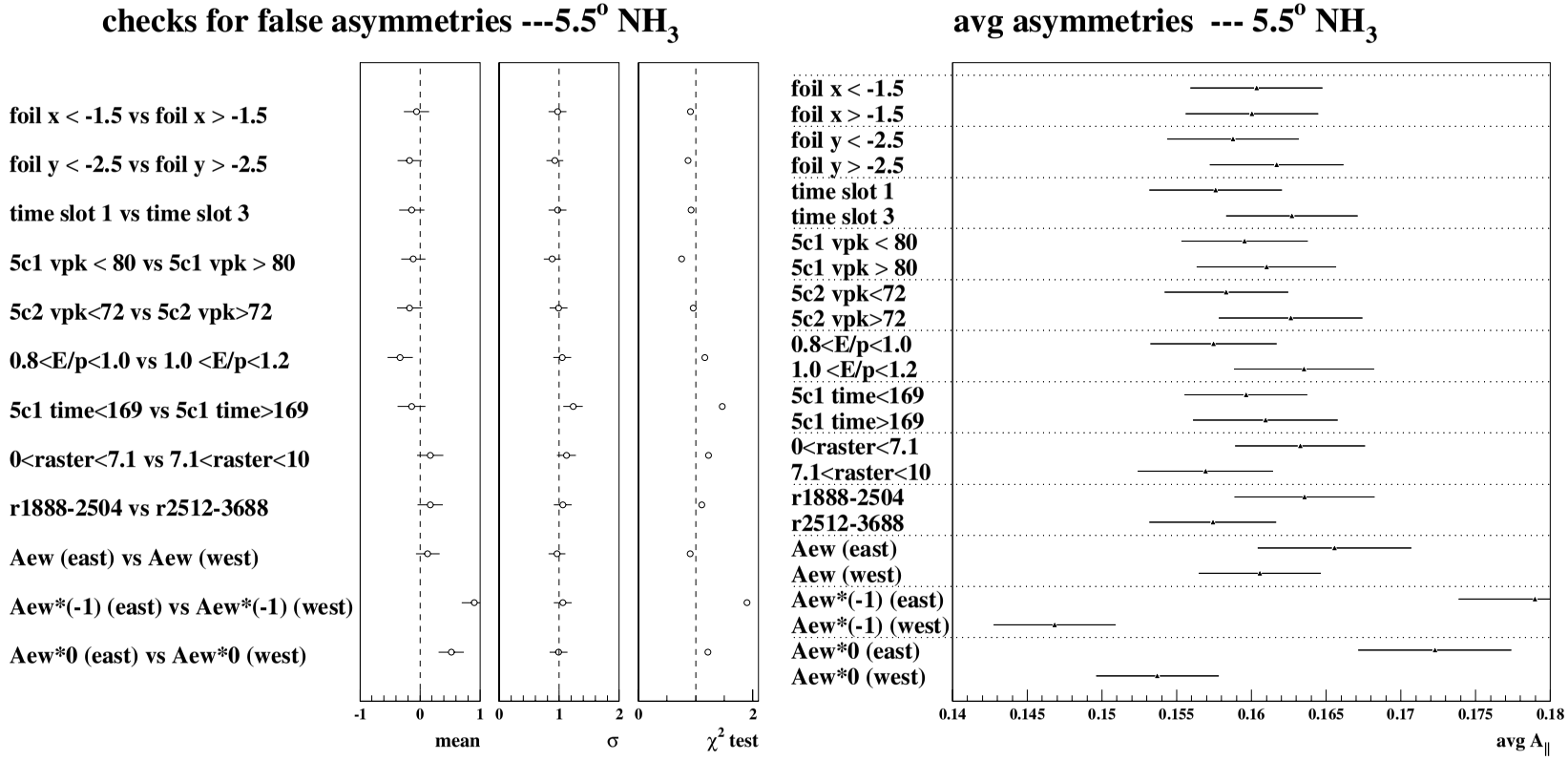

Figure 59: Same as Figure 58 but for 5.5° $^{15}NH_3$ data.

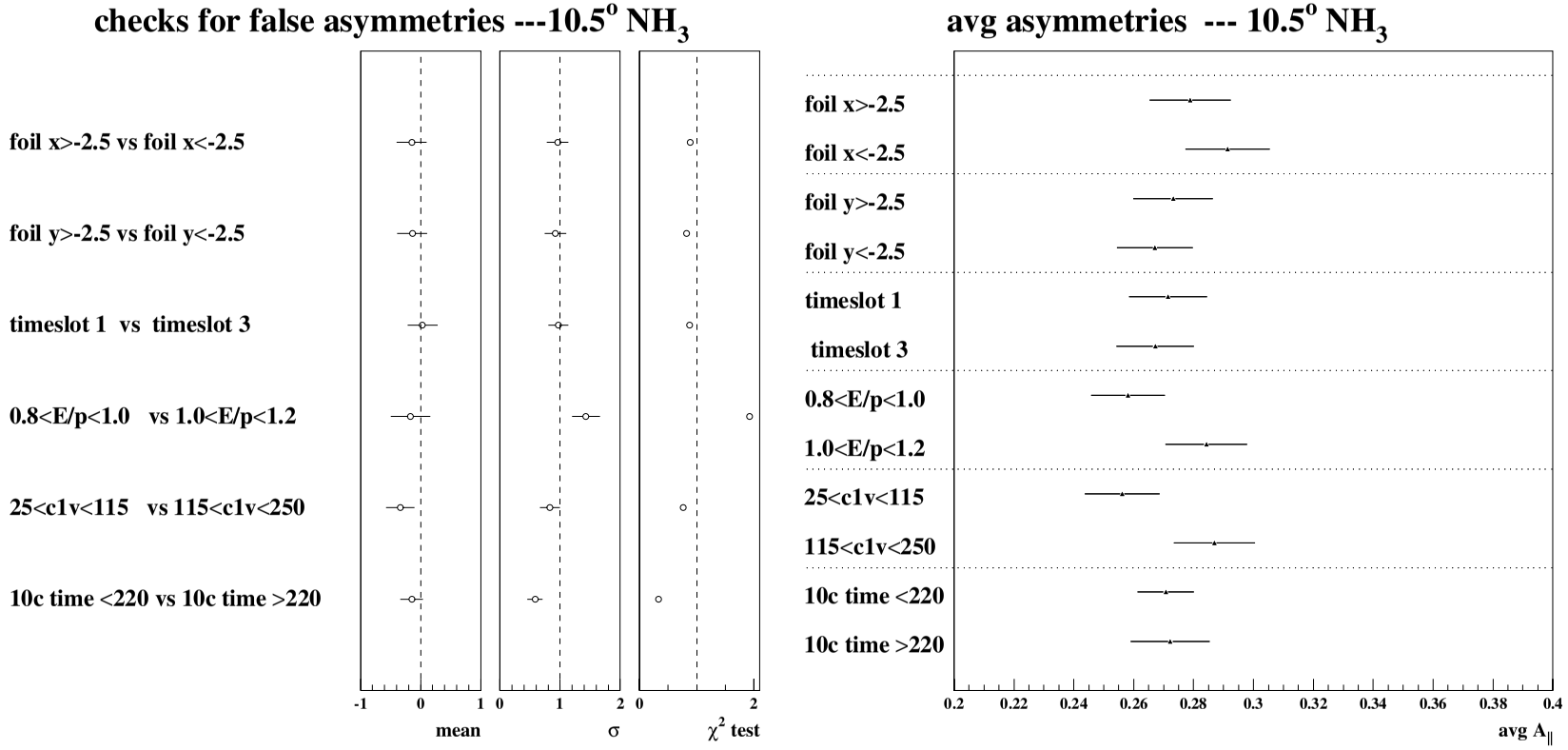

Figure 60: Same as Figure 58 but for 10.5° $^{15}NH_3$ data.

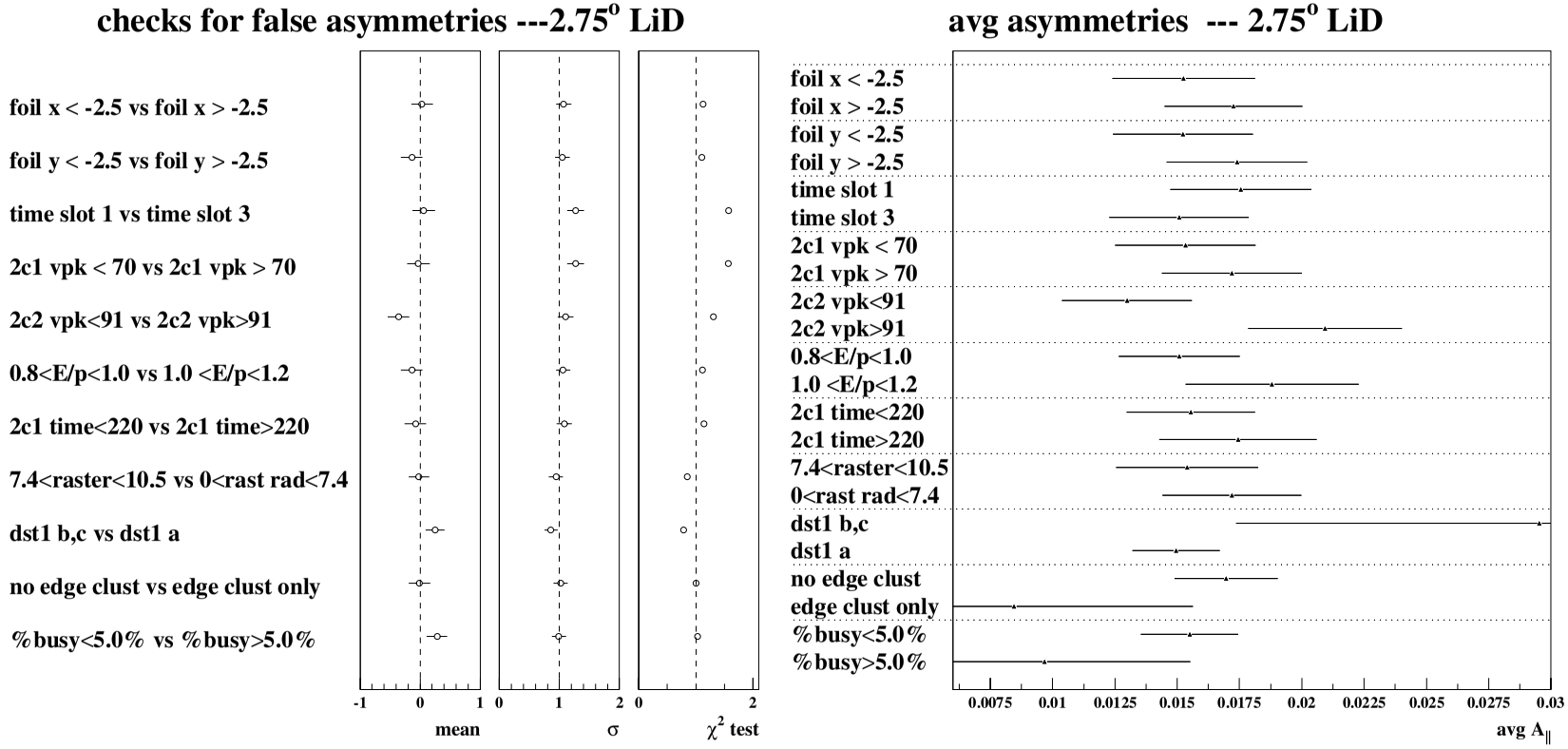

Figure 61: Same as Figure 58 but for 2.75° ^{6}LiD data.

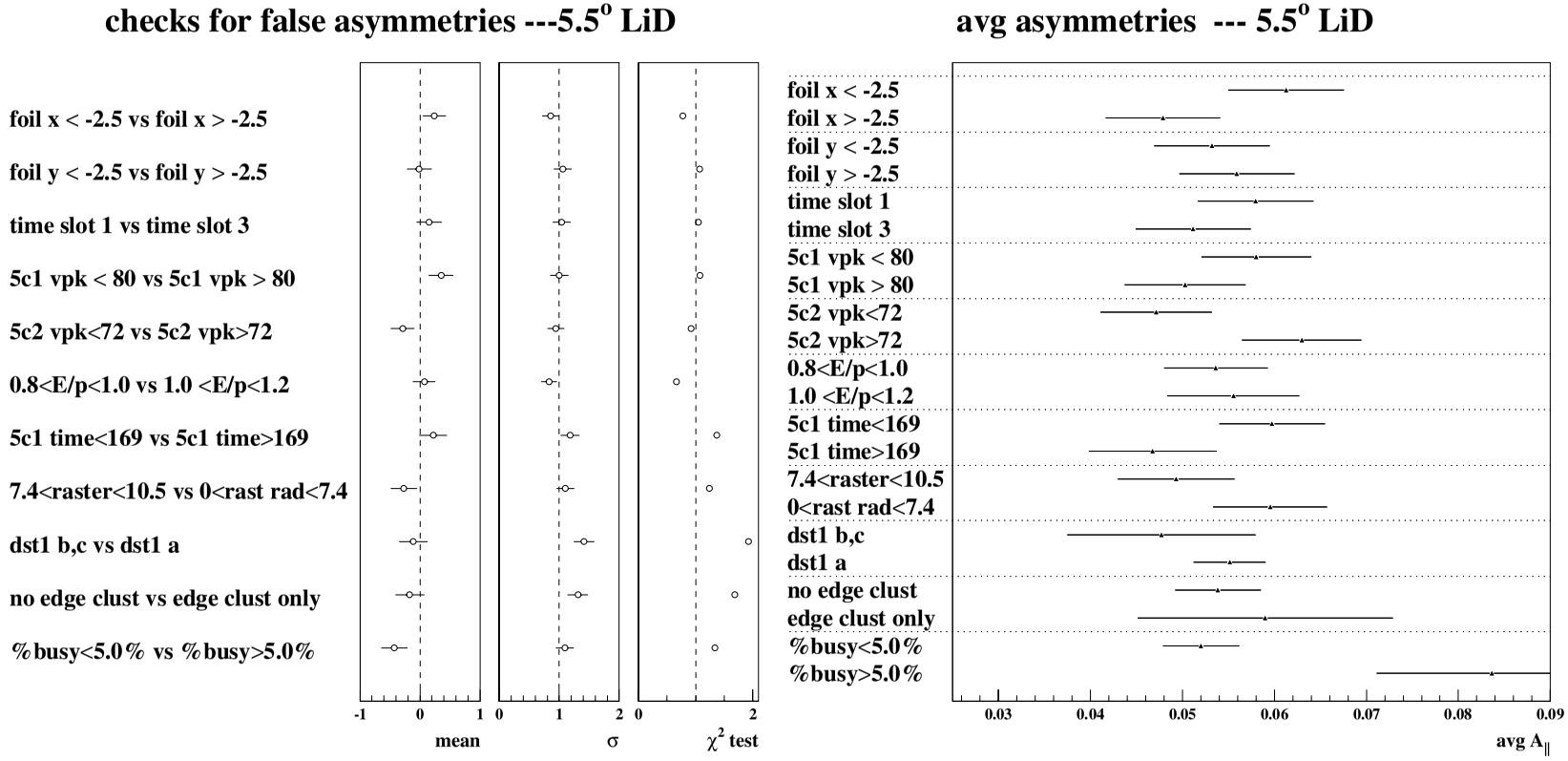

Figure 62: Same as Figure 58 but for 5.5° ^{6}LiD data.

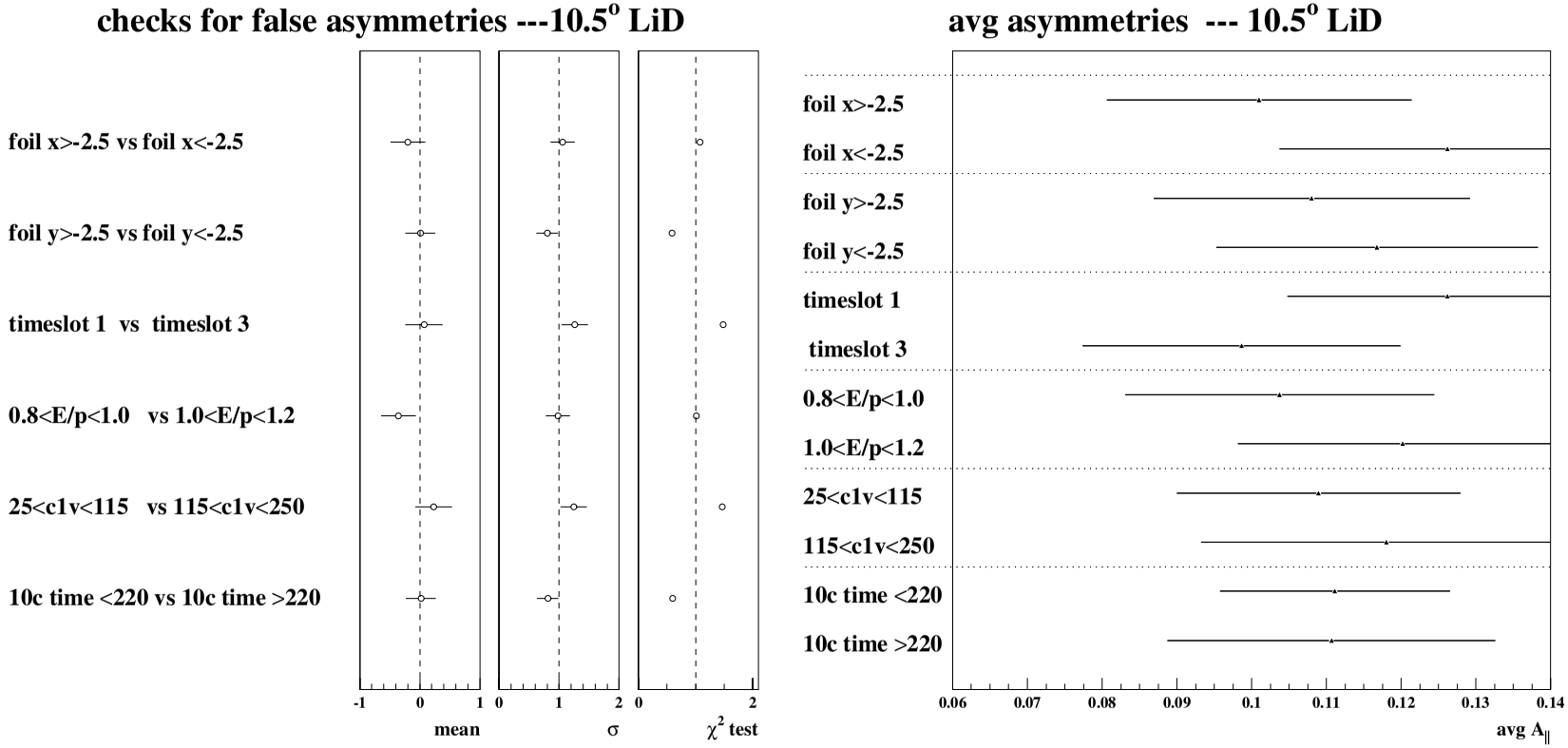

Figure 63: Same as Figure 58 but for 10.5° ^{6}LiD data. The larger error bars in this figure are due to the low tracking efficiency present in the 10.5° during the first half of E155. This led to the development of the 10.5° hybrid definition (see Section 4.7.2 for details) which was not used for the tests results shown.

few features were mentioned in the list above and are worth reiterating. Some of the *vpk* and E/p pairs do not agree as well as one would like. The lower half of the spectrum sometimes gives a lower average asymmetry, which is consistent with the idea of hadron contamination[20]. The percent busy in Figure 62 created a higher average asymmetry, which led to the removal of high percent busy runs from the final data set. Runs with a high percent busy occurred a few times early on in the E155 data taking period and was mostly resolved when the collection of proton data commenced. Figures 58 and 59 nicely display the effect of correcting for the electroweak asymmetry. Although this is a small correction, its application in the wrong direction can give quite noticeable results.

4.10 Electron Asymmetries

After applying the various corrections discussed in the previous sections, one can construct $A_{\|}(x, Q^2)$ for each type of target material and for all three spectrometers. These will be the starting point in the next chapter, during which the focus will switch to the spin structure function $g_1(x, Q^2)$ and $A_1(x, Q^2)$, the virtual photon-nucleon asymmetry. As explained in Chapter 2, these quantities can be obtained through equations which involve $A_{\|}$ and a collection of kinematic factors. Since $A_{\|}$ is central to the experiment, a worthwhile pause will be made to stop and show the intermediate result.

The fully corrected asymmetries are presented by spectrometer in Figure 64

[20]Data used in these tests were not corrected for hadron or pair symmetric backgrounds.

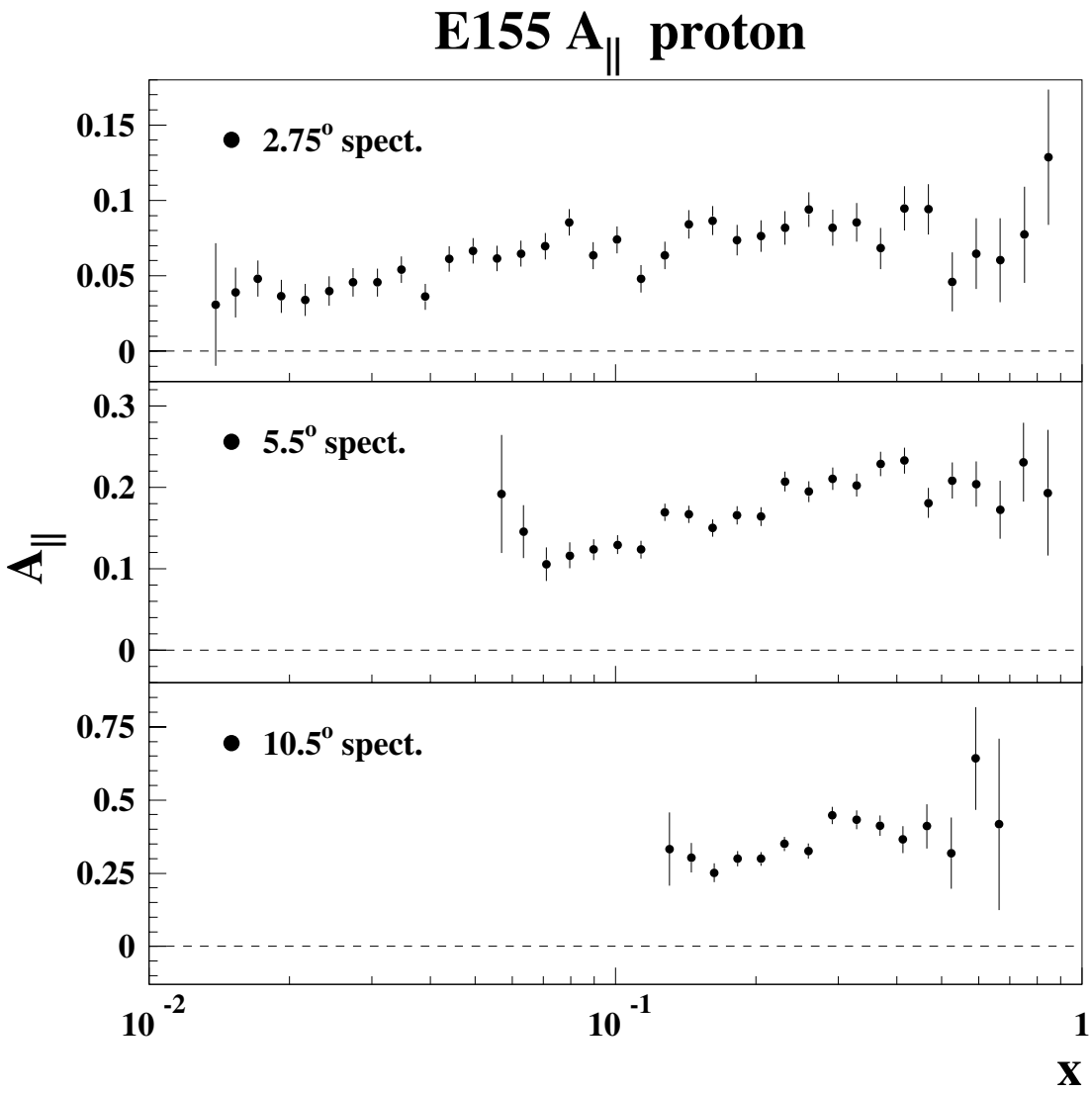

Figure 64: $A_{\|}$ measurements versus Bjorken x made on the $^{15}NH_3$ target for the 2.75°, 5.5°, and 10.5° spectrometers.

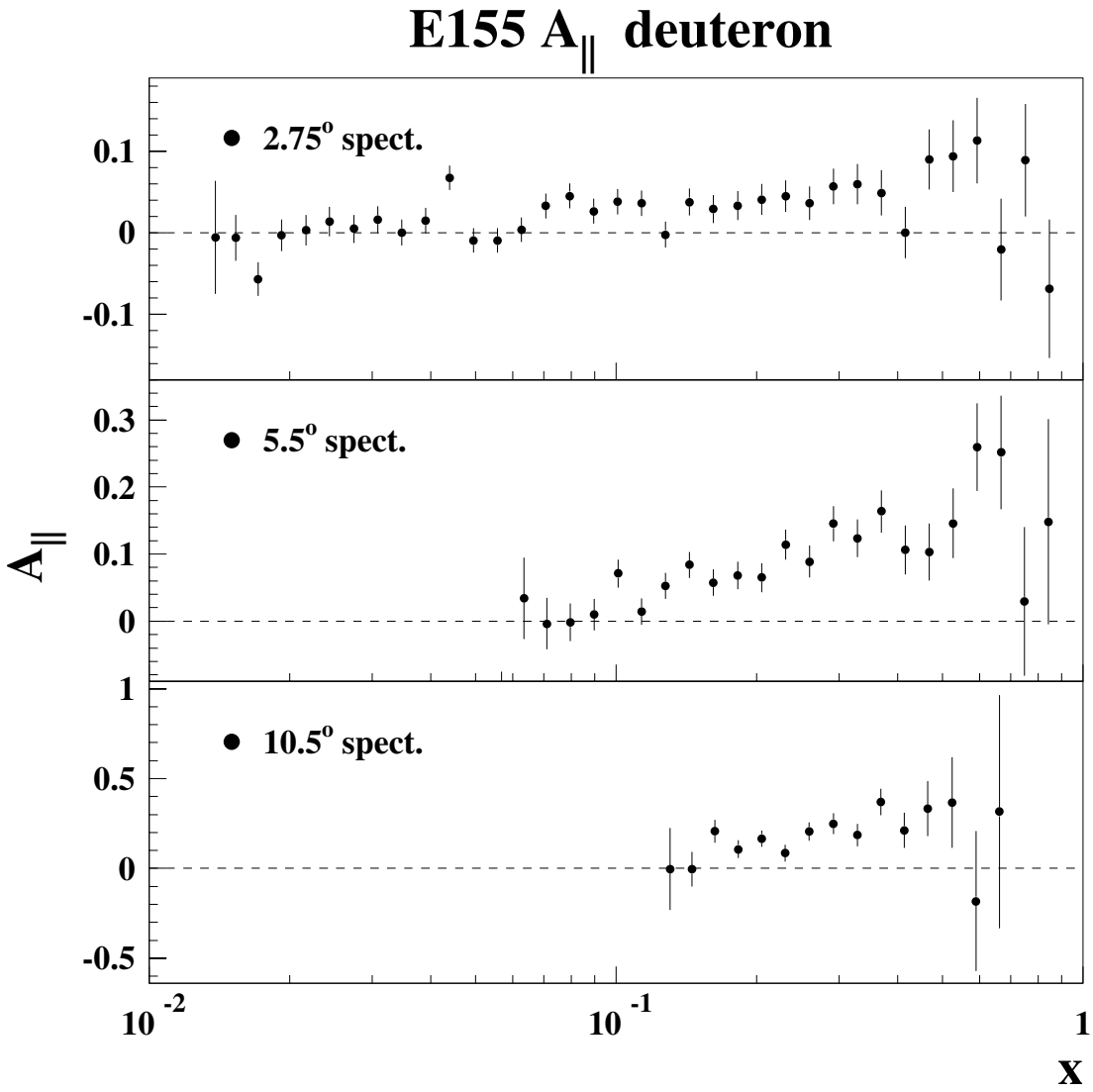

Figure 65: $A_{\parallel}$ measurements made on the ^{6}LiD target for the 2.75°, 5.5°, and 10.5° spectrometers.

Table 21: E155 results for $A_{\|}$, 2.75° spectrometer.

$\theta \approx 2.75°$

Proton			Deuteron		
$\langle x \rangle$	$\langle Q^2 \rangle$	$A_{\|} \pm stat \pm syst$	$\langle x \rangle$	$\langle Q^2 \rangle$	$A_{\|} \pm stat \pm syst$
0.014	1.00	0.031 ± 0.041 ± 0.004	0.014	1.00	-0.005 ± 0.069 ± 0.003
0.015	1.09	0.039 ± 0.016 ± 0.004	0.015	1.09	-0.006 ± 0.028 ± 0.001
0.017	1.20	0.048 ± 0.012 ± 0.004	0.017	1.20	-0.057 ± 0.020 ± 0.001
0.019	1.32	0.036 ± 0.011 ± 0.004	0.019	1.32	-0.003 ± 0.019 ± 0.001
0.022	1.45	0.034 ± 0.011 ± 0.004	0.022	1.45	0.003 ± 0.019 ± 0.001
0.024	1.59	0.040 ± 0.010 ± 0.004	0.024	1.59	0.014 ± 0.018 ± 0.001
0.027	1.73	0.046 ± 0.009 ± 0.004	0.027	1.73	0.005 ± 0.017 ± 0.001
0.031	1.88	0.045 ± 0.009 ± 0.004	0.031	1.88	0.016 ± 0.017 ± 0.001
0.035	2.04	0.054 ± 0.009 ± 0.004	0.035	2.04	0.000 ± 0.016 ± 0.001
0.039	2.22	0.036 ± 0.009 ± 0.005	0.039	2.21	0.015 ± 0.016 ± 0.001
0.044	2.40	0.061 ± 0.008 ± 0.005	0.044	2.39	0.068 ± 0.015 ± 0.001
0.049	2.59	0.067 ± 0.008 ± 0.005	0.049	2.58	-0.009 ± 0.015 ± 0.001
0.056	2.78	0.062 ± 0.008 ± 0.005	0.056	2.77	-0.009 ± 0.015 ± 0.001
0.063	2.97	0.065 ± 0.009 ± 0.005	0.063	2.97	0.004 ± 0.015 ± 0.001
0.071	3.17	0.070 ± 0.009 ± 0.005	0.071	3.17	0.033 ± 0.015 ± 0.001
0.079	3.37	0.086 ± 0.009 ± 0.006	0.079	3.36	0.045 ± 0.015 ± 0.001
0.089	3.57	0.063 ± 0.009 ± 0.006	0.089	3.57	0.027 ± 0.015 ± 0.001
0.101	3.77	0.074 ± 0.009 ± 0.006	0.101	3.77	0.038 ± 0.016 ± 0.001
0.113	3.97	0.048 ± 0.009 ± 0.006	0.113	3.97	0.036 ± 0.016 ± 0.001
0.127	4.17	0.064 ± 0.009 ± 0.006	0.128	4.17	-0.002 ± 0.016 ± 0.002
0.144	4.36	0.084 ± 0.009 ± 0.006	0.144	4.36	0.038 ± 0.016 ± 0.002
0.162	4.54	0.087 ± 0.010 ± 0.006	0.162	4.55	0.029 ± 0.017 ± 0.002
0.182	4.72	0.074 ± 0.010 ± 0.007	0.182	4.72	0.033 ± 0.018 ± 0.002
0.205	4.88	0.076 ± 0.011 ± 0.007	0.205	4.89	0.041 ± 0.019 ± 0.002
0.230	5.04	0.082 ± 0.011 ± 0.007	0.230	5.04	0.045 ± 0.020 ± 0.002
0.259	5.18	0.094 ± 0.011 ± 0.007	0.259	5.19	0.037 ± 0.021 ± 0.002
0.292	5.33	0.082 ± 0.012 ± 0.007	0.292	5.33	0.057 ± 0.022 ± 0.002
0.328	5.47	0.085 ± 0.013 ± 0.007	0.328	5.47	0.060 ± 0.025 ± 0.003
0.370	5.57	0.068 ± 0.014 ± 0.007	0.370	5.58	0.049 ± 0.028 ± 0.003
0.416	5.68	0.095 ± 0.015 ± 0.007	0.416	5.68	0.000 ± 0.031 ± 0.003
0.468	5.78	0.094 ± 0.017 ± 0.007	0.468	5.78	0.090 ± 0.037 ± 0.003
0.527	5.87	0.046 ± 0.020 ± 0.006	0.527	5.87	0.094 ± 0.044 ± 0.003
0.593	5.94	0.065 ± 0.023 ± 0.006	0.593	5.95	0.113 ± 0.053 ± 0.003
0.667	6.00	0.060 ± 0.028 ± 0.006	0.668	6.00	-0.020 ± 0.062 ± 0.003
0.751	6.06	0.077 ± 0.032 ± 0.006	0.751	6.07	0.089 ± 0.069 ± 0.003
0.846	6.12	0.129 ± 0.045 ± 0.005	0.846	6.12	-0.069 ± 0.085 ± 0.003

Table 22: E155 results for $A_{\|}$, 5.5° spectrometer.

$\theta \approx 5.5^{\circ}$

Proton			Deuteron		
$\langle x \rangle$	$\langle Q^2 \rangle$	$A_{\|} \pm stat \pm syst$	$\langle x \rangle$	$\langle Q^2 \rangle$	$A_{\|} \pm stat \pm syst$
0.057	4.01	0.192 ± 0.072 ± 0.008	0.057	4.00	-0.215 ± 0.140 ± 0.002
0.063	4.39	0.146 ± 0.032 ± 0.009	0.063	4.39	0.034 ± 0.061 ± 0.002
0.071	4.83	0.106 ± 0.021 ± 0.009	0.071	4.83	-0.004 ± 0.038 ± 0.002
0.080	5.30	0.116 ± 0.016 ± 0.010	0.080	5.30	-0.002 ± 0.028 ± 0.002
0.090	5.80	0.123 ± 0.013 ± 0.010	0.090	5.80	0.010 ± 0.023 ± 0.003
0.101	6.32	0.129 ± 0.012 ± 0.011	0.101	6.32	0.071 ± 0.021 ± 0.003
0.113	6.87	0.124 ± 0.011 ± 0.012	0.113	6.87	0.014 ± 0.020 ± 0.003
0.128	7.43	0.169 ± 0.010 ± 0.012	0.128	7.43	0.053 ± 0.019 ± 0.003
0.144	8.02	0.167 ± 0.010 ± 0.013	0.144	8.02	0.084 ± 0.019 ± 0.004
0.162	8.62	0.150 ± 0.011 ± 0.014	0.162	8.62	0.057 ± 0.020 ± 0.004
0.182	9.23	0.166 ± 0.011 ± 0.014	0.182	9.23	0.068 ± 0.021 ± 0.004
0.205	9.85	0.164 ± 0.012 ± 0.015	0.205	9.85	0.065 ± 0.021 ± 0.005
0.230	10.48	0.207 ± 0.012 ± 0.016	0.230	10.48	0.114 ± 0.023 ± 0.005
0.259	11.11	0.195 ± 0.013 ± 0.016	0.259	11.11	0.089 ± 0.024 ± 0.006
0.292	11.73	0.211 ± 0.013 ± 0.017	0.292	11.73	0.145 ± 0.026 ± 0.006
0.328	12.34	0.203 ± 0.014 ± 0.017	0.328	12.34	0.123 ± 0.028 ± 0.007
0.370	12.94	0.228 ± 0.015 ± 0.017	0.370	12.94	0.163 ± 0.032 ± 0.007
0.416	13.52	0.233 ± 0.016 ± 0.017	0.416	13.53	0.106 ± 0.036 ± 0.007
0.468	14.08	0.181 ± 0.018 ± 0.017	0.468	14.09	0.103 ± 0.043 ± 0.007
0.526	14.61	0.208 ± 0.022 ± 0.017	0.526	14.63	0.146 ± 0.052 ± 0.008
0.592	15.11	0.204 ± 0.028 ± 0.016	0.592	15.12	0.259 ± 0.065 ± 0.008
0.666	15.58	0.172 ± 0.036 ± 0.015	0.666	15.59	0.252 ± 0.085 ± 0.007
0.749	15.99	0.231 ± 0.048 ± 0.013	0.749	16.00	0.030 ± 0.111 ± 0.007
0.843	16.34	0.193 ± 0.077 ± 0.011	0.843	16.35	0.148 ± 0.153 ± 0.006

Table 23: E155 results for $A_{\|}$, 10.5° spectrometer.

$\theta \approx 10.5^{\circ}$

Proton			Deuteron		
$\langle x \rangle$	$\langle Q^2 \rangle$	$A_{\|} \pm stat \pm syst$	$\langle x \rangle$	$\langle Q^2 \rangle$	$A_{\|} \pm stat \pm syst$
0.130	10.04	0.333 ± 0.125 ± 0.017	0.130	10.04	-0.004 ± 0.228 ± 0.005
0.145	11.14	0.303 ± 0.051 ± 0.019	0.145	11.14	-0.006 ± 0.096 ± 0.006
0.162	12.35	0.251 ± 0.033 ± 0.020	0.163	12.37	0.207 ± 0.063 ± 0.006
0.182	13.70	0.299 ± 0.026 ± 0.022	0.182	13.70	0.107 ± 0.049 ± 0.007
0.205	15.13	0.299 ± 0.023 ± 0.023	0.205	15.15	0.166 ± 0.046 ± 0.008
0.230	16.66	0.349 ± 0.024 ± 0.025	0.230	16.67	0.086 ± 0.047 ± 0.009
0.259	18.28	0.326 ± 0.026 ± 0.027	0.259	18.28	0.206 ± 0.051 ± 0.010
0.291	20.03	0.447 ± 0.030 ± 0.029	0.292	20.04	0.249 ± 0.057 ± 0.011
0.328	21.86	0.433 ± 0.032 ± 0.031	0.328	21.86	0.186 ± 0.062 ± 0.012
0.369	23.80	0.413 ± 0.035 ± 0.033	0.369	23.78	0.370 ± 0.073 ± 0.013
0.413	25.85	0.365 ± 0.046 ± 0.034	0.414	25.90	0.211 ± 0.098 ± 0.015
0.465	27.94	0.410 ± 0.075 ± 0.036	0.465	28.04	0.332 ± 0.153 ± 0.016
0.524	30.12	0.318 ± 0.122 ± 0.036	0.524	30.19	0.366 ± 0.253 ± 0.017
0.590	32.30	0.642 ± 0.176 ± 0.036	0.590	32.36	-0.183 ± 0.389 ± 0.017
0.663	34.72	0.417 ± 0.293 ± 0.035	0.661	34.79	0.315 ± 0.649 ± 0.017

for the $^{15}NH_3$ target and in Figure 65 for data collected on ^{6}LiD . Tabulated versions are presented on pages 184, 185, and 186. The data are presented in the fine binning (38 x-bins) used by E154/E155 to preserve any structure that the asymmetries might have. All asymmetries shown are relatively flat except for a slight rise in going from low to high x. Both targets give a generally positive asymmetry, with the proton measurement typically possessing a larger asymmetry than the deuteron. Lastly, it is interesting to note that for a given target material, the average asymmetry scales approximately with the central scattering angle.

4.11 Hadron Asymmetries

4.11.1 Analysis

In comparison to the electron asymmetries, the hadron asymmetry analysis was relatively straight forward. The corrections applied were a subset of those used in the electron analysis. Raw asymmetries were defined the same as in Equation 2, except that the counts were collected into momentum bins. Adjustments to the asymmetry were made for beam polarization, target polarization, and dilution factor. This gave an expression for the measured asymmetry of

$$A_{LL}(p) = \frac{A^{raw}(p)}{P_b P_t f'}, \tag{30}$$

where p is the momentum of the detected hadron. For the beam and target polarizations (P_b and P_t), the values were the same as for the electron asymmetries. The manner in which the dilution factor was handled was a little different.

An average dilution factor was employed which was assumed to hold constant over the range of momenta. The quantity f' also included the $C1$ nuclear correction which was applied separately in the electron analysis (see Section 4.8.4). For reference, $C1$ was around 1.02 for $^{15}NH_3$ and 1.86 for ^{6}LiD . The C_1 correction for ^{6}LiD adjusts the dilution factor for the effective deuteron in ^{6}Li. The yield of hadrons per nucleon was assumed to be independent of the atomic number A. Possible shadowing corrections were looked for by parameterizing the cross section per nucleon as A^α. In the momentum range $10\,\mathrm{GeV} < p < 20\,\mathrm{GeV}$, a value of $\alpha = 0.0 \pm 0.1$ was found for both spectrometers [95].

The dilution factors used in constructing the hadron asymmetries were determined[21] by P. Bosted to be

$$f' = \begin{cases} 0.13 \pm 0.03 & ^{15}NH_3 \\ 0.34 \pm 0.04 & ^6\mathrm{LiD}\ . \end{cases} \tag{31}$$

These values are quite similar to their counterparts in the electron analysis when the nuclear correction factors are taken into account.

As mentioned earlier, cuts were made so that lower momentum pions and higher momentum hadrons were not included in the final data set. A discussion was given in Section 4.7 which dealt with pions below the momentum threshold of the Cherenkov tanks. In this region, Cherenkov cuts which were designed to select pions out of the hadron sample became meaningless. As can be seen in the measured π^+/e^- curve in Figure 66, some particles below threshold passed the cut.

[21] Private communication

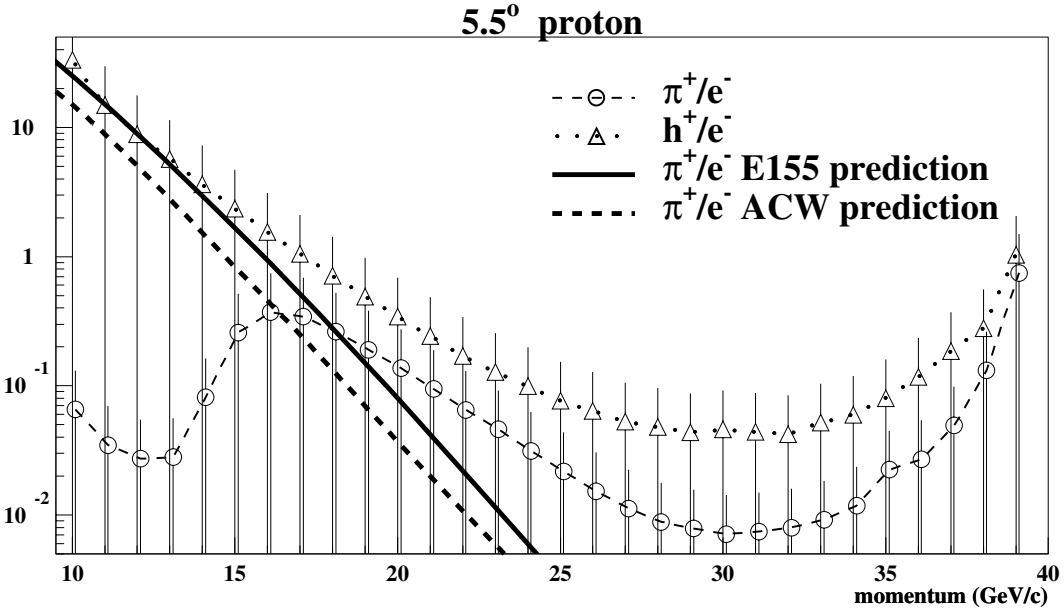

Figure 66: Measured and predicted π^+/e^- ratios for the 5.5° spectrometer. The bump in the measured curve is due to the Cherenkov pion momentum threshold. A h^+/e^- curve is included for comparison because it is dominated by π^+'s and it is not sensitive to the pion threshold of the Cherenkov detectors. The predicted curves are from References [45] and [95].

They occupy the area to the left of the peak at $p = 16$ GeV. However, these events are believed to be due to particles creating scintillation light or due to random coincidences. In either case, pions in this region could not be confidently identified without relevant Cherenkov information and so were not included in the final data set.

At the higher momentum values accessible by a spectrometer, the hadron data suffered from electron or positron contamination. Evidence of this contamination can be seen in Figure 66. The expected rate for hadrons in E155 dropped with increasing momentum. Predicted rates, two versions of which are included in Figure 66, show this behavior for the π^+'s. The measured h^+/e^- or π^+/e^- curves

in Figure 66 show that the data begin to increase above 31 GeV/c, while at lower momenta the rates are in reasonable agreement with the predicted ratios. Because of the low rates of high momentum hadrons, relatively few misidentified $e^{\pm}$ events are needed to cause a significant contamination. Instead of trying to correct for these events, say by performing a subtraction as was done in the electron analysis, these high momentum data were not included in the final data set. This is because the size of the contamination was difficult to estimate and there are not many events to be recovered at high momenta. Momentum cuts were made well below the region where the curves begin to turn upward to ensure that electrons (or positrons) were not used in constructing the hadron asymmetries.

The measured ratios which are presented in Figure 66 do not take into account the detection efficiencies for pions, hadrons, or electrons. While the electron efficiency has been determined for the various detector packages, those for pion and hadron definitions are more difficult to estimate. This is due to the heavy dependence of the definitions on one detector system, the shower counter. Since it is reasonable to assume that the efficiencies for detecting h^+'s and h^-'s (or π^+'s and π^-'s) are comparable, one can compare measured and predicted $+/-$ ratios with the hope of minimizing the sensitivity to these efficiencies. This is done for hadrons and pions in Figure 67. The E155 predictions included in the $^{15}NH_3$ plots, which use fits to the Wiser data [153], are in very rough agreement with the measured ratios. As seen in the top plot of Figure 67, the largest discrepancy appears in the 2.75° hadron ratio at high momenta. The increase in the predicted 2.75° hadron curve is due to

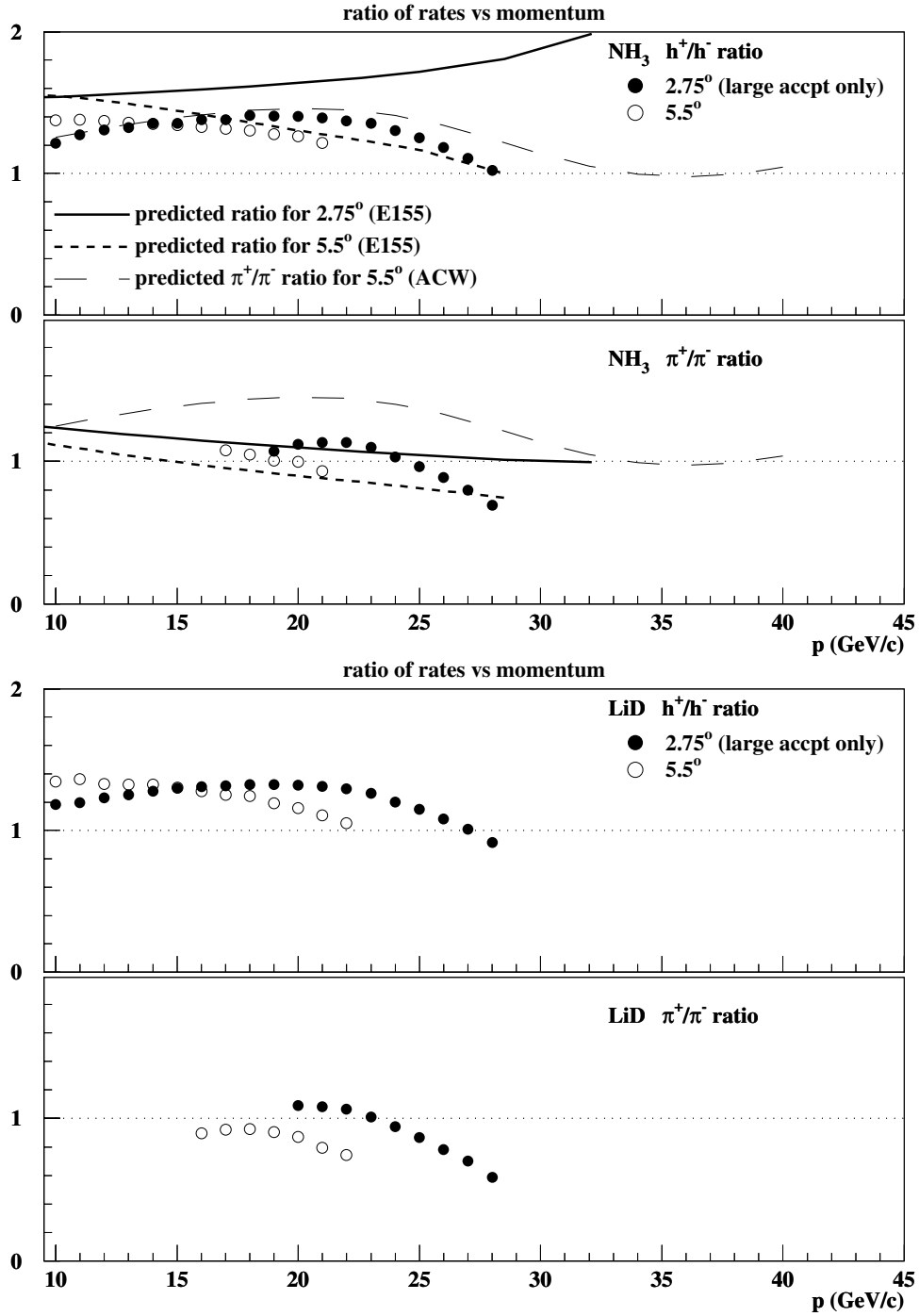

Figure 67: Measured ratios of oppositely charged hadrons and pions for both $^{15}NH_3$ and ^{6}LiD targets. The E155 curves shown in the $^{15}NH_3$ plots were calculated from the ratio of rates presented in Reference [95] which used a fit to the Wiser data [153]. The ACW curve is for π^+/π^- only and was taken from Figure 7 in Reference [47].

the expectation of more K^+'s and protons than K^-'s and anti-protons at high momentum. In this region, kaons and protons are believed to make up a bigger fraction of the hadron sample than at lower momenta. The E155 calculated ratios are reported in Reference [95] to be in good agreement with the PYTHIA Monte Carlo except for the K^+ rate. Lowering the K^+ rate by the factor of 2 needed to bring it into better agreement with the PYTHIA prediction would also improve the agreement between the predicted and measured 2.75° h^+/h^- ratio.

Also included in the $^{15}NH_3$ plots of Figure 67 is a predicted ratio of π^+/π^- rates that was presented by Afanasev, Carlson, and Wahlquist (ACW) in Reference [47]. No h^+/h^- curve was available and so the same π^+/π^- ratio is included in both plots. For this particular curve, the CTEQ [151] parton distribution functions were used as input. The ACW curve is similar in shape to the data but is larger in magnitude over most of the momentum range where the curve and data overlap. However, the ACW curve is from an earlier publication that did not included soft contributions. Additions from such sources may improve the agreement between prediction and data. Later calculations by this group [45] which included soft contributions led to a better agreement between the calculations and polarized data.

4.11.2 How to Improve the Hadron Data Set

One way the hadron asymmetry measurements could be improved was mentioned earlier. That is to correct for electron contamination at high values of momen-

tum. This is desirable because it extends the measurement into the more interesting high p_T region. However, the best procedure for such a the correction is not clear and there are so few events in that region that large uncertainties would limit the usefulness of those data.

The reasons for these difficulties, *i.e.*, lower rates and lower purity in the high momentum region of the hadron sample, stem from the primary focus of E155. The experiment was designed and optimized to detect electrons and to reject hadrons and muons. Techniques which would have improved the hadron measurement often would have done so at the expense of the electron detection efficiency. Hence such methods were not acceptable options.

For example, by setting different momentum thresholds in the Cherenkov tanks, better separation between π's, K's and protons could be achieved. This would have provided more information than did the combined hadron set. However, as mentioned above, changes such as this would have impacted the systems capability to detect electrons. As is often the case, the optimization of one measurement was in conflict with that of another.

4.11.3 Results

Results from the hadron asymmetries measured in the 2.75° and 5.5° spectrometers are presented in Figures 68 and 69. Inclusive pions, which were a subset of the hadron data that underwent more restrictive cuts, are shown in the same plots as solid points. The data also are presented in Tables 25, 26, 27, and 28.

Table 24: Average values of A_{LL} measured with the 2.75° spectrometer for polarized proton, deuteron, and neutron targets.

	$\theta \approx 2.75°$	
target	$\langle A_{LL}^{h^-} \rangle$	$\langle A_{LL}^{h^+} \rangle$
proton	0.0068 ± 0.0008	0.0135 ± 0.0020
deuteron	-0.0012 ± 0.0013	0.0021 ± 0.0023
neutron	$-0.0044 \pm$ —	-0.0075 ± 0.0013

Notes:
Neutron values are from [86]. No uncertainty was given for the fit to $A_{LL}^{h^-}$ neutron data.

These data differ from the published E155 hadron data [95] in that they use additional runs which were returned to the "good" data set since publication. The $^{15}NH_3$ measurements also include the final corrected proton polarizations [84], which were used in the published E155 g_1^p data [152] but were not available at the time of [95]. The data presented here are very similar to the published results.

The asymmetries are presented as a function of the detected particle's momentum. Data for both targets are relatively flat at low momenta. In this region the proton data are non-zero and positive while the deuteron data are consistent with zero. One can considers these results along with the E154 hadron asymmetry measurements [86] which used a neutron target. These are presented in Table 24. Similar to the case for electron asymmetries, the negative asymmetries from the neutron target show that the deuteron measurement is an average of those for the proton and neutron.

Included in the 5.5° plots are curves for calculated $\pi^{\pm}$ asymmetries that were presented in Reference [45]. For a given plot, each of the four curves corresponds to

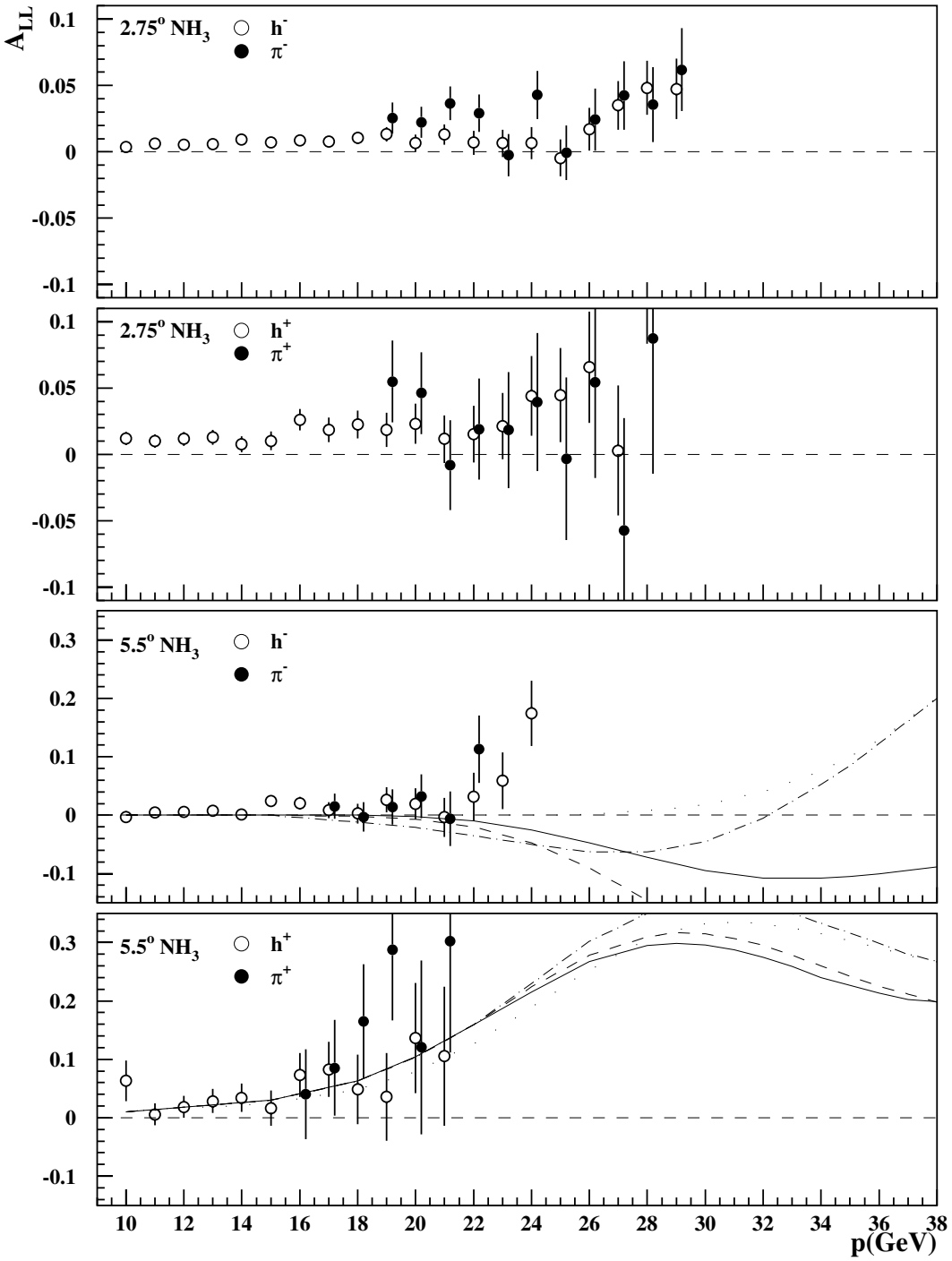

Figure 68: Inclusive hadron and pion asymmetries for 2.75° and 5.5° spectrometers using a proton target. Curves shown are for calculated $\pi^{\pm}$ asymmetries presented in Reference [45].

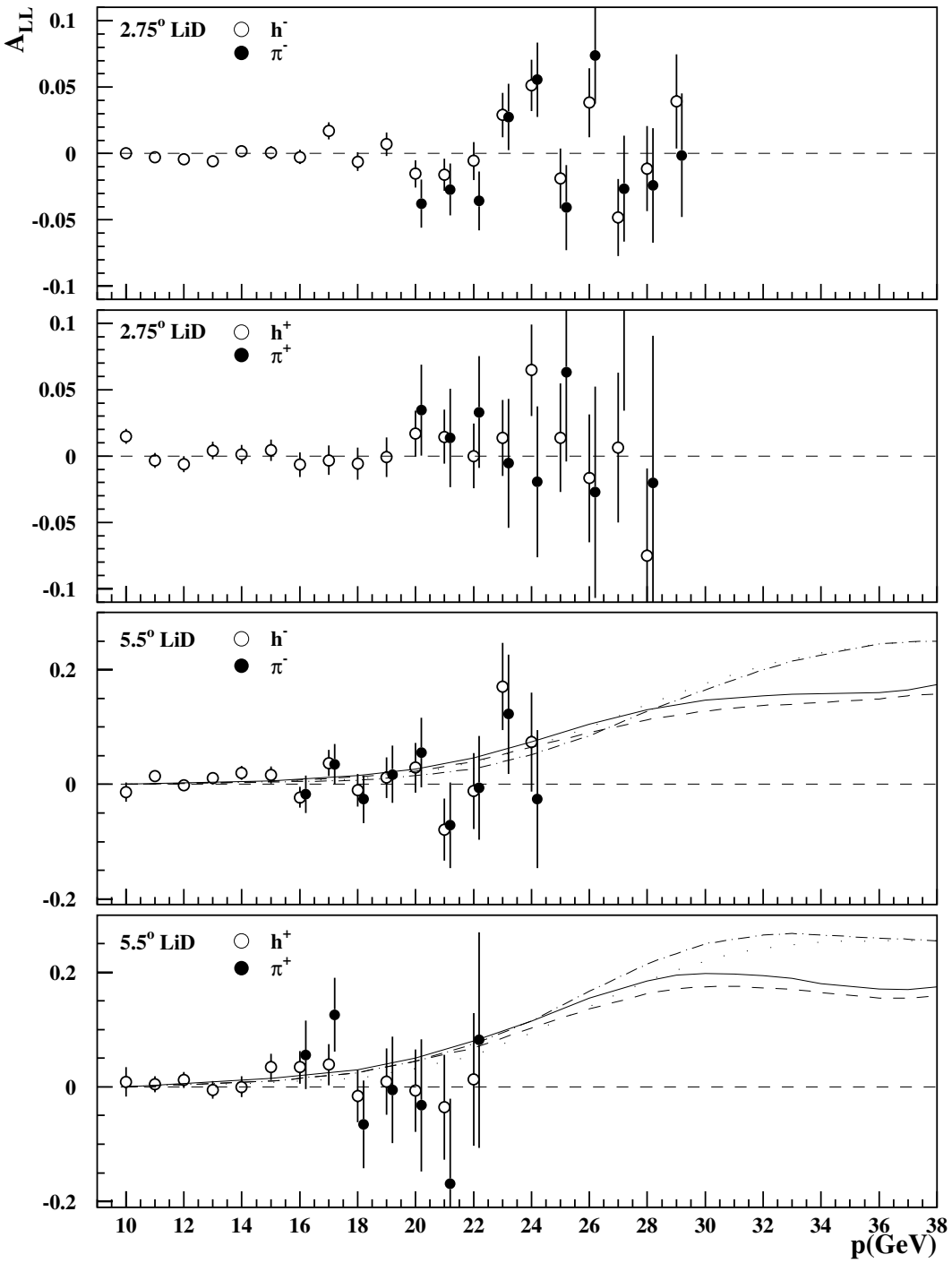

Figure 69: Inclusive hadron and pion asymmetries for 2.75° and 5.5° spectrometers using a deuteron target. Curves shown are for calculated $\pi^{\pm}$ asymmetries presented in Reference [45].

Table 25: Inclusive hadron asymmetries for the 2.75° and 5.5° spectrometers. Data were collected using the $^{15}NH_3$ target.

$A_{LL}^{h^{\pm}}(p)$ for Proton

p(GeV)	$\theta = 2.75^{\circ}\ h^-$	$\theta = 2.75^{\circ}\ h^+$	$\theta = 5.5^{\circ}\ h^-$	$\theta = 5.5^{\circ}\ h^+$
10.0	0.004 ± 0.002	0.012 ± 0.005	-0.003 ± 0.010	0.063 ± 0.035
11.0	0.006 ± 0.002	0.010 ± 0.005	0.005 ± 0.006	0.006 ± 0.019
12.0	0.005 ± 0.002	0.012 ± 0.005	0.006 ± 0.006	0.018 ± 0.019
13.0	0.006 ± 0.002	0.013 ± 0.006	0.008 ± 0.006	0.029 ± 0.021
14.0	0.009 ± 0.003	0.008 ± 0.006	0.001 ± 0.007	0.034 ± 0.024
15.0	0.007 ± 0.003	0.010 ± 0.007	0.024 ± 0.009	0.017 ± 0.030
16.0	0.009 ± 0.003	0.026 ± 0.008	0.021 ± 0.011	0.073 ± 0.038
17.0	0.008 ± 0.004	0.018 ± 0.009	0.009 ± 0.014	0.083 ± 0.047
18.0	0.011 ± 0.004	0.023 ± 0.010	0.003 ± 0.017	0.048 ± 0.060
19.0	0.013 ± 0.005	0.018 ± 0.013	0.026 ± 0.022	0.036 ± 0.075
20.0	0.006 ± 0.006	0.023 ± 0.015	0.020 ± 0.027	0.136 ± 0.094
21.0	0.013 ± 0.007	0.012 ± 0.018	-0.004 ± 0.033	0.105 ± 0.119
22.0	0.007 ± 0.009	0.015 ± 0.021	0.031 ± 0.041	—
23.0	0.006 ± 0.010	0.021 ± 0.025	0.059 ± 0.048	—
24.0	0.007 ± 0.012	0.044 ± 0.030	0.174 ± 0.056	—
25.0	-0.005 ± 0.014	0.045 ± 0.036	—	—
26.0	0.017 ± 0.016	0.066 ± 0.042	—	—
27.0	0.035 ± 0.018	0.003 ± 0.049	—	—
28.0	0.048 ± 0.020	0.141 ± 0.058	—	—
29.0	0.047 ± 0.023	—	—	—

Table 26: Inclusive pion asymmetries for the 2.75° and 5.5° spectrometers. Data were collected using the $^{15}NH_3$ target.

$A_{LL}^{\pi^{\pm}}(p)$ for Proton				
p(GeV)	$\theta = 2.75°$ π^-	$\theta = 2.75°$ π^+	$\theta = 5.5°$ π^-	$\theta = 5.5°$ π^+
16.0	—	—	—	0.040 ± 0.077
17.0	—	—	0.015 ± 0.022	0.086 ± 0.082
18.0	—	—	-0.003 ± 0.025	0.165 ± 0.098
19.0	0.026 ± 0.012	0.055 ± 0.031	0.014 ± 0.031	0.288 ± 0.121
20.0	0.022 ± 0.012	0.046 ± 0.031	0.033 ± 0.038	0.120 ± 0.149
21.0	0.037 ± 0.013	-0.008 ± 0.034	-0.006 ± 0.047	0.303 ± 0.191
22.0	0.029 ± 0.014	0.019 ± 0.038	0.113 ± 0.058	—
23.0	-0.002 ± 0.016	0.018 ± 0.044	—	—
24.0	0.043 ± 0.018	0.039 ± 0.052	—	—
25.0	-0.001 ± 0.021	-0.003 ± 0.061	—	—
26.0	0.024 ± 0.023	0.054 ± 0.072	—	—
27.0	0.043 ± 0.026	-0.057 ± 0.085	—	—
28.0	0.036 ± 0.028	0.087 ± 0.102	—	—
29.0	0.062 ± 0.031	—	—	—

a different set of Parton Distribution Functions that were used as input. Assuming the model is correct, precision data at high values of momentum would be able to distinguish between the different curves and therefore the different PDFs.

In the region of overlap, the theoretical calculations and the data are in reasonable agreement. An earlier version of the calculations [47], which were published prior to the E155 hadron results, were less compatible with the data. This is shown in Figures 3 and 4 of Reference [95], where at low momenta, the calculations typically led to curves that were larger in magnitude than the measured data. Since the release of the E155 hadron data, soft contributions were added to the theoretical calculations via the Vector Meson Dominance model. In terms of the Section 2.5.3 discussion, this was implemented by including $\Delta\sigma_{Vp\to\pi^{\pm}X}$ ($\sigma_{Vp\to\pi^{\pm}X}$) in the numer-

Table 27: Inclusive hadron asymmetries for the 2.75° and 5.5° spectrometers. Data were collected using the ^{6}LiD target.

$A_{LL}^{h^\pm}(p)$ for Deuteron

p(GeV)	$\theta = 2.75°$ h^-	$\theta = 2.75°$ h^+	$\theta = 5.5°$ h^-	$\theta = 5.5°$ h^+
10.0	0.000 ± 0.003	0.015 ± 0.006	-0.014 ± 0.017	0.009 ± 0.026
11.0	-0.003 ± 0.003	-0.003 ± 0.006	0.014 ± 0.009	0.005 ± 0.014
12.0	-0.004 ± 0.004	-0.006 ± 0.006	-0.001 ± 0.009	0.012 ± 0.014
13.0	-0.006 ± 0.004	0.004 ± 0.007	0.011 ± 0.010	-0.005 ± 0.016
14.0	0.002 ± 0.004	0.001 ± 0.007	0.020 ± 0.012	0.000 ± 0.018
15.0	0.001 ± 0.005	0.004 ± 0.008	0.016 ± 0.015	0.035 ± 0.023
16.0	-0.003 ± 0.005	-0.007 ± 0.009	-0.022 ± 0.018	0.034 ± 0.029
17.0	0.017 ± 0.006	-0.003 ± 0.011	0.037 ± 0.023	0.039 ± 0.036
18.0	-0.006 ± 0.007	-0.006 ± 0.012	-0.010 ± 0.029	-0.016 ± 0.046
19.0	0.007 ± 0.009	-0.001 ± 0.015	0.012 ± 0.035	0.009 ± 0.058
20.0	-0.015 ± 0.010	0.017 ± 0.017	0.029 ± 0.044	-0.007 ± 0.072
21.0	-0.016 ± 0.012	0.015 ± 0.020	-0.079 ± 0.054	-0.036 ± 0.092
22.0	-0.006 ± 0.014	0.000 ± 0.024	-0.011 ± 0.066	0.013 ± 0.116
23.0	0.029 ± 0.017	0.014 ± 0.029	0.171 ± 0.076	—
24.0	0.051 ± 0.019	0.065 ± 0.034	0.074 ± 0.087	—
25.0	-0.019 ± 0.022	0.014 ± 0.041	—	—
26.0	0.038 ± 0.026	-0.017 ± 0.048	—	—
27.0	-0.048 ± 0.029	0.006 ± 0.056	—	—
28.0	-0.011 ± 0.032	-0.075 ± 0.066	—	—
29.0	0.039 ± 0.035	—	—	—

Table 28: Inclusive pion asymmetries for the 2.75° and 5.5° spectrometers. Data were collected using the ^{6}LiD target.

$A_{LL}^{\pi^\pm}(p)$ for Deuteron				
p(GeV)	$\theta = 2.75°$ π^-	$\theta = 2.75°$ π^+	$\theta = 5.5°$ π^-	$\theta = 5.5°$ π^+
16.0	—	—	-0.017 ± 0.033	0.056 ± 0.060
17.0	—	—	0.035 ± 0.035	0.126 ± 0.064
18.0	—	—	-0.026 ± 0.042	-0.065 ± 0.076
19.0	—	—	0.018 ± 0.050	-0.005 ± 0.093
20.0	-0.038 ± 0.018	0.035 ± 0.034	0.056 ± 0.061	-0.032 ± 0.116
21.0	-0.027 ± 0.020	0.014 ± 0.037	-0.071 ± 0.074	-0.169 ± 0.149
22.0	-0.036 ± 0.022	0.033 ± 0.042	-0.006 ± 0.091	0.082 ± 0.188
23.0	0.027 ± 0.025	-0.005 ± 0.049	0.123 ± 0.104	—
24.0	0.056 ± 0.028	-0.020 ± 0.057	-0.026 ± 0.121	—
25.0	-0.041 ± 0.032	0.063 ± 0.067	—	—
26.0	0.074 ± 0.036	-0.027 ± 0.080	—	—
27.0	-0.026 ± 0.040	0.128 ± 0.094	—	—
28.0	-0.024 ± 0.043	-0.020 ± 0.111	—	—
29.0	-0.001 ± 0.047	—	—	—

ator (denominator) of Equation 50. The helicity dependence of this contribution was assumed to be zero and its net effect was to decrease the predicted asymmetry at low momenta.

At higher momenta, the proton data look as if the asymmetries are beginning to increase, albeit with large uncertainties. The calculations support this trend for positively charged particles in the 5.5° spectrometer. This may be the start of a region of sensitivity to the partons' polarizations. Note that in Figure 6, which shows the unpolarized differential cross sections, that this is approximately the momentum range where the hard contributions begin to overtake those from VMD. However, the authors of [45] point out that one of the requirements for accessing the gluon spin through photoproduced pions is that the asymmetries need to be measured over

a momentum region where the contributions labelled "fragmentation" (in Figure 6) dominate. Unfortunately, this condition is not met in either of the plots of Figure 6. Thus according to the improved model presented in Reference [45], photoproduced pion asymmetries have no sensitivity to the gluon spin at the kinematics of the E155 5.5° spectrometer.

CHAPTER 5

RESULTS

5.1 Spin Structure Functions

Using the fully corrected electron asymmetries from the previous chapter, one can obtain g_1 through the expression

$$g_1(x,Q^2) = \frac{A_{\parallel}(x,Q^2)F_1(x,Q^2)}{D'(x,Q^2)} + g_2^{WW}(x,Q^2)\frac{2Mx}{2E-\nu}, \tag{1}$$

where the convention is the same as that used in Section 2.1. The value used for the spin averaged structure function $F_1(x,Q^2)$ came from an NMC fit [154] to F_2 and from R1998 [11]. The contribution to g_1 from the second term was small due to both the size of g_2 and the suppression of this term by the factor $2Mx/(2E-\nu)$. For g_2, the Wandzura and Wilczek model [155] was used, which is known to be in good agreement with available data and is given by

$$g_2^{WW}(x,Q^2) = -g_1(x,Q^2) + \int_x^1 g_1(\xi,Q^2)\frac{d\xi}{\xi}. \tag{2}$$

Equation 2 was evaluated using a g_1/F_1 fit [143, 148] to a global data set. Some details of the fit are discussed in Section 5.4. The quantity g_1 is presented in Tables 29 (proton) and 30 (deuteron) at measured values of x and Q^2.

In order to compare the results to other experiments or to test predictions, a number of steps need to be taken. First, the data from the three spectrometers

Table 29: E155 Proton results for g_1/F_1 and g_1.

	$\langle x \rangle$	$\langle Q^2 \rangle$	$g_1/F_1 \pm stat \pm syst$	$g_1 \pm stat \pm syst$
2.75°	0.015	1.22	0.048 ± 0.009 ± 0.004	0.358 ± 0.069 ± 0.035
	0.025	1.59	0.057 ± 0.008 ± 0.006	0.281 ± 0.040 ± 0.030
	0.035	2.05	0.070 ± 0.008 ± 0.007	0.266 ± 0.030 ± 0.027
	0.050	2.58	0.111 ± 0.009 ± 0.009	0.313 ± 0.024 ± 0.025
	0.080	3.24	0.155 ± 0.009 ± 0.013	0.287 ± 0.017 ± 0.023
	0.125	4.03	0.186 ± 0.012 ± 0.018	0.228 ± 0.015 ± 0.022
	0.175	4.62	0.273 ± 0.023 ± 0.023	0.240 ± 0.020 ± 0.020
	0.250	5.06	0.358 ± 0.023 ± 0.030	0.210 ± 0.014 ± 0.018
	0.350	5.51	0.424 ± 0.049 ± 0.039	0.150 ± 0.017 ± 0.014
	0.500	5.77	0.561 ± 0.058 ± 0.048	0.088 ± 0.009 ± 0.008
5.5°	0.050	4.01	0.222 ± 0.088 ± 0.009	0.690 ± 0.273 ± 0.031
	0.080	5.36	0.150 ± 0.011 ± 0.013	0.303 ± 0.022 ± 0.026
	0.125	7.17	0.209 ± 0.007 ± 0.018	0.274 ± 0.010 ± 0.023
	0.175	8.90	0.247 ± 0.012 ± 0.023	0.226 ± 0.011 ± 0.021
	0.250	10.64	0.353 ± 0.011 ± 0.030	0.206 ± 0.006 ± 0.018
	0.350	12.60	0.466 ± 0.020 ± 0.039	0.154 ± 0.007 ± 0.013
	0.500	14.02	0.561 ± 0.024 ± 0.048	0.072 ± 0.003 ± 0.006
	0.750	15.70	0.622 ± 0.091 ± 0.050	0.009 ± 0.001 ± 0.001
10.5°	0.125	10.99	0.307 ± 0.050 ± 0.018	0.415 ± 0.068 ± 0.026
	0.175	13.19	0.304 ± 0.022 ± 0.023	0.282 ± 0.020 ± 0.022
	0.250	17.21	0.396 ± 0.014 ± 0.030	0.229 ± 0.008 ± 0.018
	0.350	22.73	0.500 ± 0.025 ± 0.038	0.157 ± 0.008 ± 0.012
	0.500	26.86	0.507 ± 0.042 ± 0.048	0.058 ± 0.005 ± 0.006
	0.750	34.72	0.559 ± 0.405 ± 0.050	0.006 ± 0.004 ± 0.001

Table 30: E155 deuteron results for g_1/F_1 and g_1.

	$\langle x \rangle$	$\langle Q^2 \rangle$	$g_1/F_1 \pm stat \pm syst$	$g_1 \pm stat \pm syst$
2.75°	0.015	1.22	-0.033 ± 0.016 ± 0.001	-0.234 ± 0.115 ± 0.011
	0.025	1.59	0.011 ± 0.014 ± 0.001	0.051 ± 0.068 ± 0.006
	0.035	2.05	0.016 ± 0.014 ± 0.001	0.059 ± 0.052 ± 0.005
	0.050	2.57	0.030 ± 0.015 ± 0.002	0.082 ± 0.041 ± 0.004
	0.080	3.24	0.059 ± 0.016 ± 0.003	0.103 ± 0.028 ± 0.005
	0.125	4.03	0.079 ± 0.021 ± 0.005	0.089 ± 0.024 ± 0.006
	0.175	4.62	0.107 ± 0.041 ± 0.008	0.083 ± 0.032 ± 0.006
	0.250	5.06	0.192 ± 0.042 ± 0.012	0.096 ± 0.021 ± 0.006
	0.350	5.51	0.301 ± 0.098 ± 0.017	0.086 ± 0.028 ± 0.005
	0.500	5.77	0.389 ± 0.129 ± 0.024	0.047 ± 0.016 ± 0.003
5.5°	0.050	4.00	-0.266 ± 0.170 ± 0.002	-0.787 ± 0.504 ± 0.006
	0.080	5.37	0.006 ± 0.020 ± 0.003	0.012 ± 0.038 ± 0.006
	0.125	7.16	0.079 ± 0.014 ± 0.005	0.094 ± 0.016 ± 0.006
	0.175	8.90	0.099 ± 0.022 ± 0.008	0.080 ± 0.018 ± 0.006
	0.250	10.62	0.184 ± 0.020 ± 0.012	0.090 ± 0.010 ± 0.006
	0.350	12.59	0.305 ± 0.044 ± 0.017	0.081 ± 0.012 ± 0.005
	0.500	14.01	0.349 ± 0.057 ± 0.025	0.034 ± 0.006 ± 0.002
	0.750	15.73	0.576 ± 0.220 ± 0.029	0.006 ± 0.002 ± 0.001
10.5°	0.125	10.98	-0.020 ± 0.095 ± 0.006	-0.025 ± 0.117 ± 0.008
	0.175	13.19	0.157 ± 0.042 ± 0.008	0.127 ± 0.034 ± 0.007
	0.250	17.22	0.194 ± 0.027 ± 0.012	0.094 ± 0.013 ± 0.006
	0.350	22.65	0.309 ± 0.053 ± 0.017	0.077 ± 0.013 ± 0.005
	0.500	26.97	0.330 ± 0.092 ± 0.024	0.028 ± 0.008 ± 0.002
	0.750	34.79	0.428 ± 0.903 ± 0.028	0.003 ± 0.007 ± 0.001

has to be combined. For this the data at a fixed x were evolved to a common Q^2 and then averaged together. The evolution was performed using

$$g_1(x, Q^2_{\rm com}) = \tag{3}$$

$$g_1(x, Q^2_{\rm meas}) + \left[\frac{g_1(x, Q^2_{\rm com})}{F_1(x, Q^2_{\rm com})}\right]_{fit} \times F_1(x, Q^2_{\rm com}) - \left[\frac{g_1(x, Q^2_{\rm meas})}{F_1(x, Q^2_{\rm meas})}\right]_{fit} \times F_1(x, Q^2_{\rm meas}),$$

where "com" and "meas" are used for the common and measured values of Q^2 and fit indicate ratios which came from a phenomenological fit to g_1/F_1. The fit includes a term for the Q^2 dependence of g_1/F_1. By using this additive method, the Q^2 dependence is represented in the evolution of g_1/F_1. Data evolved to $Q^2 = 5\,{\rm GeV}^2$ are shown for the proton and deuteron in the top two plots of Figure 70. Also included in these plots are data from E143 [40], Hermes [162], and SMC [161], which show the E155 results to be in agreement with existing measurements. Note that the E155 data reach a low x with higher precision than previous experiments. SMC data still extend to the lowest x bins, but with large uncertainties. The E155 data presented in Figure 70 use fine binning, *i.e.*, 38 bins in the range $0.01 < x < 0.9$ evenly separated in natural log space. Even though this tends to de-emphasize the precision of the E155 data when they are plotted along with other experiments which utilize coarser binning, the size of the E155 error bars are still competitive with those of other experiments.

In the bottom plot of Figure 70, the E155 extracted neutron result is shown along with g_1^n from E154 [18] and Hermes [163]. As was discussed in Section 2.3,

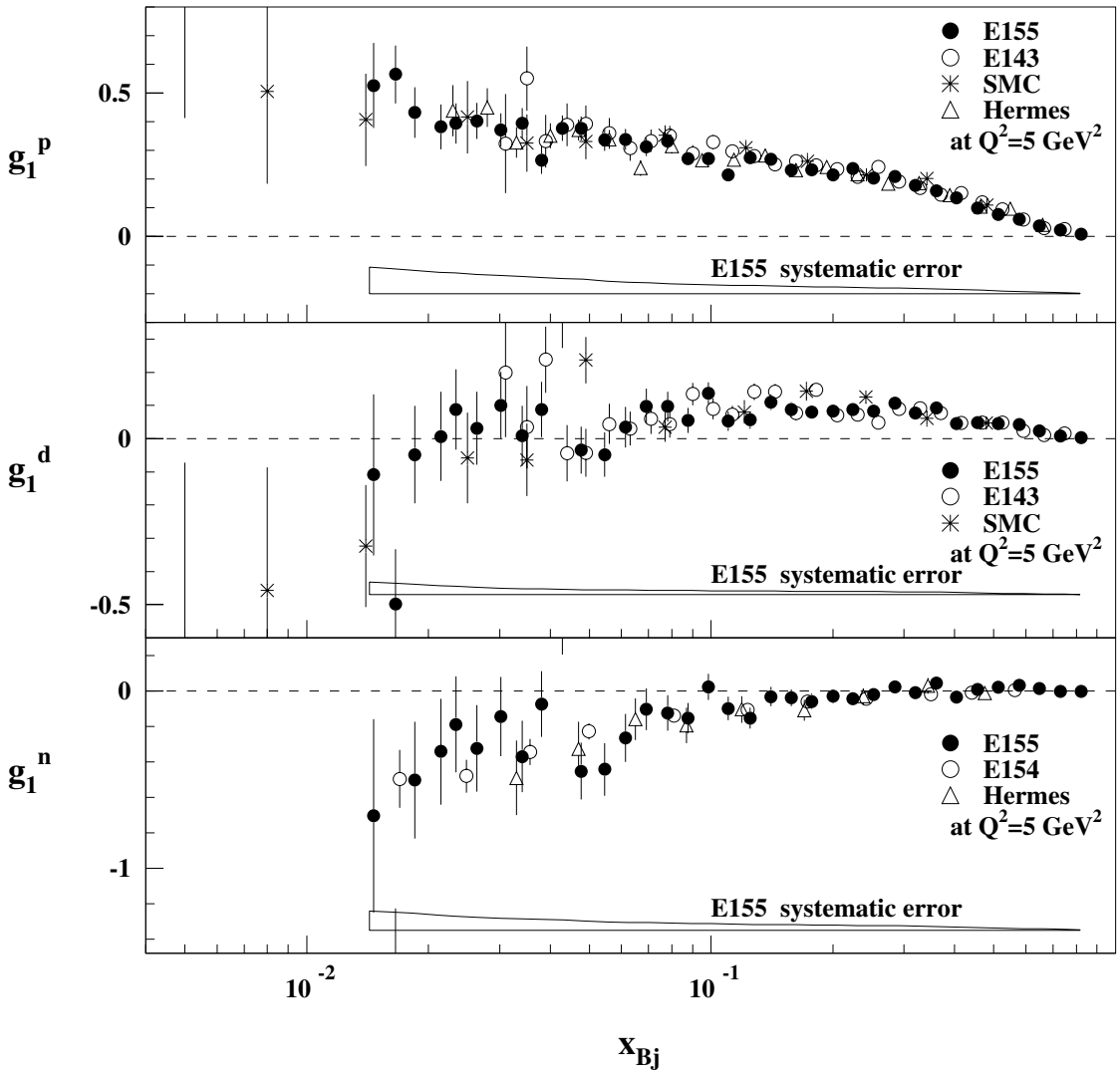

Figure 70: E155 g_1 data evolved to a common Q^2 of $5\,\mathrm{GeV}^2$ for proton, deuteron, and extracted neutron.

the neutron result was obtained using

$$g_1^n(x,Q^2) = \frac{2g_1^d(x,Q^2)}{1-1.5\omega_D} - g_1^p(x,Q^2), \tag{4}$$

where the deuteron was treated as an average of the proton and neutron. Again the results are consistent with existing data and add further support of the downward trend seen by E154 for g_1^n at low x.

One can obtain integrals in the measured regions for all three target nucleons. Since each of the spin structure functions vary slowly with x, a simple method to accomplish this is to perform a numeric integration in which a sum is taken over the point values multiplied by the width of their corresponding x bin. This leads to

$$\begin{aligned} & & \text{stat} & \quad \text{syst} \\ \int_{0.014}^{0.9} g_1^p(x,Q^2=5\,\mathrm{GeV}^2)dx &= 0.1186 \pm 0.0015 & \pm 0.0092, \\ \int_{0.014}^{0.9} g_1^d(x,Q^2=5\,\mathrm{GeV}^2)dx &= 0.0432 \pm 0.0026 & \pm 0.0028, \\ \int_{0.014}^{0.9} g_1^n(x,Q^2=5\,\mathrm{GeV}^2)dx &= -0.0236 \pm 0.0058 & \pm 0.0110. \end{aligned} \tag{5}$$

Because the statistical errors were assumed to be uncorrelated from bin to bin, they were added in quadrature with each term weighted by its corresponding bin width. Due to contributions from factors such as the beam and target polarizations, the total systematic error for different x-bins was assumed to be 100% correlated. They were combined linearly, again with each term multiplied by its bin width.

An alternative method of presenting the data is to plot xg_1 versus x. This is done for all three target types in Figure 71. An advantage to plotting this quantity is that it graphically shows the relative contributions from the different x regions to the measured integral. In the case of the proton and deuteron, a significant

fraction of the values listed in Equation 5 come from the mid to high x region. This area is considered to be sensitive to the valence quarks. Contributions to the neutron's measured integral tends to come from the mid to low regions of the x range accessible.

An estimation for the low x contribution to the integral was made using the published E154 NLO fit [156, 157]. The data set used as input to the procedure was the same as used in E154 except that it included updated SMC results. Neither E155 data nor Hermes proton results were used in the process. The low x contributions for the three target nucleons were found to be

$$\begin{array}{rcl} & & \text{stat} \quad \text{syst} \quad \text{th} \\ \int_0^{0.014} g_1^p(x, Q^2 = 5\,\text{GeV}^2)dx & = & -0.0058 \pm 0.004 \pm 0.002 \pm 0.009 \\ \int_0^{0.014} g_1^d(x, Q^2 = 5\,\text{GeV}^2)dx & = & -0.0135 \pm 0.004 \pm 0.002 \pm 0.005 \\ \int_0^{0.014} g_1^n(x, Q^2 = 5\,\text{GeV}^2)dx & = & -0.0235 \pm 0.004 \pm 0.002 \pm 0.005, \end{array} \tag{6}$$

where the uncertainties (from left to right) are statistical, systematic, and theoretical. In the past, the contribution to Γ_1 from the unmeasured high x region was estimated by fitting to the highest x bins of the measured $g_1(x)$ [135]. The form of the fit was $g_1(x) = A(1-x)^3$ where A was a fit parameter. This led to a very small contribution to the integral which was consistent with zero within uncertainties. For this analysis, the contribution from the unmeasured high x region was assumed to be negligible [1].

Note that the contribution to the first moment of the neutron from the un-

[1] Reference [156] shows the high x unmeasured region's contribution to be $\lesssim 0.0001$.

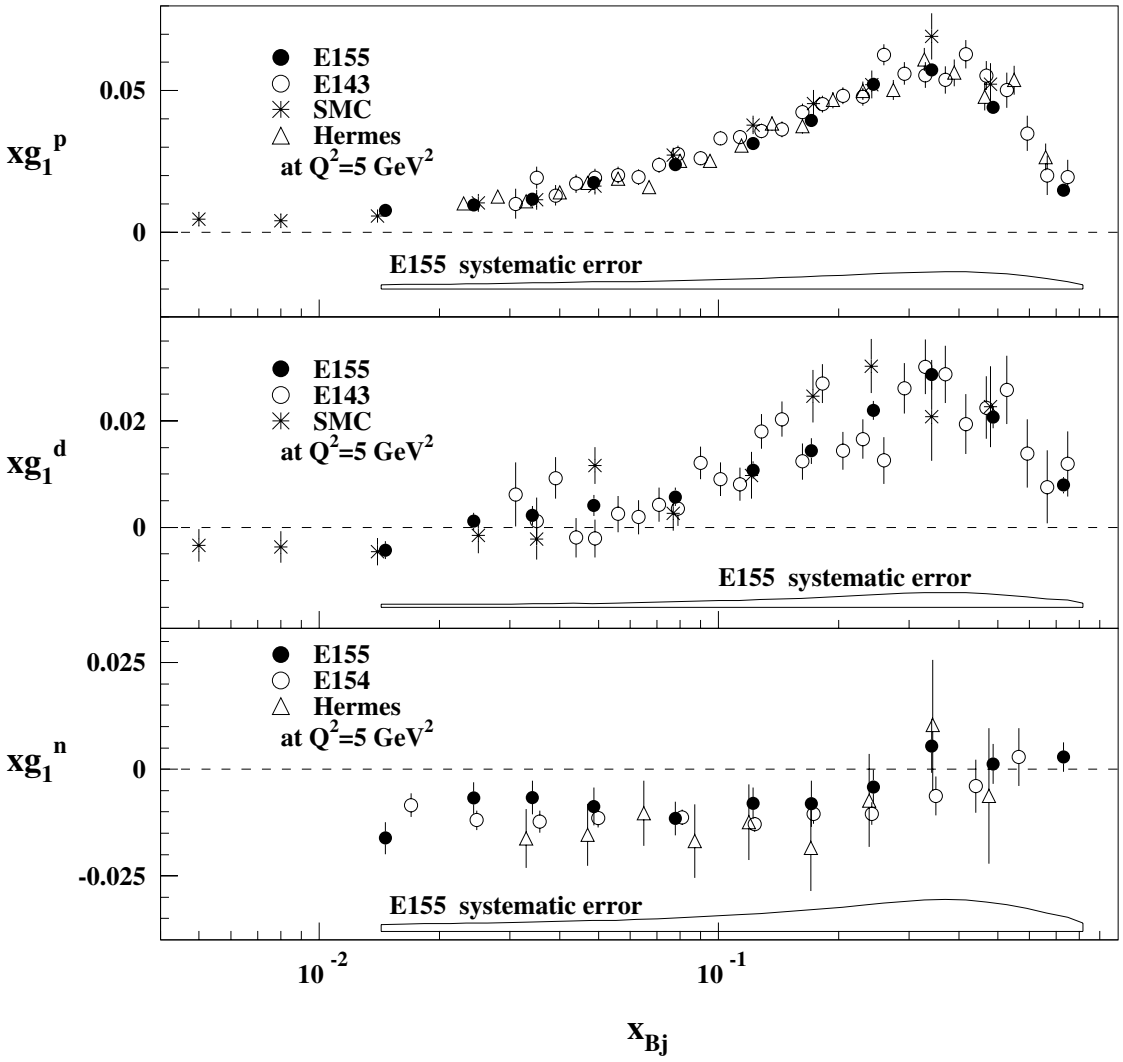

Figure 71: E155 xg_1 data evolved to common Q^2 of $5\,\mathrm{GeV}^2$ for proton, deuteron, and extracted neutron.

measured region is equal to that where the structure function has been measured. High quality low x data are needed to lessen the impact of the low x approximation.

Values for the total integral can be achieved by adding together the contributions from the low x and measured regions. Since the two pieces are independent, the statistical uncertainties can be combined in quadrature. The same holds true for the systematic contributions. For the first moments of g_1, where $\Gamma_1(Q^2 = 5\,\mathrm{GeV}^2) = \int_0^1 g_1(x, Q^2 = 5\,\mathrm{GeV}^2)dx$, one obtains

$$\begin{array}{lcl} & & \text{stat} \quad \text{syst} \quad \text{th} \\ \Gamma_1^p(Q^2 = 5\,\mathrm{GeV}^2) & = & 0.1128 \pm 0.0043 \pm 0.0094 \pm 0.009 \\ \Gamma_1^d(Q^2 = 5\,\mathrm{GeV}^2) & = & 0.0297 \pm 0.0048 \pm 0.0034 \pm 0.005 \\ \Gamma_1^n(Q^2 = 5\,\mathrm{GeV}^2) & = & -0.0471 \pm 0.0070 \pm 0.0112 \pm 0.005. \end{array} \tag{7}$$

5.2 Sum Rules

With values for the first moments of the proton, neutron, and deuteron in hand, comparisons can be made to some of the QCD sum rules. As was mentioned in Section 2.4, these have been fairly well tested and the E155 measurements were expected to confirm and improve the precision of existing results. The first of these to be looked at will be the Bjorken Sum Rule. This is obtained by taking the difference of the proton's and neutron's first moments which causes the singlet contribution to cancel. Including corrections up to $\mathcal{O}(\alpha_s^3)$ and for $Q^2 = 5\,\mathrm{GeV}^2$, the theoretical prediction for the Bjorken Sum Rule is

$$[\Gamma_1^p - \Gamma_1^n]_{Q^2=5\,\mathrm{GeV}^2} = \quad 0.182 \pm 0.005. \tag{8}$$

From the E155 measurements with the approximations described earlier, one gets for the Bjorken Sum Rule

$$[\Gamma_1^p - \Gamma_1^n]_{Q^2=5\,\mathrm{GeV}^2} = 0.1614 \pm 0.0135 \pm 0.0202 \pm 0.0210. \quad (9)$$

Combining the three uncertainties in quadrature gives

$$[\Gamma_1^p - \Gamma_1^n]_{Q^2=5\,\mathrm{GeV}^2} = 0.1614 \pm 0.0321. \quad (10)$$

This allows for an easy comparison and shows the predicted value and the E155 results to be in good agreement. The uncertainty on the measured value is equally dominated by the theoretical and systematic errors. The theoretical uncertainty comes from the approximation of the unmeasured region and can be reduced with data extending deeper into the low x region. A significant contribution to the systematic error is from known problems[2] and can be expected to be smaller in any possible future experiments.

The low x behavior of the NLO QCD fit for the proton and neutron are similar. As a result, they tend to cancel out the low x contribution to the sum rule making it more sensitive to the measured region. This is somewhat to be expected. Since to first order the Bjorken Sum Rule is the a_3 matrix element, which only depends on u and d quarks, it will be more sensitive to the valence quark helicities which are thought to dominate in the well measured mid to high x range.

For the Ellis-Jaffe Sum Rule, theoretical predictions with corrections to $\mathcal{O}(\alpha_s^3)$ [40] are presented in Table 31 along with the E155 measured values from

[2] For example, the metal target cups led to a large systematic error on the target polarization. See Section 3.2.3 for details.

Table 31: First moments of g_1 as predicted with the Ellis-Jaffe Sum Rule and measured by E155.

$\Gamma_1(Q^2 = 5\,\mathrm{GeV}^2)$	predicted (EJSR)	measured (E155)
proton	0.164 ± 0.005	0.113 ± 0.014
deuteron	0.068 ± 0.004	0.030 ± 0.008
neutron	-0.018 ± 0.004	-0.047 ± 0.014

Equation 7. As has been seen in the past [40], the measured and predicted values typically disagree by a few standard deviations. This difference has been attributed to the assumptions used in calculating the sum rule. In particular, the assumption of a null contribution of the strange quarks to the net helicity of the nucleon has been shown to be incorrect [42]. A point worth noting is that the largest number of standard deviations is in the case of the deuteron. Recall from Equation 41 that unlike Γ_1^p and Γ_1^n, the expression for Γ_1^d does not contain an a_3 term, which is the matrix element without a strange quark component. If Equations 41 and 40 are expressed in terms of $\Delta q(Q^2)$'s, then the net effect of this is that the coefficients of $\Delta u(Q^2)$ and $\Delta d(Q^2)$ are smaller for Γ_1^d, while the coefficient for $\Delta s(Q^2)$ stays the same. This makes the deuteron spin structure function more sensitive to the $\Delta s(Q^2) = 0$ assumption.

5.3 Systematic Errors

Contributions to the systematic error on the E155 g_1 measurements came from a variety of sources. Many already have been discussed at different points in the preceding sections. In this section the primary ones have been gathered to allow

Table 32: Approximate values (relative) for the different contributions to the systematic error on $A_{\parallel}$.

	P_b	P_t	f	e^+/π	C_1	C_2	RC
$^{15}NH_3$	2.5%	7%	2.5%	1%	0.5%	—	1.5%
^{6}LiD	2.5%	4%	2.9%	1%	2.7%	12.6%	4 %

a comparison between them. Those contributions associated with the E155 experimental design are listed first. Next are the uncertainties from quantities obtained from fits to other data. Such quantities were needed to transform the fully corrected $A_{\parallel}$ into g_1.

Sources in the first category mostly come from the different correction factors applied to the raw asymmetry. These factors were presented in Equations 3 and 4 on page 135. The contributions associated with the $A_{\perp}$ term were assumed to be negligible. For convenience, approximate values of the significant contributions from the $A_{\parallel}$ term are presented in Table 32 as relative uncertainties. A description of each term as well as a brief explanation of the contributions to the errors are given below.

P_b: A breakdown of the contributions to the beam polarization was presented on page 50. The dominant sources to this term came from a limited knowledge of the background shape (1.2%) and from an uncertainty in the measurement of the foil polarization (1.2%).

P_t: For the $^{15}NH_3$ data, the systematic uncertainty from the target polarization was the dominant contribution. This is shown graphically in Figure 72. The 7%

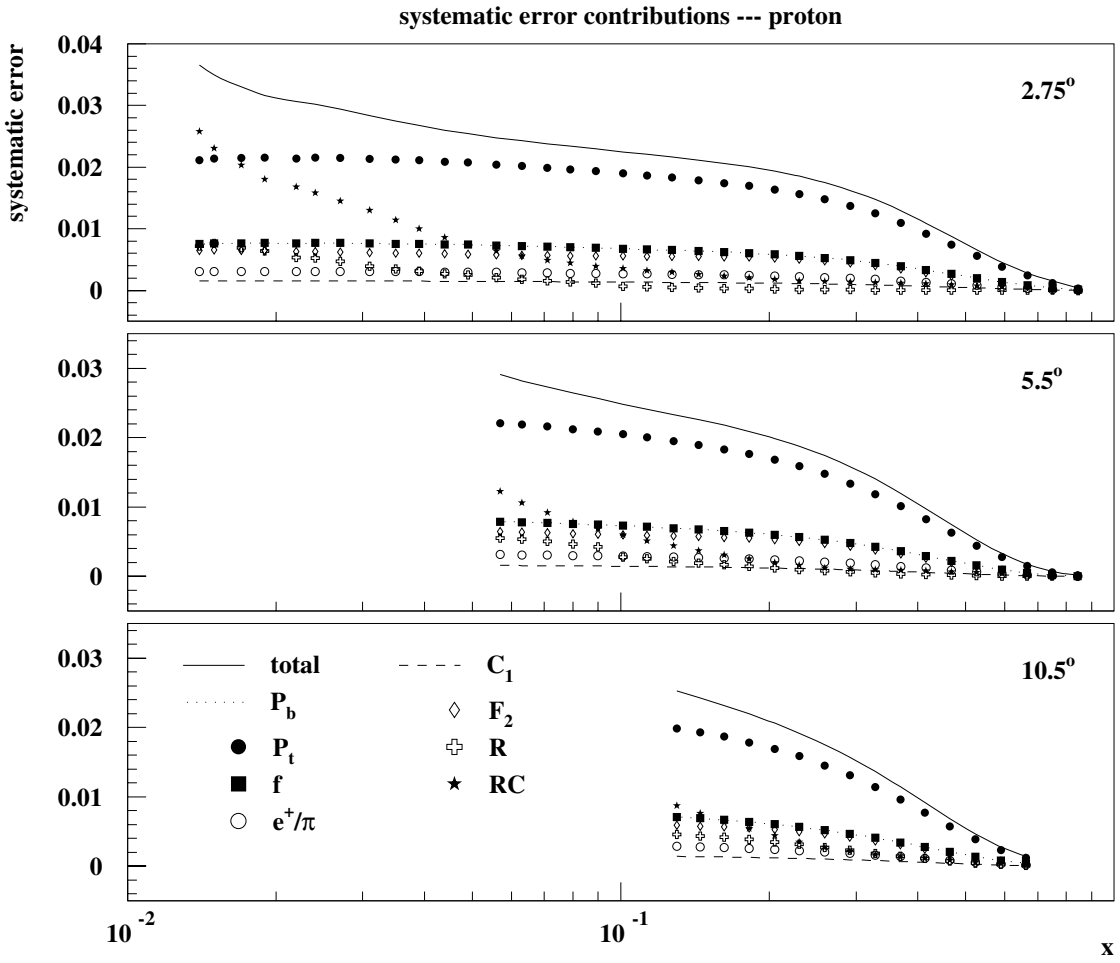

Figure 72: Individual contributions to the g_1^p systematic error. The solid line indicates the total error.

error was driven by corrections for non-linearities in the polarization measurement caused by metal target cups. Contributions to this error came from (1) scatter in the polarization in different anneal cycles and (2) from uncertainties in the TE calibrations and precision of the NMR [83].

The error on the deuteron polarization was estimated at 4%. Because of the lower NMR frequencies used to measure the deuteron polarization, it was not affected by the non-linearities that were seen with the $^{15}NH_3$ target. The un-

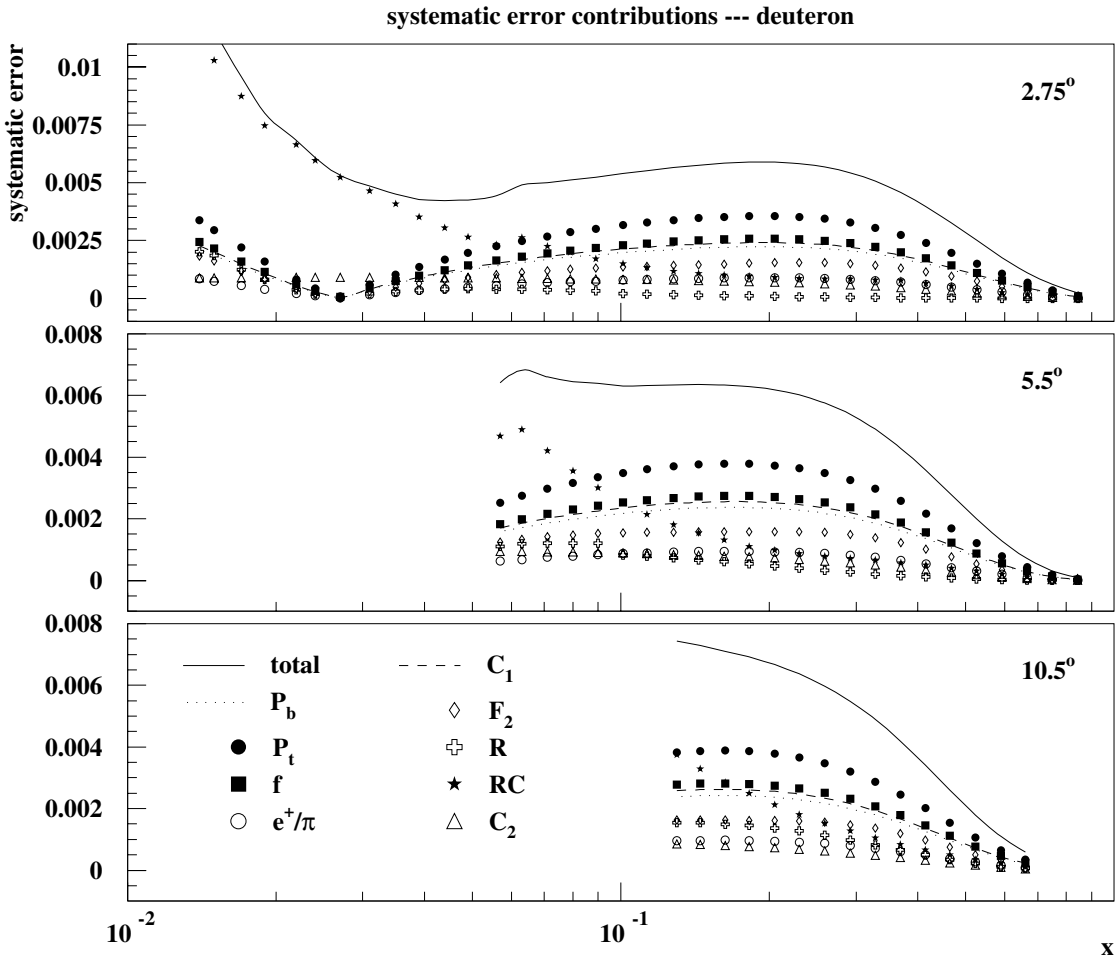

Figure 73: Individual contributions to the g_1^d systematic error. The solid line indicates the total error.

certainty on the deuteron polarization was the largest contribution in the mid x region. However, it was not much bigger than the next largest contributions, those from the dilution factor and the nuclear correction C_2. This can be seen graphically in Figure 73.

e^+/π: The contributions from the pair symmetric background/hadron background were typically around 1%.

C_1 and C_2: Only the C_1 nuclear correction factor was used for the $^{15}NH_3$ data and its relative error was estimated at 0.5%. This value came from the 20% relative uncertainty on the C_p in Equation 17 combined with a typical C_p of 0.024. The C_2 coefficient, which adjusts for the ^{14}N present in the $^{15}NH_3$ material, was assumed to be zero with no error.

For the ^6LiD target both terms were used. C_1 accounted for the effective deuteron in ^6Li and was approximately the same size as the uncertainty on the dilution factor. The C_2 coefficient is part of the correction for the residual protons in the deuterium. This was a small correction to $A_\parallel^d$, around 5%. The largest contribution to the C_2 uncertainty came from the residual proton polarization, which was small and difficult to measure. A breakdown of both the C_1 and C_2 components was presented on page 151.

f: The dilution factor error was primarily due to the uncertainty on the the packing fraction. Significant contributions also came from the uncertainty on the structure function F_2, which was used in obtaining the cross sections. The error for the ammonia target was estimated at 2.5%. For ^6LiD , 2.5% is the

error on the dilution factor and 1.5% is due to oxygen contamination of the material [131]. These two components were combined in quadrature to get the 2.9% value shown in Table 32.

RC: Contributions to the radiative corrections error came from uncertainties in the input models used for the calculation. The different categories of models were Deep Inelastic Scattering (x dependence and Q^2 dependence), unpolarized structure functions, g_2, Pauli Suppression Factor models, target models, elastic nucleon form factor, resonance asymmetry models, peaking approximation, and miscellaneous assumptions. Each category also contained additional models which were believed to be reasonable. Models in the final set were considered to be the optimum choice for their category. By substituting in each alternative model and by varying the parameters in accordance to their errors, the spread in the radiative correction calculation was determined for each category. The spread about the value obtained with the nominal model was used as the systematic error for that category. Each category was assumed to be independent and the different categories' errors were combined in quadrature.

For the integral over the measured region, the dominant contributions to the radiative corrections' systematic error came from the unpolarized structure function models and from the g_2 models. Radiative corrections were the largest uncertainty on g_1 at low x. More details of the procedure including specific

information about the models can be found in Reference [143].

F_2: The spin averaged structure function F_2 came from an NMC fit [154]. The uncertainty provided by the fit was used as the systematic error and was about 2% relative. An example of fit values using the 2.75° spectrometer's kinematics was shown in Figure 48 on page 152 along with its relative error.

R: The R1998 fit [11] was used for R. As with F_2, the uncertainty from the fit was used as its contribution to the systematic error. An example was shown on page 137. The relative uncertainty on R was around 20%.

The systematic error on g_1 and its different components are tabulated on page 219 (220) and plotted in Figure 72 (73) for the proton (deuteron). As was mentioned above, Figure 72 shows that for the proton measurement, the contribution from the target polarization dominates the systematic error. The remaining sources of uncertainties are roughly similar in size. For the deuteron measurement, the main sources of error are the radiative corrections at low x and the target polarization in the mid x range.

5.4 Q^2 Dependence

An understanding of how g_1 evolves with Q^2 is important for an accurate evaluation of Γ_1. This was a relevant factor in the results presented in Sections 5.1 and 5.2. Because of the three independent spectrometers and the wide Q^2 range accessible, the E155 data may provide insights into how g_1 varies with Q^2. One way of looking at this dependence is to compare g_1 to the well measured F_1. Tradi-

Table 33: Absolute systematic error contributions to g_1^p.

Systematic Errors Proton

	bin	$\langle x \rangle$	$\langle Q^2 \rangle$	g_1	σ_{stat}	σ_{syst}	P_b	P_t	f	e^+/π	C_1	C_2	F_2	R	RC
2.75°	1	0.015	1.22	0.3579	0.0693	0.0352	0.0079	0.0222	0.0079	0.0032	0.0016	0.0	0.0072	0.0107	0.0211
	2	0.025	1.59	0.2806	0.0395	0.0300	0.0076	0.0214	0.0076	0.0031	0.0015	0.0	0.0062	0.0047	0.0159
	3	0.035	2.05	0.2658	0.0302	0.0275	0.0076	0.0212	0.0076	0.0030	0.0015	0.0	0.0061	0.0035	0.0114
	4	0.050	2.58	0.3126	0.0240	0.0253	0.0074	0.0206	0.0074	0.0029	0.0015	0.0	0.0058	0.0023	0.0074
	5	0.080	3.24	0.2871	0.0170	0.0232	0.0069	0.0194	0.0069	0.0028	0.0014	0.0	0.0056	0.0012	0.0046
	6	0.125	4.03	0.2281	0.0150	0.0216	0.0065	0.0183	0.0065	0.0026	0.0013	0.0	0.0055	0.0005	0.0030
	7	0.175	4.62	0.2403	0.0204	0.0202	0.0061	0.0171	0.0061	0.0024	0.0012	0.0	0.0054	0.0003	0.0021
	8	0.250	5.06	0.2097	0.0136	0.0178	0.0054	0.0151	0.0054	0.0022	0.0011	0.0	0.0049	0.0001	0.0015
	9	0.350	5.51	0.1500	0.0175	0.0138	0.0042	0.0117	0.0042	0.0017	0.0008	0.0	0.0037	0.0001	0.0013
	10	0.500	5.77	0.0883	0.0092	0.0076	0.0023	0.0064	0.0023	0.0009	0.0005	0.0	0.0020	0.0000	0.0008
5.5°	4	0.050	4.01	0.6896	0.2734	0.0306	0.0082	0.0228	0.0082	0.0033	0.0016	0.0	0.0068	0.0081	0.0124
	5	0.080	5.36	0.3026	0.0224	0.0265	0.0076	0.0213	0.0076	0.0030	0.0015	0.0	0.0062	0.0048	0.0078
	6	0.125	7.17	0.2737	0.0098	0.0234	0.0070	0.0196	0.0070	0.0028	0.0014	0.0	0.0058	0.0021	0.0046
	7	0.175	8.90	0.2262	0.0107	0.0212	0.0064	0.0179	0.0064	0.0026	0.0013	0.0	0.0055	0.0015	0.0026
	8	0.250	10.64	0.2061	0.0062	0.0178	0.0054	0.0151	0.0054	0.0022	0.0011	0.0	0.0049	0.0008	0.0013
	9	0.350	12.60	0.1543	0.0068	0.0129	0.0039	0.0110	0.0039	0.0016	0.0008	0.0	0.0035	0.0004	0.0010
	10	0.500	14.02	0.0724	0.0030	0.0062	0.0019	0.0053	0.0019	0.0008	0.0004	0.0	0.0016	0.0001	0.0007
	11	0.750	15.70	0.0091	0.0013	0.0007	0.0002	0.0006	0.0002	0.0001	0.0000	0.0	0.0002	0.0000	0.0001
10.5°	6	0.125	10.99	0.4151	0.0684	0.0260	0.0072	0.0203	0.0072	0.0029	0.0014	0.0	0.0060	0.0063	0.0086
	7	0.175	13.19	0.2824	0.0200	0.0224	0.0065	0.0181	0.0065	0.0026	0.0013	0.0	0.0056	0.0039	0.0057
	8	0.250	17.21	0.2293	0.0079	0.0180	0.0053	0.0150	0.0053	0.0021	0.0011	0.0	0.0048	0.0026	0.0029
	9	0.350	22.73	0.1572	0.0080	0.0125	0.0037	0.0104	0.0037	0.0015	0.0007	0.0	0.0033	0.0016	0.0015
	10	0.500	26.86	0.0579	0.0048	0.0056	0.0017	0.0047	0.0017	0.0007	0.0003	0.0	0.0015	0.0005	0.0008
	11	0.750	34.72	0.0057	0.0041	0.0005	0.0002	0.0004	0.0002	0.0001	0.0000	0.0	0.0002	0.0000	0.0001

Notes:

Table headings are described in the text. The C_2 nuclear correction was assumed to be negligible for the proton target but has an entry here for consistency between this table and that of the deuteron.

Table 34: Absolute systematic error contributions to g_1^d.

Systematic Errors Deuteron

	bin	$\langle x \rangle$	$\langle Q^2 \rangle$	g_1	σ_{stat}	σ_{syst}	P_b	P_t	f	e^+/π	C_1	C_2	F_2	R	RC
2.75°	1	0.015	1.22	-0.2367	0.1145	0.0111	0.0019	0.0031	0.0023	0.0008	0.0021	0.0009	0.0018	0.0026	0.0094
	2	0.025	1.59	0.0507	0.0681	0.0061	0.0002	0.0002	0.0002	0.0001	0.0002	0.0009	0.0001	0.0001	0.0060
	3	0.035	2.05	0.0590	0.0520	0.0045	0.0006	0.0010	0.0007	0.0003	0.0007	0.0009	0.0005	0.0003	0.0041
	4	0.050	2.57	0.0815	0.0406	0.0043	0.0013	0.0020	0.0015	0.0005	0.0014	0.0009	0.0009	0.0004	0.0027
	5	0.080	3.24	0.1031	0.0278	0.0051	0.0018	0.0028	0.0021	0.0007	0.0019	0.0008	0.0012	0.0003	0.0021
	6	0.125	4.03	0.0892	0.0238	0.0056	0.0021	0.0033	0.0024	0.0008	0.0023	0.0008	0.0014	0.0002	0.0012
	7	0.175	4.62	0.0833	0.0320	0.0059	0.0022	0.0036	0.0026	0.0009	0.0024	0.0007	0.0015	0.0001	0.0010
	8	0.250	5.06	0.0957	0.0207	0.0057	0.0022	0.0035	0.0025	0.0009	0.0023	0.0007	0.0015	0.0001	0.0009
	9	0.350	5.51	0.0861	0.0280	0.0048	0.0018	0.0029	0.0021	0.0007	0.0020	0.0005	0.0014	0.0000	0.0008
	10	0.500	5.77	0.0470	0.0155	0.0028	0.0011	0.0017	0.0012	0.0004	0.0012	0.0003	0.0008	0.0000	0.0005
5.5°	4	0.050	4.00	-0.7862	0.5036	0.0063	0.0014	0.0023	0.0016	0.0006	0.0015	0.0010	0.0012	0.0014	0.0048
	5	0.080	5.37	0.0117	0.0379	0.0065	0.0020	0.0032	0.0023	0.0008	0.0021	0.0009	0.0015	0.0013	0.0035
	6	0.125	7.16	0.0939	0.0163	0.0063	0.0023	0.0037	0.0027	0.0009	0.0025	0.0008	0.0016	0.0007	0.0019
	7	0.175	8.90	0.0798	0.0175	0.0063	0.0024	0.0038	0.0027	0.0009	0.0026	0.0008	0.0016	0.0005	0.0012
	8	0.250	10.62	0.0903	0.0099	0.0059	0.0022	0.0035	0.0026	0.0009	0.0024	0.0007	0.0016	0.0003	0.0008
	9	0.350	12.59	0.0808	0.0115	0.0046	0.0017	0.0028	0.0020	0.0007	0.0019	0.0005	0.0013	0.0002	0.0006
	10	0.500	14.01	0.0341	0.0055	0.0024	0.0009	0.0014	0.0010	0.0004	0.0010	0.0002	0.0006	0.0001	0.0004
	11	0.750	15.73	0.0062	0.0023	0.0003	0.0001	0.0002	0.0001	0.0000	0.0001	0.0000	0.0001	0.0000	0.0001
10.5°	6	0.125	10.98	-0.0243	0.1173	0.0076	0.0024	0.0038	0.0028	0.0010	0.0026	0.0009	0.0017	0.0021	0.0037
	7	0.175	13.19	0.1275	0.0340	0.0070	0.0024	0.0039	0.0028	0.0010	0.0026	0.0008	0.0016	0.0015	0.0026
	8	0.250	17.22	0.0937	0.0130	0.0061	0.0022	0.0035	0.0026	0.0009	0.0024	0.0006	0.0016	0.0011	0.0017
	9	0.350	22.65	0.0774	0.0133	0.0045	0.0017	0.0027	0.0019	0.0007	0.0018	0.0004	0.0013	0.0007	0.0010
	10	0.500	26.97	0.0284	0.0079	0.0021	0.0008	0.0013	0.0009	0.0003	0.0009	0.0002	0.0006	0.0002	0.0004
	11	0.750	34.79	0.0032	0.0067	0.0002	0.0001	0.0001	0.0001	0.0000	0.0001	0.0000	0.0001	0.0000	0.0000

Notes:

Table headings are described in the text.

tionally the ratio g_1/F_1 has been considered as independent of Q^2. This treatment stemmed from the similarity of the DGLAP equations for the spin dependent and spin independent structure functions [159]. This assumption is consistent with the data.

In the E155 analysis, efforts were made to help improve upon the current understanding of the Q^2 dependence of g_1. Using the code developed for the E155 radiative corrections analysis, phenomenological fits were made [143, 148] on the ratio g_1/F_1 which took advantage of a global data set[3]. There is a two-fold advantage to using this ratio instead of with g_1 alone. First, g_1/F_1 is closer to the asymmetries that were measured in E155. Second, similarities between the two structure functions may cancel allowing differences to be more pronounced in the ratio. The fits were performed on proton, neutron, and deuteron data simultaneously, where the form of the fit was

$$\frac{g_1(x,Q^2)}{F_1(x,Q^2)} = x^{\alpha}(a + bx + cx^2)\left(1 + \frac{d}{Q^2}\right) \tag{11}$$

for the proton and neutron. In the case of the deuteron, Equations 11 and 4 were combined to give

$$\frac{g_1^d(x,Q^2)}{F_1^d(x,Q^2)} = \frac{1 - 1.5\omega_D}{2}\left(\frac{g_1^p(x,Q^2)}{F_1^p(x,Q^2)}\frac{F_1^p(x,Q^2)}{F_1^d(x,Q^2)} + \frac{g_1^n(x,Q^2)}{F_1^n(x,Q^2)}\frac{F_1^n(x,Q^2)}{F_1^d(x,Q^2)}\right). \tag{12}$$

In addition, fits were performed on the related quantity A_1 and different forms of the Q^2 term were tried[4]. The effect of including a Q^2 term of some sort compared

[3] This set included results from SLAC experiments E155, E154 [18], E143 [40], E142 [38], E130 [33], E80 [160] as well as data from EMC [16], SMC [161], and Hermes [162, 163].

[4] For example, a $\log Q^2$ term was also tried [143].

Table 35: Parameters from the phenomenological fit [148].

	proton	neutron
α	0.700 $\pm$ 0.082	-0.34 $\pm$ 0.52
a	0.82 $\pm$ 0.23	-0.013 $\pm$ 0.038
b	1.01 $\pm$ 0.64	-0.33 $\pm$ 0.15
c	-1.49 $\pm$ 0.60	0.76 $\pm$ 0.59
d	-0.037 $\pm$ 0.061	0.13 $\pm$ 0.46

to ignoring the dependence was that having the Q^2 term improved the quality of the fits. A lower $\chi^2/d.f.$ was obtained with the inclusion of a Q^2 term. More details on the variations and procedure used for the phenomenological fits can be found in Reference [143].

The results of the fits which used Equation 11 are presented in Table 35 and plotted along with data as a function of Q^2 in Figures 74 (proton) and 75 (deuteron). E155 measurements are shown as solid points and the data from the three spectrometers have not been combined. Bins with three E155 points correspond to regions where the spectrometers' coverage overlap in x. Each sub-plot is for a different x bin [5], where world binning (or coarse binning) has been used. The phenomenological fits represent the data well and as a function of Q^2 are quite flat. Also, the plots show how the inclusion of the E155 data nicely complement those of E143 and SMC. E155's efforts contributed a considerable amount of information useful in studying the Q^2 dependence of g_1. However, as seen by the d parameter in Table 35, which is the coefficient of the Q^2 term in Equation 11, the Q^2 dependence as parameterized

[5] See Table 36.

Table 36: World bins with the range of x values contained within each.

bin number	low x	center (bin name)	high x
0	0.006	0.008	0.010
1	0.010	0.015	0.020
2	0.020	0.025	0.030
3	0.030	0.035	0.040
4	0.040	0.05	0.060
5	0.060	0.08	0.100
6	0.100	0.125	0.150
7	0.150	0.175	0.200
8	0.200	0.25	0.300
9	0.300	0.35	0.400
10	0.400	0.5	0.600
11	0.600	0.75	0.900

here is small and consistent with zero. This holds true for both the proton and neutron.

Figures 74 and 75 also show the results of the E155 NLO QCD fit. For the mid to high x bins the NLO QCD fits tend to increase slightly with Q^2. In the lowest x bins, the slope is opposite for proton and deuteron targets. However, there are very few data points in those bins indicating the need for more high quality low x data.

5.5 NLO QCD Analysis Results

In Section 2.3 an outline was given for an NLO QCD analysis of the spin structure functions. In this section, selected details and results will be presented for the NLO QCD analysis performed on the final E155 data set. A more in depth discussion of the procedure can be found in [71] and references therein. However,

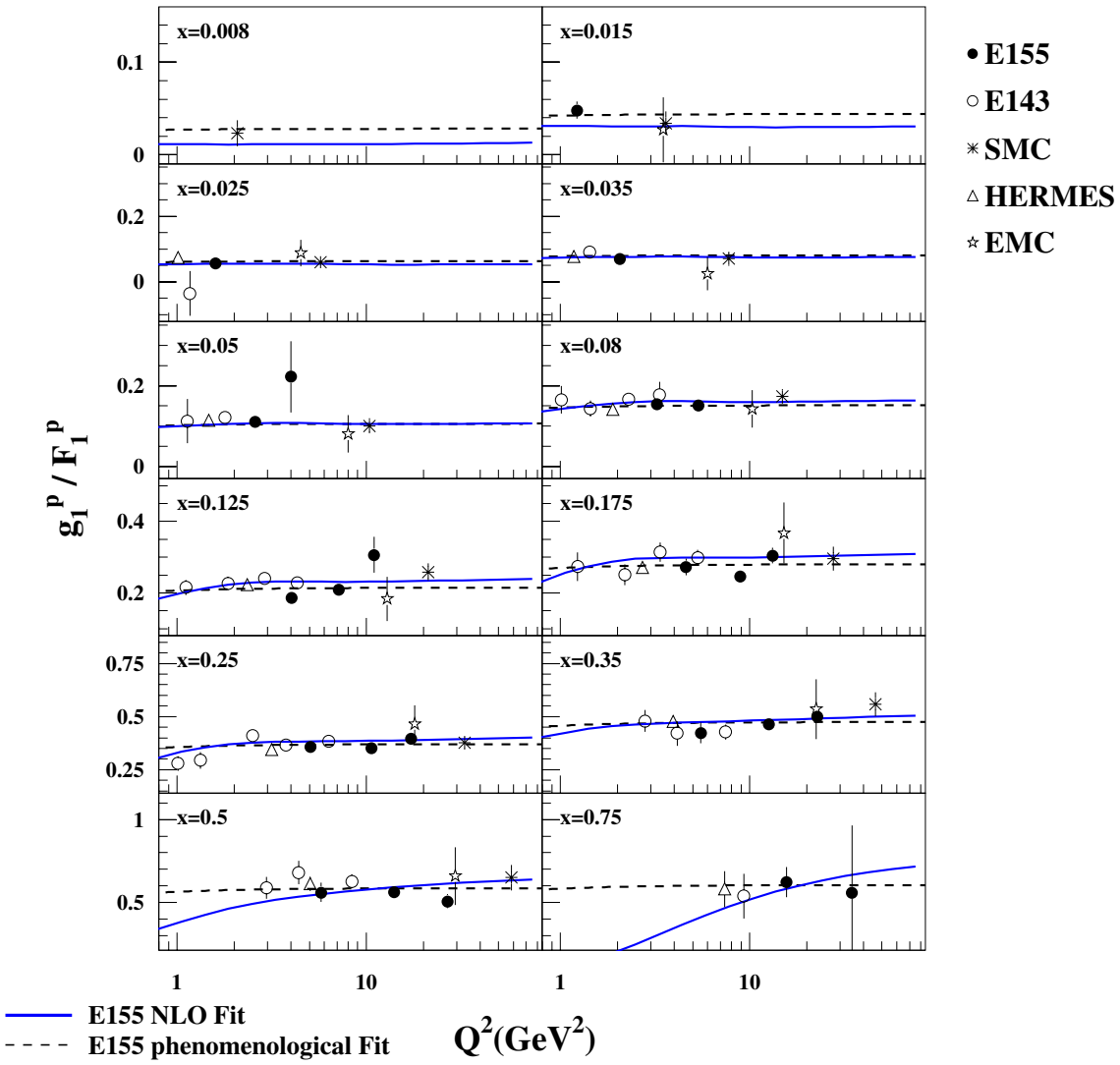

Figure 74: Proton data for g_1/F_1 as a function of Q^2. Data are plotted with statistical uncertainties.

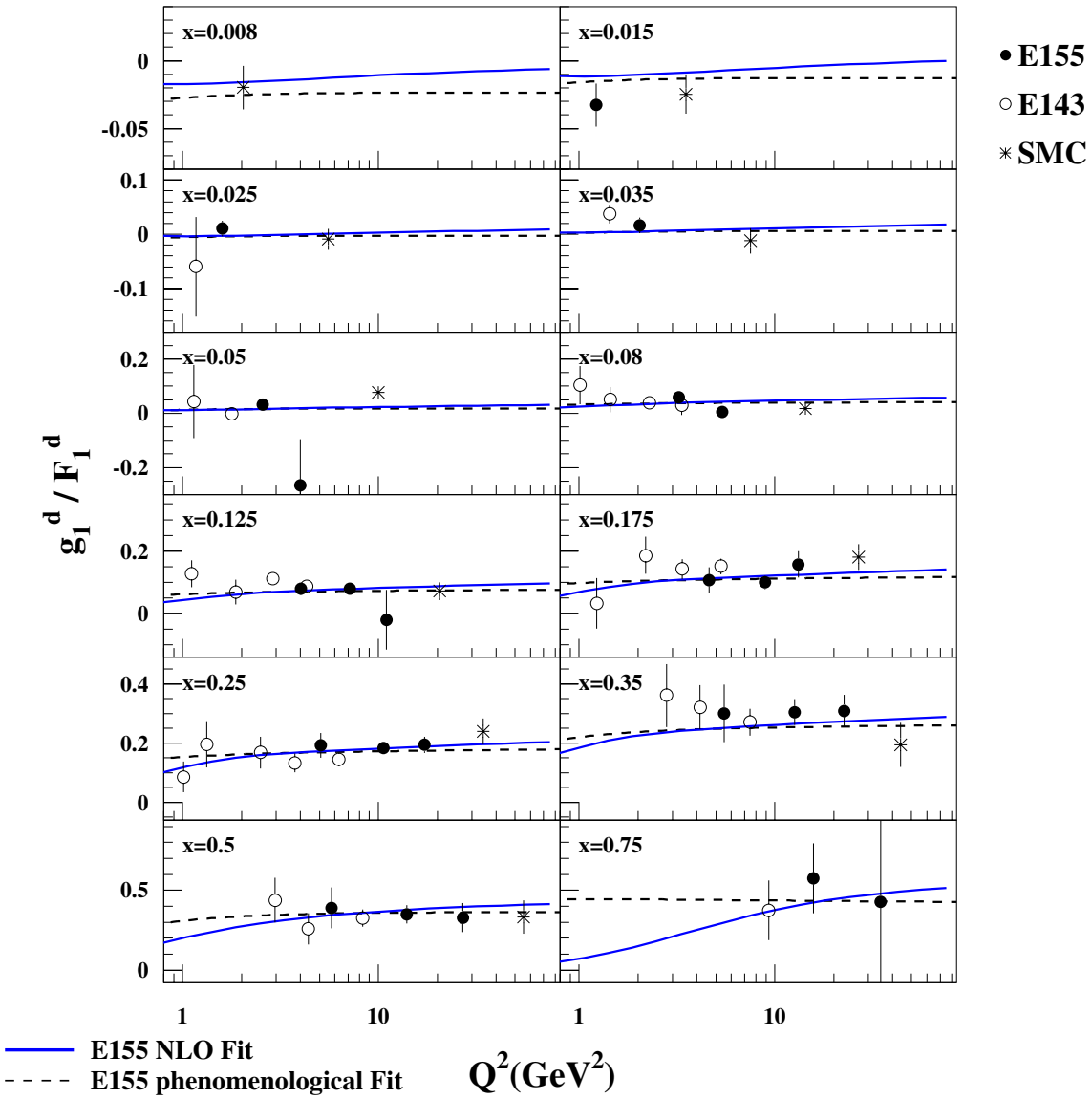

Figure 75: Deuteron data for g_1/F_1 as a function of Q^2. Data are plotted with statistical uncertainties.

the results reported in [71] differ from those shown here for several reasons. The primary ones are that more runs (*i.e.,* more data) have been included and the final proton polarization correction [84] has been used for these results.

As mentioned in Section 2.3, the starting point of the analysis was a parameterization of the polarized PDFs. This took the form

$$\Delta f(x, Q_0^2) = A_f x^{\alpha_f} f(x, Q_0^2), \tag{13}$$

where $f(x, Q_0^2)$ are the unpolarized PDFs taken from [164]. The polarized PDFs were divided into four groups: two for valence quarks, one for the gluons, and one for the sea quarks. The last group was parameterized as $\Delta\bar{Q} = \frac{1}{2}(\Delta\bar{u} + \Delta\bar{d}) + \frac{1}{5}\Delta\bar{s}$ and the unpolarized sea quarks were assumed to be flavor symmetric. The fit was performed on the world data set[6]. The fits were performed in the $\overline{MS}$ factorization scheme and used $\alpha_s(M_Z^2) = 0.114$ which corresponds to $\alpha_s(5\,\mathrm{GeV}^2) = 0.26$. An additional analysis was made using the AB scheme, but the fits did not converge. The α parameters were required to be positive and an upper limit of 2 also was imposed on α_Q and α_g. Parameters obtained from the fit for polarized PDFs are presented in Table 37. Results of the fits for g_1 for the proton, deuteron, and neutron are plotted along with data in Figure 76. The fits well represent the data. For all three target types, the fits tend toward negative values in the unmeasured low x region. Also included in each sub-plot of Figure 76 is a g_1 curve from the E155 phenomenological fits. In the measured region the NLO QCD and phenomenological fits agree

[6] This included data from this experiment (p and d) as well as E154 (n) [157], E143 (p and d) [40], E142 (n) [38], Hermes (p and n) [162, 163], SMC (p and d) [161], and EMC (p) [16]

Table 37: Coefficients for polarized parton distribution fit to world data on $g_1(x, Q^2)$.

	Value	Stat.	Syst.
A_u	0.95	$^{+0.04}_{-0.01}$	$^{+0.05}_{-0.04}$
A_d	-0.42	$^{+0.02}_{-0.04}$	$^{+0.02}_{-0.04}$
A_Q	0.01	$^{+0.47}_{-0.01}$	$^{+0.50}_{-0.12}$
A_g	0.50	$^{+0.37}_{-0.54}$	$^{+0.48}_{-1.13}$
α_u	0.57	$^{+0.05}_{-0.01}$	$^{+0.04}_{-0.02}$
α_d	0.00	$^{+0.00}_{-0.00}$	$^{+0.01}_{-0.00}$
α_Q	1.00	$^{+0.24}_{-0.22}$	$^{+0.43}_{-0.29}$
α_g	0.02	$^{+0.66}_{-0.02}$	$^{+0.78}_{-0.02}$

Table 38: Moments of the polarized parton distributions at Q^2=5 GeV^2.

	value	stat.	syst.
Δu_V	$0.71 \pm 0.02 \pm 0.04$		
Δd_V	$-0.45 \pm 0.03 \pm 0.03$		
$\Delta\overline{Q}$	$-0.01 \pm 0.01 \pm 0.02$		
ΔG	$1.62 \pm 0.78 \pm 1.13$		

well. First moments, evolved to a $Q^2 = 5\,\mathrm{GeV}^2$, are given in Table 38. While the contribution to the nucleon spin from the valence quarks is well determined, that from the sea and gluons are not.

Additional quantities are determined as a result of the NLO QCD fitting procedure such as singlet and non-singlet matrix elements and the first moments of g_1 for all three target types. These results are summarized in Table 39 and will be discussed below.

As was done earlier with the "E155 only" measurements, these can be compared to predictions or to measurements obtained through other means. To begin, the non-singlet matrix elements a_3 and a_8 can be compared to those values presented

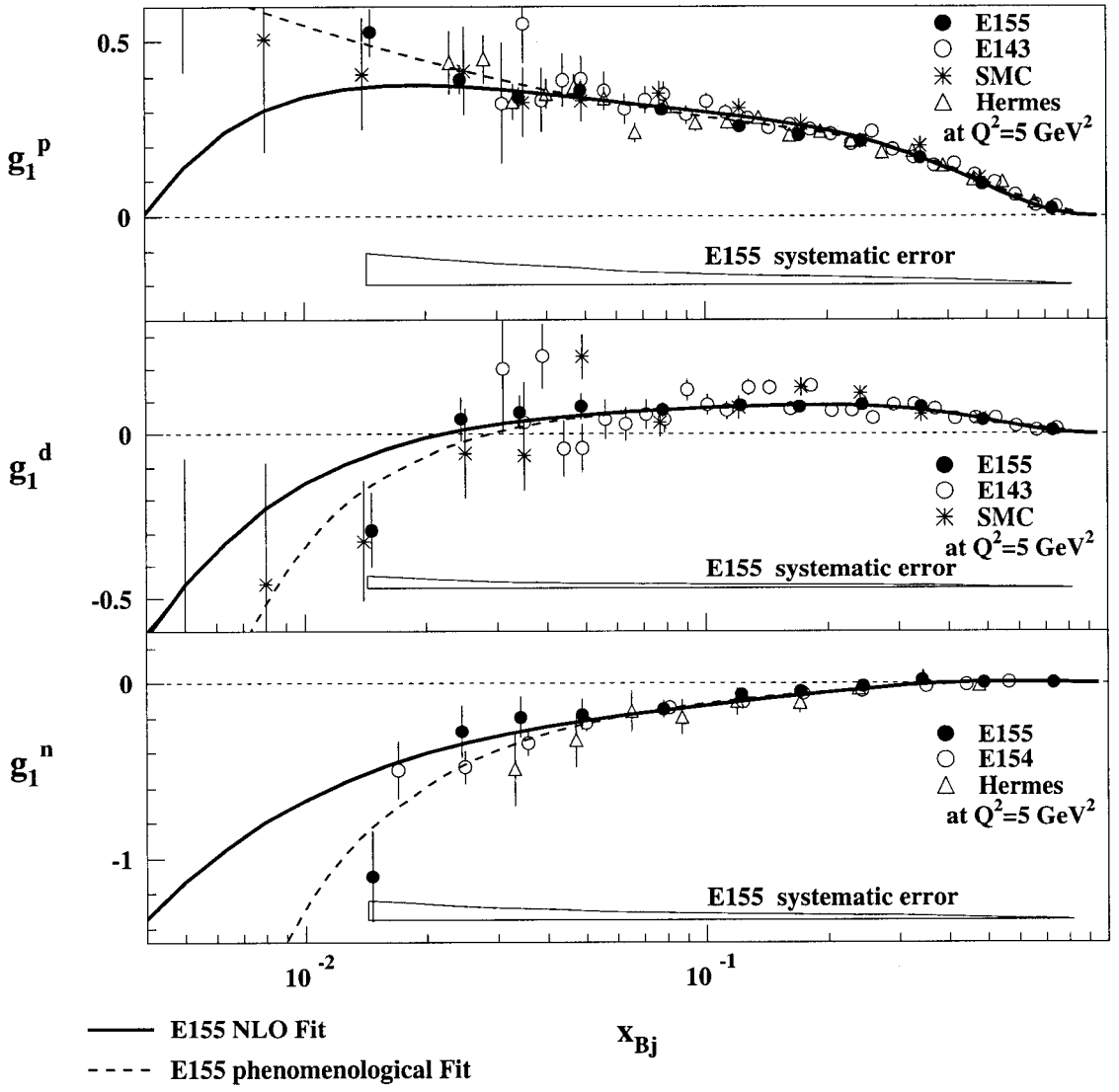

Figure 76: E155 g_1 data evolved to a common Q^2 of 5 GeV^2 for proton, deuteron, and extracted neutron. Data shown are the same as in Figure 70 except that the E155 results use world binning. Curves are from the E155 NLO QCD and phenomenological fits to world data.

Table 39: Fit results at Q^2=5 GeV^2.

	value	stat.	syst.
a_3	$1.153 \pm 0.022 \pm 0.047$		
a_8	$0.263 \pm 0.040 \pm 0.054$		
$\Delta\Sigma$	$0.229 \pm 0.041 \pm 0.057$		
Γ_1^p	$0.118 \pm 0.004 \pm 0.007$		
Γ_1^n	$-0.058 \pm 0.005 \pm 0.008$		
Γ_1^d	$0.028 \pm 0.004 \pm 0.005$		
Γ_1^{p-n}	$0.176 \pm 0.003 \pm 0.007$		

in Section 2.3 which were obtained from neutron and hyperon β-decay. These give

$$\begin{array}{lll} & \beta\text{-decay} & \text{E155 NLO} \\ a_3: & 1.2670 \pm 0.0035 & 1.153 \pm 0.052 \\ a_8: & 0.584 \ \pm 0.032 & 0.263 \pm 0.067 \end{array} \tag{14}$$

which show poor agreement between values obtained through NLO QCD analysis and β-decay. The discrepancies between the results are due to known differences. Similar values for the non-singlet matrix elements were obtained in the E154 NLO QCD analysis [157], which was the basis for the procedure used in E155. Something not done for the E155 analysis but performed for E154 was an estimation of the theoretical uncertainties for the various quantities. In E154 the theoretical uncertainty on the a_8 matrix element was $^{+0.23}_{-0.01}$ [157]. Adopting these uncertainties, which is reasonable due to the overlap between the two analyses, improves the agreement between the two values of a_8. The $\approx 2\sigma$ disagreement on the a_3 matrix element is because the calculation is done at NLO and does not include higher order corrections to the Bjorken Sum Rule. These corrections were not included so as to remain

consistent with the NLO QCD approximation.

With the NLO QCD analysis, the Bjorken Sum Rule is found to be

$$[\Gamma_1^p - \Gamma_1^n]_{Q^2=5\,\mathrm{GeV}^2} = 0.176 \pm 0.003 \pm 0.007 \tag{15}$$

which is in very good agreement with the theoretical prediction of 0.182 ± 0.005. The singlet matrix element, which in the $\overline{MS}$ scheme represents the quark contribution to the helicity of the nucleon, was determined to be

$$\Delta\Sigma = 0.229 \pm 0.041 \pm 0.057. \tag{16}$$

This is much less than the Ellis-Jaffe prediction [31] of 0.58 but is in good agreement with other measurements of this quantity made during the past decade or so. The quarks carry around 20% of the total spin of the nucleon. In contrast to the quark contribution, the spin from the gluons is still an open question. As was shown in Table 38, the gluon contribution looks positive and the current estimates suggest that it is large enough to account for the remaining spin. However, the large uncertainties also allow for a ΔG of zero. In the case of the angular momentum sum rule, this means that few constraints can be placed on the orbital angular momentum term, which will compensate or offset ΔG contribution to make up the remaining 80%.

CHAPTER 6

SUMMARY AND CONCLUSIONS

High precision data for the spin structure functions of the proton and deuteron have been presented. These data are a significant contribution to the g_1 world data set and to our understanding of the quarks' role in the net spin of the nucleon. At the present time this contribution is reasonably well determined with $\Delta\Sigma(Q^2 = 5\,\mathrm{GeV}^2) = 0.23 \pm 0.07$. Future efforts will begin to focus on other components of the nucleon spin and in particular, the gluon contribution.

Concerning the Q^2 dependence of g_1, E155 data filled in gaps that existed between the results of SMC at high Q^2 and E143 at low Q^2. A strong point of the E155 contribution was the three independent spectrometers which covered a wide range of Q^2 values. Because they sometimes overlapped in x, this enabled three measurements of different Q^2 values in one x-bin thus minimizing the systematic uncertainties common to all three spectrometers.

Our deuterium data were collected on a solid, polarized ^{6}LiD target, a first for this type of experiment. The target maintained a high polarization for an extended period of time requiring less down time for polarization driven target maintenance activities such as anneals. This opens up yet another avenue for testing and corrob-

orating our understanding of the spin structure of the nucleon.

Also presented were asymmetries constructed from the E155 inclusive pions and inclusive hadron data set. These asymmetries already have proven themselves useful. They have led to a fine tuning of a proposed model for inclusive, photoproduced pions in the form of the inclusion of soft processes. This addition improved the agreement between data and model.

There is still much to learn about the mechanisms underlying the spin of the nucleon. For example, the contributions to the first moments Γ_1 from the unmeasured low x region are significant using the current best estimates. However, these are only speculation and knowledge of the true behavior will best be gained through measurements. The low x behavior as described by the NLO QCD fits may be supported or new surprises may await. An improved precision on Γ_1 also will enable an even more rigorous test of the sum rules presented here. At the present time no experiments are approved to explore this region of kinematics. However, one could expect an effort to be included in the plans for a polarized ep collider [167] or as part of a fixed target program on some flavor of the Next Linear Collider.

The gluon contribution to the nucleon spin is still a poorly measured quantity, but this will change in upcoming years. Hermes at DESY, which is still collecting data, will be able to provide some information on ΔG through their semi-inclusive measurements [165]. The approved CERN experiment COMPASS [46] will make a measurement through photon-gluon fusion ($\vec{\gamma}^* \vec{g} \rightarrow c\bar{c}$) . Also RHIC at Brookhaven [166] is expected to make a precise determination of ΔG in polarized proton-proton

collisions using either direct photon production ($\vec{g}\vec{q} \rightarrow \gamma q$) or heavy quark production ($\vec{g}\vec{g} \rightarrow Q\bar{Q}$).

Much has been accomplished since the "spin crisis" of the late 1980's. As is often the case, progress is slow and does not always follow a straight path. The next wave of experiments have their challenges laid out before them. The spin physics community will be treated to its share of triumphs and surprises in the years to come.

APPENDIX A

E155 COLLABORATION

P. L. Anthony,[16] R. G. Arnold,[1,12] T. Averett,[5,◇] H. R. Band,[21]

M. C. Berisso,[12] H. Borel,[7] P. E. Bosted,[1,12] S. L. Bültmann,[19] M. Buenerd,[16,†]

T. Chupp,[13] S. Churchwell,[12,‡] G. R. Court,[10] D. Crabb,[19] D. Day,[19] P. Decowski,[15]

P. DePietro,[1] R. Erbacher,[16,17] R. Erickson,[16] A. Feltham,[19] H. Fonvieille,[3] E. Frlez,[19]

R. Gearhart,[16] V. Ghazikhanian,[6] J. Gomez,[18] K. A. Griffioen,[20] C. Harris,[19]

M. A. Houlden,[10] E. W. Hughes,[5] C. E. Hyde-Wright,[14] G. Igo,[6] S. Incerti,[3]

J. Jensen,[5] J. R. Johnson,[21] P. M. King,[20] Yu. G. Kolomensky,[5,12] S. E. Kuhn,[14]

R. Lindgren,[19] R. M. Lombard-Nelsen,[7] J. Marroncle,[7] J. McCarthy,[19] P. McKee,[19]

W. Meyer,[4] G. S. Mitchell,[21,×] J. Mitchell,[18] M. Olson,[9,□] S. Penttila,[11]

G. A. Peterson,[12] G. G. Petratos,[9] R. Pitthan,[16] D. Pocanic,[19] R. Prepost,[21]

C. Prescott,[16] L. M. Qin,[14] B. A. Raue,[8,18] D. Reyna,[1,◦] L. S. Rochester,[16] S. Rock,[1,12]

O. A. Rondon-Aramayo,[19] F. Sabatie,[7] I. Sick,[2] T. Smith,[13,×] L. Sorrell,[1] F. Staley,[7]

S. St.Lorant,[16] L. M. Stuart,[16,§] Z. Szalata,[1] Y. Terrien,[7] A. Tobias,[19] L. Todor,[14]

T. Toole,[1] S. Trentalange,[6] D. Walz,[16] R. C. Welsh,[13] F. R. Wesselmann,[14,19]

T. R. Wright,[21] C. C. Young,[16] M. Zeier,[2] H. Zhu,[19] B. Zihlmann[19]

[1]American University, Washington, D.C. 20016

[2]Institut für Physik der Universität Basel, CH-4056 Basel, Switzerland

[3]University Blaise Pascal, LPC IN2P3/CNRS F-63170 Aubiere Cedex, France

[4]Ruhr-Universität Bochum, Universitätstr. 150, Bochum, Germany

[5]California Institute of Technology, Pasadena, California 91125

[6]University of California, Los Angeles, California 90095

[7]DAPNIA-Service de Physique Nucleaire, CEA-Saclay, F-91191 Gif sur Yvette, France

[8]Florida International University, Miami, Florida 33199

[9]Kent State University, Kent, Ohio 44242

[10]University of Liverpool, Liverpool L69 3BX, United Kingdom

[11]Los Alamos National Laboratory, Los Alamos, New Mexico 87545

[12]University of Massachusetts, Amherst, Massachusetts 01003

[13]University of Michigan, Ann Arbor, Michigan 48109

[14]Old Dominion University, Norfolk, Virginia 23529

[15]Smith College, Northampton, Massachusetts 01063

[16]Stanford Linear Accelerator Center, Stanford, California 94309

[17]Stanford University, Stanford, California 94305

[18]Thomas Jefferson National Accelerator Facility, Newport News, Virginia 23606

[19]University of Virginia, Charlottesville, Virginia 22901

[20]The College of William and Mary , Williamsburg, Virginia 23187

[21]University of Wisconsin, Madison, Wisconsin 53706

◇ Present address: College of William and Mary, Williamsburg, VA 23187

† Permanent Address: Institut des Sciences Nucléaires, IN2P3/CNRS, 38026 Grenoble Cedex, France

‡ Present Address: Duke University, TUNL, Durham, NC 27708

× Present Address: Los Alamos National Laboratory, Los Alamos, NM 87545

□ Present Address: Saint Norbert College, DePere, WI 54115

○ Present Address: DESY, D-22603, Hamburg, Germany

§ Present Address: Lawrence Livermore National Laboratory, Livermore, CA 94551

APPENDIX B

E155 DATA WITHOUT RADIATIVE CORRECTIONS

Table 40: E155 results without Radiative Corrections for $A_{\parallel}$, 2.75° spectrometer.

$\theta \approx 2.75°$

Proton			Deuteron		
$\langle x \rangle$	$\langle Q^2 \rangle$	$A_{\parallel} \pm stat$	$\langle x \rangle$	$\langle Q^2 \rangle$	$A_{\parallel} \pm stat$
0.014	1.00	0.021 ± 0.021	0.014	1.00	0.002 ± 0.046
0.015	1.09	0.026 ± 0.009	0.015	1.09	0.001 ± 0.018
0.017	1.20	0.033 ± 0.006	0.017	1.20	-0.032 ± 0.013
0.019	1.32	0.028 ± 0.006	0.019	1.32	0.003 ± 0.012
0.022	1.45	0.029 ± 0.006	0.022	1.45	0.007 ± 0.012
0.024	1.58	0.034 ± 0.006	0.024	1.59	0.015 ± 0.012
0.027	1.73	0.039 ± 0.006	0.027	1.73	0.009 ± 0.011
0.031	1.89	0.041 ± 0.006	0.031	1.88	0.016 ± 0.011
0.035	2.04	0.048 ± 0.006	0.035	2.04	0.006 ± 0.011
0.039	2.22	0.037 ± 0.006	0.039	2.21	0.016 ± 0.011
0.044	2.40	0.056 ± 0.006	0.044	2.39	0.054 ± 0.011
0.049	2.59	0.061 ± 0.006	0.049	2.58	-0.001 ± 0.011
0.056	2.78	0.059 ± 0.006	0.056	2.77	-0.001 ± 0.011
0.063	2.97	0.062 ± 0.006	0.063	2.97	0.009 ± 0.012
0.071	3.17	0.067 ± 0.007	0.071	3.17	0.032 ± 0.012
0.079	3.37	0.080 ± 0.007	0.079	3.36	0.043 ± 0.012
0.089	3.57	0.064 ± 0.007	0.089	3.57	0.028 ± 0.013
0.101	3.77	0.072 ± 0.007	0.101	3.77	0.039 ± 0.013
0.113	3.97	0.051 ± 0.008	0.113	3.97	0.037 ± 0.014
0.128	4.17	0.064 ± 0.008	0.128	4.17	0.003 ± 0.014
0.143	4.36	0.082 ± 0.008	0.144	4.36	0.039 ± 0.015
0.162	4.54	0.085 ± 0.009	0.162	4.55	0.031 ± 0.016
0.182	4.72	0.073 ± 0.009	0.182	4.72	0.035 ± 0.017
0.205	4.88	0.075 ± 0.010	0.205	4.89	0.042 ± 0.018
0.230	5.04	0.080 ± 0.010	0.230	5.04	0.046 ± 0.020
0.259	5.18	0.092 ± 0.011	0.259	5.19	0.037 ± 0.021
0.292	5.33	0.080 ± 0.012	0.292	5.33	0.058 ± 0.023
0.328	5.46	0.083 ± 0.013	0.328	5.47	0.061 ± 0.026
0.370	5.58	0.064 ± 0.015	0.370	5.58	0.049 ± 0.030
0.416	5.68	0.094 ± 0.017	0.416	5.68	-0.004 ± 0.034
0.468	5.78	0.093 ± 0.019	0.468	5.78	0.092 ± 0.040
0.527	5.87	0.040 ± 0.022	0.527	5.87	0.096 ± 0.047
0.593	5.94	0.061 ± 0.025	0.593	5.95	0.115 ± 0.055
0.667	6.00	0.058 ± 0.029	0.668	6.00	-0.023 ± 0.063
0.751	6.06	0.078 ± 0.033	0.751	6.07	0.092 ± 0.072
0.846	6.12	0.125 ± 0.042	0.846	6.12	-0.063 ± 0.082

Table 41: E155 results without Radiative Corrections for $A_{\|}$, 5.5° spectrometer.

$\theta \approx 5.5°$					
Proton			Deuteron		
$\langle x \rangle$	$\langle Q^2 \rangle$	$A_{\|} \pm stat$	$\langle x \rangle$	$\langle Q^2 \rangle$	$A_{\|} \pm stat$
0.057	4.00	0.143 ± 0.044	0.057	4.00	-0.129 ± 0.092
0.063	4.39	0.121 ± 0.021	0.063	4.39	0.036 ± 0.042
0.071	4.83	0.100 ± 0.014	0.071	4.83	0.011 ± 0.028
0.080	5.30	0.111 ± 0.011	0.080	5.30	0.012 ± 0.021
0.090	5.80	0.120 ± 0.010	0.090	5.80	0.021 ± 0.019
0.101	6.32	0.128 ± 0.009	0.101	6.32	0.072 ± 0.017
0.113	6.87	0.126 ± 0.009	0.113	6.87	0.025 ± 0.017
0.128	7.43	0.166 ± 0.009	0.128	7.43	0.058 ± 0.017
0.144	8.02	0.166 ± 0.009	0.144	8.02	0.087 ± 0.018
0.162	8.62	0.152 ± 0.009	0.162	8.62	0.063 ± 0.018
0.182	9.23	0.167 ± 0.010	0.182	9.23	0.073 ± 0.020
0.205	9.85	0.166 ± 0.010	0.205	9.85	0.069 ± 0.021
0.230	10.48	0.206 ± 0.011	0.230	10.48	0.118 ± 0.023
0.259	11.11	0.194 ± 0.012	0.259	11.12	0.091 ± 0.025
0.292	11.73	0.209 ± 0.013	0.292	11.73	0.149 ± 0.027
0.328	12.34	0.199 ± 0.014	0.328	12.34	0.126 ± 0.030
0.370	12.94	0.225 ± 0.016	0.369	12.94	0.167 ± 0.034
0.416	13.52	0.229 ± 0.018	0.416	13.53	0.105 ± 0.039
0.468	14.08	0.171 ± 0.021	0.468	14.09	0.101 ± 0.046
0.526	14.61	0.202 ± 0.024	0.526	14.63	0.146 ± 0.055
0.592	15.11	0.199 ± 0.030	0.592	15.12	0.265 ± 0.069
0.666	15.58	0.167 ± 0.038	0.666	15.59	0.255 ± 0.088
0.749	15.99	0.229 ± 0.050	0.749	16.00	0.025 ± 0.115
0.843	16.34	0.192 ± 0.078	0.843	16.35	0.148 ± 0.156

Table 42: E155 results without Radiative Corrections for $A_{\|}$, 10.5° spectrometer.

$\theta \approx 10.5°$					
Proton			Deuteron		
$\langle x \rangle$	$\langle Q^2 \rangle$	$A_{\|} \pm stat$	$\langle x \rangle$	$\langle Q^2 \rangle$	$A_{\|} \pm stat$
0.130	10.04	0.286 ± 0.090	0.130	10.04	0.022 ± 0.182
0.145	11.14	0.276 ± 0.038	0.145	11.14	0.020 ± 0.081
0.162	12.35	0.245 ± 0.026	0.163	12.37	0.207 ± 0.056
0.182	13.70	0.292 ± 0.021	0.182	13.70	0.120 ± 0.046
0.205	15.13	0.299 ± 0.020	0.205	15.15	0.178 ± 0.045
0.230	16.66	0.349 ± 0.022	0.230	16.67	0.097 ± 0.047
0.259	18.28	0.331 ± 0.025	0.259	18.28	0.220 ± 0.053
0.291	20.03	0.449 ± 0.029	0.292	20.04	0.263 ± 0.061
0.328	21.86	0.436 ± 0.032	0.328	21.86	0.193 ± 0.068
0.369	23.80	0.412 ± 0.037	0.369	23.79	0.390 ± 0.080
0.413	25.85	0.352 ± 0.052	0.414	25.89	0.212 ± 0.107
0.465	27.94	0.397 ± 0.086	0.465	28.04	0.340 ± 0.166
0.524	30.12	0.292 ± 0.137	0.524	30.19	0.373 ± 0.272
0.590	32.30	0.650 ± 0.193	0.590	32.36	-0.214 ± 0.414
0.663	34.72	0.405 ± 0.313	0.661	34.79	0.312 ± 0.682

BIBLIOGRAPHY

[1] M. Anselmino, A. Efremov and E. Leader, "The Theory and Phenomenology of Polarized Deep Inelastic Scattering," Phys. Rept. **261**, 1 (1995) [hep-ph/9501369].

[2] F. E. Close, "An Introduction To Quarks And Partons," *Academic Press/London 1979, 481p.*

[3] J. D. Bjorken, "Asymptotic Sum Rules At Infinite Momentum," Phys. Rev. **179**, 1547 (1969).

[4] B. Adeva *et al.* [Spin Muon Collaboration (SMC)], "The Spin-Dependent Structure Function $g_1(x)$ of the Proton from Polarized Deep-Inelastic Muon Scattering," Phys. Lett. **B412**, 414 (1997).

[5] M. E. Peskin and D. V. Schroeder, "An Introduction to Quantum Field Theory," *Reading, USA: Addison-Wesley (1995) 842 p.*

[6] P. Bosted, "Polarized Asymmetry Formulas", E143 Technical Note #19 (August 1993), unpublished.

[7] T. Pussieux and R. Windmolders, "A Collection of Formulas for Spin Dependent Deep Inelastic Scattering," DAPNIA-SPHN-95-10 *Presented at Conf. on Spin Structure of the Nucleon, New Haven, Ct., Jan 6-8, 1994.*

[8] F. Halzen and A. D. Martin, "Quarks And Leptons: An Introductory Course In Modern Particle Physics," *New York, Usa: Wiley (1984) 396p.*

[9] B. Lampe and E. Reya, "Spin Physics and Polarized Structure Functions," Phys. Rept. **332**, 1 (2000) [hep-ph/9810270].

[10] E. Leader and E. Predazzi, "An Introduction to Gauge Theories and Modern Particle Physics. Vol. 1: Electroweak Interactions, the New Particles and the Parton Model," *Cambridge, UK: Univ. Pr. (1996) 508 p. (Cambridge monographs on particle physics, nuclear physics and cosmology: 3).*

[11] K. Abe *et al.* [E143 Collaboration], "Measurements of $R = \sigma_L/\sigma_T$ for $0.03 < x < 0.1$ and Fit to World Data," Phys. Lett. **B452**, 194 (1999) [hep-ex/9808028].

[12] M.G. Doncel and E. de Rafael, Nuovo Cimento **4A**, 363 (1971).

[13] J. Soffer and O. V. Teryaev, "Positivity Constraints and Flavor Dependence of Higher Twists," hep-ph/0005132.

[14] E. Leader and M. Anselmino, "A Crisis In The Parton Model: Where, Oh Where Is The Proton's Spin?," Z. Phys. **C41**, 239 (1988).

[15] J. Ashman *et al.* [European Muon Collaboration], "A Measurement of the Spin Asymmetry and Determination of the Structure Function g_1 in Deep Inelastic Muon Proton Scattering," Phys. Lett. **B206**, 364 (1988).

[16] J. Ashman *et al.* [European Muon Collaboration], "An investigation of the spin structure of the proton in deep inelastic scattering of polarized muons on polarized protons," Nucl. Phys. **B328**, 1 (1989).

[17] C. G. Callan and D. J. Gross, "High-Energy Electroproduction And The Constitution Of The Electric Current," Phys. Rev. Lett. **22**, 156 (1969).

[18] K. Abe *et al.* [E154 Collaboration], "Precision Determination of the Neutron Spin Structure Function $g_1^n(x)$," Phys. Rev. Lett. **79**, 26 (1997) [hep-ex/9705012].

[19] D. J. Gross and F. Wilczek, "Asymptotically Free Gauge Theories. 2," Phys. Rev. **D9**, 980 (1974).

[20] F. E. Close and R. G. Roberts, "Consistent Analysis of the Spin Content of the Nucleon," Phys. Lett. **B316**, 165 (1993) [hep-ph/9306289].

[21] R. Erbacher, "New F and D Constants," E155 Technical Note #69 (1998), unpublished.

[22] Review of Particle Physics, Particle Data Group (R. M. Barnett *et al.*), Eur Phys. J. **C3**, (1998).

[23] S. A. Larin and J. A. Vermaseren, "The α_s^3 Corrections to the Bjorken Sum Rule for Polarized Electroproduction and to the Gross-Llewellyn Smith Sum Rule," Phys. Lett. **B259**, 345 (1991).

[24] S. A. Larin, "The Next-to-leading QCD Approximation to the Ellis-Jaffe Sum Rule," Phys. Lett. **B334**, 192 (1994) [hep-ph/9403383].

[25] S. A. Larin, T. van Ritbergen and J. A. Vermaseren, "The α_s^3 Approximation of Quantum Chromodynamics to the Ellis-Jaffe Sum Rule," Phys. Lett. **B404**, 153 (1997) [hep-ph/9702435].

[26] R. Windmolders, "Review of Recent Results in Spin Physics," hep-ph/9905505.

[27] V. N. Gribov and L. N. Lipatov, "Deep Inelastic E P Scattering In Perturbation Theory," Yad. Fiz. **15**, 781 (1972).

V. N. Gribov and L. N. Lipatov, "E+ E- Pair Annihilation And Deep Inelastic E P Scattering In Perturbation Theory," Yad. Fiz. **15**, 1218 (1972).

G. Altarelli and G. Parisi, "Asymptotic Freedom In Parton Language," Nucl. Phys. **B126**, 298 (1977).

Y. L. Dokshitzer, "Calculation Of The Structure Functions For Deep Inelastic Scattering And E+ E- Annihilation By Perturbation Theory In Quantum Chromodynamics. (In Russian)," Sov. Phys. JETP **46**, 641 (1977).

[28] Y. Goto *et al.* [Asymmetry Analysis collaboration], "Polarized Parton Distribution Functions in the Nucleon," Phys. Rev. **D62**, 034017 (2000) [hep-ph/0001046].

[29] B. Adeva *et al.* [Spin Muon Collaboration], "A Next-to-Leading Order QCD Analysis of the Spin Structure Function g_1," Phys. Rev. **D58**, 112002 (1998).

[30] J. D. Bjorken, "Applications Of The Chiral U(6) X (6) Algebra Of Current Densities," Phys. Rev. **148**, 1467 (1966).

[31] J. Ellis and R. Jaffe, "A Sum Rule For Deep Inelastic Electroproduction From Polarized Protons," Phys. Rev. **D9**, 1444 (1974).

[32] E. V. Shuryak and A. I. Vainshtein, "Theory Of Power Corrections To Deep Inelastic Scattering In Quantum Chromodynamics. 2. Q**4 Effects: Polarized Target," Nucl. Phys. **B201**, 141 (1982).

[33] G. Baum *et al.*, "A new measurement of deep inelastic e p asymmetries," Phys. Rev. Lett. **51**, 1135 (1983).

[34] B. Adeva *et al.* [Spin Muon Collaboration], "Measurement of the spin dependent structure function $g_1(x)$ of the deuteron," Phys. Lett. **B302**, 533 (1993).

[35] G. Altarelli, R. D. Ball, S. Forte and G. Ridolfi, "Determination of the Bjorken sum and strong coupling from polarized structure functions," Nucl. Phys. **B496**, 337 (1997) [hep-ph/9701289].

[36] J. Ellis and M. Karliner, "Determination of α_s and the Nucleon Spin Decomposition Using Recent Polarized Structure Function Data," Phys. Lett. **B341**, 397 (1995) [hep-ph/9407287].

[37] R. Voss, "Experiments on Polarized Deep Inelastic Scattering," CERN-PPE-95-131 *Invited Talk at the Workshop on Deep Inelastic Scattering and QCD - DIS 95, Paris, France, 23 - 29 Apr 1995.*

[38] P. L. Anthony *et al.* [E142 Collaboration], "Deep inelastic scattering of polarized electrons by polarized He-3 and the study of the neutron spin structure," Phys. Rev. **D54**, 6620 (1996) [hep-ex/9610007].

[39] R. Brock *et al.* [CTEQ Collaboration], "Handbook of perturbative QCD: Version 1.0," Rev. Mod. Phys. **67**, 157 (1995).

[40] K. Abe *et al.* [E143 collaboration], "Measurements of the Proton and Deuteron Spin Structure Functions g_1 and g_2," Phys. Rev. **D58**, 112003 (1998) [hep-ph/9802357].

[41] B. Tipton, "Measurement of Polarized Parton Distributions with Spin-dependent Deep-inelastic Scattering", Ph. D. thesis, Massachusetts Institute of Technology, (September 1999), unpublished.

[42] A. Magnon, "The Spin Structure of the Nucleon," Nucl. Phys. **A654**, 55 (1999).

[43] R. L. Jaffe, "Where Does the Proton Really Get its Spin?," *Phys. Today 48 (1995) No. 9 24-30.*

[44] M. Lacombe, B. Loiseau, J. M. Richard, R. Vinh Mau, J. Cote, P. Pires and R. De Tourreil, "Parametrization Of The Paris N N Potential," Phys. Rev. **C21**, 861 (1980); M.J. Zuilhof and J.A. Tjon, Phys. Rev. **C22**, 2369 (1980); R.R. Machleid *et. al.*, Phys. Rep. 149, 1. (1987).

[45] A. Afanasev, C. E. Carlson and C. Wahlquist, "Soft Contributions to Hard Pion Photoproduction," Phys. Rev. **D61**, 034014 (2000) [hep-ph/9903493].

[46] G. Baum *et al.* [COMPASS Collaboration], "COMPASS: A Proposal for a Common Muon and Proton Apparatus for Structure and Spectroscopy," CERN-SPSLC-96-14.

[47] A. Afanasev, C. E. Carlson and C. Wahlquist, "Measuring Polarized Gluon and Quark Distributions with Meson Photoproduction," Phys. Rev. **D58**, 054007 (1998) [hep-ph/9706522].

[48] S. J. Brodsky, T. Kinoshita and H. Terazawa, "Two Photon Mechanism Of Particle Production By High-Energy Colliding Beams," Phys. Rev. **D4**, 1532 (1971).

[49] H. Olsen, L.C. Maximon, Phys. Rev. 110 (1958) 589.

[50] J. J. Peralta, A. P. Contogouris, B. Kamal and F. Lebessis, "Photoproduction of large p(t) hadrons by polarized beam and target," Phys. Rev. **D49**, 3148 (1994).

[51] H. Abramowicz, M. Krawczyk, K. Charchula, A. Levy and U. Maor, "Parton distributions in the photon," Int. J. Mod. Phys. **A8**, 1005 (1993).

[52] J. Babcock, E. Monsay and D. Sivers, "Quantum Chromodynamic Predictions For Inclusive Spin-Spin Asymmetries At Large Transverse Momentum," Phys. Rev. **D19**, 1483 (1979).

[53] E. W. Beier *et al.*, "Pion Production At High Transverse Momentum In 24-Gev Proton-Proton Collisions," Phys. Rev. **D18**, 2235 (1978).

[54] P. Bosetti *et al.*, "Inclusive Single-Particle Distributions in $\pi^{\pm}$p Reactions at 8 and 16 GeV/c," Nucl. Phys. **B54**, 141 (1973).

[55] S. I. Manaenkov, "Regge Description of Spin-Spin Asymmetry in Photon Diffractive Dissociation," hep-ph/9903405.

[56] R. Alley *et al.*, "The Stanford Linear Accelerator Polarized Electron Source," Nucl. Instrum. Meth. **A365**, 1 (1995).

[57] G. Mulhollan *et al.*, "Reflections on the SLAC Polarized Electron Source," *Presented at Workshop on Low-Energy Polarized Electrons, St. Petersburg, Russia, 2-5 Sep 1998.*

[58] Z.D. Farkas, H.A. Hoag, G.A. Loew and P.B. Wilson, "Sled: A Method Of Doubling Slac's Energy," *Presented at 9th Int. Conf. on High Energy Accelerators, SLAC, Stanford, Calif., May 2-7, 1974.*

[59] Z.D. Farkas, H.A. Hoag, G.A. Loew and P.B. Wilson, "Recent Progress On Sled, The Slac Energy Doubler," IEEE Trans. Nucl. Sci. **22**, 1299 (1975).

[60] R. Erickson *et al.*, "First operation of the upgraded SLAC A-Line," *Talk given at 5th European Particle Accelerator Conference (EPAC 96), Sitges, Spain, 10-14 Jun 1996.*

[61] P.S. Cooper *et al.*, "Experimental Test Of Special Relativity From A High - Gamma Electron G-2 Measurement," Phys. Rev. Lett. **42**, 1386 (1979).

[62] L. Stuart, "E154 Beam Energies and Spin Precession," E154 Technical Note #6 (1995), unpublished.

[63] S. Kuhn and M. Hing "Toriod Calibration for E143," E143 Technical Note #88 (1995), unpublished.

[64] J. Arrington *et al.*, "A Variable Energy Moeller Polarimeter at the MIT Bates Linear Accelerator Center," Nucl. Instrum. Meth. **A311**, 39 (1992).

[65] H. Band, "Beam Polarization," E155 Collaboration Meeting (June 1998), unpublished.

[66] H.R. Band, G. Mitchell, R. Prepost and T. Wright, "A Moeller Polarimeter for High Energy Electron Beams," Nucl. Instrum. Meth. **A400**, 24 (1997).

[67] P. Steiner, A. Feltham, I. Sick, M. Zeier and B. Zihlmann, "A High-Rate Coincidence Moeller Polarimeter," Nucl. Instrum. Meth. **A419**, 105 (1998).

[68] L.G. Levchuk, "The Intraatomic Motion of Bound Electrons as a Possible Source of a Systematic Error in Electron Beam Polarization Measurements by Means of a Moller polarimeter," Nucl. Instrum. Meth. **A345**, 496 (1994).

[69] H. Band, "Beam Polarization," E155 collaboration meeting, (June 1998), unpublished.

[70] A. Feltham, "Double Arm Moeller," E155 collaboration meeting, (July 1997), unpublished.

[71] G.S. Mitchell, "A Precision Measurement of the Spin Structure Function $g_1(x, Q^2)$ for the Proton and Deuteron," Ph. D. thesis, University of Wisconsin, SLAC-R-540 (June 1999).

[72] S. Bultmann *et al.*, "A Study of Lithium Deuteride as a Material for a Polarized Target," Nucl. Instrum. Meth. **A425**, 23 (1999).

[73] C.D. Jeffries, "Dynamic Orientation of Nuclei," Ann. Rev. Nuc. Sci. **14**, 101 (1964).

[74] P. McKee, private communication.

[75] D. G. Crabb and D. B. Day, "The Virginia/Basel/SLAC Polarized Target: Operation and Performance during Experiment E143 at SLAC," Nucl. Instrum. Meth. **A356**, 9 (1995).

[76] D. G. Crabb, C. B. Higley, A. D. Krisch, R. S. Raymond, T. Roser, J. A. Stewart and G. R. Court, "Observation of a 96% Proton Polarization in Irradiated Ammonia," Phys. Rev. Lett. **64**, 2627 (1990).

[77] O. A. Rondon, "Corrections to Nucleon Spin Structure Asymmetries Measured on Nuclear Polarized Targets," Phys. Rev. **C60**, 035201 (1999), and references therein.

[78] D.G. Crabb, W. Meyer, "Solid Polarized Targets for Nuclear and Particle Physics Experiements," Annu. Rev. Nucl. Part. Sci. 47 (1997) 67.

[79] W.A. Tobias, "E155 Target Model," E155 Technical Note #36 (July 1997), unpublished.

[80] T. D. Averett *et al.*, "A Solid Polarized Target for High-Luminosity Experiments," Nucl. Instrum. Meth. **A427**, 440 (1999).

[81] G. R. Court, D. W. Gifford, P. Harrison, W. G. Heyes and M. A. Houlden, "A High Precision Q Meter for the Measurement of Proton Polarization in Polarized Targets," Nucl. Instrum. Meth. **A324**, 433 (1993).

[82] T. D. Averett, "Measurement of the Spin Structure Function $g_2(x, Q^2)$ for the Proton and Deuteron," Ph. D. thesis, University of Virginia (August 1995), unpublished.

[83] P. M. McKee, "The Spin Structure Function of the Proton from SLAC Experiment E155," Ph. D. thesis, University of Virginia (August 2000), unpublished.

[84] P. McKee, "A Correction to the Proton Polarization from Radiation Damage," E155 Technical Note # 112 (2000), unpublished.

[85] G.G. Petratos *et. al.*, SLAC-PUB-5678 (1991); Proceedings of the IEEE Symposium of Nuclear Science, Santa Fe, NM (Nov. 1991).

[86] Yu. G. Kolomensky, "Precision Measurement of the Neutron Spin Dependent Structure Functions," Ph. D. thesis, University of Massachusetts, Amherst, SLAC-R-503 (February 1997).

[87] P. Bosted, "The 10.5° Spectrometer," E155 Technical Note #10 (October 1996), unpublished.

[88] P. Bosted, "E155 2.75° Spectrometer Calibration from T418," E155 Technical Note #52 (March 1998), unpublished.

[89] L. Sorrell, "A Cursory Verification of the 10.5° Momentum Resolution," E155 Technical Note #56 (May 1998), unpublished.

[90] P. Bosted, "Calibration Studies," E155 collaboration meeting, (July 1997), unpublished.

[91] M. Olson, " Precision Measurement of the g_1 Neutron Spin Structure Function," Ph. D. thesis, Kent University (May 1999), unpublished.

[92] S. Kadlec and R. Lindgren, "Design and Construction of the 10° Spectrometer Scintillator Hodoscope for E155 at SLAC," E155 Technical Note #20 (September 1996), unpublished.

[93] J. Xu, Ph. D. thesis, Syracuse University (1995), unpublished.

[94] J. V. Jelley, "Cerenkov Radiation and its Applications," Pergamon Press, 237 (1958).

[95] P. L. Anthony *et al.* [E155 Collaboration], "Inclusive Hadron Photoproduction from Longitudinally Polarized Protons and Deuterons," Phys. Lett. **B458**, 536 (1999) [hep-ph/9902412].

[96] P. Zyla, "Precision Measurement of the Neutron Spin Structure Function," Ph. D. thesis, Temple University (1998), unpublished.

[97] L. Sorrell, "Information on PMTs used for E154/E155/E155x Cherenkov System," E155 Technical Note #81 (June 1999), unpublished.

[98] M. Buénerd, "Simulation of the Cherenkov Counters of the E154/E155 Experiments," E154 Technical Note #41 (1996), unpublished.

[99] P. Baillon *et. al.*, "Ultraviolet Cerenkov Light Detector," Nucl. Instrum. Meth. **A126**, 13(1975).

[100] D. Kawall, "A Determination of the Neutron Spin Structure Function," Ph. D. thesis, Stanford University(1995), unpublished.

[101] R. Erbacher, "A Precision Measurement of the Spin Structure of the Proton at SLAC," Ph. D. thesis, Stanford University, SLAC-Report-546 (1999).

[102] M. Buénerd, "Vacuum Tightness Requirements for the E155 Cerenkov Counters from their Contamination by Oxygen and Water Vapor in E154," E155 Technical Note #22 (October 1996), unpublished.

[103] L. Sorrell, "Test Information on Mirrors used for E155/E155x Cherenkov System," E155 Technical Note #82 (1999), unpublished.

[104] P. Baillon, A. Braem, G. Gendre, G. Muratori and C. Nichols, "An Improved Method For Manufacturing Accurate And Cheap Glass Parabolic Mirrors," Nucl. Instrum. Meth. **A276**, 492 (1989).

[105] E. L. Garwin, Y. Tomkiewicz and D. Trines, "Method For Elimination Of Quartz Face Phototubes In Cerenkov Counters By Use Of Wavelength Shifter," Nucl. Instrum. Meth. **107**, 365(1973).

[106] M. Buénerd, "Background study in the E154 data," E155 Technical Note #4 (March 1996), unpublished.

[107] J. Groves and J. Olmsted, "Quenching Scintillation Light for E155," E155 Technical Note #23 (September 1996), unpublished.

[108] T. Toole, "Gas Test Results for E155 Cherenkov Detectors," E155 Technical Note #86 (July 1999), unpublished.

[109] G. T. Bartha *et. al.*, "Design And Performance Of The ASP Lead Glass Calorimeter," Nucl. Instrum. Meth. **A275** 59 (1989).

[110] R. Wigmans, "Energy Loss of Particles in Dense Matter - Calorimetry," *Lecture Notes given at ICFA School on Instrumentation in Elementary Particle Physics, Trieste, Italy, Jun 8-10, 1987.*

[111] P. King, "The 10.5° Shower Counter as Used in E155 and Recommendations for Its Operation in the E155 Extension," E155 Technical Note #74 (December 1999), unpublished.

[112] P. King, "Descriptive Listing of T418 Runs," E155 Technical Note #47 (February 1998), unpublished.

L. Sorrell, "Status of T418 Calibration Run," E155 Technical Note #48 (February 1998), unpublished.

[113] P.L. Anthony and Z.M. Szalata, "Flexible High Performance VME Based Data Acquisition System for the ESA Physics Program," SLAC-PUB-7201 (1996).

[114] P. L. Anthony and Z. M. Szalata, "Using VME to Leverage Legacy CAMAC Electronics into a High Speed Data Acquisition System," *Talk given at Nuclear Science Symposium and Medical Imaging Conference, Albuquerque, NM, 9-15 Nov 1997.* SLAC-PUB-7497 (1997).

[115] S. Incerti and F. Sabatie, "E155 Updates of the E154 Clustering Algorithm", E155 Technical Note #31 (April 1997), unpublished.

[116] P. Bosted, "Effect of Target Raster Position on 10° e+/e- Ratio and Momentum Spectrum," E155 Technical Note #53 (March 1998), unpublished.

[117] P. Bosted, " Target Polarization Study using Physics Asymmetries," E155 Technical Note #58 (May 1998), unpublished.

[118] P. Bosted, "Correction to Dilution Factor from Spectrometer Acceptance," E155 Technical Note #62 (June 1998), unpublished.

[119] P. Bosted, "E155 Luminosity Correction to the Spectrometer Rates," E155 Technical Note #63 (June 1998), unpublished.

[120] P. Bosted, " 10.5 degree electron definitions," E155 Technical Note #68 (September 1998), unpublished.

[121] W. A. Tobias, " NMR Coil Configuration and Effects Observed during the Operation of the E155 Polarized Target," *Proceedings of the Workshop on NMR in Polarized Targets, April 15 & 16, 1998*, by S. Bueltmann (ed.) and D. G. Crabb (ed.), (1998), unpublished.

[122] P. Bosted, " Problems with E155 LiD target Insert 5, bottom cell," E155 Technical Note #66 (1998), unpublished.

[123] T. Toole, "Systematic Studies," E155 collaboration meeting, (July 1997), unpublished.

[124] S. Rock, " Cerenkov Counter Efficiency and Positrons," E155 Technical Note #38 (1997), unpublished.

[125] T. Toole, " E155 Cherenkov Detector Performance," E155 Technical Note #99 (1999), unpublished.

[126] C. Y. Prescott *et al.*, "Further Measurements Of Parity Nonconservation In Inelastic Electron Scattering," Phys. Lett. **B84**, 524 (1979).

[127] P. Bosted, " Electroweak Correction to E154," E154 Technical Note #29 (1995), unpublished.

[128] R. Arnold *et al.*, "DIS-Parity: Parity Violation in Deep Inelastic Electron Scattering," SLAC-PROPOSAL-E-149.

[129] Yu. Kolomensky, "Rate Dependence Studies with "Pulse Fiction"," E155 collaboration meeting, July 1997, unpublished.

[130] T. Averett, " Dilution factor and corrections for Nitrogen and Lithium Polarizations," E155 Technical Note #27 (1997), unpublished.

[131] A. Tobias, "Lithium Deuteride Analysis," E155 Technical Note #78 (February 1999), unpublished.

[132] P. Bosted, " Solid Targets for E155," E155 Technical Note #11 (1996), unpublished.

[133] W.A. Tobias, "Target Packing Fraction and Dilution," E155 Collaboration Meeting (February 1998), unpublished.

[134] J. Bauer and O. Rondon, "Formulas for Nitrogen Correction," E143 Technical Note #71 (September 1994), unpublished.

[135] J. M. Bauer, "Measurement of the Longitudinal Deuteron Spin-Structure Function in Deep-Inelastic Scattering," Ph. D. thesis, University of Massachusetts, Amherst, SLAC-R-0492 (September 1996).

[136] O. Rondon, "Nuclear Corrections," E155 Collaboration Meeting (February 1998), unpublished.

[137] O. Rondon, " 7Li Corrections," E155 Technical Note #26 (March 1997), unpublished.

[138] B. S. Pudliner, V. R. Pandharipande, and J. Carlson, "Quantum Monte Carlo Calculations of Nuclei with A $\leq$ 7," Phys. Rev. C **56**, 1720 (1997).

[139] D. E. Reyna, "Measurement of the Spin Structure Function $g_2(x, Q^2)$ for the Neutron," Ph. D. thesis, American University, (1998), UMI-98-40874.

[140] D. E. Groom *et al.*, "Review of Particle Physics," Eur. Phys. J. **C15**, 1 (2000).

[141] S. Incerti and V. Breton, " A Method To Estimate the Pion Contamination," E154 Technical Note #36 (1996), unpublished.

[142] F. Sabatie, " Background Subtraction," E154 Technical Note #45 (1996), unpublished.

[143] F. R. Wesselmann, "Precision Measurement of the Spin Structure Function of the Proton and the Deuteron," Ph. D. thesis, Old Dominion University (2000), SLAC-R-557.

[144] D. Reyna, " E154 Radiative Corrections," E154 Technical Note #52 (January 1997), unpublished.

[145] T. V. Kukhto and N. M. Shumeiko, "Radiative Effects In Deep Inelastic Scattering Of Polarized Leptons By Polarized Nucleons," Nucl. Phys. **B219**, 412 (1983).

[146] S. Kuhn and F. R. Wesselmann, "The Radiative Dilution Factor f_{RC}," E155 Technical Note # 59 (July 1999), unpublished.

[147] F. R. Wesselmann, "Calculation of Radiative Corrections [for E155]," E155 Technical Note # 100 (September 1999), unpublished.

[148] F. R. Wesselmann, "GUF Fit to Global g_1/F_1 Data Set," E155 Technical Note # 116 (2000), unpublished.

[149] M. Kuriki, "Study of Deep Inelastic Scattering of Polarized Electrons Off Polarized Deuterons," SLAC-R-0482.

[150] "SLACSpeak: A Glossary and Acronym List," SLAC-I-41A-60000-001-R002.

[151] J. Huston, E. Kovacs, S. Kuhlmann, H. L. Lai, J. F. Owens and W. K. Tung, "A Global QCD Study of Direct Photon Production," Phys. Rev. **D51**, 6139 (1995) [hep-ph/9501230].

[152] P. L. Anthony *et al.* [E155 Collaboration], "Measurements of the Q^2-Dependence of the Proton and Neutron Spin Structure Functions g_1^p and g_1^n," hep-ph/0007248.

[153] D. E. Wiser, "Inclusive Photoproduction Of Protons, Kaons, And Pions At SLAC Energies," Ph. D. thesis, University of Wisconsin, (May 1977), UMI 77-19743.

[154] M. Arneodo *et al.* [New Muon Collaboration.], "Measurement of the Proton and the Deuteron Structure Functions, F_2^p and F_2^d," Phys. Lett. **B364**, 107 (1995) [hep-ph/9509406].

[155] S. Wandzura and F. Wilczek, "Sum Rules For Spin Dependent Electroproduction: Test Of Relativistic Constituent Quarks," Phys. Lett. **B72**, 195 (1977).

[156] G. S. Mitchell, "Low x Contributions from E154 NLO Fit," E155 Technical Note # 75 (1999), unpublished.

[157] K. Abe *et al.* [E154 Collaboration], "Next-to-Leading Order QCD Analysis of Polarized Deep Inelastic Scattering Data," Phys. Lett. **B405**, 180 (1997) [hep-ph/9705344].

[158] M. Kuriki, "Systematic Error Analysis," E143 Technical Note # 75 (1994), unpublished.

[159] K. Abe *et al.* [E143 Collaboration], "Measurements of the Q^2 Dependence of the Proton and Deuteron Spin Structure Functions g_1^p and g_1^d," Phys. Lett. **B364**, 61 (1995) [hep-ex/9511015].

[160] M. J. Alguard *et al.*, "Deep Inelastic e p Asymmetry Measurements and Comparison with the Bjorken Sum Rule and Models of the Proton Spin Structure," Phys. Rev. Lett. **41**, 70 (1978).

[161] B. Adeva *et al.* [Spin Muon Collaboration], "Spin asymmetries A_1 and Structure Functions g_1 of the Proton and the Deuteron from Polarized High Energy Muon Scattering," Phys. Rev. **D58**, 112001 (1998).

[162] A. Airapetian *et al.* [HERMES Collaboration], "Measurement of the Proton Spin Structure Function g_1^p with a Pure Hydrogen Target," Phys. Lett. **B442**, 484 (1998) [hep-ex/9807015].

[163] K. Ackerstaff *et al.* [HERMES Collaboration], "Measurement of the Neutron Spin Structure Function g_1^n with a Polarized He-3 Internal Target," Phys. Lett. **B404**, 383 (1997) [hep-ex/9703005].

[164] M. Gluck, E. Reya and A. Vogt, "Dynamical parton distributions revisited," Eur. Phys. J. **C5**, 461 (1998) [hep-ph/9806404].

[165] A. Airapetian *et al.* [HERMES Collaboration], "Measurement of the Spin Asymmetry in the Photoproduction of Pairs of High p_T Hadrons at HERMES," Phys. Rev. Lett. **84**, 2584 (2000) [hep-ex/9907020].

[166] G. Bunce, N. Saito, J. Soffer and W. Vogelsang, "Prospects for Spin Physics at RHIC," Submitted to Ann. Rev. Nucl. Part. Sci., [hep-ph/0007218].

[167] S. D. Bass and A. D. Roeck, "g_1 at Low x and Low Q^2 with Polarized ep Colliders," hep-ph/0008289.